Universidad Zaragoza
1474

Ph.D. Thesis

Ventricular Arrhythmic Risk Assessment by T-wave Morphology Markers in LQTS, Brugada Syndrome and Ischemic Cardiomyopathy

Author

Neurys Gómez Fonseca

Supervisors

Pablo Laguna Lasaosa

Juan Pablo Martínez Cortés

Universidad de Zaragoza
2026

Ventricular Arrhythmic Risk Assessment by T-wave Morphology Markers in LQTS, Brugada Syndrome and Ischemic Cardiomyopathy

Neurys Gómez Fonseca, 2026
Ventricular Arrhythmic Risk Assessment by T-wave Morphology Markers in LQTS, Brugada Syndrome and Ischemic Cardiomyopathy

Date of current version: Wednesday 28th October, 2026

This Ph.D. thesis belongs to the inter-universitary Biomedical Engineering Ph.D. Program of the University of Zaragoza and Polytechnic University of Cataluña, and has been developed within the Biomedical Signal Interpretation and Computational Simulations (BSiCoS) group of the Aragón Institute for Engineering Research (I3A), and the Department of Electronic Engineering and Communications at the University of Zaragoza (Zaragoza, Spain).

The research presented in this thesis was supported in part by University of Zaragoza-Santander Universities Ph.D. fellowship for Ibero-Amarican students, a program funded by Santander Bank, and by predoctoral research contract from the Spanish Biomedical Research Networking Center in Bioengineering, Biomaterials and Nanomedicine (CIBER-BBN), and by projects under Grants LMP94_21, funded by the Department of Science, University and Knowledge Society of the Goverment of Aragón, and TED2021-130459B-I00, funded by MCIN/AEI/10.13039/501100011033 and by the European Union NextGenerationEU/PRTR. Additional support for the research activities was provided by the Ministry of Science, Innovation and Universities, Spain, projects: PID2019-104881RBI00, PID2021-128972OA-100, PID2022-140556OB-I00, PID2023-148975OB-I00, and CNS2023-143599, and by Aragón Government group: BSiCoS T39_23R. Computations were performed by ICTS NANBIOSIS (HPC Unit 27 at University of Zaragoza).

This thesis was printed thanks to the financial support of BSiCoS Group at University of Zaragoza.

To my angels in heaven.
To my angels here on earth, Anabel and Alejandro.

ABSTRACT

Sudden cardiac death (SCD) is frequently the final manifestation of life-threatening ventricular arrhythmias arising from an electrically vulnerable myocardial substrate. Ventricular repolarization abnormalities, and particularly increased spatial and temporal heterogeneity of repolarization, play a central role in the initiation and maintenance of these arrhythmias. The electrocardiogram (ECG) provides a non-invasive representation of cardiac electrical activity and contains clinically relevant information about ventricular repolarization within the T wave. However, most conventional electrocardiographic markers rely on the measurement of intervals, amplitudes, or individual fiducial points and may therefore capture only a limited part of the information contained in the overall T-wave morphology. This limitation is particularly relevant when repolarization abnormalities are expressed through complex morphological changes rather than through simple prolongation or shortening of a specific interval.

The main objective of this thesis is to evaluate quantitative ECG-markers that characterize T-wave morphology for ventricular arrhythmic risk assessment. To this end, a time-warping methodology is used to compare T waves and quantify the temporal reparameterization required to align their morphologies. The methodology is evaluated in complementary clinical and experimental scenarios in which malignant ventricular arrhythmias represent a major concern: acute myocardial ischemia and infarction, long QT syndrome type 2 (LQT2), and Brugada syndrome (BrS). These conditions involve different pathophysiological mechanisms and electrocardiographic manifestations, allowing the capacity of the proposed markers to characterize both acquired and inherited arrhythmogenic substrates to be investigated.

A common ECG signal processing framework was developed and then adapted to the characteristics of each study. The framework includes ECG preprocessing, automatic fiducial detection and delineation, spatial transfor-

mation by principal component analysis (PCA), computation of representative mean warped T-waves (MWTWs), application-specific criteria for selecting the reference MWTW, and computation of the corresponding time-warping markers. Within this framework, a T-wave peak-to-end restricted time-warping approach was proposed to characterize morphological changes associated with repolarization dispersion specifically during terminal ventricular repolarization, while reducing the influence of the preceding ST segment. Accordingly, depending on the application, morphology was assessed either over the complete T wave or using this newly proposed restricted approach. Two complementary reference-based comparison strategies were considered. In acute ischemia studies, each waveform was compared with a subject-specific reference obtained under control conditions. In the channelopathy studies, patient-specific waveforms were compared with sex-, heart-rate-, and lead-matched normal reference waveforms derived from a large population cohort to quantify morphology variation (T-wave morphology variation (TMV) index). In addition, morphology restitution was characterized by quantifying changes in T-wave morphology with heart rate (T-wave morphology restitution (TMR) index). When these two approaches were restricted to the T-wave peak-to-end interval (T_{pe}), they yielded the T-wave peak-to-end morphology variation (TPEMV) and T-wave peak-to-end morphology restitution (TPEMR) indices, respectively.

The first application investigated T_{pe} morphology during transient coronary occlusion in patients undergoing percutaneous coronary intervention. A time-warping-based index restricted to this segment derived from the PCA lead, $d^{\mathrm{PCA}}_{w,\mathrm{T}_{pe}}$, was proposed to quantify ischemia-induced repolarization changes. The marker increased rapidly during balloon inflation, with changes that clearly exceeded the spontaneous variability observed in control recordings. These alterations occurred in a large proportion of patients and showed a spatial distribution related to the location of the occluded coronary artery. Compared with classical indices obtained from the same region of the T wave, the proposed marker provided a more sensitive and robust characterization of the changes induced by ischemia. These findings indicate that analyzing the morphology of the T_{pe} interval captures information that is not conveyed by measuring only the duration of T_{pe} interval.

The association between T_{pe} morphology changes, quantified by $d^{\mathrm{PCA}}_{w,\mathrm{T}_{pe}}$, and ventricular fibrillation (VF) was subsequently investigated in a closed-chest porcine infarction model. The longer observation period after coronary occlusion enabled the temporal evolution of $d^{\mathrm{PCA}}_{w,\mathrm{T}_{pe}}$ to be evaluated in animals that developed delayed VF and in those that remained VF free. Although the marker increased in both groups as ischemia progressed, larger and more

sustained changes were observed in animals that subsequently developed VF. Significant differences between groups appeared during the early stages of ischemia and the magnitude of those changes predicted delayed VF more accurately and consistently than the classical T_{pe} interval. These findings support $d^{\mathrm{PCA}}_{w,\mathrm{T}_{pe}}$ as a promising non-invasive marker for early prediction of delayed VF during myocardial infarction.

In a subsequent study, $d^{\mathrm{PCA}}_{w,\mathrm{T}_{pe}}$ was evaluated as a non-invasive surrogate of ventricular repolarization dispersion by directly comparing it with invasively measured dispersion of repolarization (DOR) in an open-chest porcine infarction model using simultaneous surface ECG and intramyocardial electrogram recordings. The results showed that $d^{\mathrm{PCA}}_{w,\mathrm{T}_{pe}}$, DOR, and the classical T_{pe} indices changed dynamically during coronary ligation and discriminated animals according to delayed VF susceptibility. Linear regression analyses further showed a stronger relationship between $d^{\mathrm{PCA}}_{w,\mathrm{T}_{pe}}$ and DOR than between T_{pe} and DOR. The warping-based marker also showed predictive performance comparable to that of the invasive DOR, while providing earlier and more robust prediction of delayed VF than the classical T_{pe} interval.

The evaluation of time-warping-based markers was then extended to congenital repolarization abnormalities in patients with LQT2. The TMV index quantified differences between each patient's representative T-wave morphology and a healthy population-based reference derived from the UK Biobank. More negative TMV values, reflecting greater morphological changes from the normal pattern, were significantly associated with the occurrence of cardiac events. This association remained significant after adjustment for corrected QT (QT_c) interval, sex, and an established T-wave morphology combination score (MCS), suggesting that TMV captures morphology-related information not fully conveyed by these covariates. These findings support the potential value of TMV as a complementary marker for risk stratification in LQT2.

Finally, T-wave morphology restitution and variation were investigated in patients with BrS using 24-hour Holter ECG recordings. The analyses were performed over both the complete T wave and the T_{pe} interval. TPEMR differentiated patients with BrS from controls, whereas restitution of the complete T-wave morphology, TMR, was more closely associated with the presence of a spontaneous type 1 Brugada pattern. Among the morphology variation indices, TPEMV provided the most consistent characterization of both the Brugada phenotype and spontaneous type 1 expression. However, none of the morphology-based markers consistently differentiated symptomatic from asymptomatic patients. In contrast, QRS duration showed the broadest overall differences and the clearest, although localized, separation between symp-

tomatic and asymptomatic patients. These findings support the complementary contribution of repolarization and depolarization-related ECG markers in BrS and show that their expression depends strongly on the analyzed lead and heart-rate range, although their clinical relevance remains to be established in larger and independent cohorts.

In conclusion, this thesis demonstrates that time-warping-based T-wave morphology markers provide a non-invasive and morphology-aware characterization of ventricular repolarization abnormalities across different arrhythmogenic conditions. These markers capture morphological information that may remain partially hidden when ECG analysis is reduced to fiducial-point-based indices, although their most relevant formulation and interpretation depend on the underlying condition. Rather than replacing established clinical and electrocardiographic indices, they may provide complementary information for a more comprehensive assessment of ventricular arrhythmic risk. Further studies are needed to assess their potential clinical utility.

Keywords: Sudden cardiac death; Arrhythmic risk; Time-warping; Acute ischemia; Long QT syndrome; Brugada syndrome; Electrocardiogram; T-wave morphology; Ventricular fibrillation; Ventricular repolarization dispersion.

RESUMEN

La muerte súbita cardiaca (SCD, del inglés "Sudden Cardiac Death") constituye con frecuencia la manifestación final de arritmias ventriculares potencialmente mortales que se originan en un sustrato miocárdico eléctricamente vulnerable. Las alteraciones de la repolarización ventricular y, en particular, el aumento de la heterogeneidad espacial y temporal de la repolarización desempeñan un papel central en el inicio y el mantenimiento de estas arritmias. El electrocardiograma (ECG, del inglés "Electrocardiogram") proporciona una representación no invasiva de la actividad eléctrica cardiaca y contiene, en la onda T, información clínicamente relevante sobre la repolarización ventricular. Sin embargo, la mayoría de los marcadores electrocardiográficos convencionales se basan en la medición de amplitudes o intervalos a través de puntos fiduciales individuales y, por tanto, pueden capturar solo una parte limitada de la información contenida en la morfología global de la onda T. Esta limitación resulta especialmente relevante cuando las alteraciones de la repolarización se manifiestan mediante cambios morfológicos complejos, en lugar de mediante una simple prolongación o acortamiento de un intervalo específico.

El objetivo principal de esta tesis es evaluar marcadores cuantitativos derivados del ECG que caractericen la morfología de la onda T para la evaluación del riesgo arrítmico ventricular. Para ello se utiliza una metodología basada en *time-warping* que permite comparar ondas T y cuantificar la reparametrización temporal necesaria para alinear sus morfologías. La metodología se evalúa en escenarios clínicos y experimentales complementarios en los que las arritmias ventriculares malignas constituyen una preocupación relevante: la isquemia miocárdica aguda y el infarto de miocardio, el síndrome de QT largo tipo 2 (LQT2, del inglés "Long QT Syndrome Type 2") y el síndrome de Brugada (BrS, del inglés "Brugada Syndrome"). Estas enfermedades presentan diferentes mecanismos fisiopatológicos y manifestaciones electrocardiográficas, lo que permite investigar la capacidad de los marcadores propuestos para carac-

terizar sustratos arrítmicos tanto adquiridos como hereditarios.

Se desarrolló un marco común de procesamiento de la señal de ECG, que posteriormente se adaptó a las características de cada estudio. Este marco incluye el preprocesamiento del ECG, la detección y delineación automática de puntos fiduciales, la transformación espacial mediante análisis de componentes principales (PCA, del inglés "Principal Component Analysis"), el cálculo de ondas T medias reparametrizadas representativas (MWTW, del inglés "Mean Warped T-Wave"), criterios específicos para cada aplicación destinados a seleccionar la MWTW de referencia y el cálculo de los correspondientes marcadores de *time-warping*. Dentro de este marco, se propuso un enfoque de *time-warping* restringido al intervalo entre el pico y el final de la onda T (T_{pe}, del inglés "T-wave peak-to-end interval") para caracterizar cambios morfológicos asociados con la dispersión de la repolarización, específicamente durante la repolarización ventricular terminal, reduciendo al mismo tiempo la influencia del segmento ST precedente. En consecuencia, dependiendo de la aplicación, la morfología se evaluó sobre la onda T completa o mediante este nuevo enfoque restringido. Se consideraron dos estrategias complementarias de comparación basadas en referencias. En los estudios de isquemia aguda, cada forma de onda se comparó con una referencia específica del sujeto obtenida en condiciones de control. En los estudios de las canalopatías, las formas de onda representativas de cada paciente se compararon con formas de onda normales de referencia emparejadas por sexo, frecuencia cardiaca y derivación, obtenidas a partir de una amplia cohorte poblacional, para cuantificar la variación de la morfología de la onda T (TMV, del inglés "T-wave Morphology Variation"). Además, la restitución morfológica se caracterizó mediante la cuantificación de los cambios de la morfología de la onda T con la frecuencia cardiaca, dando lugar al índice de restitución de la morfología de la onda T (TMR, del inglés "T-wave Morphology Restitution"). Cuando estos dos enfoques se restringieron al T_{pe}, dieron lugar a los índices de variación de la morfología del T_{pe} (TPEMV) y de restitución de la morfología del T_{pe} (TPEMR), respectivamente.

La primera aplicación investigó la morfología del T_{pe} durante la oclusión coronaria transitoria en pacientes sometidos a intervención coronaria percutánea. Se propuso un índice basado en *time-warping*, restringido a este segmento y obtenido a partir de la derivación PCA, $d_{w,T_{pe}}^{PCA}$, para cuantificar los cambios de la repolarización inducidos por la isquemia. El marcador aumentó rápidamente durante el inflado del balón, con cambios que superaron claramente la variabilidad espontánea observada en los registros de control. Estas alteraciones aparecieron en una elevada proporción de pacientes y mostraron una distribución espacial relacionada con la localización de la arteria coronaria ocluida. En

comparación con los índices clásicos obtenidos en la misma región de la onda T, el marcador propuesto proporcionó una caracterización más sensible y robusta de los cambios inducidos por la isquemia. Estos hallazgos indican que el análisis de la morfología del intervalo T_{pe} capta información que no queda reflejada mediante la medición exclusiva de su duración.

Posteriormente, se investigó la asociación entre los cambios en la morfología del T_{pe}, cuantificados mediante $d^{\mathrm{PCA}}_{w,T_{pe}}$, y la fibrilación ventricular (VF, del inglés "Ventricular Fibrillation") en un modelo porcino de infarto a tórax cerrado. El periodo de observación mayor posterior a la oclusión coronaria permitió evaluar la evolución temporal de $d^{\mathrm{PCA}}_{w,T_{pe}}$ en los animales que desarrollaron VF tardía y en aquellos que permanecieron libres de VF. Aunque el marcador aumentó en ambos grupos a medida que progresaba la isquemia, los animales que posteriormente desarrollaron VF presentaron cambios de mayor magnitud y más sostenidos. Las diferencias significativas entre los grupos aparecieron durante las primeras fases de la isquemia, y la magnitud de estos cambios predijo la VF tardía de forma más precisa y consistente que la duración del intervalo T_{pe}. Estos resultados respaldan a $d^{\mathrm{PCA}}_{w,T_{pe}}$ como un marcador no invasivo prometedor para la predicción temprana de la VF tardía durante el infarto de miocardio.

En un estudio posterior, $d^{\mathrm{PCA}}_{w,T_{pe}}$ se evaluó como sustituto no invasivo de la dispersión de la repolarización ventricular mediante su comparación directa con la dispersión de la repolarización (DOR, del inglés "Dispersion of Repolarization") medida invasivamente en un modelo porcino de infarto a tórax abierto, utilizando registros simultáneos de ECG de superficie y electrogramas intramiocárdicos. Los resultados mostraron que $d^{\mathrm{PCA}}_{w,T_{pe}}$, la DOR y el índice clásico T_{pe} cambiaron dinámicamente durante la ligadura coronaria y discriminaron a los animales de acuerdo con su susceptibilidad a desarrollar VF tardía. Los análisis de regresión lineal mostraron, además, una relación más estrecha entre $d^{\mathrm{PCA}}_{w,T_{pe}}$ y la DOR que entre el T_{pe} y la DOR. El marcador basado en *warping* también mostró una capacidad predictiva comparable a la de la DOR invasiva, al tiempo que proporcionó una predicción más temprana y robusta de la VF tardía que el intervalo T_{pe} clásico.

La evaluación de los marcadores basados en *time-warping* se extendió posteriormente a las alteraciones congénitas de la repolarización en pacientes con LQT2. El índice TMV cuantificó las diferencias entre la morfología representativa de la onda T de cada paciente y una referencia de población sana derivada del UK Biobank. Los valores más negativos de TMV, indicativos de mayores cambios morfológicos respecto al patrón normal, se asociaron significativamente con la aparición de eventos cardiacos. Esta asociación se mantuvo significativa tras ajustar por el intervalo QT corregido (QT_c), el sexo y un marcador combi-

nado (MCS, del inglés "T-wave morphology combination score"), lo que sugiere que TMV capta información relacionada con la morfología que no queda completamente reflejada por estas covariables. Estos resultados respaldan el valor potencial de TMV como marcador complementario para la estratificación del riesgo en LQT2.

Finalmente, se investigaron la restitución y la variación de la morfología de la onda T en pacientes con BrS mediante registros Holter de ECG de 24 horas. Los análisis se realizaron tanto sobre la onda T completa como sobre el intervalo T_{pe}. El índice TPEMR diferenció a los pacientes con BrS de los controles, mientras que la restitución de la morfología de la onda T completa, TMR, estuvo más estrechamente relacionada con la presencia de un patrón de Brugada tipo 1 espontáneo. Entre los índices de variación morfológica, TPEMV proporcionó la caracterización más consistente tanto del fenotipo de Brugada como de la expresión espontánea del patrón tipo 1. Sin embargo, ninguno de los marcadores basados en la morfología diferenciaron de manera consistente a los pacientes sintomáticos de los asintomáticos. En cambio, la duración del complejo QRS mostró las diferencias globales más amplias y la separación más clara, aunque localizada, entre pacientes sintomáticos y asintomáticos. Estos hallazgos respaldan la contribución complementaria de los marcadores de ECG relacionados con la repolarización y la despolarización en el BrS, y muestran que su expresión depende en gran medida de la derivación analizada y del rango de frecuencia cardiaca, aunque su relevancia clínica aún debe establecerse en cohortes independientes y de mayor tamaño.

En conclusión, esta tesis demuestra que los marcadores de morfología de la onda T basados en *time-warping* proporcionan una caracterización no invasiva y basada en la morfología de las alteraciones de la repolarización ventricular en diferentes condiciones arrítmicas. Estos marcadores captan información morfológica que puede quedar parcialmente oculta cuando el análisis del ECG se limita a índices basados en puntos fiduciales, aunque su formulación e interpretación más relevantes dependen de la enfermedad subyacente. En lugar de sustituir a los índices clínicos y electrocardiográficos establecidos, pueden aportar información complementaria para una evaluación más completa del riesgo arrítmico ventricular. Se requieren estudios adicionales para evaluar su posible utilidad clínica.

Palabras clave: Muerte súbita cardiaca; Riesgo arrítmico; *Time-warping*; Isquemia aguda; Síndrome de QT largo; Síndrome de Brugada; Electrocardiograma; Morfología de la onda T; Fibrilación ventricular; Dispersión de la repolarización ventricular.

ACKNOWLEDGMENTS

Reaching the end of this thesis is also an opportunity to thank all those who have accompanied me throughout these years, both scientifically and personally. To all of you, my sincerest gratitude for leaving, each in your own way, a mark on this journey.

First and foremost, I would like to thank my supervisors, Pablo Laguna and Juan Pablo Martínez, for your dedication, your constant availability, and everything I have learned by your side. Thank you for teaching me to conduct research with rigor and perseverance, but also for the warmth and humility with which you have accompanied me throughout this journey. Pablo, thank you for teaching me never to take anything for granted, to keep questioning every result until reaching the why behind it, and for your passion for research that inevitably rubs off on those of us who work with you. Thank you also for a closeness that, often quietly, has made the distance from home feel a little smaller. Juan Pablo, thank you for your patience, for every discussion and every contribution, and for the enviable serenity with which you convey, at the same time, a passion for research that encourages me to keep asking questions and always strive for a better version of everything.

I would also like to thank Julia Ramírez for her valuable contribution to the development of this thesis. Thank you for every discussion and contribution, for your rigor, and for knowing how to recognize the value of each piece of work and push it as far as it could go. And, of course, for allowing me to pick up and continue, in my own way, your warping legacy. To Alba Martín, thank you for your contributions to the work we shared and for always being available and willing to help whenever I knocked on your door.

To the research groups in Sweden and Russia, thank you for your willingness to collaborate and for the many scientific exchanges and discussions we have shared. Special thanks to Pyotr Platonov and Jan Azarov for your leadership and scientific vision. Pyotr, thank you also for welcoming me into your group

during my research stays, for the enriching discussions, and for the hospitality that made the already chilly Lund autumn much easier to bear. To Alena Abramochkina and Aleksei Savelev, thank you for all the work we did together on the data; and Aleksei, thank you also for the countless emails and for always being just a click away. My thanks also go to our collaborators at Hospital Clínic de Barcelona for their contribution to this project and for all the work we have shared.

To Angel Cano and Maikel Noriega, thank you for bringing me closer to biomedical engineering research and for accompanying me through my first steps in research. And to Maikel, also for showing me the way to BSICoS.

To everyone at BSICoS, thank you for making the group much more than just a workplace and for all the moments we have shared, both inside and outside the lab, which have made this stage of my life so much better. And special thanks to all of you who have shared an office with me along the way.

I would also like to thank the administrative staff at I3A and BSICoS for all your help throughout these years. Special thanks to Dorse Martínez for her kindness and willingness to help whenever I needed her, and to David Hernando for always being ready to lend a hand whenever a technical problem arose.

Outside the lab, thank you to all those who, over these years, have opened the doors of your lives to me and made me feel that I belonged. You have helped me build a home away from home.

To my family and friends, in Cuba and now scattered across different parts of the world, thank you for remaining close despite the distance and for accompanying me throughout this journey.

And finally, to Anabel and Alejandro, who have always been my refuge. Anabel, my traveling companion since long before any of this began, thank you for believing in that crazy idea of starting a Ph.D. far from home, for standing by me first from Cuba and then for joining me on this journey and continuing to walk by my side; for being there through the good days and the not-so-good ones and, above all, for always believing in me, even when I found it difficult to believe in myself. Alejandro, thank you for being my greatest inspiration and my guiding light every day.

CONTENTS

Abstract iii

Resumen vii

Acknowledgments xi

List of Acronyms xix

1 Introduction 1

1.1 Motivation 1
1.2 The Heart 3
1.2.1 Cardiac Anatomy and Mechanical Function 3
1.2.2 Cellular Electrophysiology 5
1.2.3 Electrical Activity of the Heart 6
1.2.4 Repolarization: Dispersion and Restitution 8
1.3 Cardiac Electrical Recordings 10
1.3.1 Electrocardiogram 11
1.3.2 Electrogram 16
1.4 Interval- and Morphology-Based Repolarization Characterization 17
1.5 Cardiomyopathies and Channelopaties Addressed in the Thesis . . 18
1.5.1 Acute Ischemia and Myocardial Infarction 18
1.5.2 Long QT Syndrome 20
1.5.3 Brugada Syndrome 24
1.6 Objective and Outline of the Thesis 30

2 General Methods for ECG Signal Processing 35
2.1 ECG Processing Pipeline 36
2.1.1 ECG Preprocessing 36
2.1.2 Fiducial Detection and Delineation 37
2.1.3 Spatial Principal Component Analysis 39
2.2 Classical ECG Markers (Intervals and Amplitudes) 41
2.3 Time-Warping Analysis 42
2.3.1 Unsigned Time-Warping Marker 44
2.3.2 Signed Time-Warping Marker 45
2.3.3 T-wave Peak-to-End Restricted Warping Analysis 46
2.3.4 Mean Warped T-Wave 47
2.3.5 Weighted Time-Warping Markers 49

3 T_{pe} Time-Warping to Track Ischemia-Induced Repolarization Changes 53
3.1 Introduction 54
3.2 Methods 55
3.2.1 Dataset 55
3.2.2 ECG Pre-processing 56
3.2.3 Quantification of T-Mave Morphology Changes 56
3.2.4 Repolarization Changes Analysis 58
3.2.5 Classical Indices of Ventricular Repolarization 60
3.2.6 Statistical Analysis 60
3.3 Results 60
3.3.1 Changes of $d^{\mathrm{PCA}}_{w,\mathrm{T}_{pe}}$ During Occlusion 60
3.3.2 Temporal Distribution Analysis 63
3.3.3 Spatial Distribution Analysis 65
3.3.4 Classic Local Measurements 66
3.4 Discussion 69
3.4.1 Time Course and Prevalence Analysis 70
3.4.2 Spatial Analysis 71
3.4.3 Classic Local Measurements 71
3.4.4 Clinical Implications 72
3.4.5 Limitations 73
3.5 Conclusions 74

4 T-Wave Peak-to-End Time-Warping predicts VF in a Porcine MI model 75
4.1 Introduction 75
4.2 Methods 77
4.2.1 Experimental Data Set and Protocol 77
4.2.2 ECG Pre-processing 78

4.2.3 Time-Warping Quantification of T_{pe} Interval Changes ... 78
4.2.4 Statistical Analysis ... 79
4.3 Results ... 80
4.3.1 Changes of $d_{w,T_{pe}}^{PCA}$ During Occlusion ... 80
4.3.2 Comparison of Indices Behavior ... 82
4.3.3 VF Prediction Analysis ... 84
4.4 Discussion ... 86
4.4.1 Time-Course of $d_{w,T_{pe}}^{PCA}$ ... 89
4.4.2 Association with VF Episodes ... 90
4.4.3 Limitations ... 91
4.5 Conclusions ... 92

5 Association Between T-wave Peak-to-End Time-Warping and VRD 93
5.1 Introduction ... 94
5.2 Methods ... 95
5.2.1 Experimental Protocol ... 95
5.2.2 Intramyocardial Electrograms Processing ... 96
5.2.3 ECG Processing ... 97
5.2.4 Quantification of T_{pe} Interval Morphology Changes ... 97
5.2.5 Statistical Analysis ... 98
5.3 Results ... 99
5.3.1 VF incidence ... 99
5.3.2 Dynamics of $d_{w,T_{pe}}^{PCA}$, DOR, and T_{pe} Along Ischemia ... 100
5.3.3 Comparison Between VF and Non-VF Groups ... 101
5.3.4 Delayed-VF Risk Prediction Value of $d_{w,T_{pe}}^{PCA}$, DOR and T_{pe} 105
5.3.5 Linear Regression Analysis Between Indices ... 106
5.4 Discussion ... 109
5.4.1 Ischemia-Induced Changes in $d_{w,T_{pe}}^{PCA}$, DOR and T_{pe} ... 110
5.4.2 Prognostic Value of $d_{w,T_{pe}}^{PCA}$, DOR and T_{pe} for VF Episodes 111
5.4.3 Limitations ... 113
5.5 Conclusions ... 114

6 T-wave Morphology for Risk Stratification in Type 2 LQTS Patients 115
6.1 Introduction ... 115
6.2 Materials and methods ... 117
6.2.1 Patient Cohort ... 117
6.2.2 Data Collection and End Points ... 118
6.2.3 ECG Signal Processing and Characterization ... 118
6.2.4 Quantification of T-Wave Morphology Changes ... 119
6.2.5 Statistical Analyses ... 121

6.3 Results . . . 122
6.3.1 Clinical and Demographic Characteristics . . . 122
6.3.2 T-wave Morphology . . . 123
6.3.3 Association of ECG Markers with Cardiac Outcomes . . . 124
6.3.4 Cardiac Events . . . 126
6.3.5 Ventricular Arrhythmias . . . 127
6.4 Discussion . . . 128
6.4.1 Limitations . . . 131
6.5 Conclusions . . . 132

7 T-Wave Peak-to-End Morphology Analysis in Brugada Syndrome 133
7.1 Introduction . . . 133
7.2 Methods . . . 135
7.2.1 Data Set . . . 135
7.2.2 ECG Pre-Processing . . . 136
7.2.3 Quantification of the $\mathbf{T}_{pe}$ Morphology Restitution . . . 136
7.2.4 Quantification of the $\mathbf{T}_{pe}$ Morphology Variation . . . 138
7.2.5 Statistical Analysis . . . 140
7.3 Results . . . 141
7.3.1 Clinical and Demographic Characteristics . . . 141
7.3.2 T-wave Morphology Restitution Markers . . . 141
7.3.3 T-wave Morphology Variation Markers . . . 144
7.3.4 Classical Repolarization and Depolarization-related ECG Markers . . . 147
7.4 Discussion . . . 150
7.4.1 Limitations . . . 153
7.5 Conclusions . . . 154

8 Conclusions and Future Work 155
8.1 Discussion of Main Achievements . . . 156
8.1.1 Methodological Framework for T-wave Morphology Assessment . . . 156
8.1.2 T-Peak-to-End Morphology in Ischemia-Induced Arrhythmic Risk . . . 156
8.1.3 T-Wave Morphology Markers in Cardiac Channelopathies 159
8.1.4 Overall Contribution to Arrhythmic Risk Stratification . . 160
8.2 General Conclusions . . . 161
8.3 Future Work . . . 162

9 Conclusiones y Trabajo Futuro **165**
9.1 Discusión de las principales aportaciones 166
9.1.1 Marco metodológico para la evaluación de la morfología de la onda T 166
9.1.2 Morfología del intervalo entre el pico y el final de la onda T en el riesgo arrítmico inducido por isquemia 167
9.1.3 Marcadores de la morfología de la onda T en canalopatías cardíacas 170
9.1.4 Contribución general a la estratificación del riesgo arrítmico 171
9.2 Conclusiones generales 172
9.3 Trabajo futuro 173

Bibliography **177**

Publications derived from the Thesis **205**

List of Figures **209**

List of Tables **219**

LIST OF ACRONYMS

ACA aborted cardiac arrest 118
ACS acute coronary syndrome 19
AP action potential 5
APDR action potential duration restitution 9
AUC area under the curve 219
AV atrioventricular 7
APD action potential duration 9
BrS Brugada syndrome iii
CE cardiac event 23
DOR dispersion of repolarization v
ECG electrocardiogram iii
EGM electrograms 10
HR heart rate 9
ICD implantable cardioverter defibrillator 118
LAD left anterior descending 56
LCX left circumflex artery 56
LM left main 56
LQTS long QT syndrome 2
LQT2 long QT syndrome type 2 iii
MCS morphology combination score 42
MWTPE mean warped T-peak-to-T-end wave 49

MWTW mean warped T-wave iv
PCA principal component analysis iv
PCI percutaneous coronary intervention 20
PC1 first principal component 97
QT QT interval 20
QT_c corrected QT v
RCA right coronary artery 56
ROC receiver operating characteristic 80
RVOT right ventricular outflow tract 26
SAE serious arrhythmic events 23
SCB sodium channel blocker 27
SPM statistical parametric mapping 99
SCD sudden cardiac death iii
SRSF square-root slope function 43
TdP torsades de pointes 20
TMR T-wave morphology restitution iv
TMV T-wave morphology variation iv
T_{pe} T-wave peak-to-end interval iv
TPEMR T-wave peak-to-end morphology restitution iv
TPEMV T-wave peak-to-end morphology variation iv
UKB UK Biobank 117
VA composite endpoint ventricular arrhythmia 23
VCG vectorcardiogram 15
VF ventricular fibrillation iv
VRD ventricular repolarization dispersion 2
VT ventricular tachycardia 2
WT wavelet transform 37

CHAPTER 1

INTRODUCTION

1.1 Motivation

1.2 The Heart

1.2.1 Cardiac Anatomy and Mechanical Function

1.2.2 Cellular Electrophysiology

1.2.3 Electrical Activity of the Heart

1.2.4 Repolarization: Dispersion and Restitution

1.3 Cardiac Electrical Recordings

1.3.1 Electrocardiogram

1.3.2 Electrogram

1.4 Interval- and Morphology-Based Repolarization Characterization

1.5 Cardiomyopathies and Channelopaties Addressed in the Thesis

1.5.1 Acute Ischemia and Myocardial Infarction

1.5.2 Long QT Syndrome

1.5.3 Brugada Syndrome

1.6 Objective and Outline of the Thesis

1.1 Motivation

Cardiovascular diseases remain the leading cause of death worldwide, and are responsible for approximately 17.9 million deaths according to recent reports from the European Society of Cardiology based on World Health Organization data [1], and they impose an immense health and economic burden both

in the United States and globally, as highlighted by the American Heart Association [2]. Their global burden is expected to remain very high and to increase in absolute numbers over the coming decades, largely driven by population aging, and current projections may even underestimate this burden because they do not fully account for the potential long-term cardiovascular impact of COVID-19 [3, 4]. Within this spectrum, SCD represents a substantial proportion of cardiovascular mortality, often occurring in settings where preventive options would theoretically be available. In most cases, SCD is the final manifestation of life-threatening ventricular arrhythmias, such as sustained ventricular tachycardia (VT) or VF, which arise on a vulnerable substrate whose nature varies across clinical settings. Thus, early prediction remains crucial for the implementation of prevention strategies.

Ventricular repolarization alterations play a central role in the development of malignant ventricular arrhythmias. Increased dispersion of repolarization across the ventricular myocardium, often referred to as ventricular repolarization dispersion (VRD), is associated with unidirectional block and can facilate the intiation and maintenance of reentrant circuits [5, 6], thereby creating a vulnerable substrate for VT and VF. This concept is relevant across different clinical settings, from cardiac ischemia to ion-channel disorders, where heterogeneous alterations in the duration and morphology of the action potential translate into complex changes in the surface T wave.

Experimental and clinical studies have consistently linked increased VRD with a higher propensity for life-threatening ventricular arrhythmias [7–9], resulting in the identification of risk indicators that are, along with other relevant clinical information, suitable for risk stratification in the routine patient management. Several biomarkers have been proposed to quantify the spatio-temporal heterogeneity of repolarization, such as the QT interval [10], T-wave width [8], the distance from the peak to the end of the T-wave (T_{pe} interval) [11], dynamic changes in the T_{pe} interval with respect to heart rhythm [12], QT interval variability [13], T-wave alternans [14], QT memory lag [15], or T-wave area dispersion [7]. However, robustly identifying in the ECG those markers of repolarization alterations that better represents the potentially harmful substrate remains an unmet demand. This challenge can also be dependent on the underlying pathologies generating the risk.

In ischemia, congenital long QT syndrome (LQTS), and BrS, ventricular arrhythmic risk emerges from distinct structural and/or functional abnormalities that manifest as different patterns of ventricular repolarization, thereby highlighting the need for disease-specific biomarkers suitable for risk stratification. Particularly in acute myocardial ischemia, while ST-segment deviations repre-

sent the primary electrocardiographic hallmark reflecting acute coronary occlusion [16–18], they provide limited insight into the underlying spatio-temporal heterogeneity of ventricular repolarization that contributes to arrhythmogenesis [19, 20]. Accordingly, complementary markers derived from T-wave morphology, such as the T_{pe} interval [11], have been proposed to better capture ischemia-induced dispersion of repolarization, although their mechanistic basis and clinical utility remain controversial [21–23].

In the context of congenital LQTS, although QTc prolongation remains the pathophysiological hallmark for diagnosis and clinical risk stratification [24,25], accumulating evidence indicate that proarrhythmic risk, particularly in LQT2 patients, may not arise solely from delayed repolarization per se, but rather from its association with increased temporal and spatial heterogeneity of repolarization [26, 27]. This has motivated the search for complementary markers capable of capturing the underlying complexity of repolarization dynamics beyond what QTc duration alone can convey. Similarly, risk stratification and clinical management of patients with BrS remain challenging due to the absence of a single, widely accepted electrocardiographic biomarker of sudden cardiac death risk, with recovered sudden cardiac death or arrhythmogenic syncope still constituting the most robust risk indicators in current practice [28, 29]. Taken together, these observations underscore that the relevance and performance of repolarization-based ECG markers are highly dependent on the underlying pathology, reinforcing the unmet need for robust and pathophysiology-oriented biomarkers capable of capturing the arrhythmogenic substrate across different clinical scenarios.

1.2 The Heart

1.2.1 Cardiac Anatomy and Mechanical Function

The heart is the central organ of the cardiovascular system and acts as a muscular pump that maintains blood flow through the pulmonary and the systemic circulation, thereby supporting the delivery of oxygen and nutrients to all tissues. It is organized into four chambers, two atria and two ventricles, that work in a coordinated manner: the right side of the heart receives venous blood and pumps it to the lungs for oxygenation, while the left side receives oxygenated blood from the lungs and delivers it to the rest of the body. A schematic representation of the cardiac chambers, valves and main inflow and outflow tracts is shown in Figure 1.1. During each cardiac cycle, the atria and

ventricles contract and relax in a tightly controlled sequence so that filling and ejection occur efficiently. This mechanical performance relies on the properties of the myocardial wall, composed of specialized cardiac muscle cells and supporting tissue, and on a precise timing of electrical activation between the right and left sides of the heart [30].

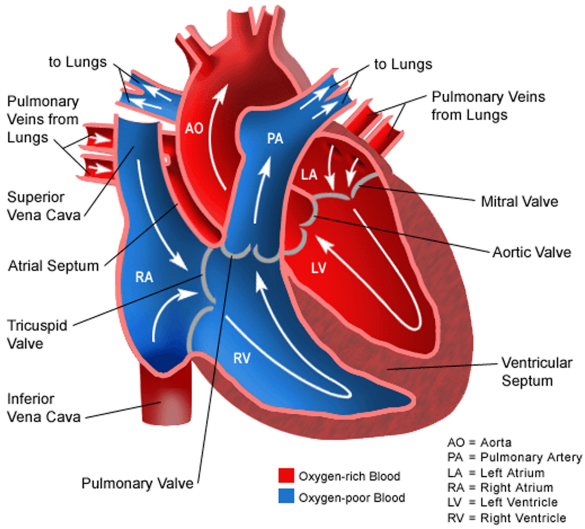


Figure 1.1: Anatomical overview of the heart showing the four chambers, valve system and main blood flow pathways. Regions in red represent oxygenated blood circulation, whereas blue regions represent deoxygenated blood circulation. Extracted from [31].

From a mechanical standpoint, each heartbeat corresponds to a cardiac cycle in which filling and ejection phases alternate in an organized manner. During diastole, the ventricles relax and their pressure falls below atrial pressure, so that the atrioventricular valves (mitral and tricuspid) open and blood flows from the atria into the ventricular cavities. Ventricular filling is completed by atrial contraction at the end of diastole. During systole, ventricular contraction increases intraventricular pressure, the atrioventricular valves close, and the semilunar valves (pulmonary and aortic) open so that blood is ejected into the pulmonary and systemic circulations. The subsequent ventricular relaxation leads to closure of the semilunar valves and the start of a new filling phase. The ability of the heart to maintain an adequate cardiac output therefore depends on the coordinated alternation between contraction and relaxation of atria and ventricles.

The pump function is sustained by the myocardium, the muscular wall of

the heart, which is primarily composed of cardiac muscle cells (myocytes) that generate force during contraction. Contraction of the atria and ventricles is initiated by waves of electrical excitation (depolarization) that propagate through the myocardium, activating the muscle fibers in a coordinated way. After systole, the myocardial cells undergo electrical recovery (repolarization) and the tissue relaxes, allowing the cardiac chambers to fill again. Thus, each mechanical cardiac cycle is the macroscopic expression of an underlying sequence of cellular depolarization and repolarization, whose electrical behavior at the single-cardiomyocyte level, and the propagation of this activity throughout the heart, will be described in the next sections [30, 32].

1.2.2 Cellular Electrophysiology

At the microscopic level, the pumping function of the heart is enabled by cardiomyocytes, excitable cells whose membranes sustain a voltage difference between the intracellular and extracellular spaces. This transmembrane voltage, known as membrane potential, is generated by ionic concentration gradients and by the selective permeability of the cell membrane to the main charge carriers, chiefly calcium (Ca^{2+}), chloride (Cl^{-}), sodium (Na^{+}), and potassium (K^{+}), being more abundant in the extracellular space, except for K^{+}, which is more abundant in the intracellular space. These ions move through specialized membrane proteins, including ion channels, exchangers and pumps, which continuously regulate ionic fluxes and maintain the electrochemical gradients required for electrical excitability.

In contractile cardiac myocytes at rest, the membrane potential is typically negative, in the range of -65 to -80 mV for atrial myocytes and -90 to -80 mV for ventricular myocytes. When a sufficiently large stimulus arrives, voltage-dependent ion channels open in a coordinated manner and the cell produces an action potential (AP), a characteristic time course of the membrane potential, which represents the electrical activity of a single cell. This electrical event precedes and triggers mechanical contraction through excitation-contraction coupling. Conversely, the recovery of the membrane voltage back to its resting level is associated with the relaxation of the myocardium and the restoration of cellular excitability for the next beat. As illustrated in Figure 1.2, the ventricular AP is commonly divided into five phases $(0-4)$, each dominated by specific ionic currents [30]:

- **Phase 0 - Rapid depolarization:** The rapid activation of fast Na^{+} channels leads to a prominent inward current ($I_{Na^{+}}$), causing an abrupt depolar-

ization and a sharp rise of the transmembrane voltage. This fast upstroke marks the onset of the action potential and underlies the excitation that precedes mechanical contraction.

- **Phase 1 - Early repolarization:** After depolarization, inactivation of fast Na^+ channels and activation of the transient outward K^+ current (I_{to}) lead to a brief repolarizing shift. As a consequence, the membrane potential drops slightly, creating the early, small downward deflection (the notch) observed in the AP morphology.

- **Phase 2 - Plateau:** A near-zero membrane potential is maintained by a balance between inward Ca^{2+} current through L-type channels (I_{CaL}) and the outward movement of K^+ through slow delayed rectifier potassium channels (I_{Ks} current). This plateau prolongs the cardiac AP and, via the rise in cytosolic Ca^{2+}, sustains excitation-contraction coupling and force generation.

- **Phase 3 - Final repolarization:** During this phase, L-type Ca^{2+} channels progressively inactivate/close, and outward K^+ currents become increasingly dominant. In particular, the slow delayed rectifier K^+ currents, I_{Ks}, remains active, ensuring a net outward current and a negative shift in the membrane potential, which in turn allows additional repolarizing K^+ currents to contribute. These include the rapid delayed rectifier potassium current (I_{Kr}) and the inward rectifier potassium current (I_{K1}). This net outward current (i.e., loss of positive charge from the cell) drives repolarization, restoring the membrane potential to negative values, thereby bringing the cell back to its basal electrical state and completing the AP.

- **Phase 4 - Resting state:** In cardiac cell is the quiescent period where the membrane potential remains close to its resting value. The cell is thus ready for the next action potential. This resting condition is maintained in part by the Na^+/K^+ - ATPase pump, which exports Na^+ and imports K^+, helping preserve the transmembrane ionic gradients.

1.2.3 Electrical Activity of the Heart

To achieve an effective and coordinated pump function, the contractile myocardium requires a timely electrical trigger and the rapid distribution of electrical excitation across the cardiac chambers with appropriate timing. Under

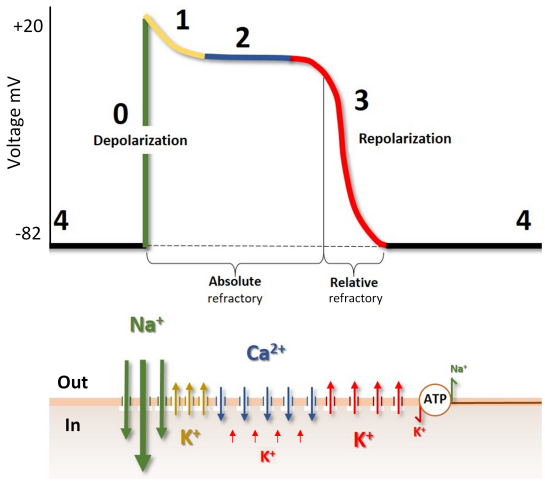


Figure 1.2: Ventricular action potential waveform divided into phases (0–4), together with the principal inward and outward ionic flows that underlie each phase. Adapted from https://studmed.uio.no/

normal conditions, each heartbeat begins in the sinoatrial (SA) node (Figure 1.3), a group of pacemaker cells located in the right atrium that spontaneously generates electrical impulses. The impulse spreads through the atria, producing atrial depolarization and contraction, and subsequently reaches the atrioventricular (AV) node, where conduction is briefly delayed to allow the ventricles to complete filling of blood after atrial contraction [30, 32].

After this short delay, the depolarizing signal is transmitted into the ventricles via the bundle of His (Figure 1.3), which runs through the interventricular septum and then divides into the right and left bundle branches. These branches convey the impulse to the right and left ventricles, respectively, and continue into an extensive Purkinje fiber network (Figure 1.3) that conducts excitation rapidly throughout the ventricular myocardium. In a typical activation sequence, the interventricular septum is depolarized first, and excitation then spreads quickly to both ventricles. From there, ventricular depolarization propagates from multiple terminal fibers of the conduction system and spreads through the ventricular wall predominantly from the endocardial surface (inner layer) toward the epicardium (outer layer) [30]. In addition, the activation pattern progresses along the ventricular myocardium toward the atrioventricular groove, contributing to an efficient and coordinated ventricular contraction. Unlike depolarization, ventricular repolarization is not carried by a dedicated conduction pathway as a cell-to-cell propagating wave. Instead, it reflects the

regional electrical recovery of myocardial tissue. Because cardiomyocytes repolarize at different rates depending on their anatomical location, the time course of recovery can differ across endocardial, epicardial and midmyocardial layers [33–36]. When these differences become markedly increased, the resulting dispersion of repolarization can give rise to a malignant arrhythmogenic substrate [37], a central concept that is closely related to this thesis.

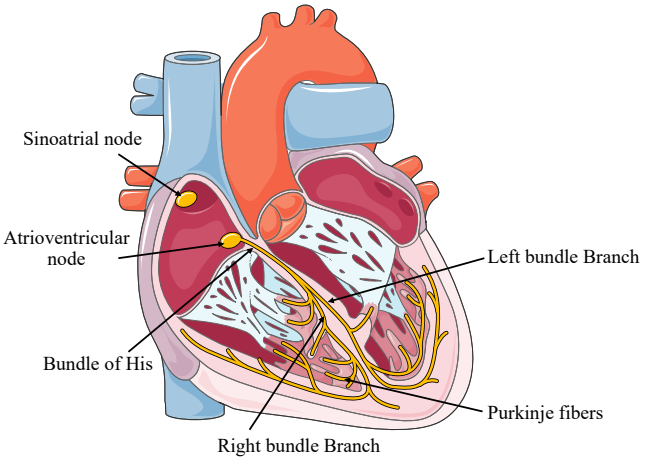


Figure 1.3: Longitudinal heart section showing the conduction system responsible for coordinated electrical activation. Adapted from `https://smart.servier.com/`.

1.2.4 Repolarization: Dispersion and Restitution

Dispersion of Repolarization

Although ventricular myocytes share a common action potential architecture, electrical recovery is not spatially uniform across the heart. At the organ level, the global pattern of repolarization reflects the combined effect of the activation sequence delivered by the conduction system and regional differences in cellular electrophysiological properties that shape action potential duration and morphology. At any given location, the moment at which a cardiac myocyte completes repolarization is determined by its activation time and by the duration of its AP. The first component depends on how quickly the impulse is conducted through the tissue (conduction velocity), whereas the second re-

flects intrinsic cellular electrophysiology. Accordingly, ventricular dispersion of repolarization arises from spatial variability in activation timing and action potential duration (APD) across myocytes, which in turn influences arrhythmia vulnerability [37].

A frequently cited notion is that, at normal heart rates heart rates (HRs), epicardial cells tend to exhibit shorter action potential duration than endocardial cells [38, 39], suggesting earlier epicardial repolarization. However, other observations indicate that epicardial repolarization can occur later rather than earlier under certain conditions [40]. Similarly, some studies have proposed that mid-myocardial cells repolarize last, so that completion of mid-wall recovery would effectively mark the end of ventricular repolarization [11, 33], yet the contribution of mid-myocardial cells to regional dispersion remains debated [41–43]. In addition, evidence suggests that delayed recovery may not form continuous transmural layers. Instead, spatially localized "islands" of delayed repolarization have been reported within the ventricular wall [44, 45].

Overall, repolarization time differences (dispersion of repolarization) are not limited to a single axis or to transmural gradients. Within the ventricles, dispersion is observed across multiple anatomical directions, including epicardium versus endocardium [39, 46–50] and apex-to-base differences [49, 51–56]. Taken together, these heterogeneous recovery patterns justify the search for non-invasive surrogates of ventricular repolarization dispersion, which will be introduced in the following sections.

Restitution of Repolarization

Ventricular repolarization is not only heterogeneous in space but also dynamic in time. When HR changes, the duration and morphology of the action potential adapt accordingly, and this rate dependence is commonly referred to as repolarization restitution. Repolarization restitution describes how ventricular electrical recovery adjusts when HR varies [57–60]. In general, faster HRs are associated with shorter APD, whereas slower HRs are associated with longer APD [61,62]. A common way to represent this behavior is the action potential duration restitution (APDR) curve, which relates APD to the preceding RR interval [62,63], as illustrated by the individual curves in Figure 1.4. Over a broad range of cycle lengths, the relationship is often relatively flat at long RR intervals and becomes steeper at shorter RR intervals [62, 63]. The local slope of the APDR curve quantifies how strongly APD changes for a given change in RR, and increased steepness has been linked to arrhythmogenesis [64–66].

Importantly, restitution does not necessarily evolve identically across my-

ocardial regions. As illustrated in Figure 1.4, regional electrophysiological differences can lead to spatially distinct APDR curves (in slope and range), so the resulting dispersion in restitution properties is heart-rate dependent itself. This concept is commonly referred to as dispersion of repolarization restitution. In general terms, it has been reported that this dispersion decreases as HR increases [6]. Several studies have also associated increased dispersion of repolarization restitution with a greater propensity for arrhythmia development [67, 68].

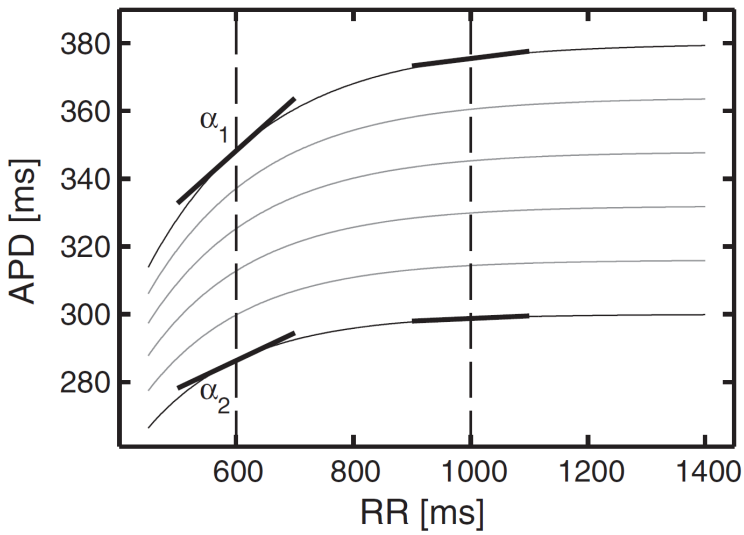


Figure 1.4: Representative APD-RR restitution curves obtained at different cardiac locations, illustrating regional differences in restitution behavior. The markers α_1 and α_2 denote the maximum and minimum local slopes, respectively, evaluated at RR = 600 ms. Extracted from [69]

1.3 Cardiac Electrical Recordings

The heart's electrical activity propagates through the torso due to the conductive properties of biological tissues, making it possible to record voltage differences generated by cardiac depolarization and repolarization using electrodes. Depending on electrode placement, recordings can capture either body-surface ECG, which provides a far-field projection of the summed cardiac electrical activity along a given axis, or intracardiac electrograms (EGM) obtained with invasive catheters that provides a more local description. In both cases, the recorded signals reflect the spatiotemporal organization of electrical acti-

vation and recovery, and their interpretation depends on electrode configuration and the anatomical relationship between the sensors and the myocardium. In general, the amplitude of the measured voltage difference depends on the amount of electrically active myocardium contributing to the wavefront. In this context, the ECG is a widely used, cost-effective and noninvasive clinical tool that carries valuable information about the heart [32].

1.3.1 Electrocardiogram

An ECG is a non-invasive recording obtained from electrodes placed on the body surface. The ECG reflects the superposition of electrical contributions from populations of cardiac cells that are undergoing depolarization and repolarization at a given time, rather than a direct measurement of cellular transmembrane potentials. The ECG is widely used in clinical practice because it is cost-effective, non-invasive, and provides valuable information about cardiac rhythm and waveform morphology.

The voltage difference measured between electrodes is referred to as a lead. Because electrical activity in the heart is inherently three-dimensional, each lead can be interpreted as a projection of the underlying electrical forces along a specific axis. As a consequence, polarity, amplitude, and waveform morphology depend strongly on electrode placement and on the geometric relationship between the heart and the recording configuration [32, 70].

Waveforms and Key Intervals

During normal rhythm, each cardiac cycle is represented in the ECG as a sequence of waves whose timing and morphology convey diagnostic information. An example ECG trace showing two consecutive cycles and the main waves and intervals is provided in Figure 1.5. Deflections are measured relative to the baseline (isoelectric line), which are intervals in which there is no net potential difference attributable to organized electrical wavefronts. The polarity and overall morphology of each waveform depend on electrode position and on the direction of the underlying electrical wavefront. A depolarization wavefront moving toward the exploring electrode typically produces a positive deflection, whereas one moving away produces a negative deflection. During repolarization, this polarity relationship is reversed: a wavefront moving toward the electrode tends to generate a negative deflection, while one moving away tends to generate a positive deflection. Moreover, because the ventricular myocardium has a larger muscle mass, ventricular depolarization generally yields

higher-amplitude deflections than atrial activity. In general, depolarization-related deflections tend to be sharper, whereas repolarization-related deflections are smoother, reflecting differences in the speed and organization of these processes in the myocardium.

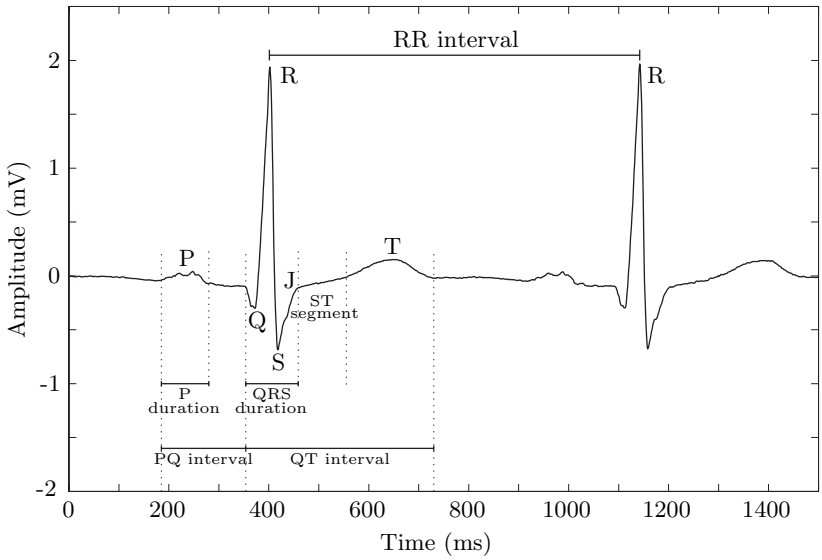


Figure 1.5: Illustration of an ECG recording over two cardiac cycles, highlighting the principal waves and the most relevant time intervals. Extracted from [32].

The P wave reflects atrial depolarization. It typically has a duration below 120 ms and an amplitude below approximately 300 μV in most leads, consistent with relatively slower propagation through atrial tissue compared with ventricular activation. Besides, it is generally positive and monophasic. After the P wave, the ECG often returns close to the baseline until ventricular depolarization begins (the PQ segment). During this near-isoelectric period, atrial-to-ventricular conduction proceeds through the AV node and the specialized conduction system, producing little net surface potential difference on the body surface ECG [32].

The QRS complex represents ventricular depolarization and results from the summation of activation in the right and left ventricles. It can include up to three main deflections (Q, R, and S) and typically lasts about 70–110 ms. Its amplitude is usually larger than that of the P wave (often around 1–2 mV and sometimes higher), largely reflecting the greater myocardial mass of the ventricles and the rapid spread of activation through the specialized

conduction system. Atrial repolarization occurs during this period but is not usually discernible because it is masked by the much larger QRS signal.

Following the QRS complex, the next segment corresponds to a brief interval in which the ECG returns near the isoelectric line because most ventricular myocytes are at similar membrane potentials during the plateau phase (phase 2) of the AP, resulting in little net current. Under physiological conditions, this reflects a period where ventricular tissue is relatively uniform in its electrical state. The segment, known as the ST segment, begins at the end of the S wave (the J point) and extends until the onset of the T wave, which marks the onset of ventricular repolarization.

The T wave reflects ventricular repolarization and is typically seen as a positive deflection in most leads. Compared with the QRS complex, it is generally broader (with a duration on the order of ∼300 ms) and smoother, consistent with ventricular repolarization being a relatively slower and less synchronized process than ventricular depolarization. Its timing, width, and position within the ECG are clearly heart-rate dependent: at higher HRs, the T wave tends to become narrower and to occur closer to the QRS complex, whereas at lower HRs it typically becomes broader and occurs further from the QRS complex; this rate dependence does not carry over to the P wave or the QRS complex. T wave may be followed by a low-amplitude U wave, whose origin remains uncertain [30, 32].

In addition to the segments and intervals described above, other time intervals are commonly measured from the ECG and are routinely used in both clinical interpretation and research. The RR interval is measured between successive R peaks, and its inverse corresponds to HR. It is a fundamental rhythm descriptor and is widely used to characterize rhythm abnormalities and to study heart rate variability (HRV). The QT interval spans from the onset of the QRS complex to the end of the T wave and reflects the overall duration of ventricular depolarization and repolarization. Because QT depends on heart rate, QT_c is frequently reported using formulas such as Bazett's or alternative corrections (e.g., Fridericia), acknowledging that correction performance can vary across heart-rate ranges and subjects [71]. Within ventricular repolarization, the T_{pe} is also commonly measured and has been used to assess repolarization dispersion, in line with the physiological concepts introduced in the previous sections.

Lead Systems

An ECG is typically recorded using a multi-lead configuration, where each lead corresponds to the voltage difference measured along a specific electrical axis. In this sense, every lead can be understood as a different spatial viewpoint of the same underlying cardiac electrical activity, because it captures the projection of depolarization and repolarization wavefronts onto that axis.

Because cardiac electrical propagation is inherently three-dimensional, no single lead fully represents the entire process. Instead, lead systems combine multiple orientations to describe electrical activity in complementary planes. In the standard clinical setting, the 12-lead ECG is commonly interpreted as providing two main perspectives: six frontal-plane leads and six precordial (chest) leads that view electrical events mainly in the horizontal/transverse plane.

Leads can be defined as bipolar or unipolar, depending on how the voltage is measured. A bipolar lead records the voltage difference between two electrodes, whereas a unipolar lead measures the voltage at one exploring electrode relative to a reference that remains approximately stable during the cardiac cycle (often described as a central terminal) [32].

In practice, the selection of a lead configuration depends on the clinical question and on practical constraints. For example, a limited number of electrodes may be sufficient when rhythm monitoring is the priority, whereas a full 12-lead configuration is preferred when waveform morphology and spatial patterns are relevant. Different recording settings (e.g., resting ECG, ambulatory monitoring, exercise testing, ICU monitoring) reflect these distinct needs.

Standard 12-lead ECG: The standard 12-lead ECG is obtained from 10 electrodes and yields 12 leads by combining (i) three bipolar limb leads (I, II, III), (ii) three augmented unipolar limb leads (aVR, aVL, aVF), and (iii) six unipolar precordial (chest) leads (V1–V6).

In the frontal plane, the limb leads are constructed from electrodes placed on the right arm (RA), left arm (LA) and left leg (LL), which can be visualized as the vertices of Einthoven's triangle with the heart at its center. The three bipolar limb leads measure voltage differences between pairs of these electrodes: lead I compares LA relative to RA and can be viewed as looking at the heart from the left side, defining zero degrees (0°); lead II compares LL relative to RA and views the heart at $+60^\circ$ relative to lead I, whereas lead III compares LL relative to LA, providing a third frontal orientation at $+120^\circ$ relative to lead I (Figure 1.6, left). The three bipolar limb leads are provided below:

$$I = V_{LA} - V_{RA} \tag{1.1}$$

$$II = V_{LL} - V_{RA} \tag{1.2}$$

$$III = V_{LL} - V_{LA} \tag{1.3}$$

The augmented unipolar limb leads are derived from the same limb electrodes but are referenced to a composite terminal obtained from the average of the remaining two limb potentials. Consequently, each augmented lead emphasizes a different frontal-plane direction that is shifted by 30° with respect to the corresponding bipolar limb-lead axes. In this convention, aVL can be viewed as oriented at −30°, aVR at 30°, and aVF at +90° in the frontal plane (Figure 1.6, left). The augmented limb leads are defined as:

$$aVR = V_{RA} - \frac{V_{LA} + V_{LL}}{2} \tag{1.4}$$

$$aVL = V_{LA} - \frac{V_{RA} + V_{LL}}{2} \tag{1.5}$$

$$aVF = V_{LL} - \frac{V_{LA} + V_{RA}}{2} \tag{1.6}$$

The six precordial leads (V1-V6) are unipolar chest leads placed along an arc on the anterior and left lateral thorax, providing a transverse-plane view (Figure 1.6, right) that complements the frontal information from limb leads. Conventionally, V1 is positioned in the fourth right intercostal space close to the sternum and V2 in the fourth left intercostal space; the remaining electrodes are placed at approximately equally spaced locations toward the left lateral chest, with V6 typically located over the mid-axillary line in the fifth left intercostal space. With this arrangement, V1–V2 primarily face the right ventricle and interventricular septum, V3–V4 the anterior wall of the left ventricle, and V5–V6 the lateral left ventricle [32].

It is also worth noting that not all twelve displayed leads are independent, since, due to the way limb leads are constructed, all limbs leads can be derived from two of them meaning that eight independent signals can represent the information contained in the full set.

Orthogonal ECG Leads: Beyond the standard 12-lead ECG, orthogonal lead systems represent cardiac electrical activity along three approximately perpendicular axes (commonly denoted X, Y, Z). In this framework, the trajectory traced by the tip of the dominant cardiac electrical vector over the cardiac cycle forms a loop commonly referred to as the vectorcardiogram (VCG), which

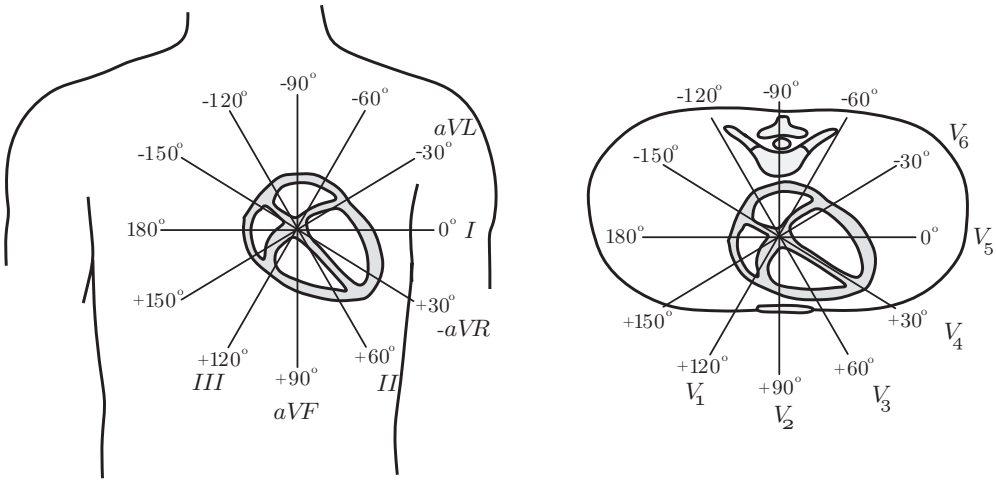


Figure 1.6: Illustration of lead-axis directions for the standard 12-lead ECG: frontal-plane limb leads (left) and transverse-plane precordial leads (right). Extracted from [32].

can also be displayed through its projections onto the orthogonal planes. This representation offers an alternative description of how the dominant electrical wavefront evolves in magnitude and direction during the cardiac cycle.

A widely used orthogonal configuration is the Frank lead system [72], which obtains the X, Y, and Z leads from linear combinations of signals recorded with a reduced set of electrodes placed at standardized locations (on the chest, back, neck, and left foot), thereby providing an approximately three-dimensional description of cardiac electrical activity. Moreover, several mathematical transformations have been proposed to relate orthogonal and standard 12-lead recordings, enabling the synthesis of VCG-like components from the conventional ECG or, conversely, the estimation of standard-lead signals from orthogonal measurements.

1.3.2 Electrogram

Intracardiac EGMs represent localized electrical activity recorded invasively with electrodes positioned in direct contact with cardiac tissue. Compared with the surface ECG, EGMs can offer a more local description of cardiac electrical activity, because the recorded potentials are dominated by near-field contributions from myocardium close to the electrode (spatial specificity). This makes EGMs well suited for analyzing propagation and for extracting local timing markers, often via slope-based criteria, of activation and recovery (time resolu-

tion) at specific sites, which can then be summarized through derived intervals. EGMs recordings can be obtained in unipolar or bipolar configurations depending on how the reference is defined [70]

A unipolar EGM records the potential difference between an exploring electrode placed on the heart relative to a distant reference electrode. Because the reference is remote, unipolar EGMs can capture both near-field activity and contributions from more distant sources (far-field). Their morphology can be interpreted in relation to the position of the electrode with respect to the propagating activation front. For instance, when the front approaches a recording site, the signal may initially show a positive component; when the front is over the electrode the potential difference can transiently approach zero; and as the wavefront passes, a negative component may appear, resulting in a biphasic deflection. At the site where activation originates, the unipolar electrogram is commonly negative, whereas at sites where activation terminates the signal can remain predominantly positive.

A bipolar EGM measures the voltage difference between two closely spaced electrodes on the heart (both acting as exploring electrodes). This configuration tends to emphasize local electrical activity and reduces far-field contributions because distant components are partially canceled by subtraction. Bipolar EGMs are typically sharper than unipolar recordings, but their morphology and amplitude depend on the inter-electrode spacing and on the direction of the activation wavefront relative to the electrode pair. For this reason, the wavefront direction cannot be inferred uniquely from bipolar morphology alone without additional geometric information. In general, spatial selectivity increases as the inter-electrode distance decreases [70].

Unipolar intramyocardial EGMs acquired from multiple sites across the ventricular myocardium in an open-chest porcine myocardial infarction model will be used in this thesis to characterize dispersion of repolarization dynamics.

1.4 Interval- and Morphology-Based Repolarization Characterization

Ventricular repolarization is commonly characterized on the surface ECG through temporal indices defined from specific fiducial points, such as the T-wave width [8], Twave peak-to-end interval, T_{pe} [11], or the QT interval [10]. These measurements provide compact and clinically interpretable descriptors of repolarization timing and have demonstrated diagnostic and prognostic value in multiple cardiac conditions. However, ventricular repolarization is a spatially

heterogeneous process, and the surface T wave results from the superposition of electrical gradients generated as different myocardial regions recover at different times [33, 73]. Consequently, not only the duration but also the shape of the T wave can reflect the underlying organization and heterogeneity of ventricular repolarization [33].

This distinction is relevant because similar interval values do not necessarily imply similar repolarization patterns, and T waves with comparable interval measurements may still exhibit different morphologies [74, 75]. Changes in the spatial and temporal distribution of ventricular recovery can modify characteristics such as T-wave amplitude, slope, symmetry, notching, or spatial relationships across leads without being fully represented by changes in the position of a limited number of fiducial points [76–79]. This has motivated the development of quantitative approaches that characterize T-wave morphology using, among others, architectural features, slope- and area-based descriptors, spatial or vectorcardiographic representations, and global waveform-comparison methods [76, 77, 80]. Such approaches have provided information complementary to conventional interval measurements in different settings, including the identification of repolarization abnormalities in LQTS, the characterization of drug-induced repolarization changes, and the detection of ischemia-induced ST-T alterations.

Importantly, morphology-based analysis provides a complementary description by considering how the waveform evolves over its entire duration rather than reducing it to a small number of temporal landmarks. In this way, waveform characteristics that are not explicitly represented by interval measurements can also be quantified, providing additional information related to the underlying repolarization process. Together, these considerations provide the rationale for the waveform-comparison approaches evaluated throughout this thesis.

1.5 Cardiomyopathies and Channelopaties Addressed in the Thesis

1.5.1 Acute Ischemia and Myocardial Infarction

Myocardial ischemia refers to a reduction in coronary blood flow that limits oxygen delivery to the myocardium. Myocardial ischemia results from an insufficient supply of oxygenated blood to the heart muscle, often caused by coronary artery narrowing, which fails to meet the increased metabolic demand

during physical or emotional stress. This phenomenon can be transient or sustained. When ischemia persists, it may progress from reversible dysfunction to irreversible cardiomyocyte death (necrosis), i.e., myocardial infarction, typically when coronary flow is abruptly and persistently interrupted. In both situations, the resulting metabolic and electrophysiological alterations can destabilize cardiac electrical activity and facilitate ventricular tachyarrhythmias, including ventricular fibrillation. Importantly, ischemia may occur with chest pain (angina) but can also be clinically silent, making objective monitoring strategies particularly relevant. In current clinical practice, these presentations are often discussed within the broader spectrum of acute coronary syndrome (ACS), which includes patients with recent changes in symptoms/signs with or without ECG changes and with or without acute elevations in cardiac troponin [81].

Electrophysiological and ECG Expression of Acute Ischemia

Acute ischemia can alter cardiac electrical activity and, when it progresses to myocardial infarction, the resulting non-viable tissue can further distort normal activation pathways and modify the dominant electrical vector, thereby producing ECG waveforms that differ from the normal pattern and may evolve over time.

Acute ischemia typically manifests on the surface ECG as changes in the ST segment and T wave (ST-T alterations), whose expression depends on the affected region and on the lead orientation. Beyond the classical ST elevation or depression, ischemia can produce broader morphological changes in repolarization, and these modifications may evolve dynamically, sometimes over short time scales. At the cellular level, ischemia induces shifts in resting and action potential characteristics, generating voltage gradients between ischemic and non-ischemic regions that contribute to injury currents and, consequently, to ST–T deviations recorded at the body surface. Because these manifestations are lead-dependent and not always unique to ischemia, there is longstanding interest in developing signal-processing-based biomarkers that capture repolarization changes more robustly than single-point local measurements. In addition, guides of European Society of Cardiology highlight that while ST-segment elevation is a key marker of acute coronary occlusion, other ECG patterns can also suggest ongoing occlusion or severe ischemia [81].

Clinical Management

From a clinical management perspective, acute coronary occlusion is primarily addressed by rapid reperfusion strategies, most commonly percutaneous coronary intervention (PCI), while fibrinolysis is considered when timely PCI is not feasible. In selected patients, surgical revascularization (coronary artery bypass grafting) is also part of the therapeutic spectrum [81]. In experimental and clinical research, PCI with balloon provides a well-controlled model of transient ischemia, as the onset and duration of coronary occlusion are defined by the inflation period and the affected artery is known. In PCI, a catheter carrying an inflatable balloon is advanced percutaneously to the target coronary segment and positioned across the narrowed or occluded region. Balloon inflation transiently expands to restore flow in clinical practice. In experimental protocols, the same maneuver can be used deliberately to produce a short or complete occlusion. As illustrated in Figure 1.7, inflation defines a precisely timed ischemic interval, and deflation marks reperfusion, yielding a controlled occlusion–reperfusion sequence for studying rapid electrical changes. Complementarily, animal models of myocardial infarction enable studying sustained ischemia leading to necrosis and its electrophysiological consequences under controlled conditions, including arrhythmic outcomes and invasive measurements. In this thesis, ischemia and infarction are studied through recordings acquired during balloon-induced coronary occlusion and through porcine myocardial infarction models, combining surface ECG analysis with invasive electrophysiological signals when available to characterize repolarization dynamics and dispersion.

1.5.2 Long QT Syndrome

Congenital long QT syndrome (LQTS) is an inherited cardiac channelopathy characterized by delayed ventricular repolarization, classically reflected as QT interval (QT) prolongation on the surface ECG, and associated with an increased susceptibility to polymorphic ventricular tachyarrhythmias, including torsades de pointes (TdP) and ventricular fibrillation. LQTS is considered relatively frequent among inherited arrhythmia syndromes, with a prevalence often reported on the order of 1:2000, although estimates vary with ascertainment and diagnostic criteria [83–85]. Genetically, most clinically diagnosed cases are explained by variants affecting ion-channel currents that shape the ventricular action potential (Figure 1.8), with three major genotypes accounting for a substantial proportion of clinically diagnosed cases:

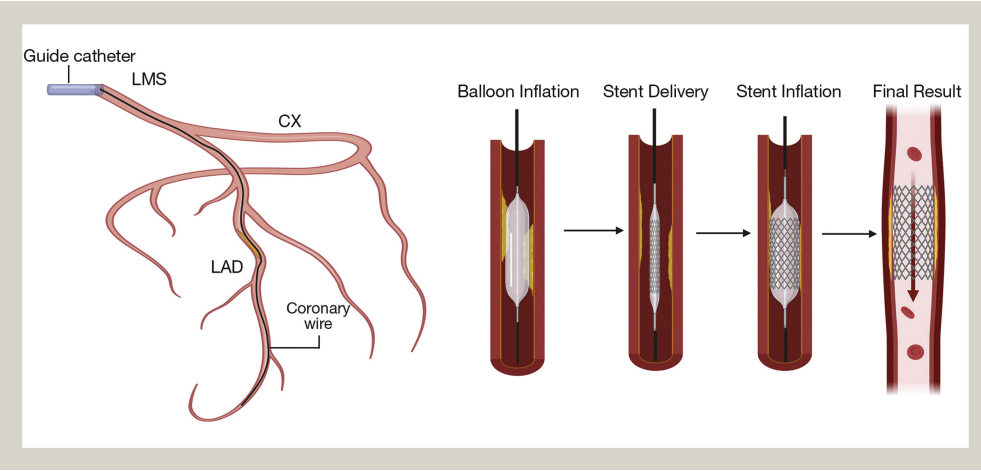


Figure 1.7: Schematic overview of percutaneous coronary intervention (PCI): coronary catheter and guidewire positioning (left) and the main procedural steps (right), including balloon inflation, stent delivery, stent expansion, and the final result. Extracted from [82].

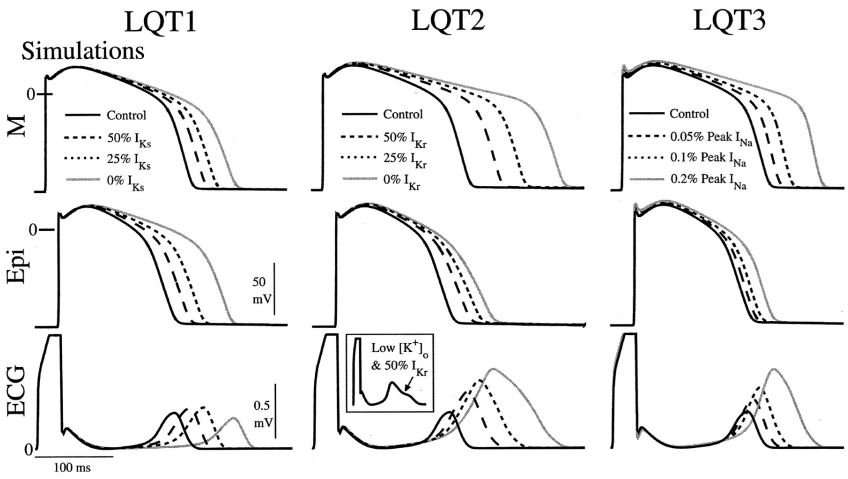
- LQTS type 1 (LQT1), caused by variants in *KCNQ1*;
- LQTS type 2 (LQT2), caused by variants in *KCNH2*; and
- LQTS type 3 (LQT3), caused by variants in *SCN5A*,

see [86, 87].

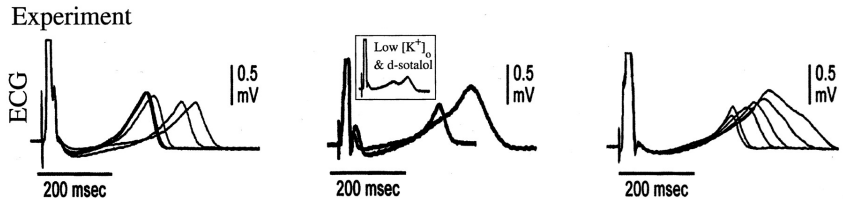
Cellular and Electrophysiological Mechanisms

At the cellular level, the three most prevalent genotypes correspond to distinct ionic mechanisms (Figure 1.8a): LQT1 is typically linked to loss-of-function variants in *KCNQ1* that reduce the slow delayed rectifier potassium current (I_{Ks}) [86,88], LQT2 to loss-of-function variants in *KCNH2* that reduce the rapid delayed rectifier potassium current (I_{Kr}) [86], and LQT3 to gain-of-function variants in *SCN5A* that increase late sodium current (I_{Na}) [86,89,90]. These alterations prolong action potential duration and amplify spatial and temporal heterogeneity of repolarization, providing both substrate (increased dispersion) and triggers (afterdepolarization-related activity) for polymorphic ventricular arrhythmias [26].

A useful mechanistic link between cellular heterogeneity and surface ECG features is the concept of transmural dispersion of repolarization. Experimental evidence has shown that, under normal and long-QT conditions, the earliest



(a)



(b)

Figure 1.8: Effects of representative LQTS mechanisms. Panel (a) illustrates the effects of ion channel mutations on simulated ventricular APs and the corresponding ECG manifestations across major genotypes (LQT1-LQT3), highlighting how different repolarization alterations can yield distinct QT and T-wave phenotypes. Panel (b) provides representative example of experimental data [91, 92] that are consistent with the patterns modeled in (a). Adapted from: [93]

repolarizing ventricular layer aligns with the T-wave peak, whereas the latest repolarizing layer aligns with the end of the T wave [11, 26, 73], supporting the interpretation of the T_{pe} as an index of repolarization dispersion [11, 26].

These repolarization gradients also help explain why LQTS is not only a "long QT" phenotype but often a "T-wave morphology" phenotype. In addition to QT prolongation, characteristic T-wave patterns may difference LQTS subtypes (Figure 1.8b), including early broad T wave in LQT1; flattened, asymmetric, notched, or bifid (notched) T waves in LQT2; and late onset T wave in LQT3 [76, 94, 95]. Derivated markers combining some of these patterns, which may increase their T-wave complexity across leads, can discriminate gene-positive LQTS patients from controls and may remain informative even

when QT_c is borderline [75, 95].

Finally, genotype-specific autonomic triggers provide a clinically relevant bridge between mechanism and presentation: LQT1 events are classically associated with high sympathetic tone during exertion (with strenuous swimming often highlighted) [86, 88, 96], LQT2 events with sudden adrenergic surges such as startle or exposure to loud noises [89, 97], and LQT3 events more frequently occurring at rest or during sleep [88].

Clinical Evaluation and Diagnosis

In clinical practice, LQTS is considered in two main scenarios: symptomatic individuals (having cardiogenic syncope, documented ventricular arrhythmias, or resuscitated cardiac arrest) and asymptomatic individuals identified through an abnormal resting ECG (prolonged QT_c) or family screening. The recommended initial evaluation integrates: (i) clinical assessment (syncope characteristics, family and medical history, and medication review), (ii) a 12-lead ECG focused on QT_c and T-wave morphology, (iii) an exercise test with emphasis on QT_c at 4-minute recovery, and (iv) echocardiography to exclude structural abnormalities [98]. Additional tests may be used selectively (Holter monitoring and further imaging when indicated), and genetic testing is typically pursued with involvement of genetics expertise. The diagnosis can then be classified using established criteria: definite LQTS when the Schwartz score is $\geqslant$3.5 [86], or a pathogenic/likely pathogenic variant in an LQTS gene is identified, or QT_c is $\geqslant$500 ms on repeated ECGs in the absence of QT-prolonging drugs [99]; probable LQTS when QT_c is between 480 and 499 ms on repeated ECGs; and possible LQTS when the LQTS risk score is 2.0–3.5 in the presence of a family history of LQTS [98].

Risk Stratification

Patients with LQTS are at risk of SCD and resuscitated cardiac arrest, often refer in the literature as serious arrhythmic events (SAE) or as the composite endpoint ventricular arrhythmia (VA). Therefore, risk stratification aims to identify individuals with a higher likelihood of SAE to guide shared decisions regarding therapies. Risk is modulated by a combination of clinical history, ECG phenotype, and genetic background [98]. Clinically, the probability of cardiac event (CE), which includes SAE and syncope, is not constant across life. CE is generally higher in childhood and tends to attenuate with age, with older patients (particularly >60 years) showing a lower LQTS arrhythmic mortality

[100–102]. Sex further interacts with age: male sex is associated with higher CE risk in childhood/early adolescence, in mid-to-late adolescence the level of risk seems comparable for males and females [103,104], whereas in adulthood female sex is associated with increased risk of CEs [105–109]. History of occurrence of prior CE is another important clinical marker [103, 104, 110–113], with a higher SAE risk particularly when syncope is recent (within 2 years) and/or recurrent [103, 110, 111].

From the ECG perspective, QT_c duration remains a central established marker [98]: higher QT_c values show a consistent stepwise association with higher event rates [105,109,114–116], and repeated measurements are clinically relevant because the maximum QT_c across serial ECGs can predict events better than a single measurement [106,117,118]. A established threshold is QT_c $\geqslant$500 ms, which identifies a higher-risk subgroup (with clearly higher annual rates of cardiac events and SAE compared with QT_c <500 ms) [119, 120], whereas genotype-positive individuals with QT_c <500 ms generally show low SAE incidence [105, 121], and those with QT_c <460 ms very low SAE risk [105, 114, 121].

Genetic information refines risk beyond single LQTS subtype classification [98]: while average rates at the subtype level differ [104, 112, 113, 121], substantial heterogeneity exists within each genotype depending on the specific variant [113, 118, 122, 123], on their location within the potassium channel [124–126], and in some cases on whether the variant acts through dominant-negative effects versus haploinsufficiency [126].

Beyond QT_c prolongation, LQTS also manifests as characteristic abnormalities where T-wave morphology reflects aspects of spatial and temporal heterogeneity that may not be summarized by a single duration value [26, 27]. In this context, the quantification of T-wave abnormalities has been suggested as a complementary source of information for both clinical detection and risk stratification. Moreover, several T-wave-derived markers have been reported as independent predictors of events [78, 127], and although the genotype specific T-wave abnormalities are qualitatively recognized, they remain difficult to quantify and have not yet been systematically integrated into clinical risk stratification [80]. Therefore, their interplay and translation into decision-making would benefit from systematic evaluation.

1.5.3 Brugada Syndrome

BrS is an inherited cardiac channelopathy characterized by an increased susceptibility to malignant ventricular arrhythmias and SCD in patients who

typically have no overt structural heart disease, and by a distinctive ECG phenotype in the right precordial leads [128–130]. The syndrome was first described in 1992 in resuscitated sudden-death patients showing a characteristic right-precordial ST-segment elevation pattern, and it is now understood as a condition with a dynamic ECG phenotype, in which the diagnostic pattern may be intermittent or concealed, and may be triggered or amplified by clinical circumstances such as fever or by sodium-channel-blocking drug exposure [130, 131]. From a genetic standpoint, BrS is most commonly associated with mutations in the *SCN5A* gene encoding the cardiac sodium channel [132], with more than 100 different mutations reported nowadays, while inheritance can show variable expressivity and incomplete penetrance [133–135]. Although the true disease burden is difficult to quantify due to concealed presentations and ECG variability, BrS has been estimated to account for ∼4-12% of sudden deaths and up to ∼20% of sudden deaths in individuals with structurally normal hearts, with less prevalent in women than men. Prevalence estimates vary widely (from ∼1:5,000 to ∼1:2,000 in some summaries), with substantial geographic differences and higher reported frequency in parts of Asia, where related sudden nocturnal death episodes have been historically described [136].

Cellular and Electrophysiological Mechanisms

Mechanistic understanding of BrS is based in its genetic substrate and in how this substrate affects the ventricular AP. Early genetic studies linked BrS primarily to loss-of-function variants in *SCN5A*, which encodes the α-subunit of the cardiac sodium channel, $Na_V1.5$ [137]. Reported variants can affect multiple channel regions, e.g. interdomain linkers, terminal domains (N and C), and transmembrane proteins [130], and have been associated with abnormal gating (activation and/or inactivation) [138] as well as reduced transport to the cell membrane [139, 140]. Functionally, $Na_V1.5$ dysfunction can shift channel kinetics toward later activation and earlier inactivation with resulting decrease in APD, thereby reducing peak I_{Na} and slowing the phase-0 upstroke of the AP [141]. Notably, within contemporary gene-disease validity frameworks, *SCN5A* remains the only gene considered definitively disease-causing for BrS [142], even though identifiable *SCN5A* variants are found in only a minority of clinically diagnosed patients [143, 144].

Beyond *SCN5A*, several additional genes have been reported in association with BrS. These reports span (i) genes related to the cardiac sodium-channel system (e.g., *SCN10A* [144, 145], genes encoding $Na_V1.5$ β-subunits [146], and genes influencing $Na_V1.5$ expression/trafficking [147, 148]), (ii) genes encoding

potassium channel (related to the transient outward current I_{to} during phase 1 of the AP) [149], (iii) genes encoding calcium channel (related to the late calcium I_{CaL} current during phase 2 of the AP) [150], alongside proteins associated with these channels [151]. Conceptually, these proposals converge on a common electrophysiological direction: a relative reduction of inward sodium/calcium current and/or a relative increase of outward potassium current [152]. However, beyond *SCN5A*, the causal relevance of many reported gene associations remains uncertain and is still a matter of debate [131, 142].

The underlying mechanism of BrS is commonly discussed through the depolarization versus repolarization hypotheses. In the depolarization framework, reduced I_{Na} and conduction discontinuity are associated with conduction delay in the right ventricular outflow tract (RVOT) and with late potentials [153,154], yielding heterogeneous depolarization in the RVOT that is considered arrhythmogenic [155, 156]. In the repolarization framework, a relative reduction of inward sodium current (I_{Na}) and a relatively increased outward potassium current (I_{to}) during phase 2 of the AP can accentuate the notch in the right ventricular epicardium AP, generating pronounced dispersion of transmural (epicardial-endocardial gradient) action-potentials that manifest in the ECG as J-point/ST-segment elevation [153, 157–159] (See Figure 1.9).

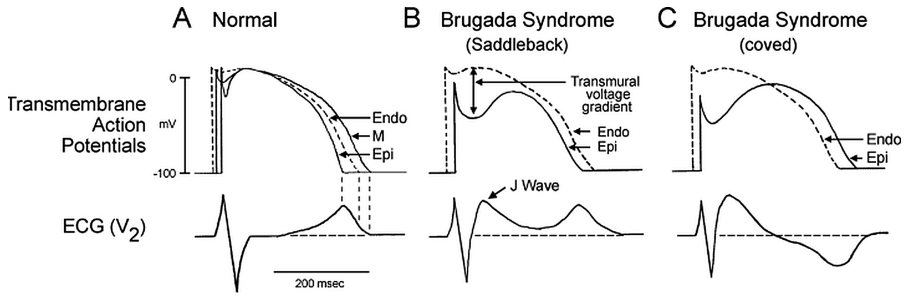


Figure 1.9: Schematic representation of the AP patterns modifications and their corresponding manifestations on the surface ECG as proposed mechanism of ST-segment elevation in Brugada syndrome. Panel A illustrates a normal setting with minimal epicardial-endocardial voltage gradients and an isoelectric ST segment. Panels B and C depict Brugada-type morphologies in which an accentuated notch in certain regions of the epicardium creates a transmural voltage gradient that appears on the surface ECG (lead V2) as J-point/ST-segment elevation, yielding a saddleback (B) or coved (C) morphology. Extracted from [160].

At the surface ECG level, this translates into the characteristic morphologies (saddleback-shaped and coved ST-elevation) classically described in right precordial leads, defining the three Brugada patterns [130, 131, 135]. Type 1 shows a coved ST-segment elevation $\geqslant$2 mm followed by T-wave inver-

sion [131, 158]. Type 2 presents a saddleback morphology with a prominent J-point elevation ($\geqslant$2) and a "trough" that remains elevated (typically $\geqslant$1 mm), followed by a positive or biphasic T wave [158]. Finally, type 3 resembles the saddleback or coved appearance with an ST-segment elevation of <1 mm [158]. Consistent with the mechanistic interpretation shown in Figure 1.9, progressive accentuation of the epicardial notch and the resulting transmural gradients can shift the phenotype from a saddleback configuration toward a coved pattern. In this setting, loss of the epicardial action-potential dome at selected sites can create marked heterogeneity and promote phase-2 re-entry, providing a mechanistic pathway to polymorphic VT/VF [157, 157, 158, 161]. Importantly, the nature of the underlying mechanism of BrS (depolarization or repolarization changes abnormalities) is still debated [152, 153]. Moreover, some studies also emphasize that evidence exists for the coexistence of depolarization and repolarization abnormalities [162–164], consistent with a convergent phenotype that may not be explained by a single mechanism.

Clinical Evaluation and Diagnosis

In routine practice, patients are typically evaluated for BrS through two main presentations: symptomatic individuals (having cardiogenic syncope, documented ventricular arrhythmias, or resuscitated cardiac arrest) and asymptomatic individuals identified through abnormal ECG morphologies (type 1 or type 2/3 Brugada patterns) or through first-degree family screening. Initial evaluation combines: (i) clinical assessment (including syncope characteristics, family and medical history, and medication review), (ii) careful ECG acquisition and interpretation, and (iii) echocardiography to exclude structural abnormalities, while further discretionary testing may be used selectively (e.g., sodium channel blocker (SCB) provocation testing, Holter monitoring, electrophysiology study, and advanced imaging such as cardiac magnetic resonance) [130, 131, 165].

The diagnostic cornerstone is a type-1 Brugada ECG pattern above described in at least one right precordial lead (V1 and V2). Because sensitivity depends on how well V1–V2 "see" the RVOT, recording high right precordial leads (2nd–4th intercostal spaces) is recommended to increase diagnostic yield since individual variations in the anatomical position of the RVOT can affect detection [166], and it is now recognized that higher lead placement can improve sensitivity compared with standard ECG configurations [167, 168]. This concept is illustrated in Figure 1.10, where relocating V1-V2 to higher precordial positions can make the characteristic ST-segment elevation pattern more

evident.

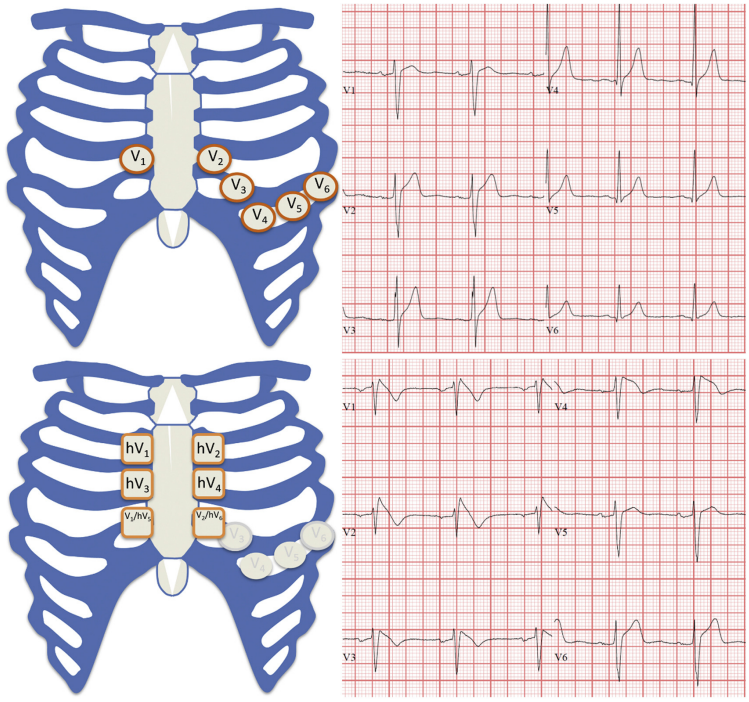


Figure 1.10: Representation of the (Top) standard- and (Buttom) high- lead placement alongside their corresponding precordial ECGs in a Brugada patient. Note the correspondence between hV5/hV6 on the high-lead ECG and V1/V2 on the standard-lead ECG. Extracted from [131].

Because Brugada patterns may be fluctuating or influenced by factors such as large meals, fever or medications [169], SCB provocation (with continuous monitoring) may be used to unmask a diagnostic pattern when suspicion persists without a spontaneous type-1 pattern, or in patients with a baseline type 2 or type 3 pattern [131, 165], acknowledging that yield and specificity vary by agent and protocol [170]. Additionally, contemporary frameworks recognize that ECG findings may need to be interpreted alongside clinical and family history, for example via integrated scoring concepts such as the Shanghai score, rather than relying on drug-induced ECG changes in isolation [165].

In summary, definite diagnostic of BrS is established with spontaneous type 1 ECG pattern in either high- or standard- lead positions, while it remains probable with type 1 pattern induced by fever or SCB provocation [131]. While genetic testing is advised for those exhibiting a type 1 BrS ECG pattern to

facilitate familial screening, the presence of an isolated pathogenic variant in a BrS susceptibility gene is not, by itself, diagnostic for BrS [165, 171].

Risk Stratification

Risk stratification in BrS aims to identify individuals at increased risk of SAEs, while avoiding overtreatment in the many patients identified through screening who remain asymptomatic. Established high-risk features include: (i) history of cardiac arrest, (ii) arrhythmic syncope, and (iii) spontaneous type-1 ECG patterns [131]. Beyond resuscitated cardiac arrest, the clinical factors with the greatest impact on SAEs are a history of cardiogenic syncope and the presence of a spontaneous type-1 ECG pattern, both validated across different cohorts [172–175]. Importantly, these two markers remain independent predictors of SAEs after adjustment for other risk factors [176–181].

Beyond these established markers, additional variables have been explored to refine risk assessment. Age and sex appear to have a limited independent role once established predictors are considered in multivariable models [176, 179, 182], although older age at diagnosis may reflect a more benign course [183] and male sex has been linked to higher risk in some analyses, but not consistently as an independent predictor after adjustment for other risk factors [176, 180, 182]. Family history of SCD or SAEs has shown inconsistent associations with outcomes, a potential predictive value has been reported only for very early familial SCD in first-degree relatives, but this requires clarification with adequate adjustment for other factors [131, 184]. In this context, "EP study" refers to an invasive electrophysiology study, often incorporating programmed ventricular stimulation (PVS) to assess arrhythmia inducibility [182, 184]. However, its role remains controversial and, given its invasive nature and limited predictive value in large registries, it is generally reserved for selected borderline scenarios rather than routine risk stratification [131, 175, 176].

Finally, several ECG-derived features have been proposed as complementary markers spanning depolarization and repolarization abnormalities, including QT_c [185], QRS fragmentation [175, 180], early repolarization patterns [179, 186], QRS duration [177, 180], duration of S-wave, and T_{pe} [177, 187, 188]. Collectively, these indices have been associated with SAEs risk and may mirror broader disturbances of the electrical substrate, but overall consistency still requires large-scale evaluation with appropriate adjustment for established risk factors.

1.6 Objective and Outline of the Thesis

The main objective of this thesis is to evaluate quantitative ECG-based markers that characterize T-wave morphology for ventricular arrhythmic risk assessment. The underlying motivation is that clinically used indices often rely on fiducial point measurements and may therefore capture only a limited portion of the information contained in ventricular repolarization, particularly when repolarization abnormalities manifest as complex morphological changes. By using a time-warping-based method to quantify differences between waveforms, the thesis aims to provide a complementary and more morphology-aware description of repolarization dynamics that can support a better understanding of arrhythmogenic substrates and ultimately may contribute to improving clinical decisions. In addition, markers derived from time-warping analysis may help to noninvasively stratify patients across different scenarios and improve the prediction of arrhythmic risk.

The work is developed and evaluated across three complementary clinical settings in which malignant ventricular arrhythmias represent a major concern: ischemic cardiomyopathy and the inherited channelopathies LQTS and BrS. A schematic overview of the overall study framework and the main research branches addressed in this thesis is shown in Figure 1.11. The content of the rest of the thesis is organized into 7 chapters, which present the methodological framework and its application to each setting, and conclude with the main findings and perspectives for future work. The thesis is summarized as follows:

- **Chapter 2:** This chapter presents the general methodological framework shared across all studies in the thesis. It describes the common ECG processing pipeline, including preprocessing, fiducial detection and delineation, and spatial anlysis through PCA. It then introduces the time-warping analysis used to quantify morphology differences and derive the main ECG markers, covering unsigned and signed formulations, mean warped T-wave estimation, and the T-wave peak-to-end restricted analysis. Finally, it summarizes the classical T-wave markers used as complementary references throughout the thesis.
- **Chapter 3:** This chapter investigates ischemia-induced repolarization changes using transient coronary occlusion during PCI as a controlled human model, characterized by a short ischemic time window. A time-warping-based analysis restricted to the T-wave peak-to-end interval, which is less affected by concomitant ST-segment deviations, is introduced to quantify morphology changes and characterize their temporal

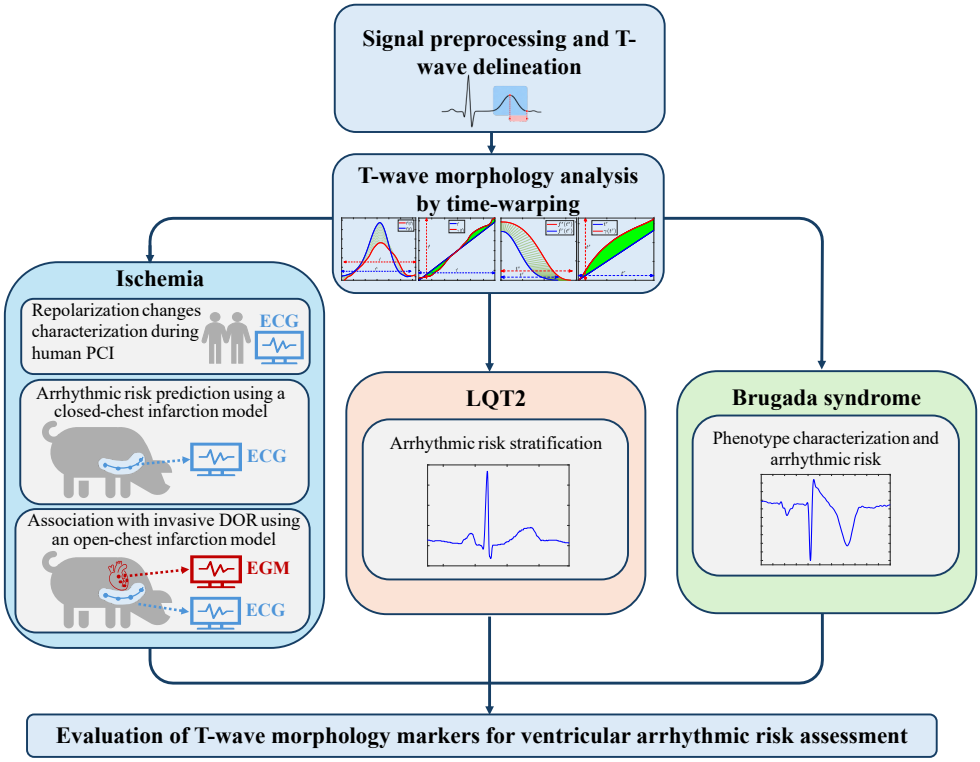


Figure 1.11: Overview of the common methodological basis and the clinical and experimental study branches used to evaluate T-wave morphology markers in ischemia, LQT2, and Brugada syndrome. Abbreviations: PCI, percutaneous coronary intervention; ECG, electrocardiogram; DOR, dispersion of repolarization; EGM, electrogram; LQT2, long QT syndrome type 2.

evolution and lead-wise behavior during ischemia. To provide a spatially global characterization, the analysis is also performed on the first principal component obtained by PCA, which emphasizes T-wave components across leads. The time-warping marker is evaluated alongside classical ischemia and repolarization indices, providing the methodological basis for its subsequent application and validation in others ischemia models.

The work described in this chapter led to the following publications:

– **N. Gómez**, J. Ramírez, J. P. Martínez, and P. Laguna, "Time-warping analysis of the T-wave peak-to-end interval to quantify ventricular repolarization dispersion during ischemia," IEEE Journal of Biomedical and Health Informatics, vol. 27, no. 11, pp. 5314–5325,

2023.

– **N. Gómez**, J. Ramírez, J. P. Martínez, and P. Laguna, "Time-warping based end-of-T-wave shape marker reflects repolarization changes during ischemia," in 2022 Computing in Cardiology (CinC), vol. 498, pp. 1–4, 2022.

- **Chapter 4:** This chapter extends the ischemia analysis to a closed-chest porcine myocardial infarction model with prolonged coronary occlusion, enabling the study of ventricular fibrillation risk under evolving ischemia. The proposed time-warping approach, restricted to the T-wave peak-to-end interval to focus on repolarization-related morphology changes, is applied to characterize dynamic ischemia-induced trends and assess its value for arrhythmic risk prediction in relation to VF outcome. A PCA-based spatial representation is also used to obtain a global characterization across leads, and the warping-derived marker is examined in comparison with the classical T_{pe} interval.

  The research presented in this chapter resulted in the following publications:

  – **N. Gómez**, J. Ramírez, A. Martín-Yebra, M. M. Demidova, P. Platonov, J. P. Martínez, and P. Laguna, "T-wave peak-to-end changes quantified by time-warping predicts ventricular fibrillation in a porcine myocardial infarction model," IEEE Transactions on Biomedical Engineering, vol. 71, no. 10, pp. 2968–2977, 2024.
  – **N. Gómez**, J. Ramírez, A. Martín-Yebra, M. M. Demidova, P. Platonov, J. P. Martínez, and P. Laguna, "Changes in T-peak-to-T-end morphology measured by time-warping are associated with ischemia-induced ventricular fibrillation in a porcine model," in 2023 Computing in Cardiology (CinC), vol. 50, pp. 1–4, 2023.
  – **N. Gómez**, J. Ramírez, A. M. Yebra, M. Demidova, P. Platonov, J. Martínez, and P. Laguna, "Los cambios en la morfología del pico al fin de la onda T, cuantificados mediante "time-warping", están asociados con la aparición de fibrilación ventricular en un modelo porcino de isquemia aguda," in CASEIB 2023. Libro de Actas del XLI Congreso Anual de la Sociedad Española de Ingeniería Biomédica (CASEIB 2023), pp. 2–5, Sociedad Española de Ingeniería Biomédica (SEIB), 2023.

- **Chapter 5:** This chapter presents a validation framework of the previous studies by analyzing ischemia-induced repolarization dispersion in an

open-chest porcine myocardial infarction model with simultaneous body-surface ECG and intramyocardial recordings. The availability of intramyocardial electrograms enables direct quantification of DOR, providing an invasive reference framework to evaluate non-invasive ECG-derived markers. Within this setting, the time-warping-based index restricted to the T-wave peak-to-end interval is assessed as a surrogate descriptor of DOR and its relationship to VF risk, using a PCA-based spatial representation to obtain a global characterization across leads and comparing against the classical T_{pe} interval.

The work described in this chapter led to the following publications:

- **N. Gómez**, A. S. Abramochkina, J. Ramírez, A. O. Ovechkin, O. G. Bernikova, P. G. Platonov, J. E. Azarov, P. Laguna and J. P. Martínez, "T-wave peak-to-end changes, quantified by time-warping, surrogates ventricular repolarization dispersion for ventricular fibrillation prediction in a porcine myocardial infarction model," IEEE Transactions on Biomedical Engineering, *In press.*
- **N. Gómez**, J. Ramírez, A. S. Tsvetkova, P. Platonov, J. E. Azarov, J. P. Martínez, and P. Laguna, "Dynamics of T-peak-to-T-end morphology changes in an open-chest porcine model, and its relation to arrhythmic events," in 2024 Computing in Cardiology (CinC), vol. 51, pp. 1–4, 2024.

- **Chapter 6:** This chapter addresses arrhythmic risk stratification in LQT2 by quantifying T-wave morphology abnormalities beyond conventional QT-based measures. A population-reference approach is adopted, where a time-warping-based marker, the TMV index, compares T-wave from each patient against the corresponding sex-, heart-rate-, and lead-matched normal reference T-wave derived from a large population cohort, enabling a geometry-aware characterization of morphology variation. The chapter evaluates the association between TMV and clinical outcomes in LQT2, and examines its value in relation to established clinical markers and complementary morphology-related indices.

  The research presented in this chapter resulted in the following publication:

  - **N. Gómez,** J. Ramírez, A. A. Savelev, P. Dahlberg, A. Svensson, N. Larsson, E. Ljungström, U. Chaudhry, J. P. Martínez, P. Laguna,

and P. G. Platonov, "Risk stratification of patients with type 2 long-QT syndrome through analysis of T-wave morphology," Journal of the American Heart Association, vol. 15, p. e048388, 2026.

- **N. Gómez**, J. Ramírez, J. P. Martínez, and P. Laguna, "Evaluation of T-wave time-warping dynamics in patients with long QT syndrome.," in 2024 13th Conference of the European Study Group on Cardiovascular Oscillations (ESGCO), pp. 1–2, 2024.

- **Chapter 7:** This chapter extends the evaluation of time-warping-based T-wave morphology markers to BrS using 24-hour Holter recordings. Morphology restitution and variation are assessed both over the complete T wave (TMR and TMV indices, respectively) and after restricting the analysis to the T_{pe} interval (TPEMR and TPEMV indices, respectively). These markers are evaluated for the characterization of the Brugada phenotype, the presence of a spontaneous type-I pattern, and the distinction between symptomatic and asymptomatic patients, while also being examined alongside classical repolarization and depolarization-related ECG markers across different leads.

  The work described in this chapter led to the following publications:

  - **N. Gómez**, J. Ramírez, A. I. Roquero, F. Palmieri, E. Arbelo, J. P. Martínez, and P. Laguna, "T-wave peak-to-end morphology restitution as biomarker in brugada syndrome," in 2025 Computing in Cardiology (CinC), vol. 52, pp. 1–4, 2025.
  - **N. Gómez**, J. Ramírez, A. Isabel Roquero, F. Palmieri, E. Arbelo Lainez, J. P. Martínez Cortés, and P. Laguna Lasaosa, "Evaluación de los cambios en la morfología del pico al fin de la onda T, cuantificados mediante "time-warping", en pacientes con síndrome de Brugada," in Actas XLII Congreso Anual de la Sociedad Española de Ingeniería Biomédica (CASEIB 2024), pp. 29–32, Sociedad Española de Ingeniería Biomédica (SEIB), 2024.

- **Chapter 8:** This chapter summarizes the main findings of the thesis, discusses the overall contributions and limitations of the work, and outlines directions for future research and clinical translation of T-wave morphology markers for arrhythmic risk assessment.

CHAPTER 2

GENERAL METHODS FOR ECG SIGNAL PROCESSING

2.1 ECG Processing Pipeline
- 2.1.1 ECG Preprocessing
- 2.1.2 Fiducial Detection and Delineation
- 2.1.3 Spatial Principal Component Analysis

2.2 Classical ECG Markers (Intervals and Amplitudes)

2.3 Time-Warping Analysis
- 2.3.1 Unsigned Time-Warping Marker
- 2.3.2 Signed Time-Warping Marker
- 2.3.3 T-wave Peak-to-End Restricted Warping Analysis
- 2.3.4 Mean Warped T-Wave
- 2.3.5 Weighted Time-Warping Markers

This chapter describes the general methodological framework underlying all studies included in this thesis. It presents the common signal processing procedures, ECG delineation strategy, spatial transformation techniques, and the mathematical formulation of the time-warping-based markers used throughout the work. Study-specific details such as population characteristics, acquisition protocols, and computational workflow are described separately within each corresponding chapter. The purpose of this chapter is therefore to provide a unified and reproducible methodological basis that supports the interpretation and comparison of the results presented in subsequent chapters.

This thesis applies the methodologies on five distinct databases, spanning

experimental animal models and clinical human populations. First, a cohort of patients undergoing PCI, STAFF-III database [189], was used to investigate transient ischemia and its impact on ventricular repolarization dynamics, quantified using time-warping-based markers. Second, a closed-chest porcine myocardial infarction model [190] was employed to evaluate the predictive value of these markers for VF. Third, an open-chest porcine myocardial infarction model [191] with simultaneous invasive recordings provided a controlled experimental setting to further study the relationship between non-invasive ECG-derived markers and DOR, and their value for predicting VF. Finally, clinical populations of LQTS [192] and BrS [193] patients were analyzed to assess the role of T-wave morphology markers in arrhythmic risk prediction.

Detailed descriptions of inclusion criteria, acquisition protocols, and endpoint definitions for each population are provided in the corresponding chapters.

2.1 ECG Processing Pipeline

2.1.1 ECG Preprocessing

ECG recordings are commonly contaminated by low-frequency baseline wander and high-frequency disturbances, which can alter the morphology of cardiac waves, hinder reliable waveform delineation, and consequently compromise subsequent markers computation [194]. For this reason, a preprocessing stage including high- and low-pass filtering was applied throughout the studies presented in this thesis to improve the signal-to-noise ratio while preserving the morphological characteristics of the QRS complex and T wave required for the subsequent analysis. General discussions on ECG preprocessing can be found in [32].

Baseline Wander

Baseline wander is a low-frequency component that may arise from respiration, body movements, or electrode-skin impedance changes. Its presence can distort amplitude measurements and affect the accurate localization of wave boundaries [194]. To mitigate this effect, a high-pass Butterworth digital filter (sixth order, zero-phase implementation) with a cut-off frequency of 0.5 Hz was applied to remove slow-varying components of the signal.

High-Frequency Noises

High-frequency ECG disturbances are mainly due to powerline interference (50/60 Hz and harmonics) and electromyographic noise, the latter being particularly challenging because its spectral content overlaps with that of the ECG signal. These components may impair waveform interpretation and reduce the accuracy of delineation, particularly for low-amplitude features such as the T wave [194]. To attenuate such interference while preserving relevant ECG content required for detection and delination, a low-pass Butterworth digital filter (sixth order, zero-phase implementation) with cut-off frequency of 40 Hz was applied. An example of the original ECG signal and the corresponding filtered signals is shown in Figures2.1a and 2.1b.

Finally, after T-wave delineation and segmentation, each extracted T wave was additionally low-pass filtered using a bidirectional sixth-order Butterworth filter (20 Hz cut-off) to attenuate residual out-of-band components and preserve the dominant frequency band relevant for the subsequent computation of morphology-based markers.

2.1.2 Fiducial Detection and Delineation

QRS detection and ECG waveform delineation were performed using algorithms fully described in Martínez et al. [195]. Specifically, Martínez et al. introduced a wavelet-based delineator that relies on a time-scale representation of the signal, which is well suited to ECG analysis given the different dominant frequency content of the QRS complex and the P and T waves. For multilead delineation, they used a rule-based strategy previously proposed by Laguna et al. [196], obtaining robust multilead fiducial points by consolidating single-lead annotations.

Single-Lead Wavelet-Based Delineation

Single-lead delineation was based on the discrete dyadic wavelet transform (WT), which decomposes the ECG into a time-scale representation allowing analysis at different temporal resolutions. Fiducial point detection was performed at the wavelet scales associated with each waveform: QRS-related activity was mainly identified at scales $2^1 - 2^2$, whereas P and T waves were characterized at scales $2^4 - 2^5$ [195]. In this framework, local maxima and minima of the WT coefficients correspond to steep slope variations in the ECG, whereas zero-crossings between opposite extrema are associated with waveform

peaks. Wave morphology and boundaries were subsequently determined using threshold-based criteria driven by the number, polarity, and temporal arrangement of the detected coefficients, defining onset and end points around the first and last significant slopes associated with each wave [195].

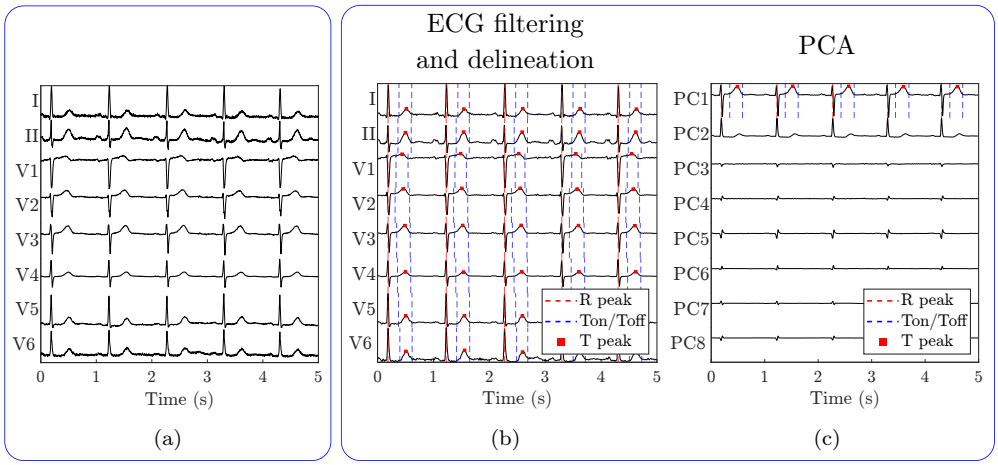


Figure 2.1: Example of the signal processing workflow from the original multilead ECG to the spatially PCA representation used for subsequent analysis. Panel (a) displays a 5 s segment of the original ECG from the 8 independent leads. Panel (b) shows the same segment after filtering, as described in Section 2.1.1, together with the delineation marks obtained as described in Section 2.1.2: the R peak (red dashed line), T-wave onset and end (blue dashed lines), and T-wave peak (red square). Panel (c) shows the corresponding principal components after applying spatial PCA to the 8 independent leads, as detailed in Section 2.1.3, with the same fiducial marks displayed on the dominant component.

Multilead Selection Rules

To derive multilead fiducial markers from the set of single-lead detections, a rule-based post-processing strategy was applied as proposed in [196]. Lead-wise annotations were first temporally ordered and evaluated for inter-lead consistency. A multilead marker was accepted only when a predefined number of neighboring annotations (k) were located within a tolerance interval Δ ms, ensuring agreement across leads. In the implementation used in this thesis, k was set to 70% of the number of leads included in the analysis, rounded to the nearest integer. The tolerance Δ was set to 4 ms for P-wave onset and end, 12 ms for QRS onset, 10 ms for QRS end, and 12 ms for T-wave onset and end.

For peak locations, the multilead annotation was obtained by combining the consistent lead-wise peak annotations using a robust central estimate (median rule). For wave boundaries, lead-wise onset and end candidates were combined by selecting the earliest onset and the latest end among the annotations satisfying the k-neighbor consistency criterion, while isolated detections were rejected [196].

Workflow

Across the studies included in this thesis, these two components were combined in a three-stage workflow. First, the wavelet-based delineator was applied in single-lead mode to obtain QRS detections in each lead [195]. Second, the multilead selection rules were used to derive robust multilead QRS reference annotations [196]. Finally, the resulting multilead QRS reference annotations were used both to define the ECG segmentation required for the implementation of spatial PCA, and to provide stable temporal references within the delineator's workflow, enabling a more reliable identification of fiducial points in the standard leads and in the PCA-transformed lead. An example of the filtered ECG signals together with the delineation marks is shown in Figure 2.1b.

2.1.3 Spatial Principal Component Analysis

Spatial principal component analysis (PCA) was used as a lead-space reduction technique to obtain a reduced set of transformed leads with enhanced waveform representation. In ECG recordings acquired from multiple leads, the different leads contain projections of the same underlying cardiac electrical activity. PCA exploits this interlead redundancy by transforming the original leads into a new set of orthogonal lead combinations ordered according to the variance captured from the data [197]. In this way, the original set of leads can be represented in a transformed system in which most of the relevant waveform energy is concentrated in the first components. In the studies presented in this thesis, the PCA transformation matrix was estimated individually for each subject using only T-wave segments selected from a study-specific learning interval, as detailed in the Methods section of each corresponding study. When multiple recordings from the same subject were analyzed, a separate transformation matrix was estimated for each recording.

If $\mathbf{x}(n) = [x_1(n), x_2(n), ..., x_L(n)]^T$ denotes the multilead signal vector at sample n, where L represents the number of independent leads, the PCA transformation can be expressed as:

$$\mathbf{w}(n) = \mathbf{\Phi}^T \mathbf{x}(n), \tag{2.1}$$

where $\mathbf{\Phi}$ is the $L \times L$ transformation matrix and $\mathbf{w}(n)$ contains the transformed components at sample n. Thus, the transformation is applied sample by sample to the multilead ECG, so that each transformed component is obtained as a linear combination of the original leads. The columns of $\mathbf{\Phi}$ are the eigenvectors of the interlead auto-correlation matrix, ordered according to descending eigenvalues. Thus, the transformed components are ranked according to the amount of signal variance they explain.

In this thesis, PCA was applied spatially to the set of available independent ECG leads, whose number and configuration varied across studies, as specified in their respective Methods sections. To estimate the transformation, the learning data were built from T-wave segments extracted from a predefined N samples temporal interval of the k-th beat of the l-th lead ECG recording, $\mathbf{x}_{k,l} = [x_{k,l}(0), \ldots, x_{k,l}(N-1)]$, assumed to represent a stable reference condition, and were then arranged, concatenating the set of K beats, $\tilde{\mathbf{x}}_l = [\mathbf{x}_{0,l}, \ldots, \mathbf{x}_{K-1,l}]^T$, and arranging the L independent leads in a data matrix $\mathbf{X} = [\tilde{\mathbf{x}}_1, \ldots, \tilde{\mathbf{x}}_L]$, with one row per time sample and one column per lead. Thus, if $M = K \times N$ denotes the number of samples used for learning, the data matrix satisfies $\mathbf{X} \in \mathbb{R}^{M \times L}$ and the $L \times L$ interlead auto-correlation matrix was estimated as:

$$\mathbf{R}_{\mathrm{X}} = \frac{1}{M} \mathbf{X}^T \mathbf{X} \tag{2.2}$$

where $\mathbf{R}_{\mathrm{X}} \in \mathbb{R}^{L \times L}$. The eigenvectors of $\mathbf{R}_{\mathrm{X}}$ define the PCA basis, whereas the associated eigenvalues quantify the variance captured by each transformed direction. Accordingly, the transformation matrix $\mathbf{\Phi}$ in (2.1) was constructed by arranging the ordered eigenvectors of $\mathbf{R}_{\mathrm{X}}$ as columns. Once the transformation matrix had been obtained, the original multilead ECG recordings are projected onto this basis to obtain the transformed leads.

Since the transformed components are ordered according to the variance explained, the first transformed lead $w_1(n)$, denoted as PC1, contains the largest amount of energy of the waveform represented in the learning data, whereas the subsequent components capture progressively smaller contributions. This property is particularly useful in ECG analysis because it concentrates the dominant morphology of the waveform of interest into the first transformed leads and provides a compact representation with improved signal-to-noise ratio for subsequent morphological characterization [197, 198]. An example of the re-

sulting principal components, derived from the same ECG segments illustrated in Figure 2.1b, is shown in Figure 2.1c.

Within this framework, the multilead QRS reference annotations described in the previous subsection were used to define the ECG segmentation required for PCA and to provide consistent temporal references for the subsequent delineation of fiducial points in both the standard leads and the PCA-transformed lead. The resulting delineated waves were then used for marker computation.

2.2 Classical ECG Markers (Intervals and Amplitudes)

In addition to the time-warping-based indices described in the following, some classical ECG derived markers were also considered throughout this thesis, either as complementary descriptors of ventricular repolarization or as reference indices for comparison with the proposed methodology. In particular, when relevant to the specific pathological setting under study, the following conventional markers were evaluated:

- ST-segment level (ST): measured as the difference between the ECG signal amplitude at 60 ms after the J point and the isoelectric level, computed as the average signal over a 10 ms segment starting 15 ms before QRS onset.
- T-wave peak amplitude (T_a): amplitude difference between the T-wave peak fiducial point and the isoelectric level.
- T-wave width (T_w): interval from T-wave onset to T-wave end.
- T-wave peak-to-end interval (T_{pe}): interval from T-wave peak to T-wave end.
- QT: Interval from QRS onset to T-wave end. When required, heart-rate correction was applied using Bazett's formula, yielding the corrected QT interval (QT_c).

These markers were used across the different studies included in this thesis according to the specific pathological setting and study objective, providing established descriptors of ventricular repolarization that help contextualize the interpretation of the proposed time-warping-based indices. When required, the different ECG markers will be denoted with the superscript l, where $l \in \{\text{PCA}, \text{I}, \text{II}, \ldots \text{V6}\}$ denotes the lead in which the index is measured.

2.3 Time-Warping Analysis

As introduced in Chapter 1, several ECG-derived biomarkers have been proposed to characterize ventricular repolarization abnormalities and the associated arrhythmogenic substrate across different pathological settings. Most of these markers rely primarily on fiducial-point measurements and therefore may not fully capture the information conveyed by the overall T-wave morphology. To address this limitation, other biomarkers have been proposed, including indices derived from vectorcardiographic information [77], the V-index [199], and more recently, the composite morphology-based descriptor morphology combination score (MCS) index [200, 201].

Within this context, time-warping analysis was introduced as a robust morphology-based framework to compare the morphology of two T waves, allowing quantification of linear and non-linear variations. The methodological basis of this approach was originally developed by Ramírez et al. [202] for the characterization of whole T-wave morphological variability, and was later extended to the analysis of T-wave morphology restitution (TMR index) which quantifies the T-wave morphological variations with respect to heart rate changes [203], and to the quantification of T-wave morphology variation (TMV index) with respect to a given reference under comparable heart-rate conditions, such as a population-defined reference [204]. Moreover, this methodology was subsequently adopted by Palmieri et al. [198] for non-invasive monitoring of blood potassium changes from T-wave morphology in hemodialysis patients, and later by Bukhari et al. [205] in a broader framework aimed at characterizing serum potassium and calcium concentrations from ECG depolarization morphology analysis.

To introduce the general time-warping methodology used to compare T-wave morphology, consider two T waves and let them be denoted as the reference, $\boldsymbol{f}^r(\boldsymbol{t}^r) = [f^r(t^r(1)), \ldots, f^r(t^r(N_r))]^T$, and the studied, $\boldsymbol{f}^s(\boldsymbol{t}^s) = [f^s(t^s(1)), \ldots, f^s(t^s(N_s))]^T$, where $\boldsymbol{t}^r = [t^r(1), \ldots, t^r(N_r))]^T$ and $\boldsymbol{t}^s = [t^s(1), \ldots, t^s(N_s))]^T$ are the corresponding uniformly sampled temporal vector, and N_r and N_s denote their total duration in samples, respectively, as shown in Figure 2.2a. For the warping computation, both T waves must have the same polarity. Prior to this analysis, both waves are shifted to align their centers of gravity so that the subsequent comparison reflects morphological changes rather than relative temporal delay. The studied T wave is then temporally aligned (warped) to the reference one, and the resulting transformation is used to quantify the morphological differences between them.

Let $\gamma(\boldsymbol{t}^r)$ be the warping function relating $\boldsymbol{t}^r$ and $\boldsymbol{t}^s$ such that the composition $[\boldsymbol{f}^s \circ \gamma](\boldsymbol{t}^r) = \boldsymbol{f}^s(\gamma(\boldsymbol{t}^r))$ denotes the time-warping or re-parameterization of the $\boldsymbol{f}^s(\boldsymbol{t}^s)$ using $\gamma(\boldsymbol{t}^r)$. In this way, $\boldsymbol{f}^s(\gamma(\boldsymbol{t}^r))$ represents the amplitude values of the studied T wave $\boldsymbol{f}^s(\boldsymbol{t}^s)$ after adapting its temporal vector to that of the reference one.

A widely used approach for time-domain warping is dynamic time warping (DTW), which determines the optimal warping function by minimizing the Euclidean distance between the two waveforms. Under this formulation, the optimal warping function is given by:

$$\gamma^*_{\text{DTW}}(\boldsymbol{t}^r) = \underset{\gamma(\boldsymbol{t}^r)}{\arg\min} \, \|\boldsymbol{f}^r(\boldsymbol{t}^r) - \boldsymbol{f}^s(\gamma(\boldsymbol{t}^r))\| \tag{2.3}$$

However, when the warping is performed directly on the original waveforms, the resulting solution may be affected by the so-called "pinching effect" [206]. This occurs when the algorithm matches points with similar amplitudes but different morphological features, such as the peak of one T wave and a non-peak point of similar amplitude on the other T wave. Such mismatches can lead to excessive local time compression, whereby a relatively long segment of one waveform is matched to a much shorter segment of the other, producing an artificial alignment that reduces amplitude differences without preserving morphological correspondence. To avoid this problem, the square-root slope function (SRSF) representation was proposed to perform the warping in a better defined geometrical space [207, 208]. For a waveform $\boldsymbol{f}(\boldsymbol{t})$, its SRSF is defined as:

$$\boldsymbol{q}_f(\boldsymbol{t}) = \text{sign}\left(\dot{\boldsymbol{f}}(\boldsymbol{t})\right)\sqrt{|\dot{\boldsymbol{f}}(\boldsymbol{t})|}. \tag{2.4}$$

Accordingly, the SRSFs corresponding to the reference and studied T waves, $\boldsymbol{f}^r(\boldsymbol{t}^r)$ and $\boldsymbol{f}^s(\boldsymbol{t}^s)$, are denoted by $\boldsymbol{q}_{f^r}(\boldsymbol{t}^r)$ and $\boldsymbol{q}_{f^s}(\boldsymbol{t}^s)$, respectively, as shown in Figure 2.2b.

The function, $\gamma^*(\boldsymbol{t}^r)$, that minimizes the amplitude difference between the SRSF of $\boldsymbol{f}^r(\boldsymbol{t}^r)$ and $\boldsymbol{f}^s(\gamma(\boldsymbol{t}^r))$, $\boldsymbol{q}_{f^r}(\boldsymbol{t}^r)$ and $\boldsymbol{q}_{[\boldsymbol{f}^s\circ\gamma]}(\boldsymbol{t}^r) = \boldsymbol{q}_{f^s}(\gamma(\boldsymbol{t}^r))\sqrt{\dot{\gamma}(\boldsymbol{t}^r)}$, respectively, is selected as the optimal warping function [207, 208],

$$\begin{aligned}\gamma^*(\boldsymbol{t}^r) &= \underset{\gamma(\boldsymbol{t}^r)}{\arg\min}\left(\|\boldsymbol{q}_{f^r}(\boldsymbol{t}^r) - \boldsymbol{q}_{|f^s\circ\gamma|}(\boldsymbol{t}^r)\|\right) \\ &= \underset{\gamma(\boldsymbol{t}^r)}{\arg\min}\left(\|\boldsymbol{q}_{f^r}(\boldsymbol{t}^r) - \boldsymbol{q}_{f^s}(\gamma(\boldsymbol{t}^r))\sqrt{\dot{\gamma}(\boldsymbol{t}^r)}\|\right)\end{aligned} \tag{2.5}$$

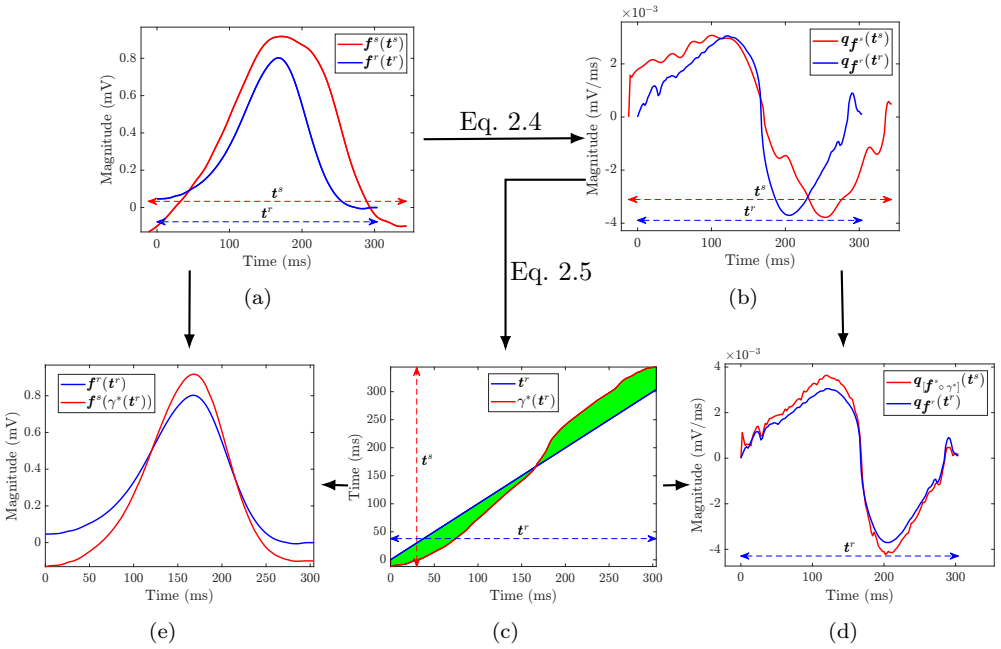


Figure 2.2: Schematic overview of the time-warping analysis used to separate temporal and amplitude differences between two T-wave morphologies. Panel (a) shows the reference T wave $\boldsymbol{f}^r(\boldsymbol{t}^r)$ (blue line) and studied T wave $\boldsymbol{f}^s(\boldsymbol{t}^s)$ (red line), the latter showing longer duration and larger amplitude. (b) Corresponding square-root slope function representations of both waveforms in (a). (c) Warping function optimally relating $\boldsymbol{t}^r$ and $\boldsymbol{t}^s$. (d) Square-root slope function representations of the reference waveform and the warped studied waveform. (e) Warped studied T wave, $\boldsymbol{f}^s(\gamma^*(\boldsymbol{t}^r))$, where time-domain differences have been compensated and the remaining mismatch with respect to the reference waveform only reflects amplitude variability.

To obtain this optimum the dynamic programming algorithm [209] was used to optimize the analysis, explained in detail in Appendix A in [202]. The warping function $\gamma^*(\boldsymbol{t}^r)$, that optimally relates $\boldsymbol{f}^s(\boldsymbol{t}^s)$ and $\boldsymbol{f}^r(\boldsymbol{t}^r)$ in Figure 2.2a is shown in Figure 2.2c. The warped waveform, $\boldsymbol{f}^s(\gamma^*(\boldsymbol{t}^r))$, which preserves the original amplitude information of the studied T wave after compensation for temporal differences, and the reference $\boldsymbol{f}^r(\boldsymbol{t}^r)$, are shown in Figure 2.2e.

2.3.1 Unsigned Time-Warping Marker

The unsigned time-warping marker [202] quantifies the overall amount of time-warping required to optimally align the studied T wave, $\boldsymbol{f}^s$, to the refer-

ence one, $\boldsymbol{f}^r$, and is defined as the average of the absolute differences between $\gamma^*(\boldsymbol{t}^r)$ and $\boldsymbol{t}^r$:

$$d_w^u = \frac{1}{N_r} \sum_{n=1}^{N_r} |\gamma^*(\boldsymbol{t}_r(n)) - \boldsymbol{t}^r(n)| \tag{2.6}$$

As illustrated in Figure 2.2, d_w^u can also be interpreted as the area between the optimal warping function $\gamma^*(\boldsymbol{t}^r)$ and $\boldsymbol{t}^r$, normalized by the duration of the reference T wave. Since the optimal warping function $\gamma^*(\boldsymbol{t}^r)$ describes how the uniformly sampled temporal vector of the studied T wave must be re-parameterized to match that of the reference wave, its deviation from the identity mapping provides a direct measure of time-domain morphological variability, regardless of the net direction of the warping. Accordingly, d_w^u reflects temporal variability in the waveform shape without distinguishing whether the studied T wave must be globally widened or compressed with respect to the reference one. Its value increases as the discrepancy between $\gamma^*(t_r)$ and the identity mapping becomes larger, and becomes zero only when no time-warping is needed.

2.3.2 Signed Time-Warping Marker

The signed time-warping marker was proposed by Palmieri et al. [198] to complement the originally proposed time-warping marker by incorporating the net direction of the time-warping, thereby allowing distinction between T-wave widening and narrowing. It is defined as:

$$d_w = \left(\frac{S_d}{|S_d|} \right) \frac{1}{N_r} \sum_{n=1}^{N_r} |\gamma^*(\boldsymbol{t}^r(n)) - \boldsymbol{t}^r(n)| \tag{2.7}$$

where S_d determines the sign of d_w and is defined as:

$$S_d = \sum_{n \in N_r^u} (\gamma^*(\boldsymbol{t}^r(n)) - \boldsymbol{t}^r(n)) + \sum_{n \notin N_r^u} (\boldsymbol{t}^r(n) - \gamma^*(\boldsymbol{t}^r(n))) \tag{2.8}$$

with N_r^u denoting the up-slope region of the T wave. In this formulation, the sign of S_d determines the predominant direction of the warping. A positive value of d_w indicates that aligning $\boldsymbol{f}^s(\boldsymbol{t}^s)$ with $\boldsymbol{f}^r(\boldsymbol{t}^r)$ predominantly requires widening of the waveform, while a negative value indicates that it predominantly requires narrowing the waveform of $\boldsymbol{f}^s(\boldsymbol{t}^s)$ to match that of $\boldsymbol{f}^r(\boldsymbol{t}^r)$.

Therefore, this signed marker preserves not only the magnitude of the time-warping, but also its direction.

The original time-warping framework also provides complementary descriptors of T-wave morphological variability. In addition to the temporal warping descriptor d_w, d_a quantifies amplitude differences remaining after temporal alignment, while d_w^{NL} and d_a^{NL} isolate the strictly non-linear components of temporal and amplitude variability, respectively [202]. Subsequent arrhythmic-risk applications of this framework were centered on d_w, including the T-wave morphology restitution (TMR) [203] and T-wave morphology variation (TMV) [204] indices, both of which were formulated from this temporal descriptor and subsequently associated with arrhythmic risk in different populations. At the same time, later applications evaluating all the original descriptors showed that their relative performance depends on the physiological settings and the process driving the waveform changes, with d_w-based temporal descriptors repeatedly showing strong associations with physiological variables under study, while the non-linear or amplitude-based markers can provide complementary information in specific settings [198, 210]. In this thesis, d_w was therefore retained as the common marker to consistently characterize temporal morphological changes across the different studies, while the complementary information potentially provided by the other descriptors was left outside the scope of the present work.

2.3.3 T-wave Peak-to-End Restricted Warping Analysis

While the general time-warping framework described above was originally formulated to compare the morphology of the whole T wave, in this thesis, as will be shown in the following chapters, a restricted version of the analysis was considered by limiting the comparison to the T_{pe} interval. This adaptation was introduced to focus the analysis on the terminal part of ventricular repolarization, which has shown particular relevance for arrhythmic risk assessment in ischemic settings and in Brugada syndrome, and to reduce the influence of morphological changes affecting the earlier portion of the T wave, such as concomitant ST-segment deviations, which may also be present in both pathological conditions.

Under this restricted approach, the same time-warping framework described above is applied, but the reference $\boldsymbol{f}^r(\boldsymbol{t}^r)$ and studied $\boldsymbol{f}^s(\boldsymbol{t}^s)$ waveforms are defined only over the T_{pe} interval as shown in Figure 2.3a. In this case, instead of being aligned with respect to the center of gravity, both waveforms were aligned with respect to the onset of the T_{pe} before the warping computation,

i.e., the T-wave peak. The corresponding time-warping marker was then computed as defined in 2.7 by averaging the absolute difference value between $\boldsymbol{t}^r$ and the optimal warping function $\gamma^*(\boldsymbol{t}^r)$, whereas in this restricted setting the sign term, S_d, was adapted to account for the net direction of the temporal reparameterization within the T_{pe} interval, and was defined as:

$$S_d = \sum_{n=1}^{N_r} \boldsymbol{t}^r(n) - \gamma_s^*(\boldsymbol{t}^r(n)) \tag{2.9}$$

Likewise, positive and negative values summarize the net direction of the temporal reparameterization relative to the reference waveform. Accordingly, positive values reflect that aligning $\boldsymbol{f}^s$ with $\boldsymbol{f}^r$ requires temporal stretching, whereas negative values correspond to a shrinking with respect to the reference waveform.

When required throughout the thesis, d_w will be denoted as $d^l_{w,\mathcal{I}}$, with $l \in \{\mathrm{PCA}, \mathrm{I}, \mathrm{II}, \ldots \mathrm{V6}\}$ denoting the lead where the index is measured and $\mathcal{I} \in \{\mathrm{T}, \mathrm{T}_{pe}\}$ indicating the part of the T-wave where the measurement is taken.

A schematic illustration of this restricted version of the warping index computed over the first PCA transformed lead, $d^{\mathrm{PCA}}_{w,\mathrm{T}_{pe}}$, is provided in Figure 2.3, which shows the original T_{pe} segments, the corresponding warping function, and the final warped T_{pe} waveform for a particular subject.

2.3.4 Mean Warped T-Wave

From a set of I T waves, $\{\boldsymbol{f}^s_1(\boldsymbol{t}^s_1), \boldsymbol{f}^s_2(\boldsymbol{t}^s_2), \ldots, \boldsymbol{f}^s_I(\boldsymbol{t}^s_I)\}$, presenting temporal and amplitude variability, it is possible to calculate a MWTW that provides an optimal representative average in both temporal and amplitude domains. Consequently, the MWTW is iteratively searched in the SRSF domain through a waveform $\bar{\boldsymbol{q}}^k(\boldsymbol{t}^r)$, where k denotes the iteration, that minimizes the average difference with respect to the SRSF transformations of all T waves in the set. The initialization is performed by taking $\bar{\boldsymbol{q}}^{k=1}(\boldsymbol{t}^r)$ as the regular average of $\{\boldsymbol{q}_{f^s_1}(\boldsymbol{t}^s_1), \boldsymbol{q}_{f^s_2}(\boldsymbol{t}^s_2), \ldots, \boldsymbol{q}_{f^s_I}(\boldsymbol{t}^s_I)\}$.

For each iteration k, the optimal set of warping functions $\{\gamma_1^{*^k}(\boldsymbol{t}_r), \gamma_2^{*^k}(\boldsymbol{t}_r), \ldots, \gamma_I^{*^k}(\boldsymbol{t}_r)\}$ is obtained by minimizing

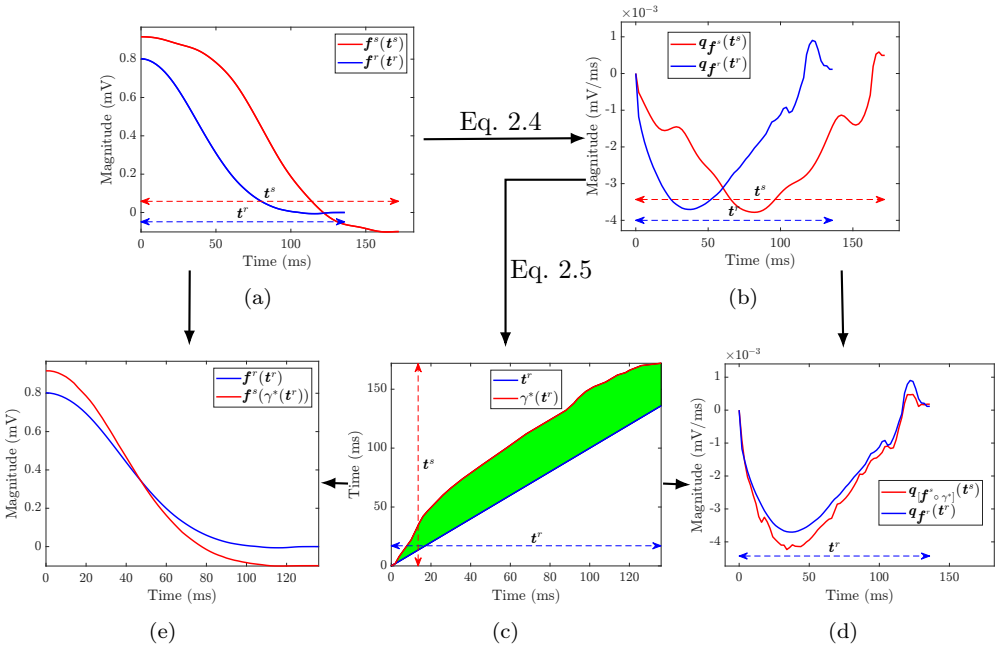


Figure 2.3: Illustration of the T_{pe}-restricted time-warping analysis. Panel (a) shows the reference T_{pe} waveform $\boldsymbol{f}^r(\boldsymbol{t}^r)$ (blue line) and the studied T_{pe} waveform $\boldsymbol{f}^s(\boldsymbol{t}^s)$ (red line). Panel (b) shows their corresponding square-root slope function representations. Panel (c) shows the optimal warping function $\gamma^*(\boldsymbol{t}^r)$. Panel (d) shows the square-root slope function representations of the reference waveform and the warped studied waveform, while panel (e) shows the warped studied waveform, $\boldsymbol{f}^s(\gamma(\boldsymbol{t}^r))$.

$$\gamma_i^{*^k}(\boldsymbol{t}_r) = \underset{\gamma_i(\boldsymbol{t}^r)}{\arg\min} \left(\|\bar{\boldsymbol{q}}^k(\boldsymbol{t}^r) - \boldsymbol{q}_{f_i^s(\gamma_i)}(\boldsymbol{t}^r)\| \right), \quad i = 1, \ldots, I. \tag{2.10}$$

The updated SRSF transformation of the MWTW is then calculated as

$$\bar{\boldsymbol{q}}^{k+1}(\boldsymbol{t}_r) = \frac{1}{I} \sum_{i=1}^{I} \boldsymbol{q}_{[f_i^s \circ \gamma_i^{*^k}]}(\boldsymbol{t}^r) \tag{2.11}$$

Equations 2.10 and 2.11 are repeated iteratively until the difference between the energies of $\bar{\boldsymbol{q}}^{k+1}(\boldsymbol{t}^r)$ and $\bar{\boldsymbol{q}}^k(\boldsymbol{t}^r)$ is lower than 0.1%. The MWTW is then retrieved by transforming $\bar{\boldsymbol{q}}^k(\boldsymbol{t}^r)$ back to the original domain. Based on the definition of the SRSF, the following relationship holds:

$$\text{sign}\left(\bar{\boldsymbol{q}}^k(\boldsymbol{t}^r)\right) = \text{sign}\left(\dot{\bar{\boldsymbol{f}}}(\boldsymbol{t}^r)\right) \tag{2.12}$$

Also, by squaring the SRSF definition:

$$\bar{\boldsymbol{q}}^k(\boldsymbol{t}^r)^2 = \left|\dot{\bar{\boldsymbol{f}}}(\boldsymbol{t}^r)\right| = \dot{\bar{\boldsymbol{f}}}(\boldsymbol{t}^r)\,\text{sign}\left(\dot{\bar{\boldsymbol{f}}}(\boldsymbol{t}^r)\right) \tag{2.13}$$

Then, solving for $\dot{\bar{\boldsymbol{f}}}(\boldsymbol{t}^r)$, and using Equation 2.12:

$$\dot{\bar{\boldsymbol{f}}}(\boldsymbol{t}^r) = \bar{\boldsymbol{q}}^k(\boldsymbol{t}^r)^2\,\text{sign}\left(\bar{\boldsymbol{q}}^k(\boldsymbol{t}^r)\right) = \bar{\boldsymbol{q}}^k(\boldsymbol{t}^r)\left|\bar{\boldsymbol{q}}^k(\boldsymbol{t}^r)\right| \tag{2.14}$$

Finally, numerically integrating Equation 2.14, and taking the integration step as the unity:

$$\bar{f}(t^r(n)) = \frac{1}{I}\sum_{i=1}^{I} f_i^s(t_i^s(1)) + \sum_{l=1}^{n} \bar{q}^k(t^r(l))\left|\bar{q}^k(t^r(l))\right| \tag{2.15}$$

When the T waves in the set present a high degree of morphological similarity, the MWTW is expected to provide a representative morphology of the whole group. In contrast, when the set includes heterogeneous morphologies, for instance a mixture of biphasic T waves together with monophasic ones, the resulting mean warped T wave will tend to resemble the dominant morphology, if one clearly prevails, or otherwise an average morphology after warping when the different patterns have similar weight. Therefore, prior to the computation of the MWTW, it may be convenient to include a preprocessing step aimed at excluding undesired or non-dominant T-wave morphologies.

In this thesis, the same methodology was also applied to the T_{pe} interval to compute the corresponding mean warped waveform, referred to as the mean warped T-peak-to-T-end wave (MWTPE) when specifically considering that restricted case.

2.3.5 Weighted Time-Warping Markers

To reduce the influence of possible delineation errors at the boundaries of the analyzed interval on the computation of the time-warping markers, weighted versions of the warping function were considered. For example, an inaccurate identification of the T-wave end may introduce spurious temporal differences near the boundary, affecting the resulting marker even in the absence of genuine morphological changes. As introduced by Palmieri et al.

in [198], two weighting functions derived from the reference T wave were defined to emphasize either the central part of the T-wave or the regions with the largest slope, while attenuating both ends of the waveform, as illustrated in Figure 2.4.

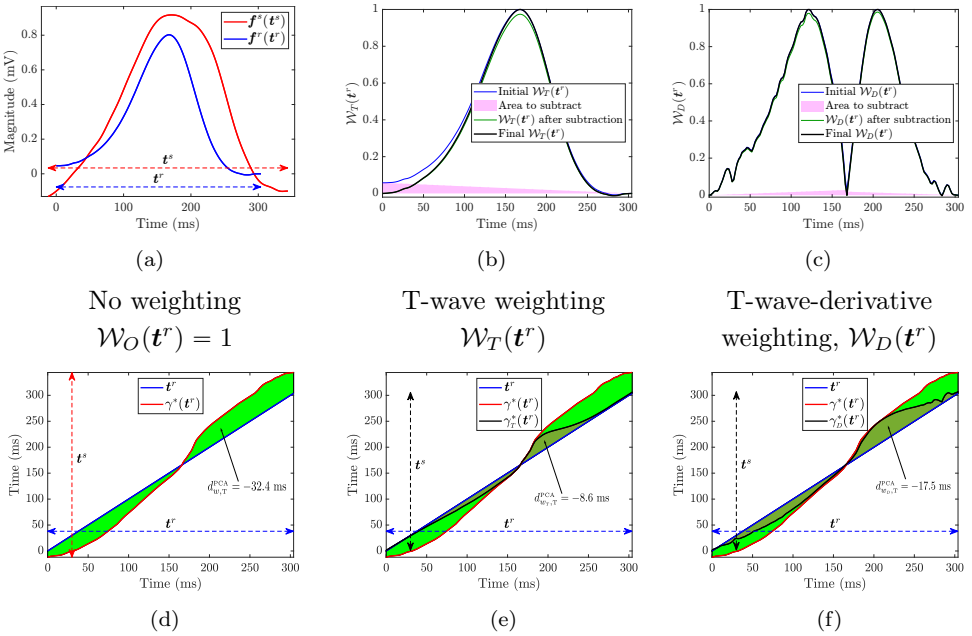


Figure 2.4: Overview of the weighting strategy applied to the computation of weighted time-warping markers. Panel (a) shows the reference and studied T waves, $\boldsymbol{f}^r(\boldsymbol{t}^r)$ and $\boldsymbol{f}^s(\boldsymbol{t}^s)$, respectively. Panels (b) and (c) display the weighting functions $\mathcal{W}_T(\boldsymbol{t}^r)$ and $\mathcal{W}_D(\boldsymbol{t}^r)$, derived from the reference T wave and its derivative, respectively. Panel (d) shows the unweighted warping function $\gamma^*(\boldsymbol{t}^r)$ ($\mathcal{W}_O(\boldsymbol{t}^r) = 1$) and the corresponding unweighted marker. Panels (e) and (f) show the weighted warping functions $\gamma^*_T(\boldsymbol{t}^r)$ and $\gamma^*_D(\boldsymbol{t}^r)$, together with the corresponding weighted markers. Light and dark green areas indicate the unweighted and weighted time-warping markers, respectively.

As described in Section 2.3, the computation is based on the reference $\boldsymbol{f}^r$ and studied $\boldsymbol{f}^s$ waveforms, and on the corresponding optimal warping function $\gamma^*(\boldsymbol{t}^r)$ relating both waves, which defines the unweighted case ($\mathcal{W}_O(\boldsymbol{t}^r) = 1$), while $\mathcal{W}_T(\boldsymbol{t}^r)$ and $\mathcal{W}_D(\boldsymbol{t}^r)$ define the T-wave-amplitude-based and derivative-based weighting functions used to obtain the corresponding weighted warping functions, shown in Figure 2.4b and Figure 2.4c, respectively.

The weighting function $\mathcal{W}_T(\boldsymbol{t}^r)$ was obtained from the normalized reference T wave. First, $\boldsymbol{f}^r(\boldsymbol{t}^r)$ was divided by its maximum value. Then, the linear function connecting its first and last samples was subtracted, and the resulting

waveform was normalized again to unit maximum. This weighting function emphasizes the central part of the T wave and reduces the contribution of its boundaries, as shown in Figure 2.4b.

The weighting function $\mathcal{W}_D(t^r)$ was derived from the absolute derivative of the reference T wave. The derivative waveform was split into two parts, taking the zero crossing at the T-wave peak as the dividing point. The same procedure used to define $\mathcal{W}_T(t^r)$ was then applied separately to each part, and both were finally joined to obtain $\mathcal{W}_D(t^r)$. In this way, the regions of maximum slope were emphasized, as illustrated in Figure 2.4c.

The weighting was applied to the previously estimated optimal warping function, rather than modifying the T waves and recomputing their alignment, since its purpose was to adjust the contribution of different temporal regions to the marker without changing the original alignment procedure. The reference T wave was used to define the weighting functions because both the warping function and the resulting marker are expressed over its temporal axis, $\boldsymbol{t}^r$, providing a consistent weighting profile for comparisons against the same reference.

The weighted warping function was then defined as

$$\gamma^*_{\Gamma}(\boldsymbol{t}^r) = \gamma^*(\boldsymbol{t}^r) \cdot \mathcal{W}_{\Gamma}(t^r), \qquad \Gamma \in \{O, T, D\}. \tag{2.16}$$

Thus, for $\Gamma = O$, the original unweighted case is recovered. The weighted time-warping marker was then re-computed as defined in Equation 2.6, but considering the corresponding weighted warping function, $\gamma^*_{\Gamma}(\boldsymbol{t}^r)$. Accordingly, throughout this thesis, when required, the $d^l_{w,\mathcal{I}}$ nomenclature defined above was further denoted as $d^l_{w_\Gamma,\mathcal{I}}$, where $\Gamma \in \{\mathrm{T}, \mathrm{D}\}$ indicates the T-wave-amplitude-based and derivative-based weighting conditions, respectively. For simplicity, the unweighted case was denoted as $d^l_{w,\mathcal{I}}$. The corresponding weighted warping functions and weighted markers, represented by the dark green areas, are shown in Figure 2.4e and Figure 2.4f, together with the original unweighted warping marker, represented by the light green area.

CHAPTER 3

TIME-WARPING ANALYSIS OF THE T-WAVE PEAK-TO-END INTERVAL TO TRACK ISCHEMIA-INDUCED REPOLARIZATION CHANGES

3.1 Introduction

3.2 Methods

3.2.1 Dataset

3.2.2 ECG Pre-processing

3.2.3 Quantification of T-Mave Morphology Changes

3.2.4 Repolarization Changes Analysis

3.2.5 Classical Indices of Ventricular Repolarization

3.2.6 Statistical Analysis

3.3 Results

3.3.1 Changes of $d^{\mathrm{PCA}}_{w,\mathrm{T}_{pe}}$ During Occlusion

3.3.2 Temporal Distribution Analysis

3.3.3 Spatial Distribution Analysis

3.3.4 Classic Local Measurements

3.4 Discussion

3.4.1 Time Course and Prevalence Analysis

3.4.2 Spatial Analysis

3.4.3 Classic Local Measurements

3.4.4 Clinical Implications

3.4.5 Limitations

3.5 Conclusions

3.1 Introduction

As described in Chapter 1, ischemia in the cardiac tissue is a substrate which increases the risk for ventricular arrhythmias, including VT and VF [211]. One of the mechanisms that increase propensity to arrhythmia under ischemia is the increased dispersion of ventricular repolarization. The link between heterogeneities resulting in dispersion of ventricular repolarization and the genesis of arrhythmias has been demonstrated both in experimental models and in clinical studies [7,8]. However, robustly identifying in the ECG those markers of repolarization alterations that better represents the potentially harmful substrate remains an unmet demand.

This chapter focuses on the study of repolarization changes from the ECG under ischemic conditions. It must be noted that many arrhythmia risk ECG biomarkers developed for non-ischemic conditions (e.g. long QT syndrome, brugada syndrome, chronic heart failure, etc.) are challenged under ischemic conditions by the presence of concurrent ST elevation/depression and early T-wave modifications which appear at the ECG simultaneously with the arrhythmia risk signatures.

ECG changes during acute ischemia include alterations in the ST-segment level and/or T-wave amplitude [212], together with alterations of the global spatio-temporal characteristics of the ECG. Those alterations have been the basis for the development of ischemia detectors and monitoring systems, being the ST-level the most widely-used [74]. However, while in some patients mild to moderate ischemia can cause low alteration on the ECG, more pronounced ST elevation/depression can occur during severe ischemia largely affecting the early part of the T-wave on the ECG [79, 212, 213]. So, it is important to consider these manifestations of ischemia in the selective development of biomarkers quantifying the degree of repolarization dispersion as a surrogate for arrhythmia risk under ischemia.

Acute ischemia induced during PCI provides an excellent model to investigate the dispersion of repolarization changes undergoing during the initial minutes of ischemia. It alters ventricular repolarization by, (a) shortening repolarization time (i.e., temporal changes) and (b) slowing the conduction speed [79], creating heterogeneity between different myocardial regions. Ischemia-induced heterogeneity has been related to the generation of ventricular arrhythmias and increased arrhythmic risk [13, 214]. However, other ischemia-induced changes

in the ECG unrelated to repolarization dispersion, such as ST elevation/depression may interfere in the computation and interpretation of risk markers developed for non-ischemic scenarios, such as T-wave alternans [215], the V-index [199] or the (TMR) [203] and (TMV) [204] indices.

As discussed in Chapter 1, several fiducial-point-based ECG markers have been proposed to characterize ventricular repolarization heterogeneity. Chapter 2 further emphasized that these markers may not fully capture the information conveyed by the overall T-wave morphology, which has motivated the development of markers trying to overcome this restriction. In particular, the time-warping framework described in Chapter 2 allows to compare the morphology of two T waves.

Under ischemic conditions, the ST elevation/depression may largely influence the above-described markers, reducing their accuracy in quantifying arrhythmic risk, limiting their utility. This is not the case for the T-peak to T-end interval, although this marker is still largely sensitive to errors in the identification of the fiducial points. To address this limitation, this chapter evaluates whether a time-warping-based morphology analysis, but restricted to the T-peak to T-end part of the T-wave, can be a proper, robust and artifact-free alternative to quantify repolarization dispersion during ischemia ischemia.

3.2 Methods

3.2.1 Dataset

The study population contained 101 patients from the STAFF III database [189] (63 males, with 35 patients with evidence of prior myocardial infarction) undergoing elective balloon percutaneous coronary intervention (PCI). The database was collected at the Charleston Area Medical Center (WV, USA), where single prolonged balloon inflation had been introduced to achieve optimal results of the PCI. Standard leads V1–V6, I, II, and III of the ECG were digitized with an amplitude resolution of 0.625 μV and a sampling rate of 1000 Hz. The remaining three standard augmented leads aVL, -aVR, and aVF were subsequently generated from the limb leads and used for the spatial analysis. The study was approved by the local Investigational Review Board and informed consent was obtained from the patients before their enrollment. All patients were clinically stable during the ECG acquisition. Patients who presented any signal loss during the recording were not included.

For each patient, 5 minutes ECG recording at rest in supine position pre-

vious to any catheter insertion or balloon inflation (control recording) and the corresponding paired ECG recording obtained during the first balloon inflation were analyzed. The duration of the occlusion period ranged from 1:09 to 7:17 minutes (mean: 4:20 minutes). The spatial distributions of the 101 balloon inflations were: left main (LM) artery in 2 patients, left anterior descending (LAD) artery in 33 patients, left circumflex artery (LCX) in 21 patients and right coronary artery (RCA) in 45 patients, distribution with each artery can be found in Table 3.2.

3.2.2 ECG Pre-processing

The ECG pre-processing workflow described in Chapter 2 was applied in this study. Briefly, this included ECG filtering, single-lead QRS delineation, multilead QRS fiducial point selection and spatial PCA tansformation .

In this chapter, the initial delineation was performed on the available standard leads (V1–V6, I, II and III). PCA was then applied to the eight independent leads to emphasize T-wave components and improve their delineation. The PCA transformation coefficients were calculated from T-wave segments contained in a 15-s window at the beginning of the recording, for control recordings, or at beginning of the balloon inflation, for PCI recordings. T-wave segmentation was performed using a fixed window referred to the corresponding QRS mark following rules in [216].

Finally, the first principal component ECG signal, i.e., the transformed lead where the T-waves have maximal energy, was delineated making use of the single-lead technique [195]. The resulting fiducial points were used for the subsequent ECG analysis. Finally, each T-wave was further filtered with a sixth order low-pass bidirectional Butterworth filter (cut-off frequency of 20 Hz).

3.2.3 Quantification of T-Mave Morphology Changes

Each recording was divided into consecutive 15-second windows, with 10 seconds overlap. For each s-th window, as shown in Figure 3.1a, a MWTPE, $\boldsymbol{f}^s(\boldsymbol{t}^s) = [f^s(t^s(1)), ..., f^s(t^s(N_s))]^T$, where $\boldsymbol{t}^s = [t^s(1), ..., t^s(N_s))]^T$, was computed following the procedure detailed in Section 2.3.4. Initially, all T-waves contained within a given window were transformed to have positive polarity. For each window, the predominant T-wave class, biphasic or monophasic, was determined as the one with the highest number of occurrences. Only T-waves from the predominant class were considered for the computation of the

MWTPE.

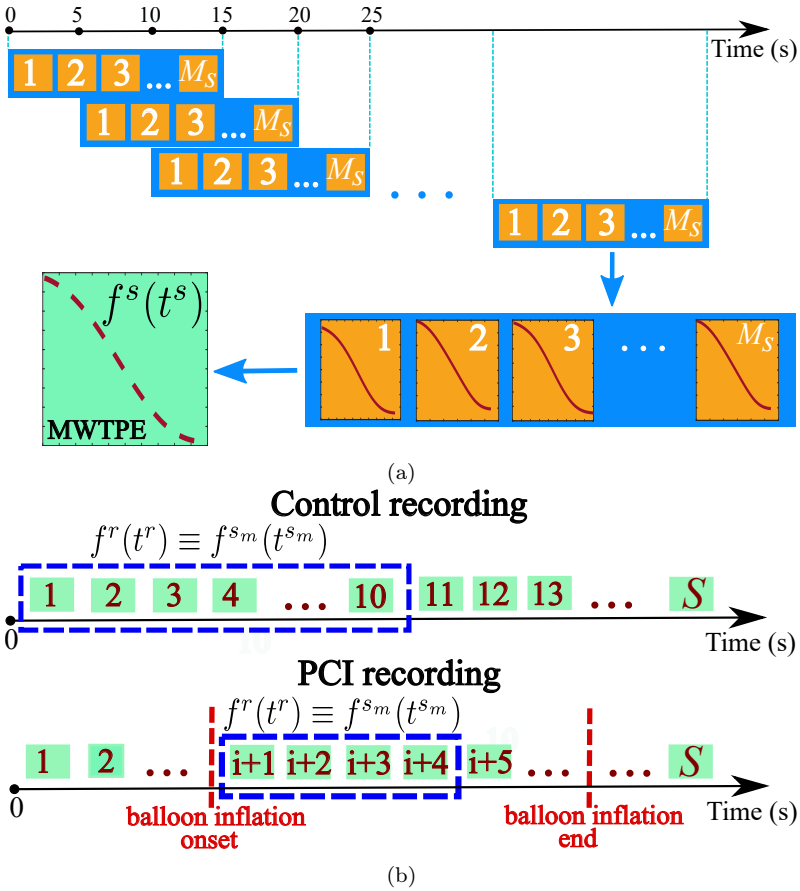


Figure 3.1: MWTPE $\boldsymbol{f}^s(\boldsymbol{t}^s)$ estimation and reference MWTPE $\boldsymbol{f}^r(\boldsymbol{t}^r)$ selection rule at the STAFF-III data-set. The $\boldsymbol{f}^s(\boldsymbol{t}^s)$ MWTPE was estimated from time-windows of 15 seconds duration and 10 seconds of overlap throughout the entire record. The reference $\boldsymbol{f}^r(\boldsymbol{t}^r)$ MWTPE was selected among the MWTPEs within 1 minute period, at the control recording, and within 30 seconds period at the beginning of the PCI recordings.

Selected T-peak-to-end waves are aligned with respect to the T-wave peak. Additionally, an extra selection rule was applied to avoid the effect of delineation errors: only those T-waves whose duration T_w satisfies $T^s_{w,m} - 40 \leqslant T_w \leqslant T^s_{w,m} + 40$ (ms) were selected for the MWTPE computation, where $T^s_{w,m}$ is the median of the T-wave duration within each s-th window. The estimated MWTPE $\boldsymbol{f}^s(\boldsymbol{t}^s)$ is representative of the dominant morphology of T-waves from peak to end in that particular s-th window.

We chose a reference MWTPE among the $\boldsymbol{f}^s$ MWTPEs from the first minute in the case of the control recording, and from the first 30 seconds after balloon inflation in case of the PCI recordings, $\boldsymbol{f}^r(\boldsymbol{t}^r)$ in Figure 3.1b, (blue dashed line rectangle). The selection period at PCI recordings is smaller to minimize ischemia-induced repolarization changes. To choose the reference MWTPE $\boldsymbol{f}^r(\boldsymbol{t}^r)$ from the most stable s-th time window, we compute a dispersion index (υ_s) in each s-th window, as:

$$\upsilon_s = \frac{\dfrac{1}{N_s}\dfrac{1}{M_s}\displaystyle\sum_{i=1}^{M_s}\left[\boldsymbol{f}_i^s(\boldsymbol{t}^s)-\boldsymbol{f}^s(\boldsymbol{t}^s)\right]^{\mathrm{T}}\left[\boldsymbol{f}_i^s(\boldsymbol{t}^s)-\boldsymbol{f}^s(\boldsymbol{t}^s)\right]}{\dfrac{1}{N_s}\left[\boldsymbol{f}^s(\boldsymbol{t}^s)\right]^{\mathrm{T}}\boldsymbol{f}^s(\boldsymbol{t}^s)}, \tag{3.1}$$

considering all pieces of T-waves $\boldsymbol{f}_i^s(\boldsymbol{t}^s)$ ($i \in \{1 \dots M_s\}$) within each window. Then, the reference MWTPE is taken as

$$\boldsymbol{f}^r(\boldsymbol{t}^r) \equiv \boldsymbol{f}^{s_m}(\boldsymbol{t}^{s_m}), \quad \text{with} \quad s_m = \arg\min_s\{\upsilon_s\}. \tag{3.2}$$

To quantify the evolution of the MWTPEs morphology along time in each patient, we applied the method described in Section 2.3.3, which estimated the index $d^{\mathrm{PCA}}_{w,\mathrm{T}pe}$ as the mean amount of warping needed to remove the time domain variation among two different waves, the reference $\boldsymbol{f}^r(\boldsymbol{t}^r)$, and the one under study $\boldsymbol{f}^s(\boldsymbol{t}^s)$. Figure 3.2a shows an example of the MWTPEs previous to time-warping, $\boldsymbol{f}^r(\boldsymbol{t}^r)$ calculated at the initial part of a PCI recording and $\boldsymbol{f}^s(\boldsymbol{t}^s)$ from two minutes later. The warping function $\gamma^*(\boldsymbol{t}^r)$, that optimally relates $\boldsymbol{f}^s(\boldsymbol{t}^s)$ and $\boldsymbol{f}^r(\boldsymbol{t}^r)$ in Figure 3.2a is shown in Figure 3.2b. The warped T-peak-to-end wave, $\boldsymbol{f}^s(\gamma(\boldsymbol{t}^r))$, and the reference $\boldsymbol{f}^r(\boldsymbol{t}^r)$, are shown in Figure 3.2c.

Based on this pairwise comparison, in order to analyze the $d^{\mathrm{PCA}}_{w,\mathrm{T}pe}$ time course during acute ischemia, its value was computed for each s-th $\boldsymbol{f}^s(\boldsymbol{t}^s)$ MWTPE, resulting in the time series $d^{\mathrm{PCA}}_{w,\mathrm{T}pe}(s)$.

3.2.4 Repolarization Changes Analysis

The analysis of repolarization changes is performed in two different ways:

1. Temporal evolution: The warping is performed on the first principal component transformed lead since it is supposed to emphasize T-wave components and so hypothesized to enhance morphological differences. For each patient, the time course variation of repolarization dispersion is evaluated as the evolution of $d^{\mathrm{PCA}}_{w,\mathrm{T}pe}(s)$, $s \in \{1, \dots, S\}$, every 5 seconds relative to the initial stage taken at reference.

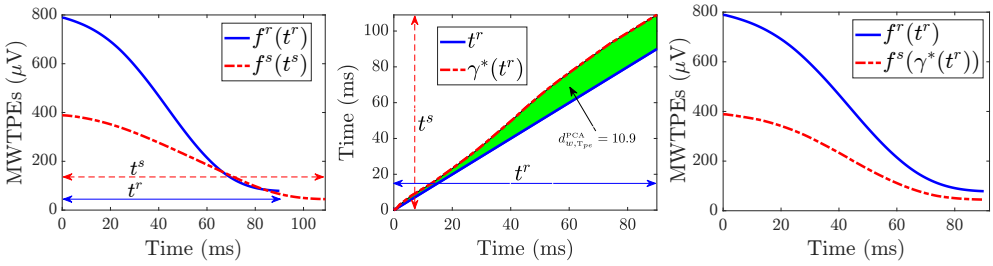


Figure 3.2: Analysis performed for time-warping index estimation from a particular patient of the STAFF-III database during the PCI procedure. Panel (a) displays both the reference $\boldsymbol{f}^r(\boldsymbol{t}^r)$ (solid blue) and a particular s-th $\boldsymbol{f}^s(\boldsymbol{t}^s)$ (doted red line) MWTPE. Panel (b) displays the warping function $\gamma^*(t^r)$ (dotted red line) that optimally relates the reference $\boldsymbol{f}^r(\boldsymbol{t}^r)$ and studied $\boldsymbol{f}^s(\boldsymbol{t}^s)$ MWTPEs. The total amount of warping, quantified by $d^{\mathrm{PCA}}_{w,\mathrm{T}pe}$, is represented by the green area between $\gamma^*(t^r)$ and t^r. Panel (c) displays both the reference $\boldsymbol{f}^r(\boldsymbol{t}^r)$ (blue line) MWTPE and the warped $\boldsymbol{f}^s(\gamma(\boldsymbol{t}^r))$ MWTPE.

2. Spatial distribution: We separately quantified the warping index in each of the 12 standard leads, and investigated the relationship between the occlusion site and spatial distribution of the $d^{\mathrm{l}}_{w,\mathrm{T}pe}(s)$, $l \in$ {V1,...,V6, aVL, I, aVR, II, aVF, III}. To have a spatially global indication of T-wave changes, the mean across patients of $d^{\mathrm{l}}_{w,\mathrm{T}pe}(s)$ maximum in each PCI recordings, is also computed and denoted $\overline{d}^{\mathrm{l}}_{w,\mathrm{T}pe}(s)$.

To analyze the warping value evaluated at any time of the PCI intervention, the value $d^{\mathrm{PCA}}_{w,\mathrm{T}pe}(s)$ is expressed in relative terms with respect to $d^{\mathrm{PCA}}_{w,\mathrm{T}pe}$ variations during the ischemia free control recording using the index $\mathcal{R}_d$. Similar to the ischemic changes sensor proposed in [74], $\mathcal{R}_d$ normalizes the change induced by ischemia using the standard deviation of $d^{\mathrm{PCA}}_{w,\mathrm{T}pe}$ measured at the control recording, where no ischemic-induced changes are expected, denoted as σ^c_d.

The $\mathcal{R}_d$ in this study is defined as,

$$\mathcal{R}_d(s) = \frac{\Delta^{\mathrm{PCI}}_d(s)}{\sigma^c_d}, \tag{3.3}$$

where the magnitude of change in $d^{\mathrm{PCA}}_{w,\mathrm{T}pe}(s)$ during PCI occlusion at any time, s, is denoted by $\Delta^{\mathrm{PCI}}_d(s)$. In order to have a robust estimation of $\Delta^{\mathrm{PCI}}_d(s)$, a linear fitting model $\hat{d}^{\mathrm{PCA}}_{w,\mathrm{T}pe}(s)$ is fit to $d^{\mathrm{PCA}}_{w,\mathrm{T}pe}(s)$ between $s = 1$ and s and defining $\Delta^{\mathrm{PCI}}_d(s)$ as the difference between $\hat{d}^{\mathrm{PCA}}_{w,\mathrm{T}pe}(s)$ and $\hat{d}^{\mathrm{PCA}}_{w,\mathrm{T}pe}(1)$. For example, a value

of $\mathcal{R}_d = 5$ means that the $d^{\text{PCA}}_{w,\text{T}_{pe}}(s)$ has increased during the occlusion 5 times the standard deviation of the change observed during the control recording σ^c_d.

3.2.5 Classical Indices of Ventricular Repolarization

To further test the robustness of $d^{\text{PCA}}_{w,\text{T}_{pe}}(s)$, we compare its performance with that from the traditional ischemic indices, ST segment level (ST), T-wave peak amplitude (T_a), T-wave width (T_w), and T-wave peak to end interval (T_{pe}), measured as detailed in Section 2.2.

Each index was measured beat-to-beat to analyze its time course during PCI, obtaining the series $\text{ST}(n)$, $\text{T}_a(n)$, $\text{T}_\text{w}(n)$ and $\text{T}_{pe}(n)$, respectively. We also analyzed the magnitude of changes observed during balloon inflation for each patient using $\mathcal{R}^{\text{PCA}}_{\mathcal{I}}$, where $\mathcal{I} \in \{\text{ST}, \text{T}_a\text{T}_\text{w}, \text{T}_{pe}\}$, defined analogously to $\mathcal{R}^{\text{PCA}}_d$ in (3.3).

3.2.6 Statistical Analysis

McNemar analysis was used to compare control with PCI recordings, and Fisher's exact test was used in the contingency tables. We used the Kruskal-Wallis test to assess differences among groups. The statistical significance was considered when p-value $\leqslant 0.05$. We used boxplots to show the distributions of data, where the central mark represents the median, the edges represent the 25th and 75th percentiles, and the whiskers represent the most extreme data points not considered as outliers. Computations were made with MATLAB® version R2020b.

3.3 Results

3.3.1 Changes of $d^{\text{PCA}}_{w,\text{T}_{pe}}$ During Occlusion

When computing $d^{\text{PCA}}_{w,\text{T}_{pe}}$ for each s-th window and each individual patient the percentage of T waves that do not satisfy the extra selection rule related to T wave duration ($T^s_{w,m} - 40 \leqslant T_w \leqslant T^s_{w,m} + 40$ (ms)), was, in average, 1.4%.

In the control recording, the standard deviation, σ^c_d, had a median of 0.54 [IQR: 0.33], ranging from 0.018 to 2.085 ms. The stability of $d^{\text{PCA}}_{w,\text{T}_{pe}}$ in the control recording was tested by estimating $\mathcal{R}^{\text{PCA}}_d$ in the second half of each control record using as reference the value obtained in its first half, showing a median of 1.00 [IQR: 1.13], ranging from 0.03 to 2.93.

The number of patients, for control and PCI stage, where $\mathcal{R}_d^{\mathrm{PCA}}$, evaluated as in (3.3) with $s = s^{\mathrm{PCIend}}$, is larger than certain thresholds (1, 2, 5 and 10) are reported in Table 3.1. Percentages of recordings with $\mathcal{R}_d^{\mathrm{PCA}}$ over a threshold in PCI, were found significantly higher than in control: $\mathcal{R}_d^{\mathrm{PCA}} > 1, 2, 5, 10$, in 94.1%, 85.11%, 64.4% and 48.5 % of PCI recordings vs 50.5% 12.9%, 0% and 0% in control, McNemar test $p = 3.7 \cdot 10^{-11}$, $p = 4.0 \cdot 10^{-21}$, $p = 5.4 \cdot 10^{-20}$ and $p = 3.6 \cdot 10^{-15}$, respectively. Details of $\mathcal{R}_d^{\mathrm{PCA}}$ prevalence during PCI recordings segregated by occluded artery, gender and the presence of previous MI are reported in Table 3.2.

Table 3.1: $\mathcal{R}_d^{\mathrm{PCA}}$ prevalence classification in the study population according to the stage test

Subset	#	$\mathcal{R}_d^{\mathrm{PCA}} > 1$	$\mathcal{R}_d^{\mathrm{PCA}} > 2$	$\mathcal{R}_d^{\mathrm{PCA}} > 5$	$\mathcal{R}_d^{\mathrm{PCA}} > 10$
Control recording	101	51 (50.5%)	13 (12.9%)	0	0
PCI recording *	101	95 (94.1%)	86 (85.11%)	65 (64.4%)	49 (48.5%)

* $p \leqslant 0.05$ PCI recordings vs Control recordings (McNemar test)

We did not find any significant differences in prevalence of repolarization changes, measured as $\mathcal{R}_d^{\mathrm{PCA}} > 2$, by occlusion site: 81.8%, 86.7%, and 85.7% for LAD, RCA and LCX, respectively. LM group was excluded in this comparison due to its small size. For larger, $\mathcal{R}_d^{\mathrm{PCA}} > 5$, changes requirements, patients with LAD occlusion reached the threshold in 66.7% of the patients and RCA in 71.1% while LCX reaches the threshold just at 52.4% of patients although the differences are not significant. Neither are differences in prevalence for $\mathcal{R}_d^{\mathrm{PCA}} > 10$.

Differences in the three subsets between the prevalence in men and women (63 and 38 patients in total, respectively) and between patients with and without evidence of a previous myocardial infarction (MI) (35 and 66, respectively) were not either statistically significant.

The $\mathcal{R}_d^{\mathrm{PCA}}$ magnitude ranged from 1.01 to 80.74 (mean/median: 17.55/9.44). The box and whiskers plots according to the occluded artery subsets are shown in Figure 3.3. There were no significant differences between the groups ($p = 0.47$ Kruskal-Wallis test), although the largest interquartile range was found for the LAD subset.

Table 3.2: $\mathcal{R}_d^{\mathrm{PCA}}$ prevalence classification in the study population according to the occluded artery, gender, and evidence of previous infarction.

Subset	#	$\mathcal{R}_d^{\mathrm{PCA}} > 1$	$\mathcal{R}_d^{\mathrm{PCA}} > 2$	$\mathcal{R}_d^{\mathrm{PCA}} > 5$	$\mathcal{R}_d^{\mathrm{PCA}} > 10$
LAD	33	31 (94.0%)	27 (81.8%)	22 (66.7%)	15 (45.5%)
diag	2	1	1	1	0
mid	6	6	4	3	2
prox	22	21	19	16	13
prox-mid	3	3	3	2	0
RCA	45	42 (93.3%)	39 (86.7%)	32(71.1%)	25 (55.6%)
dist	12	12	11	9	9
mid	14	12	12	8	4
prox	17	16	15	14	12
prox-mid	2	2	1	1	0
LCX	21	20 (95.2%)	18 (85.7%)	11 (52.4%)	9 (42.9%)
dist	6	6	6	4	2
mid	5	5	5	2	2
prox	10	9	7	5	5
LM	2	2 (100%)	2 (100%)	0	0
Male	63	60 (95.2%)	55 (87.3%)	42 (66.7%)	35 (55.6%)
Female	38	35 (92.1%)	31 (81.6%)	23 (60.5%)	14 (36.8%)
Pre-MI	35	32 (91.4%)	29 (82.9%)	20 (57.1%)	17 (48.6%)
No pre-MI	66	63 (95.5%)	57 (86.4%)	45 (68.2%)	32 (48.5%)

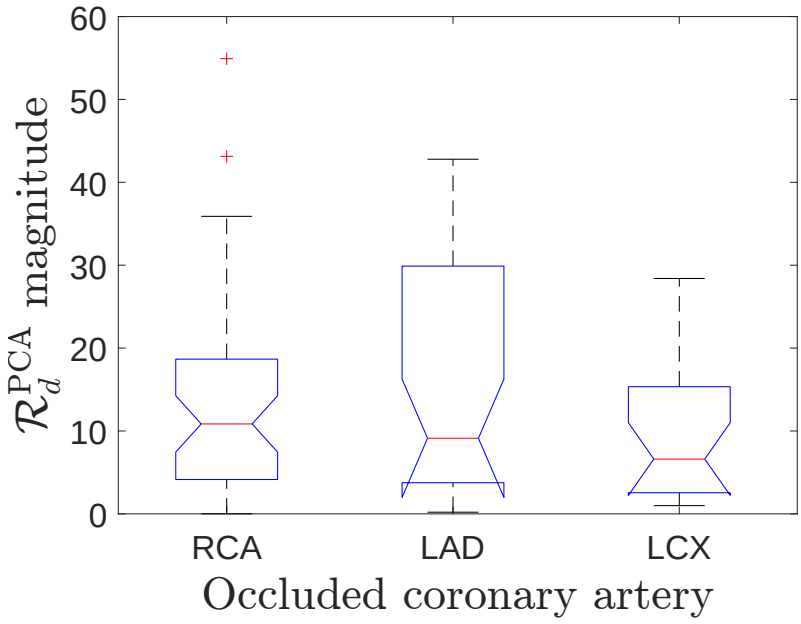


Figure 3.3: Box and whisker plots of the $\mathcal{R}_d^{\mathrm{PCA}}$ amplitudes in each patient classified by occluded artery.

3.3.2 Temporal Distribution Analysis

An example of the $d^{\mathrm{PCA}}_{w,\mathrm{T}_{pe}}(s)$ temporal evolution for a particular patient during control and PCI periods is shown in Figure 3.4a. The red trace represents, for an illustrative patient, the balloon inflation time-span. Different time instants (tagged with letters) are selected to display in Figure 3.4c the original T-wave shape. Strong T-wave peak-to-end shape variations accompanied by $d^{\mathrm{PCA}}_{w,\mathrm{T}_{pe}}(s)$ magnitude changes (ranging from 0 to 10.10 ms) were observed, which follow an increasing trend as inflation time progresses. In contrast, $d^{\mathrm{PCA}}_{w,\mathrm{T}_{pe}}(s)$ magnitude during control remains stationary, ranging from 0 to 1.8 ms. All $\boldsymbol{f}^s(\boldsymbol{t}^s)$ MWTPEs corresponding to the $d^{\mathrm{PCA}}_{w,\mathrm{T}_{pe}}(s)$ series in the control and PCI stages are shown in Figure 3.4b and Figure 3.4d, respectively. The blue line represents the reference $\boldsymbol{f}^r(\boldsymbol{t}^r)$ MWTPE. Note that the $d^{\mathrm{PCA}}_{w,\mathrm{T}_{pe}}(s)$ evolution described above follows the changes in the $\boldsymbol{f}^s(\boldsymbol{t}^s)$ MWTPEs shape. No significant changes are found in the control recording, while an increase in width and a decrease in amplitude of the $\boldsymbol{f}^s(\boldsymbol{t}^s)$ MWTPEs are observed in the balloon inflation period, as reflected in the $d^{\mathrm{PCA}}_{w,\mathrm{T}_{pe}}(s)$ trace in Figure 3.4a.

The $d^{\mathrm{PCA}}_{w,\mathrm{T}_{pe}}(s)$ averages across all patients (blue line), denoted as $\overline{d}^{\mathrm{PCA}}_{w,\mathrm{T}_{pe}}(s)$

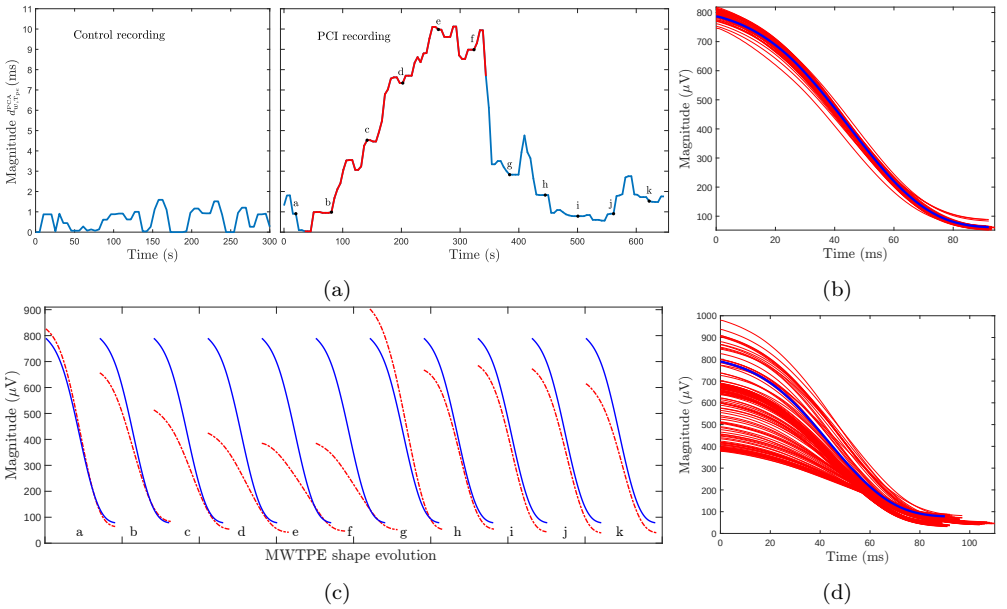


Figure 3.4: Example of time course evolution of $d^{\mathrm{PCA}}_{w,\mathrm{T}_{pe}}(s)$ series and T-wave peak-to-end shape changes during control and PCI stages from a particular patient. Panel (a) displays $d^{\mathrm{PCA}}_{w,\mathrm{T}_{pe}}(s)$ evolution, where the balloon inflation time is highlighted with a red line. The shape of both the reference $\boldsymbol{f}^r(\boldsymbol{t}^r)$ MWTPE (solid blue) and each s-th $\boldsymbol{f}^s(\boldsymbol{t}^s)$ MWTPE (red dashed line) are shown in panel (c), with letters indicating their corresponding time instants tagged in (a). Panels (b) and (d) show the $\boldsymbol{f}^s(\boldsymbol{t}^s)$ MWTPEs (red lines) corresponding to the $d^{\mathrm{PCA}}_{w,\mathrm{T}_{pe}}(s)$ series for the control and PCI stages, respectively. The blue line represents the reference $\boldsymbol{f}^r(\boldsymbol{t}^r)$ MWTPE. Note that the $d^{\mathrm{PCA}}_{w,\mathrm{T}_{pe}}(s)$ value at the end of the occlusion has already started to decrease. This is a consequence of the 15-second window, centered at the analyzing point, which enters in the computation of $\boldsymbol{f}^s(\boldsymbol{t}^s)$ and then already introducing parts where the ischemia is reducing

and segregated by occluded coronary artery, aligned to the recording onset or to the balloon inflation onset, for control and PCI recordings, respectively, are shown in Figure 3.5. All database recordings were averaged. Note that the averages have little significance from the 5-th minute onwards, due to the quick decline in number of available records, Figure 3.5b.

In the 86 recordings showing $\mathcal{R}^{\mathrm{PCA}}_d > 2$, the timing when this level of change is first reached (evaluating $\mathcal{R}^{\mathrm{PCA}}_d$ as in (3.3) but with Δ^{PCI}_d computed from the linear fit of $d^{\mathrm{PCA}}_{w,\mathrm{T}_{pe}}(s)$ just up to a given s) had a median of 15 s [IQR: 15], ranging from 5 s to 4 min 50 s. Of these, 69 patients reached $\mathcal{R}^{\mathrm{PCA}}_d > 2$ during the first 30 seconds (80.23%), while only 9 (10.47%) and 8 (9.30%) reached it between 30 and 60 seconds, and after 60 seconds, respectively. Analyzing

the time course evolution of the $d^{\mathrm{PCA}}_{w,\mathrm{T}_{pe}}(s)$ maximum in these 86 recordings we observe that 31.40% of the maximum $d^{\mathrm{PCA}}_{w,\mathrm{T}_{pe}}(s)$ amplitude was already reached in the first two minutes after balloon inflation, and extra 32.56% was reached in the following two minutes, while the remaining 36.05% was obtained after the 4-th minute of occlusion.

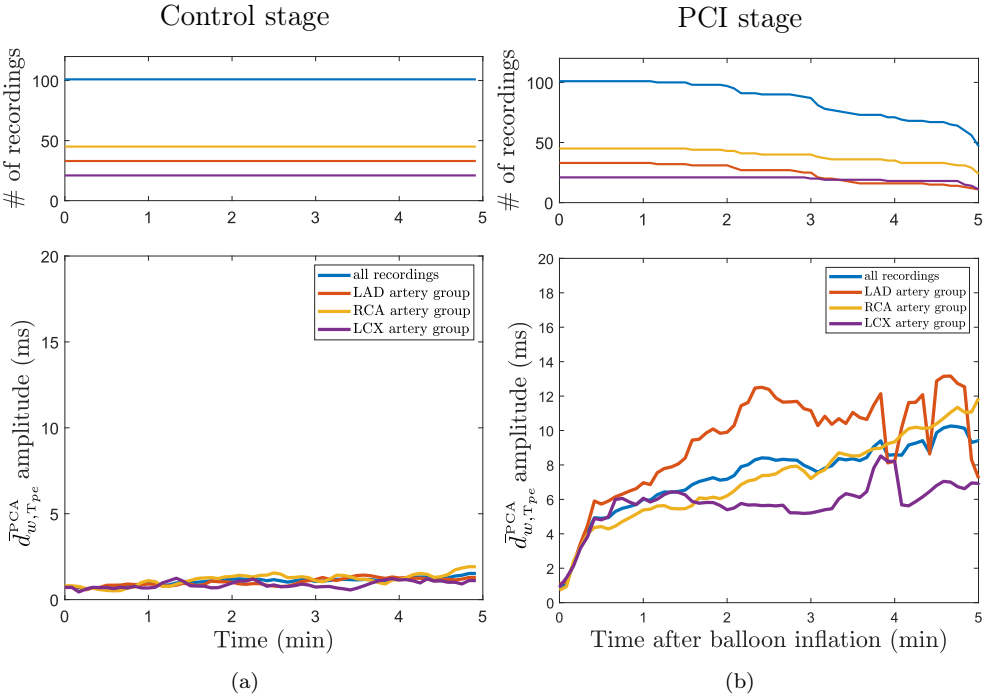


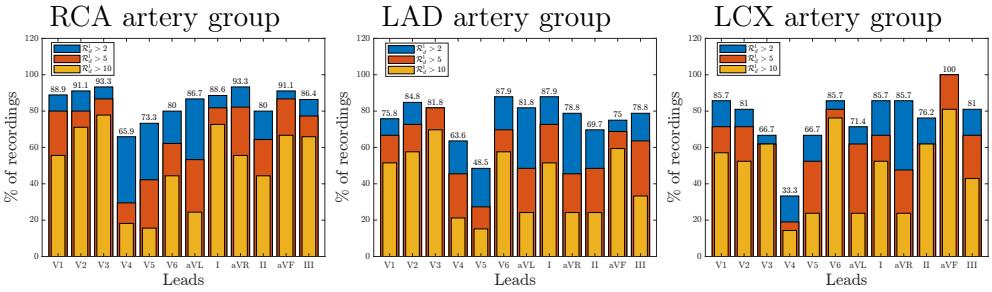
Figure 3.5: Time course of $d^{\mathrm{PCA}}_{w,\mathrm{T}_{pe}}(s)$, represented as the average across all patients $\bar{d}^{\mathrm{PCA}}_{w,\mathrm{T}_{pe}}$, in the study population and segregated by occluded artery. Alignment was performed relative to (a) the recording onset in control records and (b) the onset of the balloon inflation in PCI records. The upper panels show the number of averaged recordings, $P(s)$ at a given time s.

3.3.3 Spatial Distribution Analysis

The $d^{l}_{w,\mathrm{T}_{pe}}(s)$ and corresponding $\mathcal{R}^{l}_{d}$ magnitude was studied in each l-th lead. The percentage of patients presenting $\mathcal{R}^{l}_{d} > 2, 5, 10$ in each lead, segregated by occluded artery, is shown in Figure 3.6 by blue, red and orange bars, respectively.

$\mathcal{R}^{l}_{d} > 2$ reached a prevalence of 60% in all leads of each subset, except for l being V4 and V5 in LCX and LAD occluded artery subsets, respectively. In

the RCA subgroup, elevated $\mathcal{R}_d^l$ index reached a higher prevalence in leads $l \in \{\text{V1-V3}, \text{I}, \text{aVR}, \text{aVF}, \text{III}\}$ for $\mathcal{R}_d^l > 5$ and $\mathcal{R}_d^l > 10$. A similar outcome can be seen for LAD occlusion in the same chest leads and V6 where the prevalence increases, unlike the RCA group aVR and III (inferior wall) decreases. Note that aVR reached the highest values only in the RCA group, which gives an idea of the location of the damaged ischemic region. Interestingly, for V4 (anterior wall, which corresponding to LAD area) in $\mathcal{R}_d^l > 5$ range, low values were obtained in all occluded artery groups, although it is worth noting that for LAD subgroup reached the higher prevalence.



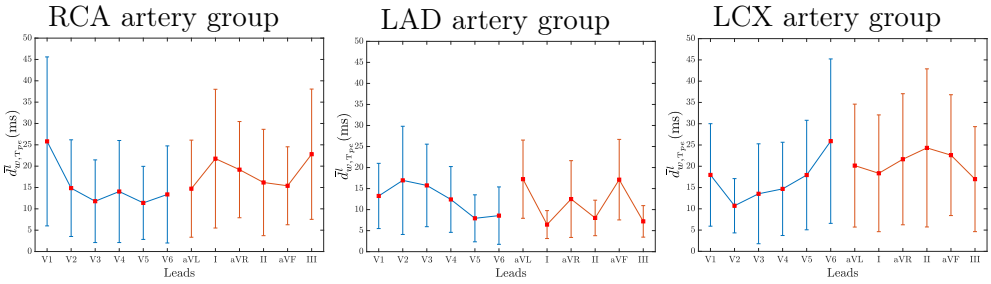
(a) (b) (c)

Figure 3.6: Percentage of patients with $\mathcal{R}_d^l > 2$ (blue bars), $\mathcal{R}_d^l > 5$ (red bars) and $\mathcal{R}_d^l > 10$ (orange bars) in each individual lead l measured at the end of occlusion and segregated by occluded coronary artery group: (a) RCA, (b) LAD and (c) LCX.

The average lead distributions of the maximum $d_{w,\mathrm{T}_{pe}}^l$ for RCA, LAD and LCX occlusions, $\bar{d}_{w,\mathrm{T}_{pe}}^l$, are shown in Figure 3.7. According to the wall that the leads looks at and the occluded artery, the highest $\bar{d}_{w,\mathrm{T}_{pe}}^l$ values at chest leads are obtained in V1-V3 in the LAD and RCA groups (V1 in RCA with the highest values) and in V4-V6 for LCX group. Regarding limb leads, the highest values in the RCA group are obtained in I, III, and aVR. In LAD group the highest values are obtained in the augmented leads and the lowest in the limb leads. In LCX which irrigates the anterior-superior and lateral sides, high values are obtained similar to their upper chest leads V5-V6 in all limb leads (aVR, II and aVF with the highest values).

3.3.4 Classic Local Measurements

The time series of the different T_a, T_{pe}, $\mathrm{T_w}$ and ST indices were estimated, and the corresponding $\mathcal{R}_{\mathcal{I}}^{\mathrm{PCA}}$ parameters were obtained at the end of occlusion to describe how ischemic variations are reflected in each index. Similar to the



(a) (b) (c)

Figure 3.7: Average lead distributions of $\bar{d}^{l}_{w,\mathrm{T}_{pe}}$ in each occluded coronary artery, segregated by group: (a) RCA, (b) LAD and (c) LCX. The square represents the mean and the error bars represent ± standard deviation.

3

$d^{\mathrm{PCA}}_{w,\mathrm{T}_{pe}}$ index, the $\mathcal{R}^{\mathrm{PCA}}_{\mathcal{I}}$ estimator was evaluated using the control recording to quantify changes of each index in the control stage. The standard deviation in the first half of the control recording, $\sigma^{c}_{\mathcal{I}}$, had a median of 1.29, 0.65, 1.22 and 0.92, while $\mathcal{R}^{\mathrm{PCA}}_{\mathcal{I}}$ had a median of 0.74, 0.64, 0.75 and 0.77 [IQR: 1.29, 0.65, 1.22 and 0.92] for T_a, T_{pe}, $\mathrm{T_w}$ and ST indices, respectively.

The $\mathcal{R}^{\mathrm{PCA}}_{\mathcal{I}}$ values from the $d^{\mathrm{PCA}}_{w,\mathrm{T}_{pe}}$ and ST indexes, at the end of the occlusion, reached higher values. The median $\mathcal{R}^{\mathrm{PCA}}_{\mathcal{I}}$ values, were 9.4, 7.7, 2.7, 3.0 and 12.0 for $d^{\mathrm{PCA}}_{w,\mathrm{T}_{pe}}$, T_a, T_{pe}, $\mathrm{T_w}$ and ST indices, respectively.

To describe the prevalence of ischemia-induced changes during PCI, we analyzed the time instants at which the different indices began to show significant variations, that is, at what instant the different threshold values were exceeded. In this way, it was possible to analyze which indexes showed a more rapid response to ischemia-induced changes and at what time of occlusion it occurred. Table 3.3 shows the percentage of recordings where $\mathcal{R}^{\mathrm{PCA}}_{\mathcal{I}}$ is larger than a given threshold $\alpha \in \{1, 5, 10\}$ at the end of balloon inflation, and the average time at which the threshold was exceeded.

The $d^{\mathrm{PCA}}_{w,\mathrm{T}_{pe}}$ values reached higher levels of sensitivity, measured by $\mathcal{R}^{\mathrm{PCA}}_{\mathcal{I}}$, than the classic indices in a greater number of patients except for $\mathcal{R}^{\mathrm{PCA}}_{\mathrm{ST}}$ which reached 67.3% and the 54.5% for $\mathcal{R}^{\mathrm{PCA}}_{\mathrm{ST}} > 5, 10$, respectively. The least sensitive indices values into each thresholds were obtained for the indices T_a, T_{pe} and $\mathrm{T_w}$, with T_{pe} being the lowest. For the indices with the highest prevalence ($d^{\mathrm{PCA}}_{w,\mathrm{T}_{pe}}$ and ST), detection in subset $\mathcal{R}^{\mathrm{PCA}}_{\mathcal{I}} > 1$ occurred at 17.4 and 14.6 seconds, respectively after the onset of occlusion.

The temporal evolution of each index during ischemia was calculated as the evolution of the corresponding $\mathcal{R}^{\mathrm{PCA}}_{\mathcal{I}}$ along balloon inflation every 5 seconds

Table 3.3: Classification of $\mathcal{R}_{\mathcal{I}}^{\text{PCA}}$ prevalence and time instant in which it was exceeded in the study population according to the different indices.

	% of patients with $\mathcal{R}_{\mathcal{I}}^{\text{PCA}}$			Average time (s) to reach $\mathcal{R}_{\mathcal{I}}^{\text{PCA}}$		
$\mathcal{I}$	> 1	> 5	> 10	> 1	> 5	> 10
$d_{w,\text{T}_{pe}}^{\text{PCA}}$	94.1	64.4	48.5	17.4	34.7	51.8
T_a	88.1	61.4	41.6	18.7	38.6	46.3
T_{pe}	81.2	34.7	13.9	14.8	41.2	51.9
T_{W}	77.2	37.6	16.8	21.4	38.8	49.9
ST	89.1	67.3	54.5	14.6	33.7	44.2

from the onset of occlusion. It was found that from the first moments of occlusion the $\mathcal{R}_{\text{T}_a}^{\text{PCA}}$, $\mathcal{R}_{\text{ST}}^{\text{PCA}}$ and $\mathcal{R}_{d}^{\text{PCA}}$ showed higher values corresponding to a stronger and faster response to the induced ischemia. The evolution of $\mathcal{R}_{\mathcal{I}}^{\text{PCA}}$ values averaged over the total study population are show in Figure 3.8.

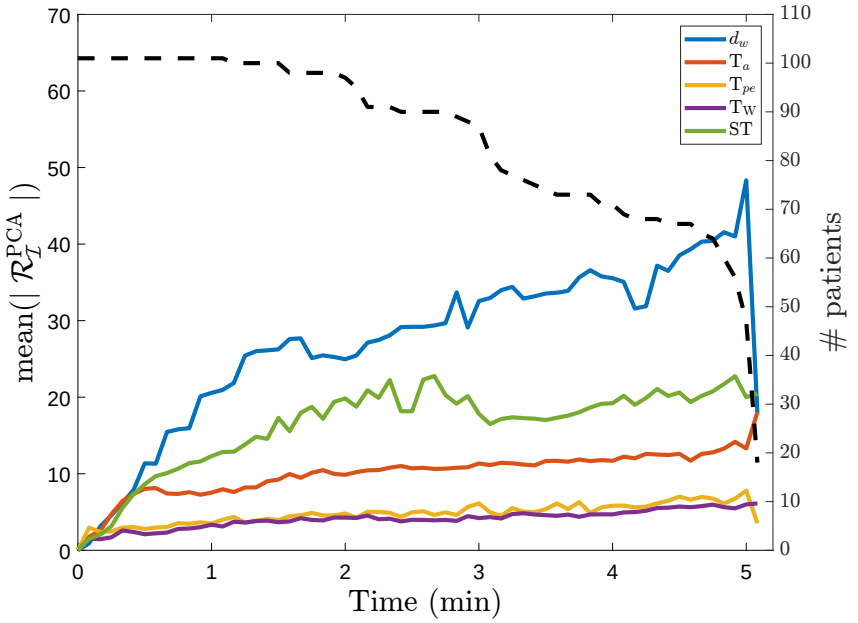


Figure 3.8: Average over patients of the $\mathcal{R}_{\mathcal{I}}^{\text{PCA}}$ time-course aligned to the onset of the balloon inflation during PCI recording, and numbers of patients averaged at a given time. Dash black line and the left y-axis correspond to the number of averaged recordings.

Figure 3.9 shows the percentage of patients presenting $\mathcal{R}_{\mathcal{I}}^{\text{PCA}} \geqslant 2, 5, 10$ for different occlusion times corresponding to times 1, 2, 3 and 4 min after balloon inflation. Note that the total number of recordings in each subset decreases

over time due to the different occlusion times. The most important variations in the ECG seem to take place in the initial minute of occlusion in the indexes studied, except for T_{pe} and T_w where only about 50% of patients exceed the threshold $\mathcal{R}_{\mathcal{I}}^{\text{PCA}} \geqslant 2$.

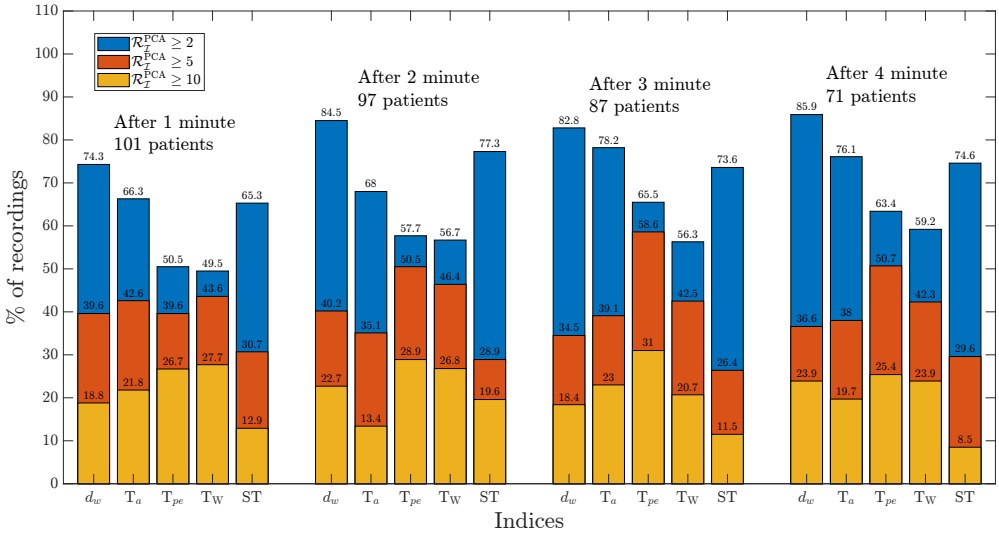


Figure 3.9: Percentage of patients with $\mathcal{R}_{\mathcal{I}}^{\text{PCA}} \geqslant 2, 5, 10$ segregated by different occlusion times group: 1 min, 2 min, 3 min and 4 min after balloon inflation.

3.4 Discussion

This study evaluates the ability of the ventricular repolarization dispersion index, $d_{w,T_{pe}}^{\text{PCA}}$, estimated from the peak to the end of the T-wave to characterize specifically the ischemia-induced dispersion of repolarization changes, thus avoiding the influence of ST segment elevation/depression. Using a warping-based assessment methodology, we measure the T_{pe} morphological changes with respect to control, quantifying time course, lead distribution, and differences with classic biomarkers. Our main findings were that $d_{w,T_{pe}}^{\text{PCA}}$, restricted to the T-wave peak-to-end, captures the changes between the peak and end of the T-wave, thus quantifying changes in ischemia-induced dispersion of repolarization, with impact on the regional differences in the spatial distribution of $d_{w,T_{pe}}^{\text{PCA}}$ according to the occluded artery. The $d_{w,T_{pe}}^{\text{PCA}}$ index better follows the ischemia-induced ECG variations than those classical indices that only consider information from specific ECG samples.

3.4.1 Time Course and Prevalence Analysis

The study of the time-course evolution of the $d^{\mathrm{PCA}}_{w,\mathrm{T}_{pe}}$ index confirmed its ability to robustly capture the variations of the T-peak to T-end morphology, hypothesized to specifically represent the ischemia-induced dispersion of repolarization changes, avoiding early T-waves and ischemia-induced ST elevation/depression changes.

A significant increase in the magnitude of $d^{\mathrm{PCA}}_{w,\mathrm{T}_{pe}}$ during PCI has been demonstrated as time elapses. As we actually expected, the ranges of values at control and during PCI were different: the $d^{\mathrm{PCA}}_{w,\mathrm{T}_{pe}}$ ranged in a narrow range in control, and in a wider range during PCI (see Figure 3.5b). Moreover, the changes observed at the end of balloon inflation quantified using $\mathcal{R}^{\mathrm{PCA}}_{d}$, estimated from $d^{\mathrm{PCA}}_{w,\mathrm{T}_{pe}}$ as described in (3.3), were (on median) 8 times larger than those obtained during the steady-state test at control recordings. The latter suggests that, in control conditions (without induced ischemic changes) the mean and standard deviation of $\mathcal{R}^{\mathrm{PCA}}_{d}$ have small values since they only reflect normal ECG variability. The low values during the steady-state test at control recordings indicate a quite stable behavior (note that a value of 1 denotes a change in the second half comparable to the standard deviation in the first half).

In this work we have used different threshold values over $\mathcal{R}^{\mathrm{PCA}}_{d}$ to quantify repolarization changes over-passing the threshold. It is important to note that threshold values for clinical use as risk markers require further experimental studies, in order to establish the level of normal variations such as changes induced by respiration, other underlying cardiac diseases, etc.

Different degrees of prevalence, where $\mathcal{R}^{\mathrm{PCA}}_{d}$ was larger than certain thresholds were reported in Table 3.3, resulting in all cases statistically significant in paired comparison between the PCI stage and the corresponding control stage, indicating that this index can be used to quantify ischemia-induced changes on ventricular repolarization from changes within their normal variations. Of the 86 patients who achieved $\mathcal{R}^{\mathrm{PCA}}_{d} > 2$, 80.23% did it within the first 30 seconds, supporting the hypothesis that variations in ventricular repolarization, quantified by $d^{\mathrm{PCA}}_{w,\mathrm{T}_{pe}}$, could begin to appear very soon after the blood supply to a given part of the heart is compromised.

A greater interquartile range of $\mathcal{R}^{\mathrm{PCA}}_{d}$ was observed for the LAD occluded patients as compared to patients with other occluded arteries even if those changes were found not to be statistically significant, possibly due to the small sample size. A larger study group as well as more information on the extent of the damaged area would be necessary to obtain relevant conclusions.

3.4.2 Spatial Analysis

The spatial distribution of $d^{\mathrm{PCA}}_{w,\mathrm{T}_{pe}}$ warping indicates how electrical activity is affected, as reflected in the T_{pe} interval, for the different occluded arteries. We found regional differences in the spatial distribution of $d^{\mathrm{PCA}}_{w,\mathrm{T}_{pe}}$ according to the occluded artery. The vast majority of the highest degrees of prevalence, both for $\mathcal{R}^l_d > 2$ and $\mathcal{R}^l_d > 5$, correspond to the region of the myocardium irrigated by the arteries as shown in Figure 3.6, where higher prevalence of $\mathcal{R}^l_d$ index in leads $l \in \{\mathrm{V1\text{-}V3}, \mathrm{I}, \mathrm{aVR}, \mathrm{aVF}, \mathrm{III}\}$ for RCA group and higher prevalence of $\mathcal{R}^l_d$ index in leads $l \in \{\mathrm{V1\text{-}V3}, \mathrm{V6}\}$ and marked decrease in aVR and III (inferior wall) for RCA group were found.

Regional differences were also found in the maximum $d^{\mathrm{PCA}}_{w,\mathrm{T}_{pe}}$ reached, depending on the occluded artery and the wall that the leads look at. Although the differences found were not strong, these findings suggest a certain capacity of the $d^{\mathrm{PCA}}_{w,\mathrm{T}_{pe}}$ index to indicate the location of the ischemia, considering also that occlusions were done at different locations within the major arteries and there are no reports on the size of the damaged area. The lead distribution across the LAD and LCX subsets are in line with those reported in [215] using T-wave repolarization alternans analysis in the same study population.

The discrepancies in the spatial distribution of $\mathcal{R}^l_d$ and $\overline{d}^l_{w,\mathrm{T}_{pe}}$ (Figure 3.6 and 3.7) can be attributed to patient-to-patient and lead-to-lead differences in σ^c_d, which quantifies the stability of the measurement during the control recording.

3.4.3 Classic Local Measurements

We have demonstrated that the warping-based $d^{\mathrm{PCA}}_{w,\mathrm{T}_{pe}}$ index, which takes into account all the morphological information of the entire interval studied, from T peak to T end, can better represent the ischemia-induced ECG variations than those indices that only consider information from specific ECG samples as T_{pe}. At the end of occlusion, $\mathcal{R}^{\mathrm{PCA}}_{\mathcal{I}}$ values of 37.1, 13.9, 6.0, 5.6 and 27.7 were reached for $d^{\mathrm{PCA}}_{w,\mathrm{T}_{pe}}$, T_a, T_{pe}, $\mathrm{T_w}$ and ST, respectively. $\mathcal{R}^{\mathrm{PCA}}_d$ achieved higher values than those corresponding to classic indices (see also Figure 3.8, Average of $\mathcal{R}^{\mathrm{PCA}}_{\mathcal{I}}$ time-course). Only $\mathcal{R}^{\mathrm{PCA}}_{\mathrm{ST}}$ approached the value of $\mathcal{R}^{\mathrm{PCA}}_d$, making the ST level the measure based on fidicial points most sensitive to ischemic changes, as it is already known in routine clinical practice where it is the index most commonly used. However, the underlying physiological mechanisms for ST elevation do not need to be the same as for T-peak to T-end interval morphology changes, as they reflect different physiological effects

induced by ischemia. For ST segment elevation/depression, the mechanism can be the injury current generated by ischemia, while for the T_{pe} interval analysis the mechanism may be more related to repolarization dispersion generated by ischemia, which is typically considered a surrogate for arrhythmia risk,

T_a, T_{pe} and T_w indices had the lowest values, and therefore, lower sensitivity. However, it must be taken into account that each index reflects different ischemia-related phenomena. Comparing $\mathcal{R}_d^{\text{PCA}}$ with $\mathcal{R}_{T_{pe}}^{\text{PCA}}$, which are indices characterizing the same area of the T-wave, they reach values of the change index of 9.4 and 2.7, respectively, showing that $d_{w,T_{pe}}^{\text{PCA}}$ is more sensitive than T_{pe}, either because it betters reflect the underlying physiological changes, or because the stability of the measurement is higher or for a combination of both.

According to the data in Table 3.3, $d_{w,T_{pe}}^{\text{PCA}}$ and ST indices were also the most sensitive, with their corresponding $\mathcal{R}_{\mathcal{I}}^{\text{PCA}}$ estimators exceeding the thresholds in a greater number of patients. The ST marker had the earliest reaction compared to any other index for all thresholds. However, the temporal differences of the indices achieving the threshold are not very wide (< 8 s in all cases). Again, the more meaningful comparison is between $d_{w,T_{pe}}^{\text{PCA}}$ and T_{pe}, having $d_{w,T_{pe}}^{\text{PCA}}$ the largest reaction, with no conclusive results in terms of earlier appearance.

The analysis of percentage of patients presenting $\mathcal{R}_{\mathcal{I}}^{\text{PCA}} > 2, 5, 10$ for different occlusion times (see Figure 3.9) discloses different degrees of prevalence of the studied indices when crossing different thresholds, with $d_{w,T_{pe}}^{\text{PCA}}$ and ST reaching the highest values, well in line with previous findings. From an overall perspective, it can be seen that, during the first minute, more than 60% of the total change appears, whereas in the second and third minute changes it continues to increase but there is a deceleration in the rate of variation. As time progresses the number of patients with $\mathcal{R}_{\mathcal{I}}^{\text{PCA}} > 2$ increases, with $d_{w,T_{pe}}^{\text{PCA}}$ being the most sensitive in all cases, while for $\mathcal{R}_{\mathcal{I}}^{\text{PCA}} > 5, 10$, there are others indices more sensitive than $d_{w,T_{pe}}^{\text{PCA}}$.

3.4.4 Clinical Implications

In this study we have available both control and induced ischemia ECG recordings. In clinical practice, however, it would be difficult to obtain non-ischemic control data to compare with, although $d_{w,T_{pe}}^{\text{PCA}}$ can still be computed with respect to a pre-ischemic ECG, if available, or with respect to a reference point, like in this study where the reference is taken at the beginning of the occlusion, thus allowing monitoring of T wave changes. In a scenario with

available ECG recordings restricted to a stationary ischemia the methodology can not be applied. When applicable, the establishment of proper thresholds for $d^{\mathrm{PCA}}_{w,\mathrm{T}_{pe}}$, under normal or ischemic conditions, remains a challenge. Threshold values need to be established for detection or alarm triggering, and be applied to the raw $d^{\mathrm{PCA}}_{w,\mathrm{T}_{pe}}$, or T_{pe}, not requiring a control recording. Note that the relative $\mathcal{R}^{\mathrm{PCA}}_{\mathcal{I}}$ magnitude is used in this study just to characterize how $d^{\mathrm{PCA}}_{w,\mathrm{T}_{pe}}$ and T_{pe} changed during PCI as compared to changes in control, in order to determine their sensitivity.

Previous studies suggest that the T-peak-to-T-end interval is a strong ventricular arrhythmic marker in ischemic conditions [217]. This interval also avoids the location of T-onset in ischemia, which is very challenging due to the ST segment elevation/depression and early T wave modifications induced by ischemia. The index $d^{\mathrm{PCA}}_{w,\mathrm{T}_{pe}}$ aims to be an alternative to the T_{pe} interval in measuring ventricular repolarization dispersion more robustly. Further studies need to be designed to establish the proper thresholds to trigger arrhythmia alarms in clinical practice under ischemic conditions.

In Table 3.2 we can see that men had larger $\mathcal{R}^{\mathrm{PCA}}_{d}$ than women. It is known that women have shorter T-peak-to-T-end interval values than men [218, 219], which may also imply a reduced dynamic range in T_{pe} prolongation induced by ischemia in women, which would be congruent with the results shown in Table 3.2.

3.4.5 Limitations

The present study shows the power of $d^{\mathrm{PCA}}_{w,\mathrm{T}_{pe}}$ to monitor T-peak to T-end morphology changes induced by ischemia, and also that those changes are more prominently identified than by using other indices such as the T_{pe} interval. However, the study does not establish that $d^{\mathrm{PCA}}_{w,\mathrm{T}_{pe}}$ is as surrogate for arrhythmia risk marker under ischemia, since the occlusions were not long enough to generate arrhythmia. Other studies in animal models or other clinical scenarios should be tested to evaluate if the methodological sensitivity improvement of $d^{\mathrm{PCA}}_{w,\mathrm{T}_{pe}}$ with respect to T_{pe} translates to clinical superiority.

The proposed methodology is designed to capture morphological variations of the final part of the T wave that mainly represent an elongation. In this study we have not found any extreme ischemia-induced T-peak-to-T-end variations affecting the method hypothesis. However, in addition to possible erroneous extraction of the T_{pe} interval morphology due to excessive noise and delineation errors, subjects combining ischemia with other arrhythmia causing other changes in the T wave final part (as moving from regular to biphasic,

etc), can lead to misleading results when trying to fit two different morphologies, not just prolonged T waves. This would prevent interpreting $d^{\mathrm{PCA}}_{w,\mathrm{T}_{pe}}$ as suggested in this work.

The extent of ischemic injury was not quantified in this study, limiting the interpretation of the spatial differences observed according to the occluded coronary artery. Another important consideration is that the relative index $\mathcal{R}^{\mathrm{PCA}}_{\mathcal{I}}$ depends on the variability measured during control recordings. Consequently, its magnitude may be influenced not only by the extent of ischemia-induced changes but also by the baseline stability of the corresponding ECG marker, including both its sensitivity to noise and physiological variability. Finally, although the classical ECG indices and the time-warping-based marker were derived from the same preprocessed signals and fiducial annotations, and temporal median filtering was applied to the classical indices to reduce the influence of outliers and short-term fluctuations, differences in their sensitivity to noise and physiological variability cannot be completely ruled out. Therefore, the relative contributions of additional morphological information and potential differences in robustness to the higher sensitivity observed for the time-warping-based marker remain to be established.

3.5 Conclusions

In this chapter, the T-wave time-warping based index, $d^{\mathrm{PCA}}_{w,\mathrm{T}_{pe}}$, restricted to the T-peak-to-end interval, was shown to track ischemia-induced morphology changes of the final part of the T-wave, hypothesized to be a surrogate of repolarization dispersion changes. The observed increase in the $d^{\mathrm{PCA}}_{w,\mathrm{T}_{pe}}$ and $\mathcal{R}^{\mathrm{PCA}}_{d}$ indexes during ischemia progression suggests its value as surrogate marker for the ischemia-induced increase of repolarization dispersion. In the next chapter, this warping index is further evaluated in a porcine myocardial infarction models to assess its potential as ventricular arrhythmic risk marker during ischemia.

CHAPTER 4

T-WAVE PEAK-TO-END CHANGES QUANTIFIED BY TIME-WARPING PREDICTS VENTRICULAR FIBRILLATION IN A PORCINE MYOCARDIAL INFARCTION MODEL

4.1 Introduction

4.2 Methods

4.2.1 Experimental Data Set and Protocol

4.2.2 ECG Pre-processing

4.2.3 Time-Warping Quantification of T_{pe} Interval Changes

4.2.4 Statistical Analysis

4.3 Results

4.3.1 Changes of $d^{\mathrm{PCA}}_{w,\mathrm{T}_{pe}}$ During Occlusion

4.3.2 Comparison of Indices Behavior

4.3.3 VF Prediction Analysis

4.4 Discussion

4.4.1 Time-Course of $d^{\mathrm{PCA}}_{w,\mathrm{T}_{pe}}$

4.4.2 Association with VF Episodes

4.4.3 Limitations

4.5 Conclusions

4.1 Introduction

After demonstrating in the previous chapter that T-peak-to-end time-warping marker, $d^{\mathrm{PCA}}_{w,\mathrm{T}_{pe}}$, can track ischemia-induced changes in ventricular repolariza-

tion in humans, the next step is to assess whether this marker can also be associated with arrhythmic risk. VF is a major life-threatening complication of acute myocardial infarction and represents one of the main mechanisms leading to SCD [220, 221]. In this setting, identification of ischemia-induced repolarization abnormalities associated with VF susceptibility is essential for improving arrhythmic risk stratification.

Porcine myocardial infarction models provide an excellent analog to investigate VRD changes occurring with the development of acute ischemia. In particular, LAD artery ischemia models in pigs offer a huge value for studying human ischemia, as the LAD artery supplies a significant portion of the left ventricle in both pigs and humans, providing valuable insights into the mechanisms of the ischemic myocardium in humans. Some earlier studies have also chosen LAD artery to induce acute myocardial infarction [222–225]. Moreover, in studies where there is a limited number of experimental animals, only LAD artery occlusions are sometimes induced to achieve reproducibility of myocardial lesion [190].

Building on the previous chapter, where T-peak-to-end morphology was shown to be sensitive to ischemia-induced repolarization changes, the present chapter further explores this repolarization window in the context of arrhythmic risk assessment. In this regard, the T_{pe} interval was introduced as a surrogate measure of VRD in [11] and as a potential predictive index for arrhythmic risk in [226, 227]. Its potential to stratify arrhythmic risk has been evaluated using an arterially perfused canine ventricular wedge [11], where it was proposed as a measure of transmural dispersion of repolarization. In the context of acute myocardial infarction, Azarov *et al.* [217] demonstrated the relationship between the evolution of the T_{pe} index and the development of an arrhythmogenic substrate in a porcine myocardial infarction model.

Although $d^{\mathrm{PCA}}_{w,\mathrm{T}_{pe}}$ demonstrated a great ability in quantifying ischemia-induced VRD changes in a 5-min ischemia model in humans in Chapter 3, the time span was not large enough to evaluate its potential for arrhythmia risk prediction. The aim of the study in this chapter was to analyze the time-course of the T_{pe} warping-based $d^{\mathrm{PCA}}_{w,\mathrm{T}_{pe}}$ VRD index during ischemia progression and to test whether its evolution could predict impending VF in a porcine myocardial infarction model.

4.2 Methods

4.2.1 Experimental Data Set and Protocol

This study uses a closed-chest porcine myocardial infarction model implemented at Lund University (Lund, Sweden). A detailed description of the experimental protocol can be found in [190]. Myocardial ischemia and infarction was induced by a 40-minute-long balloon inflation in the LAD coronary artery in 32 pigs. A 12-lead ECG with a sampling rate of 1024 Hz and amplitude resolution of 1.18 μV per bit was recorded at baseline and during coronary occlusion period using "Kardiotechnica-04-8", INCART, St.Petersburg, Russia.

The animal research study followed the guidelines in the Care and Use of Laboratory Animals guide by the US National Institutes of Health (NIH Publication No. 85-23, revised 1996) and received approval from the local animal research ethics committee.

Table 4.1: Pig population and VF distribution.

Group	Pigs	Subgroup	Pigs	Occurrence time of VF event: mean [range] (min:s)
Non-VF	16	-	16	-
VF	16	Early VF	7	2:45 [0:49-7:3]
		Delayed-VF	10*	21:18 [17:40-30:50]

*one pig in the Delayed-VF group also suffered Early VF.

The pig population is divided as presented in Table 4.1. From the total study group (32 pigs), 16 pigs did not have a VF event, while a total of 17 VF episodes were annotated in the remaining group. The VF group is further subdivided according to the VF occurrence time: a first subgroup (Early VF) is composed of 7 pigs suffering VF within the first 10 minutes of occlusion, and a second one (Delayed-VF), composed by the 10 pigs suffering VF after minute 10 from occlusion. One pig suffered VF twice, one in each of the defined periods.

These two distinct subsets of VF are in line with the previously reported arrhythmic patterns [228, 229], where VF episodes were observed in two different periods of time, which are believed to have different underlying mechanisms. On this basis, the present study specifically focused on the delayed arrhythmic phase, otherwise the one which allows for preventive interventions in the patient management. This choice was also motivated by the objective of char-

acterizing the progressive evolution of ischemia-induced repolarization changes before arrhythmia onset, for which VF occurring within the first minutes of occlusion provides only a limited observation window. Early-VF episodes occurring within the first 10 minutes of occlusion were therefore excluded from the analysis.

4.2.2 ECG Pre-processing

The ECG pre-processing and spatial transformation followed the general pipeline described in Chapter 2 and applied in Chapter 3. Briefly, the eight independent ECG leads were filtered, delineated and transformed using PCA, with the first principal component used for the subsequent analysis.

In this study, the PCA eigenvectors and eigenvalues were estimated using the first minute of the baseline period, selecting T wave windows starting and ending at fixed distances from the corresponding QRS mark following the rules used in [216]. The resulting T waves in the first PCA-transformed lead were segmented and further filtered using a bidirectional sixth-order Butterworth low-pass filter with a 20-Hz cut-off frequency before morphology analysis.

4.2.3 Time-Warping Quantification of T_{pe} Interval Changes

For each pig, ischemia-induced dynamic T peak-to-end waveform changes over time were quantified by both T_{pe} interval and by the time warping index $d^{\mathrm{PCA}}_{w,\mathrm{T}_{pe}}$.

The $d^{\mathrm{PCA}}_{w,\mathrm{T}_{pe}}$ computation followed the methodology detailed in Section 2.3 and further evaluated in Chapter 3. In brief, for each recording, a MWTPE $\boldsymbol{f}^s(\boldsymbol{t}^s)$ was extracted from each s-th 15-second sliding window (with 10-second overlap) over the entire record. The reference MWTPE $\boldsymbol{f}^r(\boldsymbol{t}^r)$ was computed in a 60-second window at the beginning of the baseline stage. Then, temporal reparametrization (warping) was computed between each MWTPE along the recording and the reference, yielding the $d^{\mathrm{PCA}}_{w,\mathrm{T}_{pe}}$ series. Figure 4.1 illustrates the $d^{\mathrm{PCA}}_{w,\mathrm{T}_{pe}}$ series estimation procedure.

In order to test the impact of the first part of the T-wave (up to T-peak) on our hypothesis, we applied the same methodology to the whole T-wave ($d^{\mathrm{PCA}}_{w,\mathrm{T}}$ index). Since the T-wave onset (T_o) is strongly influenced by ischemic conditions and, therefore, highly exposed to delineation errors, we chose the end of the QRS complex (QRS_e) to mark the beginning of the T-wave. Recall that $\mathcal{I} \in \{\mathrm{T}, \mathrm{T}_{pe}\}$ in $d^{\mathrm{PCA}}_{w,\mathcal{I}}$ refers to the part of the T-wave over which the index is computed.

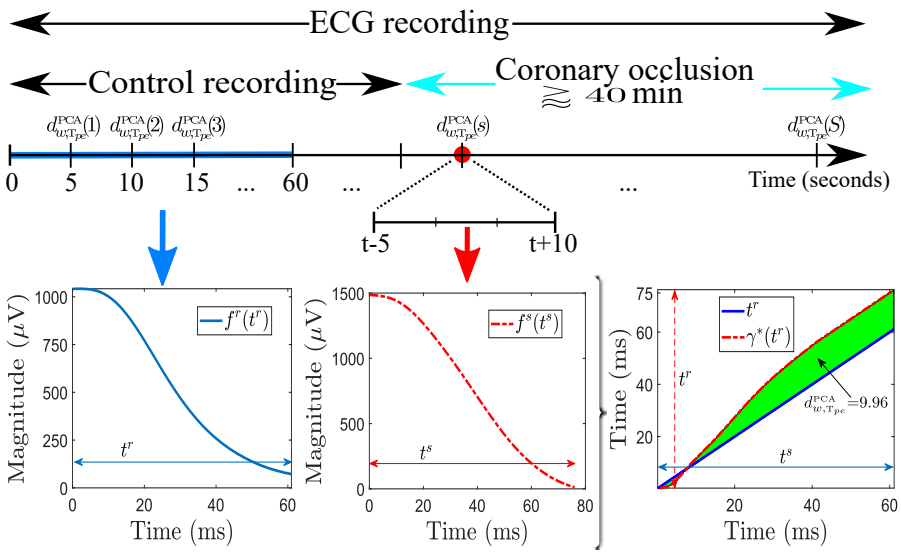


Figure 4.1: Diagram of the method to obtain each MWTPE, the reference MWTPE, and the $d^{\mathrm{PCA}}_{w,\mathrm{T}_{pe}}$ series. The MWTPE $\boldsymbol{f}^s(\boldsymbol{t}^s)$ was extracted from each s-th 15-second windows (represented by red color), with 5 seconds sliding and 10 seconds overlap the entire record, while MWTPE $\boldsymbol{f}^r(\boldsymbol{t}^r)$ was estimated from the waves within the first 60 seconds, at the beginning of the baseline period (blue color). The bottom rightmost graph shown the warping function $\gamma^*(t^r)$ (dotted red line) relating optimally the reference $\boldsymbol{f}^r(\boldsymbol{t}^r)$ and studied $\boldsymbol{f}^s(\boldsymbol{t}^s)$ MWTPEs. The green region between $\gamma^*(t^r)$ and t^r denotes the total warping amount, quantified by $d^{\mathrm{PCA}}_{w,\mathrm{T}_{pe}}$.

The T_{pe} interval was also estimated for each i-th beat to serve as a comparative reference to assess the added value of the $d^{\mathrm{PCA}}_{w,\mathrm{T}_{pe}}$. A median filter was then applied to the resulting $\mathrm{T}^{\mathrm{PCA}}_{pe}$ series using a 15-second sliding window and 5 seconds of overlap to achieve the same resolution as that of the $d^{\mathrm{PCA}}_{w,\mathrm{T}_{pe}}$ index.

4.2.4 Statistical Analysis

The dynamic analysis of the ischemia-induced changes was performed by evaluating the time courses of $d^{\mathrm{PCA}}_{w,\mathrm{T}_{pe}}$, $\mathrm{T}^{\mathrm{PCA}}_{pe}$ and $d^{\mathrm{PCA}}_{w,\mathrm{T}}$ every 5 seconds in the baseline and the occlusion stages, presenting them as running averages and standard deviations. Average values during the first 5 minutes following recording onset (0-5), the last 5 minutes before the occlusion onset, the 0-5, 5-10, 10-15, 15-20, 20-25 five minutes intervals after occlusion, and during 15-10, 10-5 and 5-0 five minutes intervals, prior to a VF episode, were also computed, see Figure 4.3, top panel, for a schematic representation by arrows of the intervals. These

values were compared between the group of VF-free pigs (Non-VF group) and those pigs who suffered Delayed-VF during coronary occlusion (Delayed-VF group). The Mann-Whitney test was used for comparisons between Non-VF and Delayed-VF groups. A p-value $\leqslant 0.05$ was used to declare statistical significance.

To analyze the relationship between indices and VF-susceptibility, the maximum values into the above-mentioned periods were assessed. Receiver operating characteristic (ROC) curve analysis was used to find the true positive and false positive rate as the threshold varies. The optimal thesholds were taken as those that minimize the distance to the upper left corner of the ROC curve. Then, the Cox regression analysis and Kaplan–Meier survival functions were used to comparatively analyze their predictive value. All computations were performed using MATLAB® version R2022a.

4.3 Results

4.3.1 Changes of $d^{\mathrm{PCA}}_{w,\mathrm{T}_{pe}}$ During Occlusion

Figure 4.2 shows, for a particular pig from the database, noticeable changes in the ECG beats and T_{pe} waveform during the occlusion, together with their projection on the first PCA transformed lead. Note that the greatest changes in the ECG morphology appear on the leads most directly covering the LAD artery perfused area (V2-V4).

Changes in the T_{pe} waveform were captured by the $d^{\mathrm{PCA}}_{w,\mathrm{T}_{pe}}$ index, with an increasing trend beginning immediately after the start of the occlusion. An example of the time course of $d^{\mathrm{PCA}}_{w,\mathrm{T}_{pe}}(s)$ during baseline and occlusion for two particular animals, one who suffered VF and one who did not, is shown in Figure 4.3. The dashed black line represents the balloon inflation instant and the dashed red lines indicate the occurrence of the VF episode. Strong intra-individual differences on the T_{pe} morphology variations in terms of $d^{\mathrm{PCA}}_{w,\mathrm{T}_{pe}}(s)$ magnitude changes were observed. These differences follow a more emphasized increasing trend as inflation time progresses for the pig who had VF than for the one that did not, ranging from 4.92 to 44.51 ms and from 1.94 to 7.52 ms, respectively, on the pigs in Figure 4.3. In both baseline recordings, $d^{\mathrm{PCA}}_{w,\mathrm{T}_{pe}}(s)$ magnitude remains almost stationary, ranging from 0 to 8.67 and from 0 to 3.15 ms, respectively.

Across all the studied pigs, no significant T_{pe} morphology changes were found during baseline, with an inter-recordings median [IQR] value of the intra-

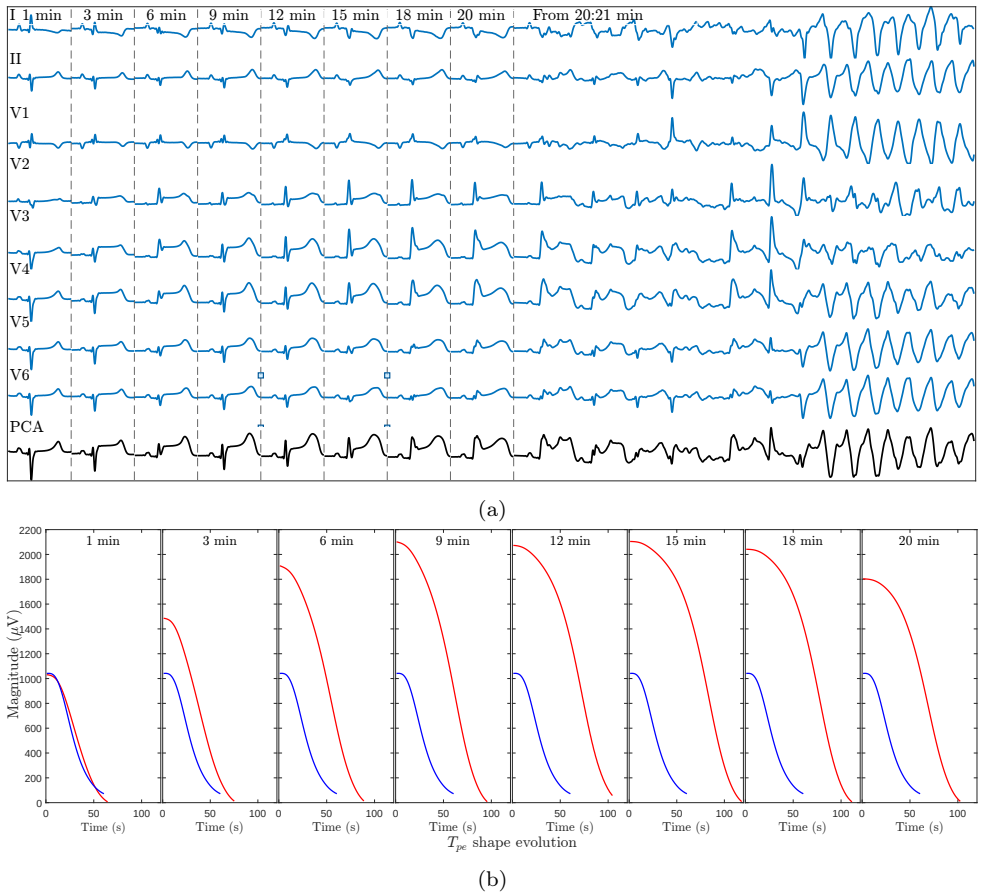


Figure 4.2: Example of an ECG signal and T_{pe} interval waveform changes during coronary occlusion for a particular pig. Panel (a) shows representative QRST complexes recorded in 8 independent ECG leads and their projection on the first PCA transformed lead at 1, 3, 6, 9, 12, 15, 18, 20th and 21th minutes of LAD-occlusion, followed by ventricular fibrillation episode. Note that from the 20:21 min onwards the ECG beat shape is lost and the VF episode starts. Panel (b) shows the MWTPEs at the first PCA lead corresponding to each s-th window where ECG beat from panel (a) is contained, the blue line represents the reference $\boldsymbol{f}^r(\boldsymbol{t}^r)$ MWTPE and the red line each s-th given $\boldsymbol{f}^s(\boldsymbol{t}^s)$ MWTPE.

recording median of 1.60 [1.33] ms. Six pigs showed a minor trend of change at the end of the control recording, as illustrated in Figure 4.3, which may be due to catheter manipulations immediately before occlusion. In contrast, strong ischemia-induced changes, reflected in T_{pe} morphology changes (width and amplitude changes, together with the presence of T-wave alternans) and increased $d^{\mathrm{PCA}}_{w,\mathrm{T}_{pe}}$ magnitude were noted during the balloon inflation period in

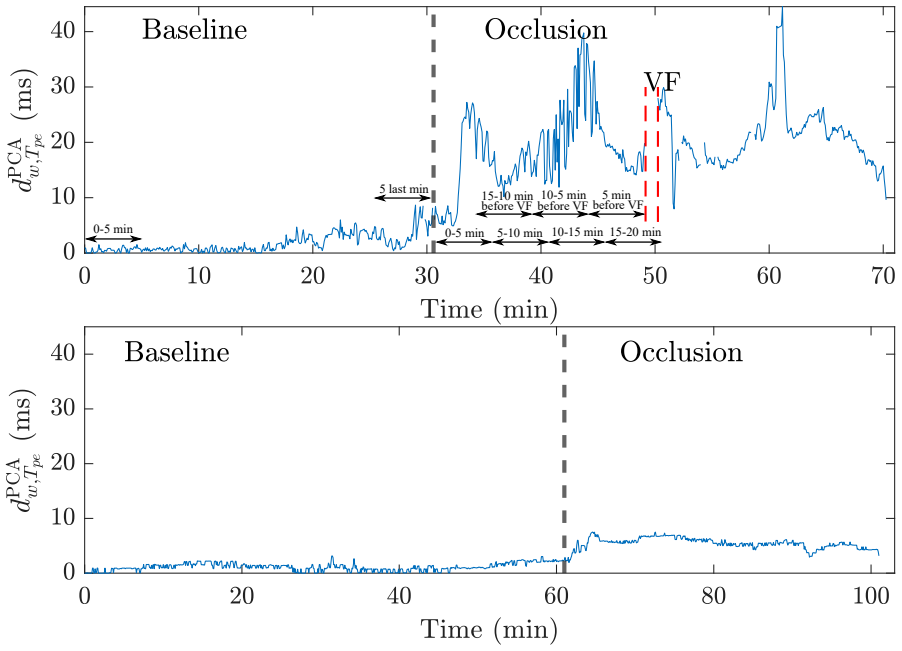


Figure 4.3: Example of $d^{\mathrm{PCA}}_{w,\mathrm{T}_{pe}}(s)$ time course evolution along baseline and occlusion period for two particular animals, one who suffered a VF event (top) and one who did not (bottom). The black dashed line represents the onset of balloon inflation and the red dashed line, the occurrence of the VF episode.

most of the pigs with intra-recording median values reaching 14.58 [17.72] ms.

4.3.2 Comparison of Indices Behavior

The $d^{\mathrm{PCA}}_{w,\mathrm{T}_{pe}}$ and $\mathrm{T}^{\mathrm{PCA}}_{pe}$ indices showed similar behavior over time, characterized by an increase in their magnitudes from the beginning of the occlusion, with the greatest changes occurring in the first 5 minutes and remaining relatively stable thereafter. The average time course (blue line) and standard deviation (red line) of $d^{\mathrm{PCA}}_{w,\mathrm{T}_{pe}}$ and $\mathrm{T}^{\mathrm{PCA}}_{pe}$ indices across animals for the Non-VF and the Delayed-VF groups, both during baseline and occlusion stages, aligned to the recording onset or to the balloon inflation onset, respectively, are shown in Figure 4.4. All recordings for each subset were averaged. Note that the number of available recordings declines as time elapses, at baseline due to the variable recording duration and at occlusion due to the different VF occurrence times.

The $d^{\mathrm{PCA}}_{w,\mathrm{T}_{pe}}$ and $\mathrm{T}^{\mathrm{PCA}}_{pe}$ indices exhibited similar behavior during baseline for

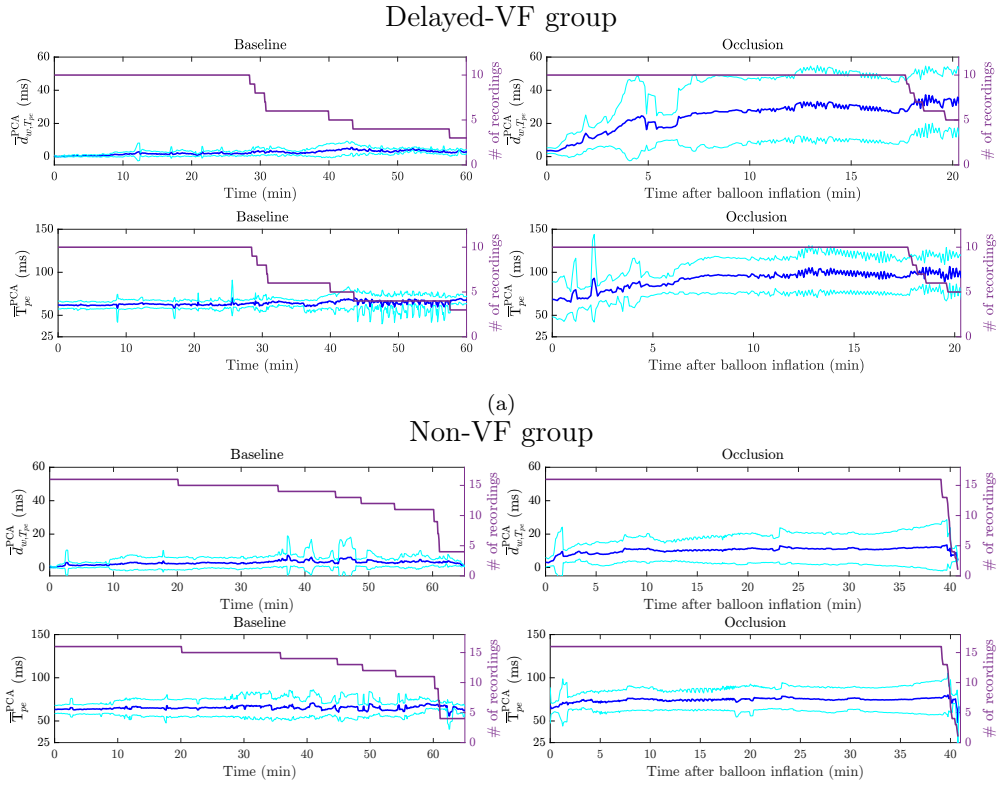


Figure 4.4: Average time course of $d^{\mathrm{PCA}}_{w,\mathrm{T}_{pe}}$ and $\mathrm{T}^{\mathrm{PCA}}_{pe}$ indices (mean (blue line) $\pm$ standard deviation (cyan lines)) relative to the onset of the recording in baseline and to the balloon inflation onset during occlusion stage for pigs who suffered VF (Delayed-VF group) in panel (a) and for Non-VF group in panel (b). Purple line and the right y-axis indicate the number of averaged recordings at each given time. Note that the time span of the Delayed-VF and Non-VF groups are different for the occlusion stage due to the VF episodes occurrence. At baseline, the recording time is variable among pigs.

the two groups of pigs, while $d^{\mathrm{PCA}}_{w,\mathrm{T}}$ showed a wider range of early changes but there were no significant differences between groups in the 5 minutes prior to the onset of balloon inflation. The average of $d^{\mathrm{PCA}}_{w,\mathrm{T}_{pe}}$, $\mathrm{T}^{\mathrm{PCA}}_{pe}$ and $d^{\mathrm{PCA}}_{w,\mathrm{T}}$ indices measured in the first 5 minutes after the baseline recording onset, at the last 5 minutes before the occlusion onset, at the 0-5, 5-10, 10-15, 15-20, 20-25 minutes from the occlusion onset and at the 15-10, 10-5 and 5 minutes prior to VF episode (or 21:18 min if no VF episode is present) are displayed in Figure 4.5. The median magnitude for each interval and group and p-values of the comparison between groups (Mann-Whitney test) is shown in Table 4.2. During

occlusion, significant differences were found in the magnitude of the $d^{\mathrm{PCA}}_{w,\mathrm{T}_{pe}}$ and $\mathrm{T}^{\mathrm{PCA}}_{pe}$ indices when comparing VF-susceptible pigs (Delayed-VF group) and the Non-VF group from the first 5 minutes of balloon inflation, ranged from a negligible variation immediately before the onset of the occlusion to more pronounced differences as time elapses. Note that, during the first 5 minutes of ischemia, both $d^{\mathrm{PCA}}_{w,\mathrm{T}_{pe}}$ ($p = 0.037$) and $\mathrm{T}^{\mathrm{PCA}}_{pe}$ ($p = 0.042$) showed significant differences between the Delayed-VF and Non-VF groups, whereas no significant difference was found for $d^{\mathrm{PCA}}_{w,\mathrm{T}}$ ($p = 0.617$), highlighting the early discriminative value of measurements focused on the T_{pe} interval.

During the first 5 minutes of ischemia, significant differences between the Delayed-VF and Non-VF groups were observed for both $d^{\mathrm{PCA}}w, \mathrm{T}_{pe}$ ($p = 0.037$) and $\mathrm{T}pe^{\mathrm{PCA}}$ ($p = 0.042$), whereas no significant difference was found for $d^{\mathrm{PCA}}w, \mathrm{T}$ ($p = 0.617$), highlighting the early discriminative value of indices restricted to the T_{pe} interval.

4.3.3 VF Prediction Analysis

The significantly greater increase of $d^{\mathrm{PCA}}_{w,\mathrm{T}_{pe}}$ and $\mathrm{T}^{\mathrm{PCA}}_{pe}$ magnitude as the duration of the occlusion progresses in the VF-susceptible pigs compared to the Non-VF pigs offered a rationale for assessing their values for predicting VF episodes. Therefore, the association between the maximum amplitude of both indices (together with that of the $d^{\mathrm{PCA}}_{w,\mathrm{T}}$ index as comparative reference) and the subsequent VF episode at the intervals 0-5, 5-10 minutes (first minutes of occlusion) and 5-0 minutes before the episode of VF, was studied using the ROC curve, shown in Figure 4.6 and completed in Table 4.3. Results show improved detection ability for $d^{\mathrm{PCA}}_{w,\mathrm{T}_{pe}}$ (AUC=0.85) as compared with $\mathrm{T}^{\mathrm{PCA}}_{pe}$ (AUC=0.79) within the early 5-10 minutes interval. Taking the threshold that minimizes the distance to the upper left corner of the ROC curve, results show that $d^{\mathrm{PCA}}_{w,\mathrm{T}_{pe}}$ predicts the presence of VF episodes with Se=90%, Sp=75% for a threshold set to 20.0 ms, whereas the $\mathrm{T}^{\mathrm{PCA}}_{pe}$ index distinguishes between both groups with a lower accuracy (Se=80%, Sp=69% for a threshold set to 85.4 ms) and for $d^{\mathrm{PCA}}_{w,\mathrm{T}}$ index there was no significant association between the index magnitude and the delayed-VF occurrence. For the 1 to 5 minutes interval, lower values of AUC were obtained for $d^{\mathrm{PCA}}_{w,\mathrm{T}_{pe}}$, $\mathrm{T}^{\mathrm{PCA}}_{pe}$ and $d^{\mathrm{PCA}}_{w,\mathrm{T}}$ indices (AUC = 0.74, 0.66 and 0.60, respectively).

The presented analysis showed a significant association between both indices and the trigger of VF episodes at the time span prior to the arrhythmic window (more clinically relevant than the 5-minute interval before VF). The Cox regression analysis of $d^{\mathrm{PCA}}_{w,\mathrm{T}_{pe}} \geqslant 20.0$ predicted impending VF episodes with

Table 4.2: Median and p-value from selected intervals for $d^{\mathrm{PCA}}_{w,\mathrm{T}_{pe}}$, $\mathrm{T}^{\mathrm{PCA}}_{pe}$ and $d^{\mathrm{PCA}}_{w,\mathrm{T}}$ indices segregated by VF susceptibility.

		Control stage		Occlusion stage							
Index		0-5 min onset	5-0 min before occl	0-5 min	5-10 min	10-15 min	15-20 min	20-25 min	15-10 min before VF	10-5 min before VF	5-0 min before VF
$d^{\mathrm{PCA}}_{w,\mathrm{T}_{pe}}$	Delayed-VF group median (s)	0.3	2.7	12.5	18.8	26.8	24.0	31.0	18.6	25.0	28.8
	Non-VF group median (s)	0.4	2.4	6.3	7.6	8.0	7.8	7.8	8.5	7.2	6.0
	p-value	0.340	0.843	**0.037**	**0.001**	**0.001**	**0.008**	**0.003**	**0.016**	**0.002**	**0.004**
$\mathrm{T}^{\mathrm{PCA}}_{pe}$	Delayed-VF group median (s)	61.5	61.0	80.0	89.0	99.0	92.6	99.0	88.9	94.2	95.5
	Non-VF group median (s)	63.7	63.5	70.8	72.9	73.0	72.3	72.6	73.5	71.0	72.8
	p-value	0.187	0.383	**0.042**	**0.003**	**0.002**	**0.008**	**0.019**	**0.030**	**0.003**	**0.002**
$d^{\mathrm{PCA}}_{w,\mathrm{T}}$	Delayed-VF group median (s)	1.9	9.5	34.4	50.0	42.5	39.7	55.0	34.8	37.9	49.8
	Non-VF group median (s)	2.5	17.3	37.8	40.5	32.9	34.1	42.2	40.9	29.6	38.7
	p-value	0.654	0.295	0.617	0.414	0.257	0.216	0.076	0.732	0.544	0.12

Bold values indicate significance, $p < 0.05$.

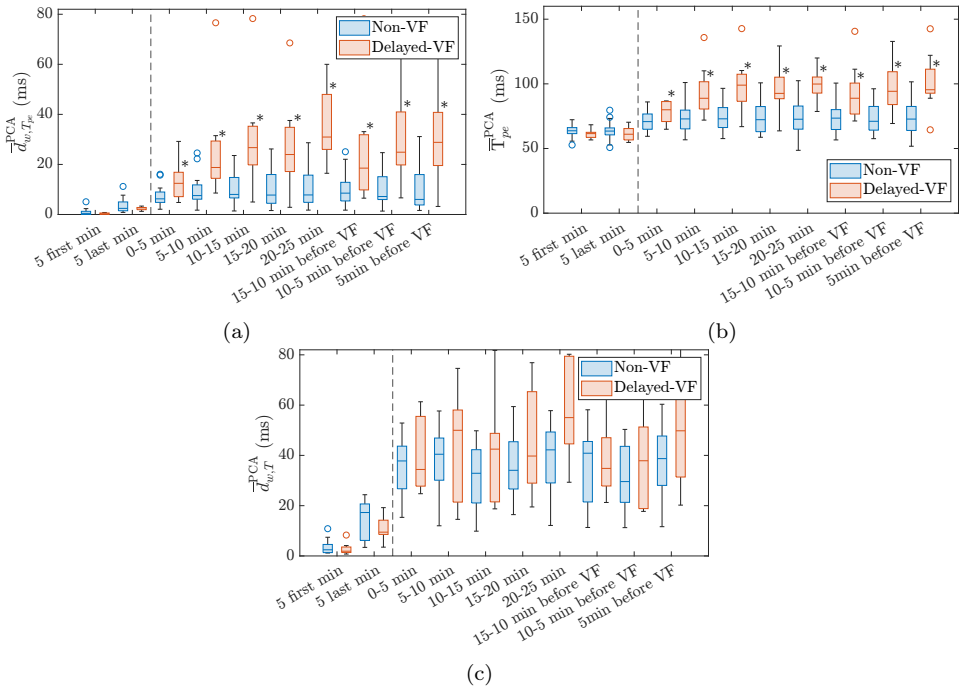


Figure 4.5: Box plots distributions of $d^{\mathrm{PCA}}_{w,\mathrm{T}_{pe}}$ (a), $\mathrm{T}^{\mathrm{PCA}}_{pe}$ (b) and $d^{\mathrm{PCA}}_{w,\mathrm{T}}$ (c) for the Delayed-VF group (red) and Non-VF group (blue), measured in the first five minutes, 0-5, after the recording onset, at the last five minutes, 5-0, prior the occlusion onset, during occlusion recording at the 1-5, 5-10, 10-15, 15-20, 20-25 five minutes intervals and at the 15-10, 10-5 and 5-0 five minutes intervals prior to VF episode. The black dashed line represents the beginning of balloon inflation and * indicates statistical significance for comparison between groups.

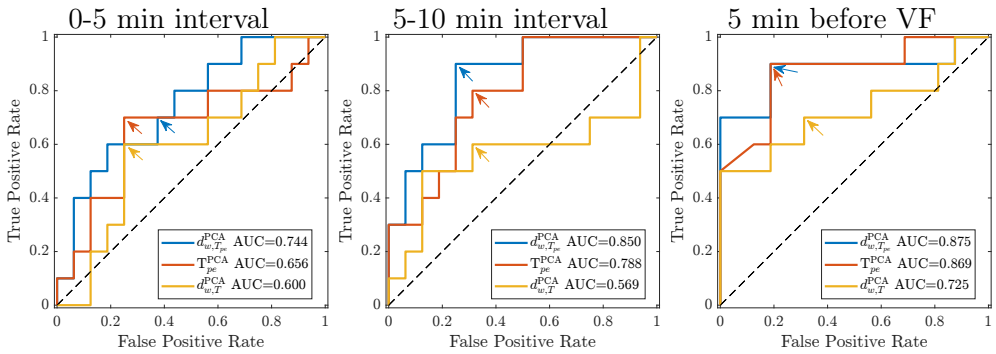
a hazard ratio of 12.5, whereas $\mathrm{T}^{\mathrm{PCA}}_{pe} \geqslant 85.4$ showed a hazard ratio of 5.5, see Table 4.4. The Kaplan–Meier survival functions for $d^{\mathrm{PCA}}_{w,\mathrm{T}_{pe}}$ and $\mathrm{T}^{\mathrm{PCA}}_{pe}$ indices are shown in Figure 4.7. Significant differences in VF occurrence between the group of pigs with $d^{\mathrm{PCA}}_{w,\mathrm{T}_{pe}} \geqslant 20.0$ ms and the group with < 20.0 ms were obtained (Long Rank $p = 0.002$), whereas a $p = 0.016$ was obtained when the index $\mathrm{T}^{\mathrm{PCA}}_{pe}$ was used for classification.

4.4 Discussion

The present study analyzes the behavior of the $d^{\mathrm{PCA}}_{w,\mathrm{T}_{pe}}$ index, restricted from the peak to the end of the T-wave, in a porcine model of prolonged ischemia, and assesses its VF predictive value as ischemia progresses. Changes in T-peak-

Table 4.3: Threshold values together with sensibility and specificity values for VF prediction, and the AUC for $d_{w,\mathrm{T}_{pe}}^{\mathrm{PCA}}$, $\mathrm{T}_{pe}^{\mathrm{PCA}}$ and $d_{w,\mathrm{T}}^{\mathrm{PCA}}$ indices, calculated at three different time intervals.

	$d_{w,\mathrm{T}_{pe}}^{\mathrm{PCA}}$				$\mathrm{T}_{pe}^{\mathrm{PCA}}$				$d_{w,\mathrm{T}}^{\mathrm{PCA}}$			
Intervals	Thresholds (ms)	Se (%)	Sp (%)	AUC	Thresholds (ms)	Se (%)	Sp (%)	AUC	Thresholds (ms)	Se (%)	Sp (%)	AUC
1-5 min	13.4	70.0	62.5	0.74	83.0	70.0	75.0	0.66	67.6	60.0	75.0	0.60
5-10 min	20.0	90.0	75.0	0.85	85.4	80.0	69.0	0.79	57.9	60.0	68.8	0.57
5-0 before VF	22.0	90.0	81.3	0.88	94.7	90.0	81.3	0.87	60.0	70.0	68.8	0.73

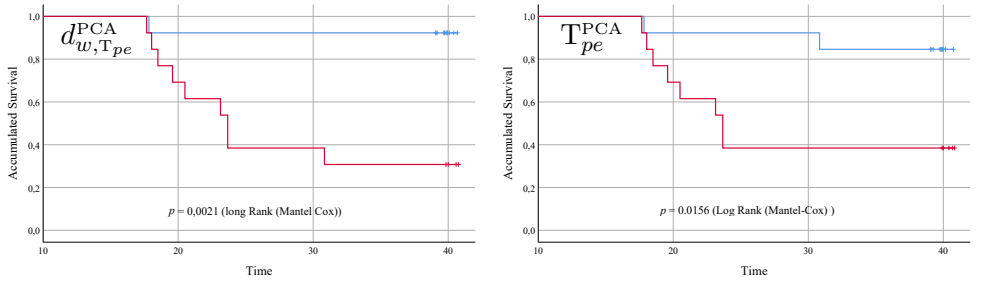


(a) (b) (c)

Figure 4.6: Identification of the optimal $d^{\mathrm{PCA}}_{w,\mathrm{T}_{pe}}$, $\mathrm{T}^{\mathrm{PCA}}_{pe}$ and $d^{\mathrm{PCA}}_{w,\mathrm{T}}$ cut-off values to predict VF during the occlusion. The ROC curve for three intervals: 0-5 minutes (panel (a)) and 5-10 five minutes intervals (panel (b)) after beginning of the occlusion and 5-0 five minutes interval prior to VF episode (panel (c)), are presented. The value of the area under the curve (AUC) is reported at the inside of the panels and the location on the ROC of the optimal thresholds have been marked using color coded arrows.

Table 4.4: Association of $d^{\mathrm{PCA}}_{w,\mathrm{T}_{pe}}$ and $\mathrm{T}^{\mathrm{PCA}}_{pe}$ with the ocurrence of VF episodes.

	Risk Threshold	Hazard ratio (95% CI)	p-value
$d^{\mathrm{PCA}}_{w,\mathrm{T}_{pe}}$	20.0 s	12.5 1.57-99.63	**0.017**
$\mathrm{T}^{\mathrm{PCA}}_{pe}$	85.4 s	5.5 1.16-26.25	**0.032**



(a) (b)

Figure 4.7: Kaplan–Meier survival curves for the pigs with $d^{\mathrm{PCA}}_{w,\mathrm{T}_{pe}} \geqslant 20.0$ ms and $d^{\mathrm{PCA}}_{w,\mathrm{T}_{pe}} < 20.0$ ms (a) and for the pigs with $\mathrm{T}^{\mathrm{PCA}}_{pe} \geqslant 85.4$ and $\mathrm{T}^{\mathrm{PCA}}_{pe} < 85.4$ (b) at the 5-10 minutes interval from the balloon inflation onset. The p value (Long Rank) is indicated.

to-T-end morphology were measured using a time-warping-based morphological assessment methodology, characterizing its time course and comparing it with the classical index, T_{pe}^{PCA}, and the whole T wave, $d_{w,T}^{PCA}$ index. Our main finding is that $d_{w,T_{pe}}^{PCA}$ predicts VF episodes more robustly and strongly than T_{pe}^{PCA} index, whereas $d_{w,T}^{PCA}$ is not able to discriminate pigs with and without VF episodes.

4.4.1 Time-Course of $d_{w,T_{pe}}^{PCA}$

The analysis of the time course of $d_{w,T_{pe}}^{PCA}$ confirmed, as in [230], the ability to reflect the ischemia-induced changes of repolarization dispersion through the monitoring of the morphological variations from the peak to the end of the T wave, avoiding early changes of the T wave under the ischemia-induced ST elevation/depression influence. We demonstrated that $d_{w,T_{pe}}^{PCA}$ showed a stationary behavior during baseline, while larger changes were observed during the 40-min of occlusion. As expected, the intra-recording median value for baseline oscillates in a narrow range while for the occlusion stage, the range is much wider (with median and IQR value 13 times larger than those obtained at baseline). The low values at baseline (non-ischemia conditions) indicate a stable $d_{w,T_{pe}}^{PCA}$ behavior, reflecting just natural ECG beat-to-beat variability.

From the occlusion onset, strong ischemic-induced changes were verified at the T_{pe} waveform, reflected by a well-marked increase trend of the $d_{w,T_{pe}}^{PCA}$ magnitude as the exposure time to ischemia elapses. The changes were greater for the VF-susceptible pigs group than for the pigs who did not suffer VF (see Figure 4.3 and 4.4). It is likely that this marked increase is related to the differential shortening of the repolarization time of the action potential in the ischemic myocardium. These findings are in line with those reported in [217], where they described a marked T_{pe} increase during coronary occlusion as a consequence of the shortening of the Q-to-Tpeak interval, QTc_{peak}, together with moderate changes in the Q-to-Tend interval, QTc, along the whole recording.

The spatial lead-wise profile of $d_{w,T_{pe}}^{L}$, L$\in${V1,...,V6, aVL, I, aVR, II, aVF, III}, analyzed under ischemia showed distinct distributions depending on the occluded artery [230], suggesting a relation with the ischemia location, although the differences in lead profile were not strong. Moreover, there is a gain in delineation robustness when PCA-transformed lead is used. Additionally, this study does not include occlusions in arteries other than LAD, mitigating the possible lead-dependency of results, limited to inter-individual artery tree configuration variability. We have therefore decided to analyze a unique time-warping based index computed from the global PCA-transformed lead instead of from specific leads.

4.4.2 Association with VF Episodes

Both $d^{\mathrm{PCA}}_{w,\mathrm{T}_{pe}}$ and $\mathrm{T}^{\mathrm{PCA}}_{pe}$ indices presented an increasing trend as ischemia progressed. The greatest changes occurred in the first 5 minutes from the beginning of the coronary occlusion, remaining relatively stable thereafter for the Non-VF group and with a higher rate of increase for the Delayed-VF group. The average time course of the $d^{\mathrm{PCA}}_{w,\mathrm{T}_{pe}}$ index denotes a visibly smoother signal trend than for $\mathrm{T}^{\mathrm{PCA}}_{pe}$ index, implying an improved robustness of $d^{\mathrm{PCA}}_{w,\mathrm{T}_{pe}}$ over $\mathrm{T}^{\mathrm{PCA}}_{pe}$ to quantify ischemia-induced repolarization changes, that could be attributed to a more accurate representation of the underlying physiological changes, to higher measurement stability, or to a combination of both factors.

According to the statistical analysis, $d^{\mathrm{PCA}}_{w,\mathrm{T}_{pe}}$ and $\mathrm{T}^{\mathrm{PCA}}_{pe}$ indices captured changes in the T_{pe} interval, and their magnitudes were statistically different between Non-VF and Delayed-VF groups. The fact that $d^{\mathrm{PCA}}_{w,\mathrm{T}_{pe}}$ and $\mathrm{T}^{\mathrm{PCA}}_{pe}$ indices presented significant intergroup differences from the first interval (0-5 min) suggests that both indices are sensitive enough to capture the ischemic-induced VRD changes as soon as blood supply in the artery coronary is compromised. Furthermore, the p-value of the Mann-Whitney test for mean differences was smaller for $d^{\mathrm{PCA}}_{w,\mathrm{T}_{pe}}$ in the intervals presented in Figure 4.5 and Table 4.2, except for a small difference in the 5-minutes interval before VF, supporting the hypothesis that $d^{\mathrm{PCA}}_{w,\mathrm{T}_{pe}}$ is a more robust measure of the changes in the T-peak-to-T-end interval than the $\mathrm{T}^{\mathrm{PCA}}_{pe}$ index for arrhythmia prediction. In contrast, $d^{\mathrm{PCA}}_{w,\mathrm{T}}$ increases since the beginning of the exposure to ischemia and reaches a slightly higher, but not statistically significant, range for the Delayed-VF group than for the Non-VF group at all intervals. The latter confirmed that the first part of the T wave (up to T-peak) negatively influences risk markers and is of no value in discriminating between groups, either because it does not specifically represent ischemia-induced dispersion of repolarization or because ST-segment depression/elevation masks morphological changes related to arrhythmic risk.

As above-mentioned, $d^{\mathrm{PCA}}_{w,\mathrm{T}_{pe}}$ and $\mathrm{T}^{\mathrm{PCA}}_{pe}$ magnitudes increased significantly for the Delayed-VF group with respect to the Non-VF group, allowing us to evaluate them as VF predictors. Both indices distinguished between groups within the last 5 minutes before VF episode interval, always favoring $d^{\mathrm{PCA}}_{w,\mathrm{T}_{pe}}$. Likewise, and more clinically relevant, $d^{\mathrm{PCA}}_{w,\mathrm{T}_{pe}}$ was also able to discriminate between groups already from the prior interval to the arrhythimic window (5-10 min interval), and even for the earlier 0-5 min interval. The AUC for $d^{\mathrm{PCA}}_{w,\mathrm{T}_{pe}}$ was systematically greater than that of the $\mathrm{T}^{\mathrm{PCA}}_{pe}$ index. In brief, a $d^{\mathrm{PCA}}_{w,\mathrm{T}_{pe}}$ increase beyond the cut-off value of 20.0 ms in the early 5-10 min interval from the occlusion onset predicted impending VF episodes with 90.0% of Se and

75.0% of Sp, while a cut-off value of 85.4 ms for T_{pe}^{PCA} index achieved 80.0% of Se and 69.0% of Sp. Moreover, a higher hazard ratio was obtained for $d_{w,T_{pe}}^{PCA}$ (12.5) than for T_{pe}^{PCA} (5.5) by the Cox regression analysis.

We have analyzed and focused on the Delayed-VF episodes, which are believed to have different underlying mechanisms than the early VF [229], and they typically occur after patient's initial interaction with healthcare professionals. According to speed of infarct progression in pigs, which has been estimated to be approximately 7 times faster with respect to that of the humans [231], the analyzed VF in this study corresponds to the arrhythmias reported in humans after around two hours. Therefore, being able to predict Delayed-VF does have a potential clinical significance.

4.4.3 Limitations

In this experimental study, only LAD occlusions were induced, therefore we were not able to evaluate the behavior of $d_{w,T_{pe}}^{PCA}$ with regard to different localization of ischemia, which are known to have also an effect on arrhythmic risk. Another potential issue is the fact that the pigs were anesthetized. Hence, it is crucial to further evaluate the index in high-risk humans population and to exercise caution when extrapolating our findings in pigs to clinical settings.

Other aspect to mention is the need for a T-wave reference when evaluating the risk. This reference, here taken at the first 60 s of baseline stage, may not be available in a clinical setting, requiring alternative ways to obtain it. They could be extracted from prerecorded control ECG recordings, or, when not available, average patterns extracted from large patient libraries, as done in [204].

A further limitation is that Early-VF episodes occurring within the first 10 minutes of occlusion were excluded from the analysis. Consequently, the present findings specifically apply to the delayed arrhythmic phase and cannot be extrapolated to VF occurring during the early phase of acute ischemia. Furthermore, although the anesthetic procedure and the duration and location of the LAD occlusion were standardized across animals, other individual-level data, such as age, sex and weight, as well as the individual extent of the ischemic territory, were not available for the present analysis. Therefore, potential between-group differences in these characteristics could not be assessed. Finally, although between-group differences and associations with VF occurrence were identified, the statistical analyses did not assess whether these findings were independent of potential confounding factors. No multivariable adjustment for baseline characteristics or electrocardiographic variables, such

as age, body weight, resting heart rate or QT_c, was performed, and therefore residual confounding cannot be excluded.

4.5 Conclusions

This chapter showed that the time-warping-based morphology index, $d^{\mathrm{PCA}}_{w,\mathrm{T}_{pe}}$, restricted from the peak to end of T-wave, captures the changes in ischemia-induced ventricular repolarization dispersion. The dynamic increases of $d^{\mathrm{PCA}}_{w,\mathrm{T}_{pe}}$ magnitude beyond certain thresholds predict VF episodes better than $\mathrm{T}^{\mathrm{PCA}}_{pe}$ as ischemia progresses in a myocardial infarction porcine model, supporting further evaluation studies as a non-invasive marker of ischemia-induced arrhythmic risk.

CHAPTER 5

ASSOCIATION BETWEEN T-WAVE PEAK-TO-END MORPHOLOGY CHANGES, QUANTIFIED BY TIME-WARPING, AND VENTRICULAR REPOLARIZATION DISPERSION IN A PORCINE INFARCTION MODEL

5.1 Introduction

5.2 Methods

5.2.1 Experimental Protocol

5.2.2 Intramyocardial Electrograms Processing

5.2.3 ECG Processing

5.2.4 Quantification of T_{pe} Interval Morphology Changes

5.2.5 Statistical Analysis

5.3 Results

5.3.1 VF incidence

5.3.2 Dynamics of $d_{w,T_{pe}}^{PCA}$, DOR, and T_{pe} Along Ischemia

5.3.3 Comparison Between VF and Non-VF Groups

5.3.4 Delayed-VF Risk Prediction Value of $d_{w,T_{pe}}^{PCA}$, DOR and T_{pe}

5.3.5 Linear Regression Analysis Between Indices

5.4 Discussion

5.4.1 Ischemia-Induced Changes in $d_{w,T_{pe}}^{PCA}$, DOR and T_{pe}

5.4.2 Prognostic Value of $d_{w,T_{pe}}^{PCA}$, DOR and T_{pe} for VF Episodes

5.4.3 Limitations

5.5 Conclusions

5.1 Introduction

Ischemia-induced changes in ventricular repolarization play a central role in the development of ventricular arrhythmias, as shown in the previous chapters. Under ischemic conditions, one key factor that increases vulnerability to life-threatening arrhythmias is an increase in dispersion of repolarization (DOR) [232–234]. Increased DOR reflects greater heterogeneity in repolarization timings across myocardial regions, a substrate that facilitates unidirectional conduction block and reentry, thereby leading to the development of VF [232, 233]. This mechanistic link has been consistently demonstrated in experimental studies with animal models [233, 235–237] employing intracardiac recordings, which have established DOR as a robust index of arrhythmic susceptibility.

Despite its well-established physiological basis and predictive value, the measurement of DOR requires direct intracardiac recordings, making it inherently invasive and dependent on specialized equipment and expertise. These constraints limit its applicability to controlled experimental settings or to selected patient populations undergoing invasive electrophysiological procedures, where direct intracardiac recordings are feasible. Consequently, there is a pressing need for non-invasive approaches capable of capturing the same underlying repolarization heterogeneity with sufficient accuracy and robustness [33, 234]. Such alternatives would not only broaden access to arrhythmic-risk assessment in clinical practice, but also facilitate large-scale studies where invasive measurements are not feasible.

In this context, and as discussed in previous chapters, the T_{pe} interval has emerged as a reliable surrogate [234], with a number of experimental, computational, and clinical studies supporting its role in reflecting the magnitude of repolarization dispersion [235, 238, 239] and its dynamics [12], and studying whether it represents transmural, apico-basal, or a combination of the two types of gradients [40, 226, 238]. Importantly, unlike other indices, the applicability of T_{pe} under ischemic conditions is less affected by concomitant ST-segment elevation/depression or global T-wave alterations, further underscoring its translational relevance. However, T_{pe} relies solely on temporal fiducial points and therefore does not account for the full morphological information of the T wave. Moreover, a recent study [240] demonstrated two things undermining T_{pe}: 1) T_{pe} systematically underestimates DOR and (importantly) this underestimation is severalfold greater in ischemia than in normal conditions, and 2) The size of the ischemic area affects the T_{pe}-DOR relationship (especially when T_{pe} is measured in single leads).

Building on this rationale, Chapter 3 assessed the time-warping-based index, $d^{\mathrm{PCA}}_{w,\mathrm{T}_{pe}}$, hypothesized to be a surrogate of repolarization dispersion changes. In humans, this index was able to effectively track morphology changes induced by five minutes of ischemia during PCI [230]. Subsequently, in Chapter 4, as the time frame was extended, we demonstrated its predictive value for VF in a 40-minute closed-chest porcine infarction model [241]. Extending these studies, the present chapter provides a validation framework using an open-chest porcine infarction model with simultaneous surface ECG and intracardiac recordings, allowing DOR computation. We hypothesize that the time-warping-based index, $d^{\mathrm{PCA}}_{w,\mathrm{T}_{pe}}$, can serve as a non-invasive, reliable and robust surrogate of DOR, less sensitive to artifacts and delineation errors than T_{pe}, and we test its predictive value for ventricular fibrillation under ischemia.

5.2 Methods

5.2.1 Experimental Protocol

This study was conducted in domestic pigs (n = 55, weight range 31-46 kg) using an open-chest myocardial infarction model. All experimental procedures conformed to the Guide for the Care and Use of Laboratory Animals (8th Edition, National Academies Press, 2011) and to Directive 2010/63/EU on the protection of animals used for scientific purposes. The protocol was approved by the local ethics committee of the Institute of Physiology of the Komi Science Centre, Russian Academy of Sciences (decision October 10, 2016, amendment May 22, 2019). A detailed description of the surgical preparation has been previously reported in [191] and is briefly summarized below.

Animals received anesthesia with propofol (Norbrook Laboratories Ltd., UK, 1 mg/kg, i.v.), zoletil (Virbac S.A., Carros, France, 10–15 mg/kg, i.m.) and xylazine (Interchemie, Castenray, Netherlands, 0.5 mg/kg, i.m.), followed by intubation and mechanical ventilation. Access to the heart was achieved through a midsternal incision.

Myocardial ischemia was induced by ligation of LCX (n = 10) and LAD coronary artery (n = 45). Following placement of the coronary ligature (not tightened) and intramyocardial leads, the thorax was temporarily closed to allow approximately 30 minutes of stabilization, after which baseline recordings were acquired. Ischemia was then induced by tightening the ligature and the thorax was again reclosed. Recordings were then continuously acquired throughout the occlusion period until either the end of the 40-minute protocol

or immediately after spontaneous VF development. At the end of the experiment, animals were euthanized under deep anesthesia by intravenous potassium chloride.

In summary, intramyocardial electrograms and continuous body surface ECG were recorded simultaneously throughout the protocol. The first ones were acquired using a custom-built recording system (resolution: 16 bit, bandwidth: 0.05-1000 Hz, sampling rate: 4000 Hz) through three flexible plunge electrodes, each bearing 16 recording terminals (48 potential recording sites in total). The electrodes were inserted transmurally in the anterior ventricular region and drawn through the left ventricular free wall, interventricular septum and right ventricular free wall at basal, middle and apical levels, depending on coronary anatomy and surgical access. Intramyocardial electrograms were recorded in unipolar configuration using Wilson's central terminal as reference, while the later were recorded with the KT-07-3/12 system (INCART, St. Petersburg, Russia, sampling rate: 1028 Hz, dynamic range: $\pm$310 mV, 19-bit ADC, amplitude resolution: 1.18 μV per bit).

5.2.2 Intramyocardial Electrograms Processing

Intramyocardial data analysis was carried out at baseline (5 min before occlusion) and at ten discrete time instants, $t \in \mathcal{T}$, with $\mathcal{T} = \{1, 2.5, 5, 10, 15, 20, 25, 30, 35, 40\}$ min during coronary ligation, from raw, unaveraged beats. Only electrograms corresponding to contacts located within the myocardial wall were considered for analysis; contacts lying in the ventricular cavities or in the pericardial space were excluded. For each intramyocardial lead l at each time instant t, end of repolarization time (RT_t^l) was determined as the interval from QRS-complex onset to the point of maximum first derivative of the intramyocardial electrogram voltage signal (dV/dt) within the T wave. For each animal and time instant t, dispersion of repolarization (DOR) was then quantified as the difference between maximal and minimal RTs across all leads,

$$\mathrm{DOR}_t = \max_l\{\mathrm{RT}_t^l\} - \min_l\{\mathrm{R}T_t^l\}. \tag{5.1}$$

The risk of outlier sensitivity from these extreme metrics is mitigated by visual inspection of the delineation marks and chosen due to the reduced available data points, preventing the use of other statistically based metrics.

5.2.3 ECG Processing

The ECG pre-processing and spatial transformation followed the general pipeline described in Chapter 2 and previously applied in Chapters 3 and 4. As in Chapter 4, the PCA transformation was learned from T-wave windows selected during the first minute of the baseline period. The first principal component (PC1) time series was then used for T-wave segmentation and subsequent morphology analysis. Segmented T waves were additionally low-pass filtered using a bidirectional sixth-order Butterworth filter with a 20-Hz cut-off frequency before marker computation.

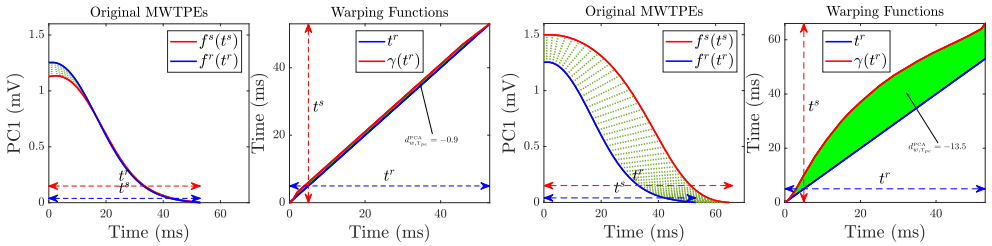
5.2.4 Quantification of T_{pe} Interval Morphology Changes

In this study, dynamic changes in T_{pe} morphology were quantified using the warping-based index derived from the PC1, $d^{\mathrm{PCA}}_{w,\mathrm{T}_{pe}}$. The full methodological description was described in Chapter 2 and applied in Chapter 4. In summary, throughout each ECG recording, 15-second sliding windows (with 10-second overlap) were selected. Within each s-th window, the $d^{\mathrm{PCA}}_{w,\mathrm{T}_{pe}}$ index was computed from the temporal reparametrization (warping) between each window MWTPE $\boldsymbol{f}^s(\boldsymbol{t}^s)$ and the reference MWTPE $\boldsymbol{f}^r(\boldsymbol{t}^r)$ thereby obtaining a $d^{\mathrm{PCA}}_{w,\mathrm{T}_{pe}}$ value per each s-th sliding window.

In this study, $d^{\mathrm{PCA}}_{w,\mathrm{T}_{pe}}$ was computed using the signed time-warping-based formulation, as detailed in Section 2.3.2, allowing the index to retain not only the magnitude of the temporal reparameterization but also its predominant direction relative to the reference. Positive and negative values summarize the net direction of the temporal reparameterization relative to the reference waveform. Accordingly, positive values reflect that aligning MWTPE $\boldsymbol{f}^s$ with MWTPE $\boldsymbol{f}^r$ requires temporal stretching, whereas negative values correspond to a shrinking with respect to the reference waveform. After computing the full $d^{\mathrm{PCA}}_{w,\mathrm{T}_{pe}}$ series, the values corresponding to the set of predefined analysis time instants, $\mathcal{T}$, were selected to ensure comparability between ECG and intramyocardial measures.

An illustrative example of the warping process at two different stages is shown in Figure 5.1, corresponding to baseline (5 min before occlusion onset) and to 5 min after ischemia onset. In each case, the left panels show the original reference and studied MWTPE waveforms and how temporal samples must be non-uniformly shifted to achieve alignment, whereas the right panels show the corresponding warping function. Note that the proposed $d^{\mathrm{PCA}}_{w,\mathrm{T}_{pe}}$ index does not reflect a simple uniform stretching/shrinking, but the overall amount

of warping required to match both waveforms.



(a) (b)

Figure 5.1: Time-warping analysis underlining the calculation of $d^{\mathrm{PCA}}_{w,\mathrm{T}_{pe}}$ index for a particular pig at two moments of the protocol: (a) baseline (at 5 min before occlusion onset) and (b) at 5 min after ischemia onset. In each panel, the left subpanel shows the reference MWTPE $\boldsymbol{f}^r$ (blue) and the study MWTPE $\boldsymbol{f}^s$ (red), showing the non-uniform temporal reparametrization required for alignment. The right subpanels displays the corresponding optimal warping function $\gamma^*(\boldsymbol{t}^r)$ (red) relative to the reference $\boldsymbol{t}^r$ (blue). The green shaded area represents the amount of warping quantified by $d^{\mathrm{PCA}}_{w,\mathrm{T}_{pe}}$ index.

The T_{pe} interval was additionally computed to provide a classical reference for comparison with the warping-based index. For each i-th beat in the PCA transformed lead, $\mathrm{T}_{pe}(i)$ was defined as in Section 2.2. A sliding-window median filter (15-second length, 5-second overlap) was then applied to the T_{pe} series to obtain temporal resolution equivalent to that of the $d^{\mathrm{PCA}}_{w,\mathrm{T}_{pe}}$ series. Finally, values corresponding to the predefined time instants, $\mathcal{T}$, were also selected.

To enable a complementary, pre-event aligned comparison across animals, two additional measurements were selected immediately before VF onset in animals that developed VF. These were taken from the 0-5 min and 5-10 min intervals preceding the VF episode. In non-VF animals, the same reference points were aligned to a fixed time (27:10 min from occlusion onset), chosen as the median time to VF among VF-susceptible pigs, ensuring comparability across groups.

5.2.5 Statistical Analysis

The analysis of ischemia-induced changes was conducted by assessing the temporal evolution of $d^{\mathrm{PCA}}_{w,\mathrm{T}_{pe}}$, T_{pe} and DOR indices throughout the time instants, $\mathcal{T}$, defined above during baseline and coronary occlusion. These values aligned with the onset of coronary occlusion, as well as those including the two

pre-event evaluation points described above, were compared between the two pig groups. Data normality was assessed using the Shapiro-Wilk test. To ensure a consistent statistical framework across indices and time points, pointwise inter-group comparisons were performed using the Mann-Whitney U test, with significance set at $p \leqslant 0.05$. Data are summarized as median and interquartile range.

Statistical parametric mapping (SPM) [242] was used to assess whether the temporal trajectories of the indices differed between groups accounting for the temporal dependence between consecutive observations and allowing the identification of time intervals over which inter-group difference exceed the critical statistical threshold. This analysis was performed over the early common time window (Baseline, 1, 2.5, 5, 10, and 15 min), thereby avoiding the unequal temporal coverage resulting from the variable timing of VF occurrence across animals.

Linear regression analyses were performed individually for each pig to assess the relationship between $d^{\mathrm{PCA}}_{w,\mathrm{T}_{pe}}$ and DOR across time, and also between T_{pe} and DOR. From each fit, the slope and coefficient of determination (R^2) were obtained to characterize population-level tendencies and to compare Delayed-VF and Non-VF groups.

The association between the indices and VF risk was further examined using ROC curves at each of the 10 predefined time points. Optimal thresholds for each index were determined as the point minimizing the Euclidean distance to the upper left corner of the ROC space, and corresponding sensitivity and specificity values were then reported. Differences between AUCs were assessed using DeLong's test for correlated ROC curves. Accordingly, Cox proportional hazards models and Kaplan–Meier survival analysis were applied to access and compare their predictive performance, with hazard ratios (HRs) and 95% confidence intervals estimated for the occurrence of time-dependent VF episodes. All analyses were performed in MATLAB (R2023a, MathWorks, USA).

5.3 Results

5.3.1 VF incidence

From the the total study population, 29 animals developed VF during coronary occlusion, while 26 pigs did not have any VF episode. VF cases were further clustered into Early-VF (15 cases) and Delayed-VF episodes (14 cases), depending on whether they ocurred before of after the 10th minute from is-

chemia onset, a classification consistent with previously reported studies [229]. No follow up on VF evolution/termination is performed. Details of the distribution are provided in Table 5.1. In line with prior evidence suggesting distinct underlying mechanisms for each subset [228,229], and considering that ischemic injury in humans develops several-fold more slowly than in experimental models [231], only Delayed-VF episodes were included for analyses as those are more clinically relevant and interesting to be predicting, allowing sufficient reaction time after occlusion in real-life settings. This approach, consistent with the study in Chapter 4, led to the exclusion of early VF cases in the analysis.

Table 5.1: Distribution of VF incidence by groups

Group	Subgroup	Pigs	VF event onset time mean [range] (min:s)
Non-VF	-	26	-
VF	Early-VF	15	3:16 [1:00-8:30]
	Delayed-VF	14	27:10 [18:00-41:00]

5.3.2 Dynamics of $d^{\mathrm{PCA}}_{w,\mathrm{T}_{pe}}$, DOR, and T_{pe} Along Ischemia

Alterations in the T-peak-to-end waveform were quantified by the $d^{\mathrm{PCA}}_{w,\mathrm{T}_{pe}}$ index, which showed a decreasing negative trend shortly after the onset of occlusion. An illustrative time course of $d^{\mathrm{PCA}}_{w,\mathrm{T}_{pe}}$ throughout baseline and coronary occlusion is presented in Figure 5.2 for two representative pigs, one that developed VF and one that remained VF-free. To illustrate the dynamics of the indices, DOR values from intramyocardial leads and the corresponding $d^{\mathrm{PCA}}_{w,\mathrm{T}_{pe}}$ values at the predefined $\mathcal{T}$ time instants are annotated along the time axis. During baseline and the first minutes of the ischemia, $d^{\mathrm{PCA}}_{w,\mathrm{T}_{pe}}$ values remained close to zero, while DOR showed the smaller dispersion values. Following coronary occlusion, $d^{\mathrm{PCA}}_{w,\mathrm{T}_{pe}}$ magnitude for the pig that developed VF progressively decreased to more negative values, indicating T-peak-to-end widening from the reference, whereas DOR values steadily increased during ischemia. In contrast, both $d^{\mathrm{PCA}}_{w,\mathrm{T}_{pe}}$ and DOR showed relatively stable trends for the pigs that did not develop VF. In this example, $d^{\mathrm{PCA}}_{w,\mathrm{T}_{pe}}$ values ranged from -0.5 to -20.9 ms in the VF pig and from 0.3 to 2.6 ms in the Non-VF pig, while the corresponding DOR values spanned from 42 to 159 and 42.5 to 110.3 ms, respectively.

Across the entire study cohort, all three indices ($d^{\mathrm{PCA}}_{w,\mathrm{T}_{pe}}$, DOR and T_{pe}) remained relatively stable at baseline, with median [IQR] values centered at

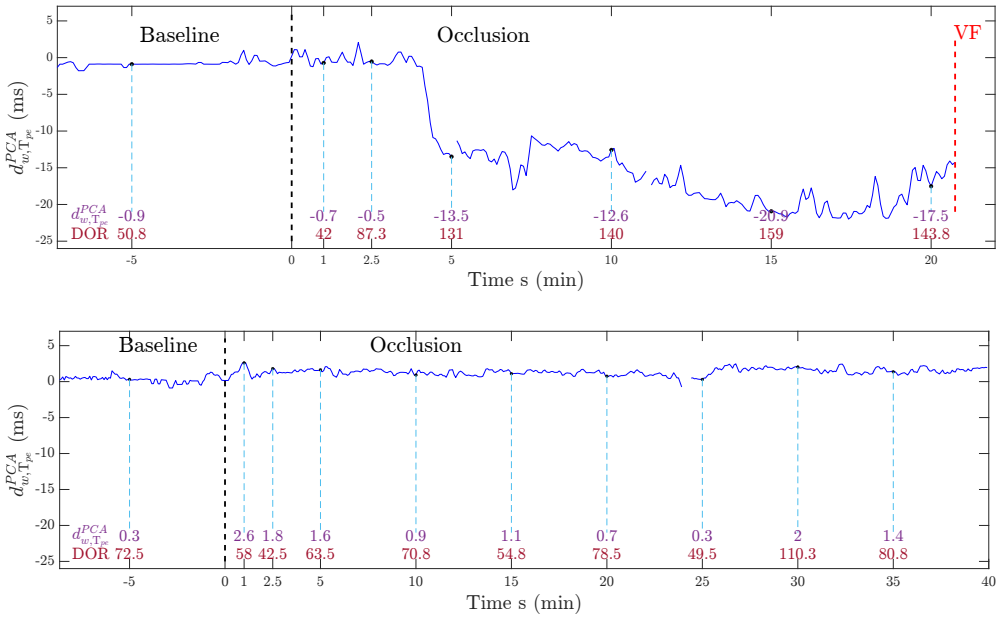


Figure 5.2: Representative time course of $d^{\mathrm{PCA}}_{w,\mathrm{T}_{pe}}$ index during baseline and coronary occlusion for two pigs, one that developed VF (top panel) and one that remained VF-free (bottom panel). The black dashed line marks the onset of occlusion, and the red dashed line the occurrence of VF event. At the predefined study instants $t \in \mathcal{T}$ (blue dashed lines), both the $d^{\mathrm{PCA}}_{w,\mathrm{T}_{pe}}$ (purple) and the DOR (dark red) values (both in ms) are indicated.

zero for $d^{\mathrm{PCA}}_{w,\mathrm{T}_{pe}}$ and low dispersion for DOR and T_{pe} indices, see Table 5.2. A few animals exhibited slight drifts at the predefined time point of 5 minutes before occlusion onset, likely related to technical manipulations preceding occlusion. In contrast, pronounced ischemia-induced changes were observed after coronary ligation, with $d^{\mathrm{PCA}}_{w,\mathrm{T}_{pe}}$ values progressively shifting toward more negative magnitudes, while DOR and T_{pe} showed a marked increase. Median [IQR] values at two representative time points during the occlusion, early (5 min) and later (20 min) after occlusion onset, are given in Table 5.2, reflecting substantial repolarization changes across most animals.

5.3.3 Comparison Between VF and Non-VF Groups

From the beginning of coronary occlusion, all three indices exhibited similar but opposite trends, with $d^{\mathrm{PCA}}_{w,\mathrm{T}_{pe}}$ decreasing while DOR and T_{pe} increased. In the Delayed-VF group, $d^{\mathrm{PCA}}_{w,\mathrm{T}_{pe}}$ values progressively shifted toward more neg-

Table 5.2: Values of the indexes across the cohort, median [IQR] (ms) in baseline and occlusion period

Index	Baseline	Occlusion	
		5 min	20 min
$d^{\mathrm{PCA}}_{w,\mathrm{T}_{pe}}$	0 [4.1]	-3.3 [14.5]	-5.31 [20.3]
DOR	80.8 [40.4]	122.5 [51.7]	146.0 [56.2]
T_{pe}	56.0 [9.5]	59.0 [16.0]	62.0 [27.0]

ative magnitudes, while DOR and T_{pe} values steadily increased, in contrast to the relatively stable patterns observed in Non-VF animals. Figure 5.3 depicts the distribution of $d^{\mathrm{PCA}}_{w,\mathrm{T}_{pe}}$, DOR and T_{pe} values at baseline (5 min before occlusion onset) and throughout coronary occlusion at predefined time instants, $\mathcal{T}$, for both the Delayed-VF and Non-VF groups. For comparative purposes, two additional measurements were included, either immediately preceding VF onset (taken from 0–5 and 5–10 min intervals before VF event or before 27:10 in the animals without VF). The corresponding median [IQR] values and Mann–Whitney p-values are summarized in Table 5.3.

At baseline, all three indices exhibited comparable distributions between Delayed-VF and Non-VF pigs, with no significant differences. However, during occlusion, group separation rapidly emerged. Significant differences in $d^{\mathrm{PCA}}_{w,\mathrm{T}_{pe}}$ were already present at 1 min after coronary occlusion ($p = 0.026$) and persisted at subsequent time points, with median values becoming progressively more negative in the Delayed-VF group. Note that negative $d^{\mathrm{PCA}}_{w,\mathrm{T}_{pe}}$ values indicate an expansion of the T_{pe} interval relative to the reference waveform, requiring a temporal shrinking for alignment, thus concordant with T_{pe} prolongation and increased DOR. For DOR, differences reached significance from 2.5 min onwards ($p = 0.014$) and remained elevated in the Delayed-VF group throughout ischemia. Importantly, and in contrast to the earlier changes in $d^{\mathrm{PCA}}_{w,\mathrm{T}_{pe}}$ and DOR, T_{pe} index reached significance only at 5 min, remaining significant thereafter at most time points, except at 20 and 30 min. Notably, at all time instants but 10 min, $d^{\mathrm{PCA}}_{w,\mathrm{T}_{pe}}$ yielded smaller p-values than T_{pe}, indicating greater sensitivity of $d^{\mathrm{PCA}}_{w,\mathrm{T}_{pe}}$ to the ischemia-induced changes in the T wave. The divergence between groups was particularly emphasized at 5, 10, and 15 minutes, which were selected as representative time points for subsequent survival and risk prediction analyses.

Importantly, taking the VF onset as reference, $d^{\mathrm{PCA}}_{w,\mathrm{T}_{pe}}$, DOR and T_{pe} displayed marked inter-group divergence at the times from 0–5, and 5-10, min

Table 5.3: Medians and p-values at specific time points for $d^{\mathrm{PCA}}_{w,\mathrm{T}_{pe}}$, DOR and T_{pe} indices stratified by delayed-VF susceptibility. For Non-VF animals, the two last measurements were taken considering 27:10 min from occlusion onset as the reference.

Time t	N	$d^{\mathrm{PCA}}_{w,\mathrm{T}_{pe}}$			DOR			T_{pe}		
		Non-VF	Delayed-VF	p-value	Non-VF	Delayed-VF	p-value	Non-VF	Delayed-VF	p-value
5 min before occl	26/14	0 [3.9]	0 [4.0]	0.4098	80.8 [40.5]	80.8 [43.6]	0.9643	55.5 [12.0]	56.0 [10.5]	0.5709
1 min	26/14	1.4 [6.1]	-7.6 [11.0]	**0.0264**	81.0 [44.5]	111.8 [56.2]	0.1978	54.0 [7.5]	60.0 [19.0]	0.2422
2.5 min	26/14	0 [7.0]	-12.9 [19.1]	**0.0011**	81.0 [67.4]	131.5 [62.3]	**0.0143**	56.0 [10.8]	68.0 [29.5]	0.0643
5 min	26/14	-1.9 [7.7]	-12.9 [19.1]	**0.0003**	110.8 [68.4]	147.9 [69.0]	**0.0025**	56.0 [8.5]	70.0 [24.5]	**0.0043**
10 min	26/14	-1.4 [8.1]	-15.3 [16.2]	**0.0019**	127.5 [53.9]	188.0 [57.8]	**0.0006**	56.0 [13.0]	73.5 [23.0]	**0.0017**
15 min	26/14	-0.3 [7.8]	-20.3 [19.4]	**0.0041**	128.0 [63.7]	209.5 [81.0]	**0.0008**	56.0 [15.3]	78.0 [27.0]	**0.0052**
20 min	26/11	0 [10.40]	-18.3 [14.6]	**0.0043**	139.7 [57.9]	198.8 [80.2]	**0.0029**	57.0 [24.0]	74.0 [24.0]	0.0765
25 min	26/9	-1.4 [9.2]	-23.8 [18.9]	**0.0076**	145.5 [64.7]	216.1 [137.3]	**0.0246**	56.0 [15.3]	84.0 [37.0]	**0.0114**
30 min	26/5	-1.1 [12.0]	-17.1 [28.8]	**0.0315**	144.4 [69.8]	219.7 [87.2]	0.0941	56.0 [17.0]	69.8 [42.3]	0.3054
35 min	26/3	0.2 [8.9]	-15.1 [10.0]	**0.0171**	140.5 [87.2]	221.0 [70.5]	0.0540	56.0 [12.3]	76.0 [15.0]	0.0649
5-10 min before VF	26/14	0 [10.4]	-19.6 [15.8]	**0.0110**	139.7 [57.9]	214.8 [84.0]	**0.0022**	57.0 [24.0]	80.0 [30.0]	**0.0143**
0-5 min before VF	26/14	-1.4 [9.2]	-17.1 [25.3]	**0.0036**	145.5 [64.7]	198.8 [79.8]	**0.0088**	56.0 [15.3]	76.0 [37.6]	**0.0422**

Bold values indicate significance, $p < 0.05$.

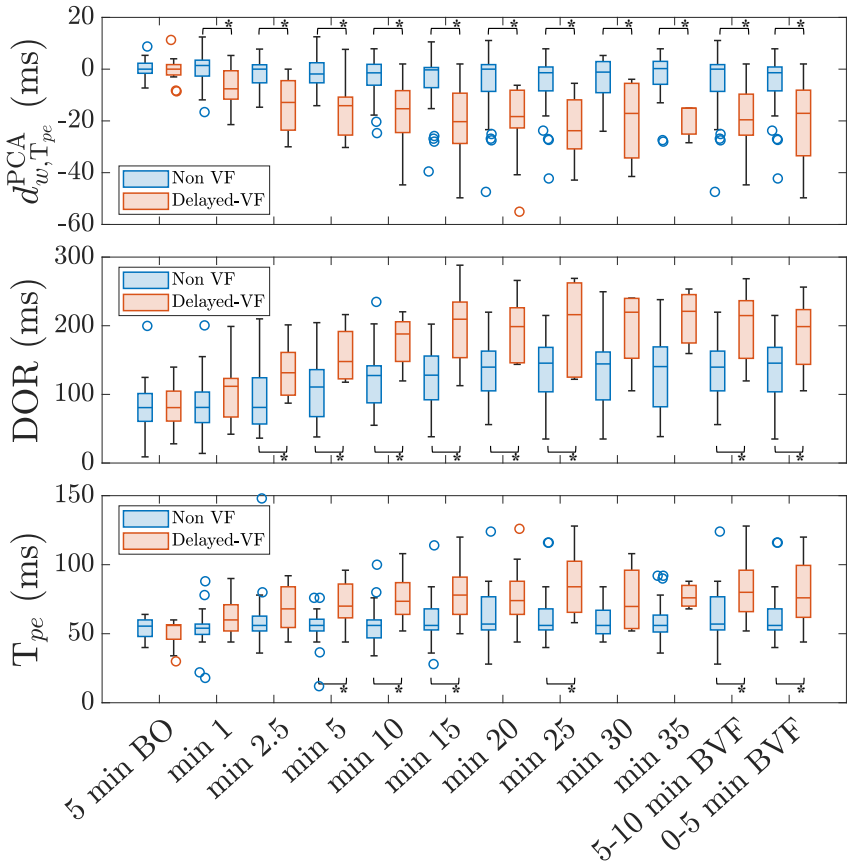


Figure 5.3: Boxplots distribution of $d^{\mathrm{PCA}}_{w,\mathrm{T}_{pe}}$, DOR and T_{pe} values at predefined time points, shown for the delayed-VF group (red) and the Non-VF group (blue). Specific time points were at baseline (5 min before occlusion onset), during coronary occlusion (at 1, 2.5, 5, 10, 15, 20, 25, 30, 35, and 40 min), and immediately before VF onset (at points from 0–5 and 5–10 min intervals prior to VF). In Non-VF pigs, these two additional reference measurements were taken with respect to 27:10 min from occlusion onset. BO and BVF denote before occlusion onset and before VF onset, respectively. * indicates statistical significance for comparison between groups.

before VF, see Table 5.3.

The complementary SPM analysis, shown in Figure 5.4, identified significant temporal clusters for all three indices. Specifically, DOR and T_{pe} values were higher in the Delayed-VF group than in the Non-VF group ($p = 0.006$ and 0.002, respectively) and $d^{\mathrm{PCA}}_{w,\mathrm{T}_{pe}}$ values were lower in the Delayed-VF group ($p < 0.001$). This analysis confirmed sustained temporal differences between groups while accounting for temporal dependence across consecutive time points.

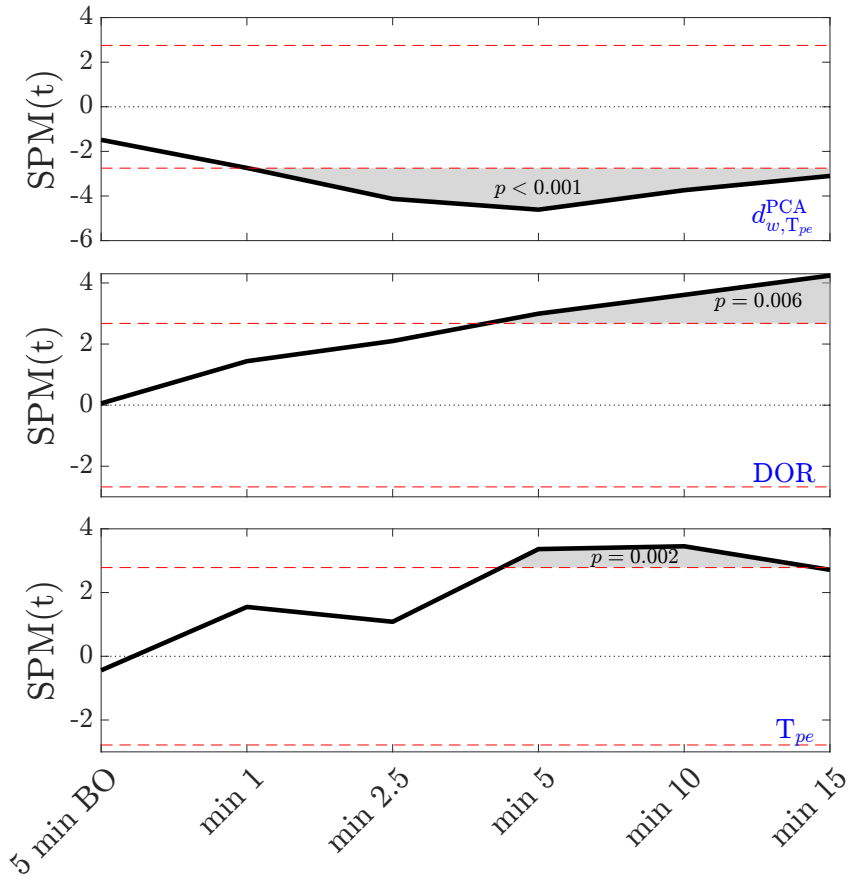
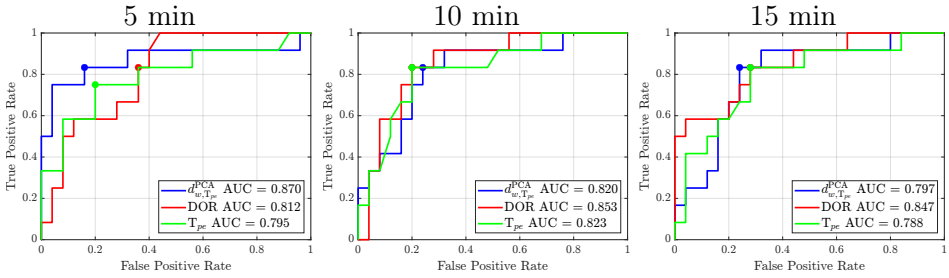


Figure 5.4: SPM results for the comparison between Delayed-VF and Non-VF groups over the time window (5 min before occlusion, 1, 2.5, 5, 10, and 15 min after occlusion onset) for $d^{\mathrm{PCA}}_{w,\mathrm{T}_{pe}}$, DOR and T_{pe}. The solid black curve represents the SPM(t) statistic, and the dashed red lines indicate the critical threshold for statistical significance. Significant temporal clusters are highlighted in gray, with the corresponding cluster-level p-values reported in each panel. BO denotes before occlusion onset.

5.3.4 Delayed-VF Risk Prediction Value of $d^{\mathrm{PCA}}_{w,\mathrm{T}_{pe}}$, DOR and T_{pe}

ROC analysis was performed to assess the predictive performance of $d^{\mathrm{PCA}}_{w,\mathrm{T}_{pe}}$, DOR and T_{pe} indices at representative ischemic time points $t \in \{5, 10, 15\}$ minutes after occlusion, as shown in Figure 5.5 and detailed in Table 5.4. At 5 minutes, $d^{\mathrm{PCA}}_{w,\mathrm{T}_{pe}}$ showed a numerically higher AUC than DOR and T_{pe} indices, whereas at 10 and 15 minutes the three indices reached comparable discriminatory capacity, with DOR reaching the highest performance (Table 5.4). De-

Long's test for correlated ROC curves indicated that AUC differences were not statistically significant at 5, 10, and 15 minutes. Overall, these results highlight the ability of the three indices to discriminate VF susceptibility, with $d^{\mathrm{PCA}}_{w,\mathrm{T}pe}$ showing earlier sensitivity while DOR and T_{pe} maintained stable performance at later stages.



(a) (b) (c)

Figure 5.5: ROC analysis for delayed-VF risk prediction of $d^{\mathrm{PCA}}_{w,\mathrm{T}_{pe}}$, DOR and T_{pe} indices at t of 5 (a), 10 (b), and 15 (c) minutes after coronary occlusion. Optimal cut-off values for delayed-VF prediction are marked on the plot. The AUC is also indicated.

Survival analyses were conducted to further evaluate the prognostic value of $d^{\mathrm{PCA}}_{w,\mathrm{T}_{pe}}$, DOR and T_{pe}. Figure 5.6 shows the Kaplan–Meier curves stratified by the optimal cut-off values identified in the ROC analysis, while Table 5.5 summarizes the corresponding Cox regression outcomes. At 5 minutes after occlusion, $d^{\mathrm{PCA}}_{w,\mathrm{T}_{pe}}$ values below –8.0 ms were associated with a markedly increased of delayed-VF risk (HR = 11.95, 95% CI: 2.60–54.97, $p = 0.0015$), compared to pigs with higher values. This association is less marked for T_{pe} and surprisingly also for DOR at that time point. At 10 and 15 minutes, all three indices showed comparable associations with increased VF risk (HR range 7.65–10.21; p-values from 0.0028 to 0.0088), see Table 5.5. Kaplan–Meier survival curves stratified by these thresholds diverged significantly between groups at 5, 10, and 15 minutes, with log-rank p-values of 0.0001, 0.0007, and 0.0007 for $d^{\mathrm{PCA}}_{w,\mathrm{T}_{pe}}$, 0.0092, 0.0004, and 0.0019 for DOR, and 0.0016, 0.002 and 0.0019 for T_{pe}, respectively. These results are consistent with the Cox regression results summarized in Table 5.5.

5.3.5 Linear Regression Analysis Between Indices

Linear regression analyses were also conducted to evaluate the direct association between $d^{\mathrm{PCA}}_{w,\mathrm{T}_{pe}}$ and DOR, and between T_{pe} and DOR, measured in time instants $t \in \mathcal{T}$. Slopes and coefficients of determination (R^2) obtained for each

Table 5.4: ROC-derived threshold values, sensitivity, specificity, and AUC for delayed-VF prediction using $d^{\mathrm{PCA}}_{w,\mathrm{T}_{pe}}$, DOR and T_{pe} indices, calculated at $t \in \{5, 10, 15\}$ minutes after coronary occlusion. p-values from DeLong's test for correlated ROC curves are also reported for the comparisons $d^{\mathrm{PCA}}_{w,\mathrm{T}_{pe}}$ vs DOR and $d^{\mathrm{PCA}}_{w,\mathrm{T}_{pe}}$ vs T_{pe}

Time (t)	$d^{\mathrm{PCA}}_{w,\mathrm{T}_{pe}}$				DOR				T_{pe}				p-value	
	Thr. (ms)	Se (%)	Sp (%)	AUC	Thr. (ms)	Se (%)	Sp (%)	AUC	Thr. (ms)	Se (%)	Sp (%)	AUC	$d^{\mathrm{PCA}}_{w,\mathrm{T}_{pe}}$ vs DOR	$d^{\mathrm{PCA}}_{w,\mathrm{T}_{pe}}$ vs T_{pe}
5 min	-8.0	83.3	84.0	0.870	122.5	83.3	64.0	0.812	64.0	75.0	80.0	0.795	0.5089	0.0710
10 min	-7.1	83.3	76.0	0.820	146.4	83.3	80.0	0.853	64.0	83.3	80.0	0.823	0.6736	0.9093
15 min	-7.9	83.3	76.0	0.797	148.0	83.3	72.0	0.847	64.0	83.3	72.0	0.788	0.4680	0.7977

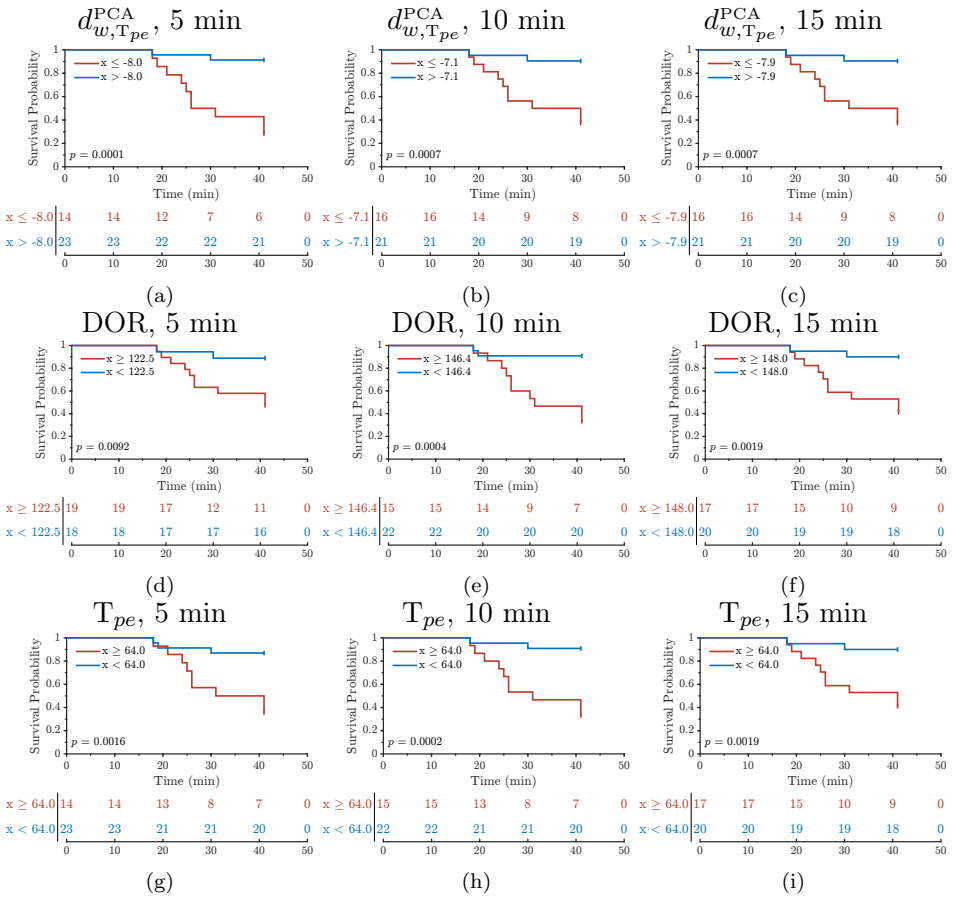


Figure 5.6: Kaplan-Meier survival curves for VF occurrence based on thresholds derived from ROC analysis. Panels (a–c) show survival probabilities stratified by $d^{\mathrm{PCA}}_{w,\mathrm{T}_{pe}}$ at 5, 10, and 15 minutes after coronary occlusion, respectively. Panels (d–f) and (g-i) depict the corresponding results at the same time points for DOR and T_{pe}, respectively. Threshold values are indicated within each plot, and Log-Rank p-values are reported.

animal were summarized at the group level (Table 5.6). For the overall population, the median [IQR] slope with a low median [IQR] R^2 reflects considerable variability, see Table 5.6. When stratified by VF susceptibility, the Delayed-VF group exhibited a more consistent negative relationship (higher absolute slope values) with also higher R^2 values, whereas the Non-VF group showed negligible association with low slope and R^2 values. Interestingly, R^2 between $d^{\mathrm{PCA}}_{w,\mathrm{T}_{pe}}$ and DOR is higher than the one between T_{pe} and DOR, suggesting that $d^{\mathrm{PCA}}_{w,\mathrm{T}_{pe}}$ tracks repolarization heterogeneity more faithfully.

Table 5.5: Cox regression results for delayed-VF stratification by $d^{\mathrm{PCA}}_{w,\mathrm{T}_{pe}}$, DOR and T_{pe} indices at 5, 10, and 15 minutes after occlusion, including ROC-derived thresholds, hazard ratios, 95% CI, and p-values

Index	Time t	Risk Threshold	Hazard ratio	95% CI	p-value
$d^{\mathrm{PCA}}_{w,\mathrm{T}_{pe}}$	5 min	-8.0	11.95	2.60-54.97	**0.0015**
	10 min	-7.1	8.81	1.92-40.41	**0.0051**
	15 min	-7.9	8.81	1.92-40.41	**0.0051**
DOR	5 min	122.5	5.86	1.28-26.81	**0.0227**
	10 min	146.4	9.53	2.07-43.81	**0.0038**
	15 min	148.0	7.65	1.67-35.08	**0.0088**
T_{pe}	5 min	64.0	6.25	1.68-23.21	**0.0062**
	10 min	64.0	10.21	2.22-46.9	**0.0028**
	15 min	64.0	7.65	1.67-35.1	**0.0088**

Bold values indicate significance, $p < 0.05$.

Table 5.6: Slope and R^2 for $d^{\mathrm{PCA}}_{w,\mathrm{T}_{pe}}$ vs. DOR and T_{pe} vs. DOR; median [IQR] across pigs

Group	$d^{\mathrm{PCA}}_{w,\mathrm{T}_{pe}}$ and DOR		T_{pe} and DOR	
	Slope	R^2	Slope	R^2
All population	-1.81 [5.08]	0.07 [0.43]	0.89 [2.97]	0.06 [0.27]
Delayed-VF	-2.72 [3.63]	0.33 [0.49]	2.12 [1.99]	0.16 [0.35]
Non-VF	-0.80 [5.60]	0.01 [0.28]	0.06 [3.19]	0.04 [0.22]

5.4 Discussion

In this chapter we analyze the performance of the warping-based index $d^{\mathrm{PCA}}_{w,\mathrm{T}_{pe}}$ as a non-invasive surrogate of ventricular repolarization dispersion, through its direct comparison with invasively measured DOR in an open-chest porcine model of acute myocardial infarction, with the classical T_{pe} interval included for benchmarking. Our main findings were that all three indices discriminated between the Delayed-VF and Non-VF groups after the onset of coronary occlusion, with $d^{\mathrm{PCA}}_{w,\mathrm{T}_{pe}}$ providing a stronger and earlier separation than T_{pe}. Risk analysis demonstrated that these indices also provided significant predictive ability for VF occurrence at multiple time points. In addition, regression analysis showed that the relationship between $d^{\mathrm{PCA}}_{w,\mathrm{T}_{pe}}$ and DOR was more consistent

in VF-susceptible animals. This association was stronger than the corresponding relationship between T_{pe} and DOR, underscoring the value of $d^{\mathrm{PCA}}_{w,T_{pe}}$ as delayed-VF non-invasive risk predictor in contrast to the invasive nature of DOR.

5.4.1 Ischemia-Induced Changes in $d^{\mathrm{PCA}}_{w,T_{pe}}$, DOR and T_{pe}

The time course of $d^{\mathrm{PCA}}_{w,T_{pe}}$ index observed in this study is well aligned with prior observations in a similar study [241]. By concentrating on T-peak–to-end morphology, we show that the index $d^{\mathrm{PCA}}_{w,T_{pe}}$ correlates with the ischemia-induced changes in repolarization dispersion as measured by DOR. At baseline, $d^{\mathrm{PCA}}_{w,T_{pe}}$, DOR and T_{pe} remained relatively stable along time, just reflecting the spontaneous variability, together with the measurement inaccuracies, of repolarization dispersion across beats. Following coronary occlusion, however, these indices showed systematic changes over time: $d^{\mathrm{PCA}}_{w,T_{pe}}$ progressively decreased to more negative values, in parallel to an increase of the T_{pe} interval relative to baseline, whereas DOR and T_{pe} increased steadily, denoting greater dispersion of repolarization across myocardial regions. The trends were particularly pronounced in animals that later developed VF, indicating that ischemia accentuates repolarization heterogeneity in a manner linked to arrhythmic susceptibility. Comparable time-dependent patterns have been reported in porcine infarction models [235–237], where ischemia augments repolarization dispersion and predisposes to VF.

The growing differentiation between the Delayed-VF and Non-VF groups (see Figure 5.3) aligns with the established role of increased repolarization dispersion in creating an arrhythmogenic substrate. Enhanced heterogeneity facilitates unidirectional block and re-entry, thereby predisposing the myocardium to malignant rhythms under ischemic stress [211, 217, 234]. DOR, quantified from intracardiac electrograms, has long been regarded as a robust invasive marker of such electrical instability. The way $d^{\mathrm{PCA}}_{w,T_{pe}}$ tracked ischemia-induced changes in repolarization, highly correlated with DOR, supports its mechanistic link to repolarization heterogeneity and underscores its potential as a physiologically grounded non-invasive surrogate of the invasive DOR.

Notably, $d^{\mathrm{PCA}}_{w,T_{pe}}$ not only differentiated the Delayed-VF and Non-VF groups more strongly, but also did so earlier than T_{pe}. We attribute this to its sensitivity to distributed morphological changes throughout the T_{pe} interval, whereas T_{pe} captures only the information condensed in a single duration measure. This advantage echoes our previous findings, where $d^{\mathrm{PCA}}_{w,T_{pe}}$ outperformed T_{pe} during ischemia in a closed-chest porcine model [241], thus reinforcing the value of

$d^{\mathrm{PCA}}_{w,\mathrm{T}_{pe}}$ to specifically represent the DOR induced by ischemia.

The overall temporal pattern observed in this study was further supported by the complementary SPM analysis (see Figure 5.4), which identified sustained inter-group differences in the temporal evolution of the indices, while accounting for temporal dependence between consecutive time points. Importantly, the significant $d^{\mathrm{PCA}}_{w,\mathrm{T}_{pe}}$ cluster showed the same direction of change as that observed throughout the study, reinforcing the association between lower values in Delayed-VF animals and greater repolarization dispersion during induced ischemia.

5.4.2 Prognostic Value of $d^{\mathrm{PCA}}_{w,\mathrm{T}_{pe}}$, DOR and T_{pe} for VF Episodes

The evaluation of VF prediction in this open-chest porcine model revealed that the three indices consistently discriminated between delayed-VF susceptible and non-susceptible animals across representative time points. ROC analysis demonstrated significant discriminatory capacity, with $d^{\mathrm{PCA}}_{w,\mathrm{T}_{pe}}$ achieving even higher sensitivity at 5 minutes, while maintaining comparable performance with DOR and T_{pe} at later stages. These findings indicate that ischemia-induced modifications of the T_{pe} waveform morphology conveys comparable discriminatory ability to that of directly measured DOR, reflecting transmural, apico-basal or a global dispersion of the cardiac repolarization.

Survival analyses further strengthened this evidence. Cox regression models confirmed significant associations of these indices with delayed-VF risk, with hazard ratios ranging from 5.86 to 11.95 across time points (Table 5.5), while Kaplan–Meier survival curves (Figure 5.6) showed clear separation between groups stratified by the ROC-derived thresholds at 5, 10, and 15 minutes. The observation that predictive capacity was sustained across multiple time points underscores the robustness of these indices, with $d^{\mathrm{PCA}}_{w,\mathrm{T}_{pe}}$ generally outperforming T_{pe} while retaining the notable advantage of being derived from the surface ECG. This performance suggests that $d^{\mathrm{PCA}}_{w,\mathrm{T}_{pe}}$ can serve not only as a surrogate of DOR but also as a practical tool for arrhythmic risk assessment under ischemic conditions.

The correlation between $d^{\mathrm{PCA}}_{w,\mathrm{T}_{pe}}$ and T_{pe} across the temporal series of each animal was also computed. As expected, both indices showed a strong inverse association, with a median [IQR] correlation of $R = -0.88$ [0.22] across all pigs. This high inverse correlation confirms that both indices track related ischemia-induced repolarization changes but not exactly equal. In practice, this difference is reflected in the earlier and stronger separation between Delayed-VF and Non-VF animals observed for $d^{\mathrm{PCA}}_{w,\mathrm{T}_{pe}}$, suggesting that the warping-based

marker captures additional temporal-morphological information beyond that summarized by T_{pe}.

Importantly, linear regression analyses provided complementary insight into supporting the hypothesis of a mechanistic coherence between indices. Although overall linear relationships were modest for non-VF susceptible animals, compatible with a reduced range of variations in the index values, VF-susceptible animals exhibited a stronger and more consistent negative relationship between $d^{\mathrm{PCA}}_{w,\mathrm{T}_{pe}}$ and DOR, reflected by higher R^2 values compared to Non-VF pigs. This inverse association further reinforces that increases in DOR are associated with $d^{\mathrm{PCA}}_{w,\mathrm{T}_{pe}}$ becoming more negative. In contrast, the linear association between T_{pe} and DOR was weaker, showing smaller absolute slopes and lower R^2 on average. This pattern suggests that in animals predisposed to VF, $d^{\mathrm{PCA}}_{w,\mathrm{T}_{pe}}$ faithfully reflects the heterogeneity of repolarization dispersion captured by intracardiac DOR, highlighting its potential as a physiologically grounded non-invasive index closely aligned with intracardiac DOR.

These findings can be better interpreted in light of previous work on ischemia-related repolarization markers. Progressive T_{pe} prolongation has been linked to increased arrhythmic vulnerability during acute ischemia in animal models [217, 235], supporting its role as a marker of repolarization heterogeneity [236, 237]. It has also been shown that T_{pe} underestimates DOR, particularly under ischemic conditions, with the mismatch further modulated by ischemic area size, especially in single-lead measurements [240]. Viewed together, these observations help explain why, in the present study, both $d^{\mathrm{PCA}}_{w,\mathrm{T}_{pe}}$ and T_{pe} tracked related ischemia-induced repolarization changes, while the warping-based index showed a stronger relationship with DOR and an earlier discrimination of VF susceptibility. This advantage may also be facilitated by the use of a PCA-derived global lead, which provides a more spatially integrated representation of repolarization than single-lead measurements. This interpretation is also consistent with broader evidence across different clinical settings, including ischemic heart disease [243, 244], heart failure [245, 246], Brugada syndrome [188, 247], and hypertension [248], indicating that T_{pe} prolongation is associated with arrhythmic risk, but that its prognostic value is moderate and should be interpreted together with other markers rather than in isolation [249]. In this context, the present work does not challenge the relevance of T_{pe}, but builds upon it by showing that incorporating the full morphology of the same interval may provide a more sensitive non-invasive representation of the evolving arrhythmogenic substrate than relying on fiducial points alone.

Findings in this chapter also align well with those presented in Chapter 3 using PCI in humans, where $d^{\mathrm{PCA}}_{w,\mathrm{T}_{pe}}$ was validated as a sensitive marker of tran-

sient ischemia-induced repolarization changes [230], and in Chapter 4 using a closed-chest porcine infarction model, where it demonstrated predictive value for delayed-VF occurrence [241]. The present work provides validation of $d^{\mathrm{PCA}}_{w,\mathrm{T}pe}$ as a surrogate for the invasive DOR measurements in an open-chest infarction model. These findings gain further translational relevance from the fact that ischemic injury develops several-fold slower in humans compared with experimental models [231], providing a clinically feasible window for monitoring and intervention.

5.4.3 Limitations

The present findings should be interpreted in light of some limitations. The number of animals included was relatively small, which may affect the statistical power, although the consistency across multiple analyses supports the robustness of the observations. In addition, the open-chest porcine model allowed unique simultaneous recordings of surface ECG and invasive DOR, but it departs from clinical conditions and may not fully capture the dynamics of ischemia in closed-chest or chronic settings. Although the thorax was reclosed during ECG recordings and precordial leads V4–V6 were repositioned to minimize thoracotomy-related effects, potential alterations in surface ECG morphology cannot be completely ruled out. Another consideration is that all animals were under anesthesia, which may alter electrophysiological responses compared to conscious states, and thus caution is needed when extrapolating these results to human scenarios. Additionally, although Early-VF cases were not included in the present analyses, a dedicated evaluation of this subgroup may provide complementary information and should be addressed in future work. Accordingly, the present findings are restricted to Delayed-VF and should not be extrapolated to Early-VF episodes, which may involve distinct underlying mechanisms.

The invasive DOR measurement also presents certain methodological limitations. During ischemia, substantial alterations in unipolar EGM morphology may make the identification of the maximum first derivative (dV/dt) within the T wave difficult or ambiguous, potentially affecting the accuracy of local repolarization time estimates. Although delineation marks were visually inspected, measurement uncertainty cannot be completely excluded. Furthermore, the limited spatial coverage provided by the intramyocardial electrodes does not encompass the entire ventricular myocardium, including the endocardial and epicardial surfaces. Consequently, the calculated DOR reflects repolarization dispersion within the sampled regions and may underestimate the dispersion

across the entire myocardium. Finally, post-repolarization refractoriness during ischemia may cause myocardial refractoriness to persist beyond electrical repolarization. Therefore, DOR derived from repolarization times should not be interpreted as a direct measure of the spatial dispersion of refractoriness.

Previous studies in ischemia induced during PCI in humans [230] show regional markers differences function of the occluded artery. Here, the analysis using a spatially integrated global PCA lead prevents a detailed spatial analysis, which will also require larger subpopulations at the different occluded arteries, worth to be considered in future studies.

From a methodological perspective, the computation of $d_{w,\mathrm{T}_{pe}}^{\mathrm{PCA}}$ relies on accurate ECG preprocessing, including delineation and PCA transformation, which could introduce variability across implementations if not standardized. Furthermore, the need of a reference waveform, while appropriate in this controlled experimental setup, might be less straightforward in clinical practice where a stable reference segment is not always available. Alternative approaches, such as deriving references from patient-specific control recordings or from population-based templates, warrant further exploration in translational studies.

5.5 Conclusions

This chapter extended the previous evaluation of T-peak-to-end morphology by testing its relationship with invasive measurements of DOR in an open-chest porcine infarction model. The warping-based index $d_{w,\mathrm{T}_{pe}}^{\mathrm{PCA}}$ may be a potential non-invasive surrogate of ventricular repolarization dispersion measured by the invasive DOR, showing comparable predictive performance for delayed-VF occurrence under ischemic conditions, while performing earlier and more robustly than the classical T_{pe} index. These results call for further validation in human cohorts to establish clinical applicability and evaluate its potencial role in arrhythmic risk stratification under ischemic conditions.

CHAPTER 6

RISK STRATIFICATION OF TYPE 2 LONG QT SYNDROME PATIENTS THROUGH ANALYSIS OF T-WAVE MORPHOLOGY

6.1 Introduction

6.2 Materials and methods

6.2.1 Patient Cohort

6.2.2 Data Collection and End Points

6.2.3 ECG Signal Processing and Characterization

6.2.4 Quantification of T-Wave Morphology Changes

6.2.5 Statistical Analyses

6.3 Results

6.3.1 Clinical and Demographic Characteristics

6.3.2 T-wave Morphology

6.3.3 Association of ECG Markers with Cardiac Outcomes

6.3.4 Cardiac Events

6.3.5 Ventricular Arrhythmias

6.4 Discussion

6.4.1 Limitations

6.5 Conclusions

6.1 Introduction

This chapter shifts the focus from ischemia-induced repolarization changes to congenital repolarization abnormalities by evaluating T-wave morphology in type 2 long-QT syndrome (LQT2). LQT2 is caused by pathogenic variants in the KCNH2 gene and represents one of the most prevalent and clinically

significant subtypes [26, 86, 114]. It is characterized by disorders of myocardial repolarization that are associated with an increased propensity to atypical polymorphic ventricular tachycardia called TdP [250, 251], which can manifest as syncopal episodes or lead to a SCD [86, 250, 251]. The need to properly identify high-risk patients has prompted a growing body of research focused on improving risk prediction and early intervention beyond conventional clinical and electrocardiographic parameters.

As discussed in Chapter 1, QT_c prolongation remains the pathophysiological hallmark for diagnosis and clinical risk stratification in LQTS. However, approximately 25–50% of genetically affected and asymptomatic individuals may present borderline or even normal QT_c durations at rest [75, 95, 252], underscoring the limitations of relying solely on the QT_c interval for risk assessment. In LQT2, arrhythmic vulnerability is therefore not fully explained by repolarization delay itself, but is also linked to the temporal and spatial heterogeneity of the repolarization dynamics [26, 27]. This view, supported by both experimental models and clinical observations [27, 45, 127, 253], has prompted the search for complementary markers capable of capturing the underlaying complexity of repolarization dynamics beyond what QT_c duration alone can convey.

In LQT2, the resulting dysfunction of the rapid delayed rectifier potassium current [26] (I_{Kr}) leads to delayed ventricular repolarization, which manifests electrocardiographically as low-amplitude, asymmetric, notched, flattened, or bifid T-waves [80, 127, 254]. Although these genotype-specific T-wave abnormalities are qualitatively recognized and may offer insights beyond QT_c, they remain difficult to quantify and have not yet been systematically integrated into clinical risk stratification [80]. Clinically, the occurrence of arrhythmic events in LQT2 despite borderline or normal QT_c [127] further draw attention to this gap and supports the need for complementary approaches that capture the arrhythmogenic substrate beyond conventional QT_c measurements.

Although several existing T-wave-based biomarkers aimed at enhancing risk stratification are commonly categorized as morphology-based markers for LQTS, most of them rely on temporal measurements derived from ECG fiducial points [94, 95, 255, 256], and therefore do not fully capture the morphological complexity of the T-wave. In order to overcome these limitations, biomarkers such as the morphology combination score (MCS) [200, 201] and others based on information provided by the vectorcardiogram have been evaluated [256, 257]. Separately, a previous study demonstrated the value of the warping-based approach evaluated in this thesis, in quantifying T-wave morphology variations with respect to a population-based reference T-wave (TMV index) [204], which

provides a global assessment of T-wave morphology and is the metric adopted in the study presented in this chapter. We hypothesized that a global assessment of T-wave morphology using the TMV index may uncover relevant differences in repolarization dynamics beyond what conventional QT-based or fiducial-point-based markers can reveal. Therefore, the aim of this study was to assess the association between the TMV index and the risk of cardiac events in a cohort of LQT2 patients.

6.2 Materials and methods

6.2.1 Patient Cohort

The study population comprised individuals diagnosed with LQT2 recruited at the cardiogenetic clinics of the tertiary care academic hospitals in Lund, Gothenburg and Linköping (Sweden). Inclusion criteria were patients (1) carrying a pathogenic or likely pathogenic genetic variant in KCNH2 (LQT2), as confirmed by standard genetic testing according to clinical routines, and (2) at least 16 years old, in order to avoid potential variability in T-wave morphology typically observed in pediatric and adolescent populations. Patients with multiple LQTS-related genetic variants (>1) were not included in this study. Eight independent standard leads (I, II, and V1–V6) were collected during a 10-second resting recording in the supine position and digital ECG files were exported from either GE MUSE ECG database (GE Healthcare, Chicago, IL, USA) or Cardiolex ECG database (Cardiolex Medical AB, Solna, Sweden). Signals were acquired at a sampling frequency of 500 Hz and with an amplitude resolution of 4.88 μV. The earliest ECG ever recorded at or after the age of 16 was used for analysis. The study received the Local Ethical Review Board approval 2024-05551-02 (Lund, Sweden), in accordance with national and international ethical and deontological standards.

The reference cohort consisted of 23,962 middle-aged adults with no history of cardiovascular disease, selected from the UK Biobank (UKB) [258]. A reference library of normal T-wave morphologies, clustered by sex, heart rate, and lead, was previously derived from standard 10-second, 8-independent-lead resting ECGs available from the UKB database, as described by Ramírez et al. [204] Data access for this component of the study was granted under UKB application 8256. All participants provided informed consent, and the study received institutional ethics approval.

6.2.2 Data Collection and End Points

Study data corresponding to the first cohort (LQT2 patients) were collected and managed using REDCap electronic data capture tools hosted at hospitals in Lund, Gothenburg and Linköping (Sweden) [259,260]. Clinical data included demographic information, ECG findings, ongoing treatments (including QT-prolonging medications), and clinical events documented both retrospectively (before inclusion into the registry) and prospectively throughout long-term follow-up. Beta-blocker use was specifically collected to enable time-dependent analysis of its potential impact on cardiac outcomes.

The primary endpoint was defined as the first lifetime occurrence of a cardiac event (CE), defined as the occurrence of syncope (a sudden, transient loss of consciousness with rapid recovery) or the composite endpoint ventricular arrhythmia (VA). Accordingly, the first lifetime CE was ascertained from the complete medical record and could occur either before or after the first digital ECG used for TMV computation. Each patient contributed a single event time corresponding to the first lifetime CE. VA includes documented episodes of TdP, sustained VT, appropriate intervention by implantable cardioverter defibrillator (ICD), aborted cardiac arrest (ACA) requiring external defibrillation, or LQTS-related SCD (abrupt in onset and without an identifiable cause, whether witnessed or unwitnessed). VA was considered as a secondary endpoint.

6.2.3 ECG Signal Processing and Characterization

The ECG pre-processing pipeline for the clinical LQT2 cohort followed the general filtering and delineation procedures and PCA transformation described in Chapter 2. Specifically, in this cohort, the PCA transformation was derived from the T-waves contained within each 10-second ECG recording. Then, from each 10-second ECG recording, the median beat was extracted for each of the 8 independent leads and the PC1 (Panel A in Figure 6.1 shows the median beat in lead I). QRS and T-wave onset and end timings were then annotated using a wavelet-based delineation method [195]. In order to match the T-wave segmentation strategy used in the UK biobank cohort, the T-wave segmentation window was subsequently adjusted by moving the T-wave boundaries (T_{on} and T_{off}) forward in time from the end of the QRS complex, QRS_{off}, by an offset linearly proportional to the RR interval (in ms), defining $T_{on} = QRS_{off} + 40$ ms$\times$RR/1000 and moving the T_{off} ahead from the delineation mark by 40 ms$\times$RR/1000. Finally, each isolated T-wave was fur-

ther filtered using a sixth-order bidirectional low-pass Butterworth filter with a cut-off frequency of 20 Hz to eliminate residual high-frequency content.

6.2.4 Quantification of T-Wave Morphology Changes

To assess T-wave morphology changes, we used TMV index, a dynamic time-warping-based algorithm previously validated for quantifying morphology changes relative to reference repolarization patterns [204]. TMV reflects the signed average time-warping required to optimally align each point of the T-wave under study to a representative normal reference T-wave, thus providing a geometry-aware measure of morphological variation. In brief, each median T-wave, $\boldsymbol{f}^s(\boldsymbol{t}^s)$, derived from each 10-second ECG recording as described above, was compared with its corresponding sex-, heart-rate- and lead-matched average reference waveform, $\boldsymbol{f}^r(\boldsymbol{t}^r)$, derived from the UKB population cohort (Panel C in Figure 6.1). Similarly to $d_{w,\mathrm{T}}^{\mathrm{PCA}}$, TMV is defined as detailed in Section 2.3.2.

Note that $\gamma(\boldsymbol{t}^r)$ (solid red line in panel D of Figure 6.1) is the optimal warping function that reparametrizes the time dimension of the patient's T-wave to best match its corresponding reference waveform $\boldsymbol{f}^r(\boldsymbol{t}^r)$. In this study, TMV is additionally reported with T-wave- and derivative-based weighting variables, as described in Section 2.3.5, which have recently shown improved robustness against to noise [198]. TMV is depicted as the average green dashed line area in panel D of Figure 6.1. TMV is additionally reported as a signed index (see Section2.3.2), whose sign follows the net amount of warping. A positive (negative) sign indicates that aligning the wave under study with the reference one predominantly requires stretching (shrinking) the waveform, and larger absolute TMV values indicate greater deviation from normal T-wave morphology. Figure 6.1 summarizes the processing pipeline used to compute the TMV index for each patient. All outcome and risk analyses were performed exclusively in the LQT2 cohort.

Given prior reports linking lower T-wave amplitude with increased arrhythmic risk [127] and showing genotype-dependent, circadian modulation of beat-to-beat T-wave amplitude variability in LQTS [27], we included a simple amplitude metric computed directly from the median beat of each 10-second ECG recording. T-wave amplitude, T_{Amp}, was defined as the absolute difference between the signal amplitude at the automatically-annotated T-wave peak (wavelet-based method [195]) and the mean voltage of an isoelectric segment of the same beat. The isoelectric segment was defined as a window of 10 ms×RR/1000 within the PR interval whose end was positioned

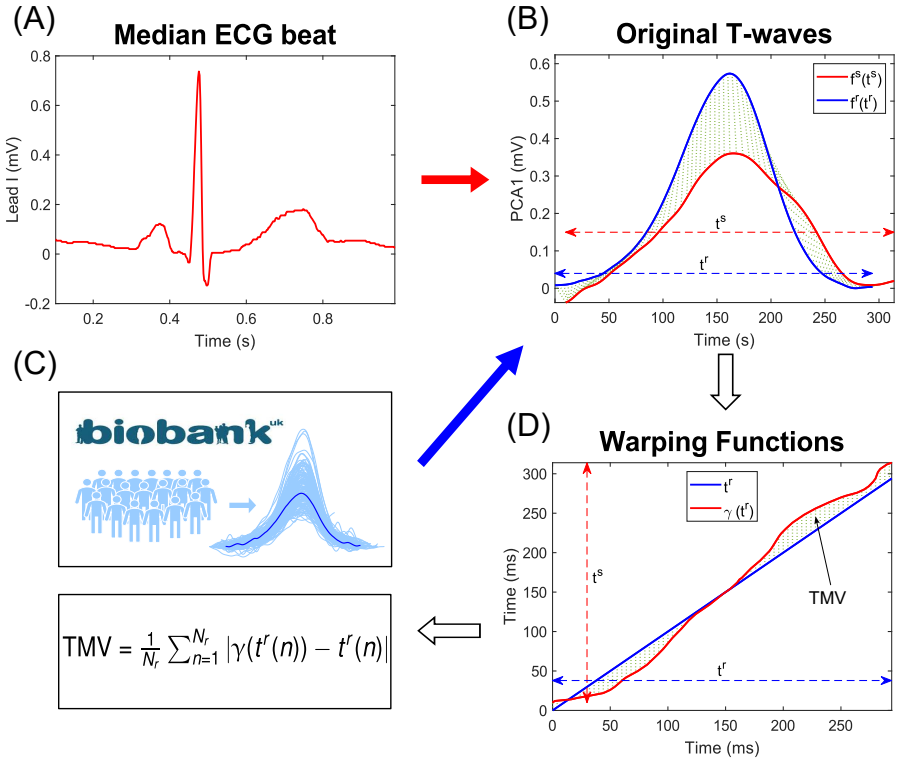


Figure 6.1: Diagram of the method to obtain the time-warping-based index, TMV. The color blue across panels corresponds to the healthy general condition, and the red one to LQT2. A, illustrative median ECG beat derived from the 10-second ECG recording in lead I for a particular patient. B, a median T-wave (red line) extracted from panel A for an individual patient together its corresponding sex-, heart rate–, and lead-specific normal reference wave (blue line) derived from the UKB cohort represented by panel C. The green dashed lines illustrate temporal pointwise differences that would be necessary to optimally match $\boldsymbol{f}^s$ wave with $\boldsymbol{f}^r$ wave. D, warping function $\gamma(\boldsymbol{t}^r)$ (solid red line) that optimally relates the reference $\boldsymbol{f}^r(\boldsymbol{t}^r)$ and studied $\boldsymbol{f}^s(\boldsymbol{t}^s)$ waves. TMV index representing the total amount of warping is depicted by the green dashed line area between $\gamma(\boldsymbol{t}^r)$ and $\boldsymbol{t}^r$.

15 ms×RR/1000 before QRS onset. If the window extended beyond the PR segment, it was truncated to remain within PR. Similarly, considering prior literature on morphology-based risk markers, we also included the Morphology Combination Score (MCS) [261] as a benchmark comparator. MCS was obtained from the QT Guard Plus software (GE Healthcare) using each median beat. This algorithm computes MCS from T-wave flatness, asymmetry, and notching, according to the methodology proposed by Andersen at al. [261] and further explored in subsequent studies [76, 200, 201].

To further evaluate the added value of the warping-based index, standard clinical measurements were extracted from each available ECG recording to serve as comparative references. RR and QT intervals were measured in milliseconds, and QT values were corrected for heart rate using Bazett's formula.

In addition to the full-T-wave TMV indices, the same unweighted and weighted warping-based versions were computed over the T-peak-to-end interval, yielding the corresponding T-wave peak-to-end morphology variation (TPEMV) indices.

The workflow was fully automated (median-beat annotatin and TMV computation). Visual inspection of annotated median beats and the TMV graphical output was then performed as a verification step of the automated output (no manual re-annotation was required).

6.2.5 Statistical Analyses

All data were first assessed for distributional normality using the Shapiro-Wilk test. Continuous variables are summarized as mean ± standard deviation (SD) or as median and interquartile range [IQR], depending on distribution. Categorical variables are presented as absolute frequencies and percentages. Group comparisons were performed using the student's t-test or Mann-Whitney U test for continuous variables, and the χ^2 or Fisher's exact test for categorical variables, as appropriate.

The TMV index was initially evaluated as a continuous variable in Cox regression analysis, but did not show a statistically significant association with cardiac events. However, exploratory Kaplan-Meier analyses stratified by TMV quartiles showed that the differences in event-free survival were not uniform across the distribution, with the largest separation observed for the lowest quartile. This pattern suggested a potentially non-linear association and motivated the use of a dichotomized analysis. Therefore, we dichotomized TMV using the population's 25th percentile as cut-off value. Kaplan–Meier survival curves

were generated to assess cumulative event-free survival, and differences between groups were evaluated using the log-rank test. The association with clinical events was evaluated using Cox proportional hazards regression to estimate hazard ratios (HRs) and 95% confidence intervals (CIs) for the first lifetime occurrence of age-dependent CE, using age as the time scale [114, 262] (birth as time origin), with follow-up censored at the age of 60 years, in line with previous LQTS studies [110, 263] and assuming no population-scale changes in the distribution of TMV values throughout the lifespan. Consistent with these genotype-based LQTS studies, LQTS is considered a congenital channelopathy in which the underlying electrophysiological substrate, reflecting the peculiarities of the ion currents specific for the affected individual, is genetically determined and present from birth. Accordingly, the first available adult ECG has been commonly used as a representative marker of the genotype-related repolarization phenotype and tested for its association with events that occurred prior to the index ECG and during follow-up.

Multivariable Cox models adjusted for QT_c, sex, and MCS were also performed. The proportional hazards assumption was assessed using standard graphical diagnostics (log-minus-log plots) and time-dependence checks (introduction of a time-dependent covariate into the model). Model discrimination was summarized using Uno's C-index for the Cox models. Model calibration was assessed at time 50 years using internal bootstrap validation with 400 resamples and comparing predicted and observed event risk, and an optimism-corrected calibration to reduce overfitting-related bias from using the same dataset for model development and evaluation. Beta-blocker therapy was not included in the main multivariable models and was considered only in sensitivity analyses due to its potential confounding effect and time-varying nature. All statistical analyses were two-tailed and considered significant if p-value < 0.05. Analyses were performed using MATLAB R2024b and IBM SPSS Statistics for Windows 29.0.1.0 (IBM Corporation, Armonk, NY, USA).

6.3 Results

6.3.1 Clinical and Demographic Characteristics

A total of 54 patients with congenital LQT2 were included in the study. Table 6.1 summarizes the demographic variables, baseline ECG intervals (RR, QRS, QT_c), and treatment status up to age 60 years. The cohort had a median age at first ECG of 35 years and a balanced sex distribution. At baseline, rest-

ing heart rate was in the low-normal range, QRS duration was within normal limits with no evidence of intraventricular conduction delay, and QT_c was moderately prolonged with inter-individual variability, consistent with the LQT2 phenotype. The vast majority was treated with beta-blockers.

Table 6.1: Clinical characteristics of LQT2 patients

Characteristics	LQT2 patients (n=54)
Demographic	
Male, No. (%)	25 (45.45)
Age at first ECG, years	35 [21–47]
Age at end of follow-up	52 [37–66]
Electrocardiography	
RR, ms	951 [843–1110]
QRS, ms	88 [82–96]
QT_c, ms	472 [449–499]
Treatment (up to age 60), No. (%)	
β-blockers	46 (85)
ICD	15 (28)
Pacemaker	7 (13)
Cardiac events lifelong (No. (%))*	32 (58)
Syncope	28 (51)
Documented VA	11 (20)
Cardiac events, before 60 y.o. (No. (%))	25 (46)
Of those Documented VA	10 (18)

Data are presented as No. (%) or median [Q1–Q3]. Documented VA included TdP, VT, appropriate ICD therapy, ACA and SCD.
Abbreviations: VA, ventricular arrhythmias; TdP, Torsades de pointes; VT, ventricular tachycardia; ICD, implantable cardioverter-defibrillator; ACA, aborted cardiac arrest; SCD, sudden cardiac death.
*Syncope and documented VA are not mutually exclusive; patients with both are counted in both rows but only once in CE ($\geqslant$1 event).

6.3.2 T-wave Morphology

Analysis of the TMV and its weighted versions across PC1 and eight independent leads revealed a consistent pattern, with statistical significance emerging from the derivative-weighted TMV in lead I in this cohort. By contrast,

the corresponding TPEMV indices, evaluated using the same unweighted and weighted formulations, did not yield statistically significant findings in PC1 or any of the eight independent leads. Therefore, descriptive ECG-derived metrics and clinical outcome analyses are reported for this lead-I derivative-weighted TMV marker, hereafter refered to simply as TMV. The simple amplitude metric, T_{Amp}, showed a median [Q1 Q3] of 0.17 [0.12 0.23] mV across the cohort. Beyond amplitude, the distribution of the TMV index across LQT2 patients ranged from -32.81 to 24.78 ms, with median [Q1 Q3] of -12.96 [-18.41 -7.81] ms. Note that, since the warping indices are signed, negative values indicate a temporal compression (shrinkage) of the repolarization phase required to align the patient waveform with the reference waveform, reflecting a broader or delayed repolarization phase in the original signal. When comparing by sex, TMV did not differ between males and females, with median [Q1 Q3] values of -12.64 [-20.27 -8.12] ms in males and -13.68 [-17.01 -6.92] ms in females ($p = 0.808$). The cohort's 25th percentile (Q1= -18.41 ms) was used as cut-off to evaluate associations of the TMV index with relevant clinical and electrocardiographic variables.

As summarized in Table 6.2, demographic profiles were comparable between patients with low TMV and those with higher TMV, with no differences in sex distribution or age at the first ECG. Baseline RR and QRS did not differ between groups, with comparable resting heart rates and uniformly narrow QRS complexes. In contrast, QT_c was higher in the LQT2 subjects with lower TMV. Regarding treatment, beta-blocker use did not differ significantly between groups, ICD implantation was significantly more frequent in the low-TMV group, whereas pacemaker use was similar in both groups. Among T-wave metrics, the MCS index was significantly higher in the low-TMV group, while T_{Amp} index showed no between-group difference.

6.3.3 Association of ECG Markers with Cardiac Outcomes

At least one cardiac event occurred in 32 patients experiencing at least one cardiac event; 28 patients had syncope and 11 had documented VA (categories not mutually exclusive). Neither T_{Amp} nor MCS demonstrated a significant association with the risk of CE (T_{Amp}: HR 0.53, 95% CI 0.00-7.10, $p = 0.240$; MCS: HR 1.25, 95% CI 0.67-2.38, $p = 0.489$). Both analyses yielded wide confidence intervals and concordant non-significant results, indicating no predictive value in this cohort. In contrast, patients with low TMV ($\leqslant$ -18.41 ms) were more likely to experience cardiac events, either syncope or VA, than those with higher TMV (93% vs 43%, Table 6.2). Importantly, this pattern remained sta-

Table 6.2: Characteristics of LQT2 patients based on cut-offs of the 25th percentile (Q1) of the TMV index

Characteristics	TMV $\leqslant$ Q1	TMV > Q1	p-value
Number	14	40	
Demographic			
Male, No. (%)	7 (50)	18 (45)	0.762
Age at first ECG, years	28 [18–44]	37 [24–51]	0.235
Electrocardiography			
RR, ms	951 [819–1112]	950 [866–1098]	0.569
QRS, ms	88 [82–90]	88 [82–97]	0.504
QT_c, ms	508 [498–517]	463 [442–480]	**0.003**
T wave			
MCS	1.89 $\pm$0.58	1.24 $\pm$0.41	< **0.001**
T_{Amp}, (mV)	0.16 $\pm$0.05	0.18 $\pm$0.08	0.413
Treatment (up to age 60), No. (%)			
β-blockers	14 (100)	31 (78)	0.092
ICD	8 (57)	7 (18)	**0.012**
Pacemaker	2 (14)	5 (13)	1.000
CE lifelong (No. (%))*	13 (93)	19 (48)	**0.004**
Syncope	11 (79)	17 (43)	**0.030**
Documented VA	6 (43)	5 (13)	**0.024**
CE, before 60 y.o. (No. (%))	13 (93)	17 (43)	**0.001**
Of those Documented VA	6 (43)	4 (10)	**0.013**

In this cohort, Q1 (25th percentile) of TMV corresponds to -18.41 ms.
Data are presented as No. (%) or median [Q1–Q3]. Documented VA included TdP, VT, appropriate ICD therapy, ACA and SCD.
Abbreviations: VA, ventricular arrhythmias; TdP, Torsades de pointes; VT, ventricular tachycardia; ICD, implantable cardioverter-defibrillator; ACA, aborted cardiac arrest; SCD, sudden cardiac death; MCS, Morphology Combination Score; CE, Cardiac events.
Bold values indicate significance, $p < 0.05$.
*Syncope and documented VA are not mutually exclusive; patients with both are counted in both rows but only once in CE.

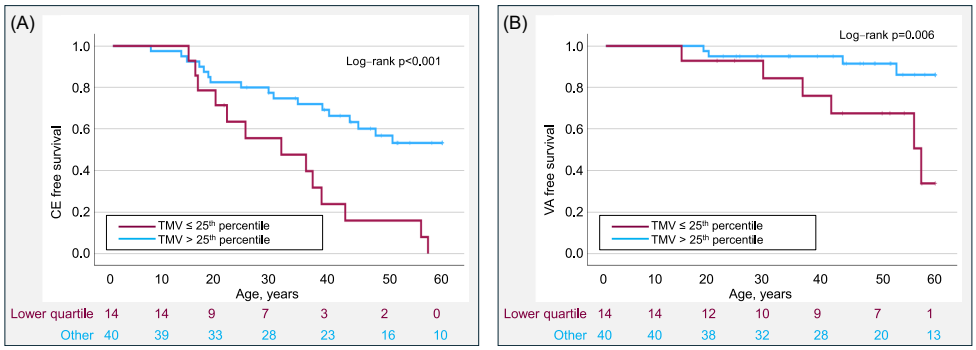


Figure 6.2: Probability of cardiac-event-free survival over lifetime censored at age of 60 in LQT2 patients dichotomized by the 25th percentile cut-off of the lead I-derived TMV index: time to first cardiac event (panel A) and time to first ventricular arrhythmia (panel B).

tistically significant when considering VA alone, as shown by the comparison of VA proportions between groups (43% vs 10%).

6.3.4 Cardiac Events

Figure 6.2 (panel A) shows Kaplan-Meier survival curves for time to first CE, comparing LQT2 patients below the 25th-percentile TMV cutoff (purple line) with the remainder of the cohort (blue line). Patients in the lowest-quartile group exhibited markedly reduced event-free survival compared to the rest of the cohort, with an early and sustained separation of curves. The log-rank test indicated a significant difference between groups ($p < 0.001$). Accordingly, TMV $\leqslant$ -18.41 ms was associated with increased risk in the univariate model (HR 3.505, 95% CI 1.673 - 7.341; $p < 0.001$). In multivariable analyses, the association remained significant after adjustment for QT_c and after additional adjustment for sex and MCS. Full multivariable estimates are provided in Tabla 6.3, while the univariate analysis of the remaining ECG leads in which no significant findings were found is presented in Table 6.4. Across those leads, TMV showed similar risk estimates, however not reaching statistical significance. Model discrimination for the univariable TMV Cox model was modest (Uno's C-index = 0.61 (95% CI 0.533 - 0.693)) and increased slightly in the fully adjusted model (TMV + QT_c + sex + MCS; Uno's C-index = 0.65 (95% CI 0.539 - 0.754)). Internal bootstrap calibration suggested reasonable agreement between predicted and observed risk at the 50-year time horizon after optimism correction. The mean absolute calibration error was 4.3%, with higher deviation at the extremes.

Table 6.3: Risk of cardiac events and ventricular arrhythmias in LQT2 patients: Cox regression analysis dichotomized by the 25th percentile of the TMV index derived from lead I.

Adjustment	HR	95% CI	p-value
Cardiac events			
Univariable	3.505	1.673–7.341	$<$ **0.001**
QT_c	2.92	1.111–7.676	**0.030**
QT_c and sex	3.375	1.256–9.067	**0.016**
QT_c, sex, and MCS	4.061	1.369–12.046	**0.012**
Ventricular arrhythmias			
Univariable	4.978	1.4–17.705	**0.013**
QT_c	3.035	0.625–14.728	0.168
QT_c and sex	3.116	0.629–15.430	0.164

Bold values indicate significance, $p < 0.05$.

Table 6.4: Risk of cardiac events in LQT2 patients: Cox regression analysis dichotomized by the 25th percentile of the TMV index derived from leads PC1, II and V1–V6.

Lead	HR	95% CI	p-value
PC1	2.09	0.97–4,47	0.059
II	1.78	0.81–3.89	0.149
V1	1.96	0.92–4.20	0.830
V2	1.82	0.83–4.00	0.135
V3	1.13	0.50–2.54	0.722
V4	1.60	0.71–3.61	0.255
V5	1.88	0.85–4.15	0.119
V6	1.88	0.88–4.02	0.105

As a sensitivity analysis, we additionally included beta-blocker therapy in the fully adjusted model (TMV + QT_c + sex + MCS) and the association remained significant (HR 4.137, 95% CI 1.405-12.183; $p = 0.010$).

6.3.5 Ventricular Arrhythmias

Figure 6.2 (panel B) shows the Kaplan-Meier curve for time to first VA, where the TMV $\leqslant$ -18.41 ms group also had lower VA-free survival, with a similar early divergence maintained across the recorded clinical history (log-rank $p = 0.006$). In the univariate Cox model, low TMV ($\leqslant$ -18.41 ms) was

associated with increased risk of VA (HR 4.978, 95% CI 1.4 - 17.705; $p = 0.013$). In multivariable models, estimates were directionally similar but did not reach statistical significance: adjusted HRs ranged from 2.623 to 3.116, but all 95% CIs crossed 1.0 (smallest $p = 0.164$). Corresponding hazard ratios and confidence intervals are reported in Tabla 6.3.

6.4 Discussion

The present study assesses the association of the TMV index with cardiac events in patients with LQT2. Changes in T-wave morphology in each of the 8 independent leads were quantified by means of a time-warping-based method that quantifies morphological variations with respect to a healthy population-based reference T-wave. Our main findings are that the TMV index in lead I was significantly associated with an increased risk of cardiac events in LQT2 patients. More negative values of TMV index, reflecting broader T-waves and greater morphological dissimilarity from the normal T-wave pattern, were linked to the occurrence of CE after adjustment for QT_c prolongation, and the association remained significant in models further adjusted for sex and MCS, a T-wave morphology index earlier studied in the context of type 2 LQTS or interventions involving IKr (human ether-à-go-go-related gene, hERG) channel inhibition. When ventricular arrhythmia was considered as the endpoint, the association was significant in the univariate model but did not persist after multivariable adjustment.

While many studies have explored T-wave morphology in LQTS, only a few have successfully provided prognostic information beyond subtype classification or comparison with healthy controls. Among them, visually assessed abnormalities, such as flat or notched T-waves, have shown associations with increased cardiac risk in LQT2 carriers with normal QT_c [254]. A more quantitative approach was proposed by Sugrue et al., who identified the T-wave center of gravity x-axis in lead I (computed over the last 25% of wave) as an independent predictor of breakthrough cardiac events in LQT2 patients, showing prognostic value beyond QT_c in that subgroup [78]. In line with this lead-dependent pattern, TMV association with cardiac events emerged in lead I, whereas other leads did not reach statistical significance (see Table 6.4) suggesting that repolarization vector alignment and cohort-specific factors influence lead-specific detectability. In addition, this concordance with lead I may reflect that TMV, although computed over the full T wave, can be dominated by late or terminal repolarization mismatches relative to the reference, and may therefore capture

tail-weighted integral properties of the T wave, as summarized by the lead-I center-of-gravity metric. More recently, the three-dimensional T-wave vector magnitude has been shown to identify high-risk LQT2 mutation carriers with normal QT_c [127]. Most of these approaches are constrained to subsets of patients without QT prolongation. In contrast, our approach is the first to apply a warping-based method to this context, capturing subtle morphological variations across the full T wave and showing an association with higher risk in LQT2 patients that is independent of QT_c duration. Specifically, we applied a single TMV cut-off ($\leqslant$ -18.41 ms) to categorize patients in this cohort, which captured the most pronounced T-wave morphological changes associated with increased risk.

Survival analysis revealed a consistent trend: patients with wider T-waves and more pronounced T-wave morphological changes, as indicated by more negative TMV values, had significantly lower event-free survival compared to the rest of the cohort, reflecting a higher vulnerability to cardiac events when the T-wave morphology differs largely from the normal pattern. Moreover, Cox regression analyses point to the same risk profile, further supporting the consistency of the TMV index. The association persisted after adjustment for QT_c, suggesting that TMV captures relevant information not fully conveyed by QT_c prolongation alone. The association persisted after adjustment for sex and remained significant with additional adjustment for MCS, indicating that TMV provides additional information not conveyed by these covariates.

Unlike the ischemic settings examined in the preceding chapters, restricting the analysis to the T-peak-to-end interval did not yield statistically significant findings in this LQT2 cohort. This suggests that, although late or terminal repolarization mismatches may contribute substantially to the full-T-wave TMV, the relevant morphology-related information was not retained when the T-peak-to-end interval was analyzed in isolation.

Although MCS values were significantly higher in the low-TMV group (Table 6.2), indicating morphological abnormalities that covary with TMV, MCS itself was not associated with cardiac events in this cohort. This pattern suggests that between-group contrasts can arise from correlated morphology features without translating into independent prognostic signal at the patient level. In other words, MCS appears to track with TMV cross-sectionally but does not carry sufficient information to inform risk on its own in this cohort, likely reflecting a smaller effect size and lower sensitivity of MCS, which would require a larger cohort to detect its association with outcomes. By contrast, TMV remained associated with outcomes after multivariable adjustment, MCS included, indicating that TMV captures the information not included in

MCS. Conceptually, the warping-based approach may better summarize temporally dispersed repolarization changes that are less accessible to composite asymmetry/notch/flatness aggregates. Separately, T-wave amplitude values were overall low across the cohort, consistent with the low-amplitude T-wave phenotype often described in LQT2. However, associations with cardiac events were consistently non-significant, indicating limited precision that may reflect the small sample size. Taken together with the TMV results, these findings suggest that neither T_{Amp} nor MCS had discriminant value here, whereas a full-T-wave, warping-based measure captured morphology information relevant to risk in LQT2 within our dataset.

A plausible mechanistic rationale for the observed findings is that loss-of-function of the rapid delayed rectifier potassium current (I_{K_r}) from KCNH2 mutations amplifies temporal and spatial heterogeneity of repolarization, manifesting as T-wave morphology changes. Such changes may not be fully captured by QT_c duration alone. By applying a full-T-wave, morphology-aware alignment, as provided by the warping-based strategy, the TMV index quantifies pointwise timing variations relative to a population reference and thereby reflects broader or temporally dispersed repolarization patterns characteristic of LQT2. This provides a concise morphological summary that complements the QT_c and helps to discriminate patients with significantly lower event-free survival within this genotype, including those with borderline or moderately prolonged QT_c.

A possible explanation for the lack of statistical significance in the adjusted models for VA is the limited number of events available for analysis (10 events before age 60), which reduces statistical power and inflates confidence intervals. The inclusion of prespecified covariates (QT_c, sex, MCS) may also have attenuated estimates by distributing shared prognostic information. Further confirmation in larger cohorts, containing more VA events, will be essential in subsequent studies.

While the role of sex in modulating arrhythmic risk among LQT2 patients has previously been suggested by Cortez et al., who reported that abnormal T-wave morphology conferred higher risk in women with normal QTc but not in men [127], Sugrue et al. did not report sex-stratified results in their analysis of morphology-based ECG markers in a size-comparable cohort [78]. In our study, TMV distributions did not differ by sex (Table 6.2), suggesting a relatively homogeneous morphological substrate between males and females. Moreover, including sex as a covariate did not alter the association between TMV and cardiac events, indicating that the prognostic value of TMV was independent of sex in our models. We did not perform sex-specific risk analyses due to

the limited cohort size and number of events, so these observations should be interpreted with caution and more robustly evaluated in larger, sex-balanced cohorts.

Despite extensive explorations of ECG metrics to refine risk stratification in LQTS, progress toward routine use of morphology-based markers has been limited by variability in measurement protocols and challenges in validation and standardization. Within this context, TMV offers a single-lead measure of full T-wave morphological variations relative to a large and consistent population template, thereby facilitating straightforward large-scale comparison with normal patterns and enabling prespecified dichotomization for clinical analyses. From a clinical perspective, TMV may serve as a valuable complement to existing risk stratification tools in LQT2 patients, including those with borderline or prolonged QT_c values. As TMV index is computable directly from T-wave morphology and does not rely on specific fiducial points, it may be well suited for automated implementation in digital ECG platforms. Future studies should aim to validate these findings in larger, prospective cohorts and evaluate whether warping-index-based classification improves clinical decision-making or risk prediction models.

6.4.1 Limitations

This study has limitations that should be acknowledged. First, this single-cohort study has a retrospective nature and is intended to be exploratory (hypothesis-generating); therefore, the findings should be interpreted accordingly. Second, the UKB cohort used to derive the reference T-wave morphologies was not age-matched to the LQT2 cohort. Since aging affects T-wave morphology and duration, age-related differences between the two populations may have influenced the estimated TMV values. Third, the overall LQT2 cohort size was limited, which restricted the ability to perform subgroup risk analyses and may have reduced power to detect weak associations. Accordingly, stratified analyses by sex or by QT_c interval range (e.g., normal vs. prolonged) were not conducted due to the relatively low number of events across both groups. Thus, no formal sex-related risk interaction analysis was performed either. In addition, the high concentration of events in the lowest TMV quartile leaves few event-free individuals in that stratum, which may reduce the stability of adjusted estimates and contribute to wide confidence intervals. Consequently, validation in larger cohort is needed to confirm its clinical utility and generalizability and to enable a robust assessment of model performance (including discrimination and calibration).

6.5 Conclusions

This chapter extended the evaluation of time-warping-based T-wave morphology markers to congenital repolarization abnormalities by assessing their association with arrhythmic risk in a cohort of LQT2 patients. T-wave morphology abnormalities quantified by the TMV index showed a statistically significant association with the risk of cardiac events in a cohort of LQT2 patients, which included those with prolonged or borderline QT_c values, after adjustment for QT_c, sex, and MCS. This marker reflect repolarization abnormalities not captured by QT_c duration and may complement current risk stratification strategies. Further validation in prospective, multicenter cohorts is warranted to support their potential integration into clinical clinical practice.

CHAPTER 7

T-WAVE PEAK-TO-END MORPHOLOGY ANALYSIS IN BRUGADA SYNDROME

7.1 Introduction

7.2 Methods

7.2.1 Data Set

7.2.2 ECG Pre-Processing

7.2.3 Quantification of the $\mathbf{T}_{pe}$ Morphology Restitution

7.2.4 Quantification of the $\mathbf{T}_{pe}$ Morphology Variation

7.2.5 Statistical Analysis

7.3 Results

7.3.1 Clinical and Demographic Characteristics

7.3.2 T-wave Morphology Restitution Markers

7.3.3 T-wave Morphology Variation Markers

7.3.4 Classical Repolarization and Depolarization-related ECG Markers

7.4 Discussion

7.4.1 Limitations

7.5 Conclusions

7.1 Introduction

This chapter further extends the evaluation of T-wave morphology markers to Brugada syndrome (BrS), a primary electrical disease in which arrhythmic risk stratification remains particularly challenging. BrS is a genetic disorder

that affects the ion channels of the cardiac myocites, resulting in distinctive abnormal electrocardiographic patterns and a high predisposition to malignant ventricular arrhythmias and SCD [158]. Risk stratification and management of patients with BrS remains a major clinical challenge due to the lack of accepted biomarkers of SCD risk. To date, recovered SCD or arrhythmogenic syncope are considered the most robust risk indicators in these patients [28, 29].

Together with the depolarization hypothesis, repolarization disorders represent one of the two main explanations regarding the pathophysiological mechanisms behind the Brugada pattern [153], which remain controversial. Heterogeneity in ventricular restitution properties has been linked to the development of repolarization dispersion gradients, which, when pronounced, increase the risk of malignant ventricular arrhythmias [264], so its evaluation in the context of patients with BrS seems relevant. However, direct APDR dynamics evaluation remains impractical due to its invasive nature, driving the development of indirect non-invasive alternatives. A T-wave morphology-based APDR index quantifying the variations in the overall morphology of the T-wave with heart rate, T-wave morphology restitution (TMR) index [203], has recently been reported and linked with SCD in chronic heart failure and the general population.

The TMR index therefore provides a restitution-based assessment of the T-wave morphology changes, which may be relevant in the context of the repolarization hypotesis in BrS. However typical Brugada electrocardiography patterns, including the presence of coved ST segment elevation (type 1 Brugada pattern) or saddle-back ST elevation (type 2 Brugada pattern), largely distorts the T wave initial part. In addition, as initial chapters have shown, the dispersion of ventricular repolarization reflected in the T_{pe} interval, when captured by a warping-based index computed in a spatially transformed PCA lead, $d_{w,T_{pe}}^{PCA}$, has also potential for arrhythmia risk prediction, avoiding the earlier part of the T wave. Taken together, these results suggest the exploration of this technique for risk stratification in BrS patients. For this reason, in this chapter, TMR index is evaluated not only over the complete T wave, but also after restricting the analysis to the T_{pe} interval, TPEMR index. This restricted analysis allows the variations in the terminal part of the ventricular repolarization to be assessed with heart rate, while reducing the influence of the earlier ST segment.

Beyond restitution-based analysis, ventricular repolarization changes quantified through warping-based morphology indices have also shown value when evaluated with respect to a population reference. As shown in the previous chapter, the TMV index allows T-wave morphology differences to be quanti-

fied relative to a reference population, providing a complementary approach to the assessment of arrhythmic risk [192, 204]. This motivates its evaluation in BrS, where altered ventricular repolarization may be reflected not only in the dynamic response of T-wave morphology to heart rate, but also in morphology differences with respect to normal reference patterns. Therefore, in this chapter, TMV is also assessed over the complete T wave and after restriction to the T_{pe} interval.

This chapter aims to evaluate TMR and TMV indices in BrS, both over the complete T wave and restricted to the T_{pe} interval, TPEMR and TPEMV, respectively, testing whether they can discriminate between control and BrS patients and between symptomatic (BrS-S) and asymptomatic (BrS-A) BrS patients.

7.2 Methods

7.2.1 Data Set

The study population comprised 156 subjects: 115 patients with BrS and 41 healthy control subjects. ECG recordings were collected using a continuous 12-lead ECG Holter monitor (Spiderview Plus, Livanova-Sorin Group, ELA Medical, Montrouge, France) with a 2.5 μV amplitude resolution (16-bit) and a sampling frequency of 1000 Hz. The median recording duration was 23.97 h, ranging from 18.98 to 25.15 h. Recordings were acquired using a modified configuration with high-positioned precordial leads, commonly used in BrS, simultaneously recorded at the second, third, and fourth intercostal spaces (IC) on the right ($V1_{2IC}$, $V1_{3IC}$, $V1_{4IC}$) and left ($V2_{2IC}$, $V2_{3IC}$, $V2_{4IC}$) sides of the sternum. This study was approved by the Ethics Committee of the Hospital Clínic of Barcelona (Reg. HCB/2020/0306) in accordance with ethical standards and deontological guidelines.

The BrS cohort was grouped according to the presence or absence of spontaneous type-I Brugada pattern, as BrS-I or BrS-II, respectively. From BrS population, patients who experienced cardiac-related syncope and/or SCD events before ECG recording, as well as those who suffered major events during follow up (VF and/or ventricular tachyarrhythmias), or met clinical criteria for ICD implantation, were classified as symptomatic BrS patients, group (BrS-S), while patients with no events were labeled as asymptomatic BrS patients, group (BrS-A).

For the computation of TMV index, the same UK Biobank-derived reference

library described in Section 6.2.1 was used. This reference population was used to obtain sex-, heart rate-, and lead-specific normal T-wave patterns from 10-s, 8-independent-standard-lead resting ECG recordings against which the BrS patterns were compared.

7.2.2 ECG Pre-Processing

ECG preprocessing followed the general strategy described in Chapter 2, including the common filtering procedure used throughout this thesis. Then, a wavelet-based single-lead ECG delineator [195], specifically adapted to improve delineation in the presence of typical Brugada ECG patterns as implemented in [265], and followed by a multilead delineation selection rule [196], was applied. Next, spatial PCA transformation was derived from the 6 chest leads, learning the transformation coefficients from the correlations in the T wave segment to emphasize this wave. The ECG segments used to derive the transformation were selected from periods with heart rates between 60 and 70 bpm. Finally, standard leads and the PC1 transformed lead were delineated, each T-wave segmented and further low-pass filtered (20 Hz cut-off) for subsequent analysis.

7.2.3 Quantification of the T_{pe} Morphology Restitution

T-wave peak-to-end morphology restitution index, TPEMR, was measured for each patient using the method described in [241] for the time-warping quantification index, $d^{\mathrm{PCA}}_{w,\mathrm{T}_{pe}}$, and normalizing by the intrasubject RR range used for $d^{\mathrm{PCA}}_{w,\mathrm{T}_{pe}}$ derivation. Initially, the beats are clustered in bins based on their RR interval, and a histogram with 10-ms bins was generated with data from the entire 24-hour recording. Subsequently, the two more extreme RR intervals bins containing at least 500 beats were considered. From those bins, the one closer to the median bin was selected together with its symmetric bin with respect to the median, labeled as RR_1 and RR_2 as shown in Figure 7.1a, were selected.

A mean warped T-wave peak-to-end (MWTPE), as detailed in Section 2.3.4, was computed for each of the two selected bins, and $d^{\mathrm{PCA}}_{w,\mathrm{T}_{pe}}$ was computed as the temporal reparametrization between both MWTPEs: the one from bin RR_1 and the analogously defined from bin RR_2 (see Figure 7.1b). Biphasic T-waves were discarded for the MWTPE estimation. If positive and negative T waves were present in the same bin, only the dominant class within that bin was considered to compute the MWTPEs. The amount of warping needed to eliminate the time differences between them is quantified by the warping-

based index $d^{\mathrm{PCA}}_{w,\mathrm{T}_{pe}}$ between these two MWTPEs, reflecting the variations on repolarization dispersion between T waves belonging to RR_1 and RR_2 bins.

In order to attenuate the undesired effects of T wave delineation errors, $d^{\mathrm{PCA}}_{w,\mathrm{T}_{pe}}$ was computed using the T-wave- and derivative-weighted implementation described in Section 2.3.5, which has recently shown improved robustness. The $d^{\mathrm{PCA}}_{w,\mathrm{T}_{pe}}$ index, illustrated in Figure 7.1c, where the sum of the green and yellow areas represent the original unweighted estimation, while the yellow area represents the derivative-weighted estimation, measures the amount of warping needed to fit the two MWTPEs.

The TPEMR index was then calculated by dividing the absolute value of $d^{\mathrm{PCA}}_{w,\mathrm{T}_{pe}}$ by the RR range:

$$\mathrm{TPEMR} = \frac{|d^{\mathrm{PCA}}_{w,\mathrm{T}_{pe}}|}{\Delta\mathrm{RR}}. \tag{7.1}$$

where $\Delta\mathrm{RR} = \mathrm{RR}_2 - \mathrm{RR}_1$ (Figure 7.1a).

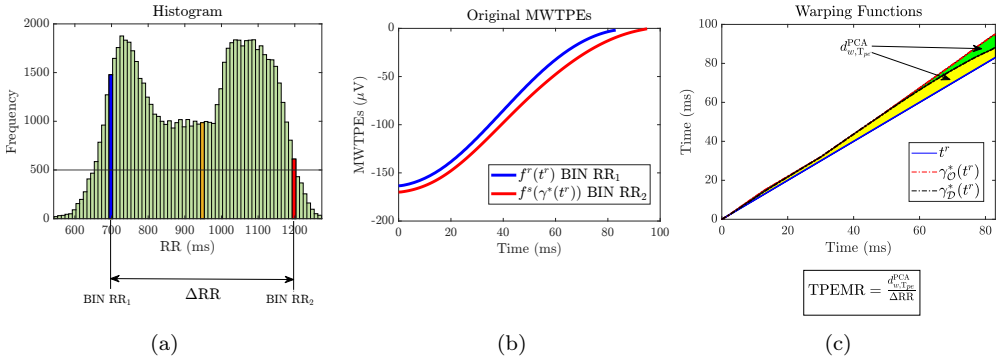


Figure 7.1: Estimation of the T-wave peak-to-end morphology restitution index, TPEMR. (a) Histogram of RR intervals; the orange bar indicates the median RR interval, while blue and red bars denote the two bins defining the maximum intra-subject RR range, ΔRR. (b) MWTPEs corresponding to the RR values highlighted in panel (a). (c) Estimation of the $d^{\mathrm{PCA}}_{w,\mathrm{T_{pe}}}$ index obtained by time-warping of the two MWTPEs, where the sum of the green and yellow areas represent the original unweighted estimatation, while the yellow area represents the derivative-weighted estimation. The TPEMR index is calculated as $|d^{\mathrm{PCA}}_{w,\mathrm{T_{pe}}}|$ normalized by ΔRR.

To complement the morphology-based restitution assessment, the duration-based $\Delta\mathrm{T}_{pe}$ marker, previously proposed to quantify restitution dispersion from dynamic changes in the surface-ECG T_{pe} interval [12], was also evaluated as a benchmark using the same RR_1 and RR_2 bins:

$$\Delta \mathrm{T}_{pe} = \frac{|\mathrm{T}_{pe}^{\mathrm{RR1}} - \mathrm{T}_{pe}^{\mathrm{RR2}}|}{\Delta \mathrm{RR}} \tag{7.2}$$

where $\mathrm{T}_{pe}^{\mathrm{RR1}}$ and $\mathrm{T}_{pe}^{\mathrm{RR2}}$ denote the median T_{pe} duration of the beats included in the corresponding RR bins.

In addition to the PCA-transformed lead, both TPEMR and $\Delta \mathrm{T}_{pe}$ were independently computed in $\mathrm{V1}_{\mathrm{2IC}}$ and $\mathrm{V2}_{\mathrm{2IC}}$, using the corresponding lead-specific MWTPEs, warping indices, and median T_{pe} durations.

7.2.4 Quantification of the T_{pe} Morphology Variation

The TMV analysis performed in Chapter 6 was extended in this chapter to the T_{pe} interval and to 24-hour Holter recordings, yielding the T_{pe} morphology variation index, TPEMV. Initially, for each lead, each beat was grouped into a RR interval bin, $B_b = [0.20 + 0.05b : 0.25 + 0.05b]$ s, with $b \in \{0, 1, \ldots, 32\}$, and an additional bin B_{33} containing beats with RR $\geqslant$ 1.85 s (see Figure 7.2). Within each bin, beats presenting biphasic T waves were discarded. If beats with positive and negative T waves were present in the same bin, only the beats whose T waves belonged to the dominant polarity class within that bin were retained. A preliminary median beat was then computed from the remaining beats and used as a reference template to further refine beat selection. The correlation between each beat and this median beat was calculated, and only beats with a correlation $\geqslant 0.8$ were retained for the final estimation. For each RR bin, a MWTPE was then computed as detailed in Section 2.3.4.

For each patient, RR bin, and analyzed lead, the median RR interval of the beats contained in the bin was used to select the corresponding normal reference waveform from the UK Biobank-derived reference library. This reference waveform was matched by sex, heart rate, and lead, as described in Section 7.2.1. The TPEMV value for each bin was then obtained by computing the warping-based index between the RR-bin- and lead-specific patient MWTPE and the corresponding reference MWTPE, as illustrated in Figure 7.2. The resulting TPEMV values quantify the morphology differences between the patient-specific T_{pe} interval and the corresponding normal reference pattern for each available RR bin.

Since BrS recordings were acquired using high-positioned chest leads, while the UK Biobank reference library was derived from the standard chest leads, TPEMV was computed only for the Brugada leads corresponding to the standard chest configuration, i.e., those located at the fourth intercostal space.

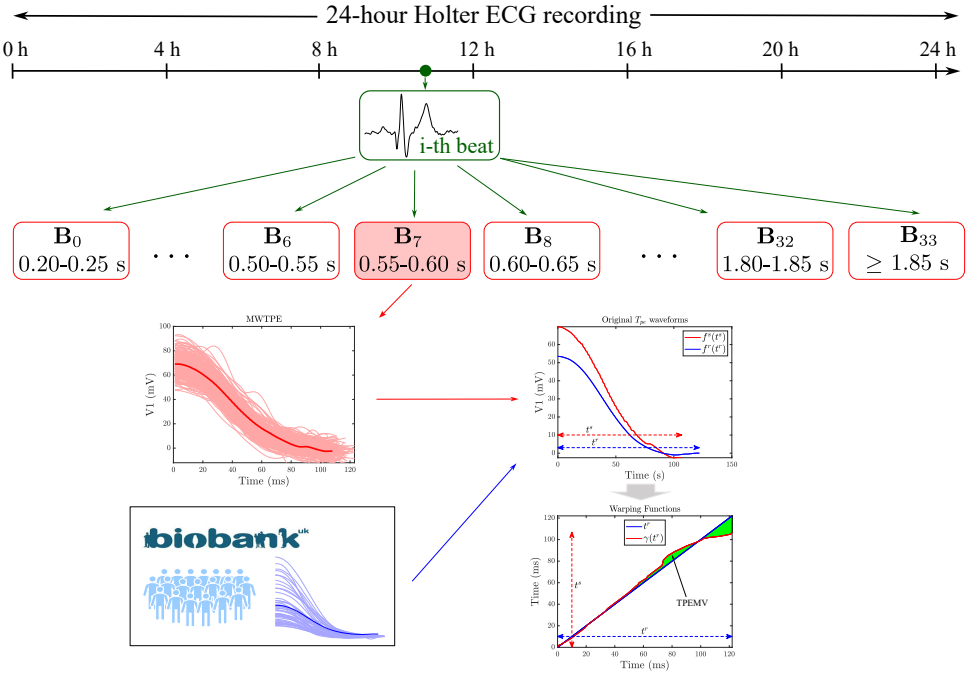


Figure 7.2: Diagram of the method to obtain the time-warping-based index, TPEMV. Beats from the 24-hour Holter ECG recording were assigned to RR interval bins, B_b, according to their corresponding RR value. For each RR bin and analyzed lead, a patient-specific MWTPE was computed from the beats retained within that bin. The median RR interval of the beats in the bin was used, together with sex and lead information, to select the corresponding normal reference waveform from the UK Biobank-derived reference library. The TPEMV index was then obtained by the time-warping of the patient-specific MWTPE and its matched reference waveform. The resulting warping function quantified the morphology variation between both T_{pe} segments, with the shaded area in green representing the amount of warping used to compute TPEMV.

These leads, hereafter denoted as $V1_{4IC}$, and $V2_{4IC}$, were compared with the corresponding standard V1 and V2 reference waveforms from the UK Biobank library, respectively. This ensured that morphology variation was quantified only between comparable chest lead configurations.

In addition to the warping-based indices, classical ECG markers were computed within the same RR bins to provide reference measurements for comparison. For each b-th RR bin defined for the TPEMV computation, the T_{pe} interval, T_{pe}, and T-wave width, T_w, were obtained as the median of the corresponding values within each bin. Additionally, given the coexistence of repolarization and depolarization hypotheses in BrS, QRS width, QRS_d, was also computed as a depolarization-related reference marker.

The same procedures described above in both Sections 7.2.3 and 7.2.4 were repeated using the complete T wave, yielding the corresponding TMR and TMV indices, respectively.

7.2.5 Statistical Analysis

Statistical analyses were performed to evaluate differences in the proposed morphology-based markers between control subjects (CG) and patients with BrS, between symptomatic (BrS-S) and asymptomatic (BrS-A) BrS patients, and between BrS-I and BrS-II patients.

For TPEMR, ΔT_{pe}, and TMR, comparisons were performed using one value per subject and analyzed lead. For TPEMV and TMV, comparisons were performed independently for each RR bin and analyzed lead. The same analysis was applied to the classical ECG markers used for comparison, including T_{pe}, T_w, and QRS_d.

Data normality was assessed using the Shapiro-Wilk test. For two-group comparisons, normally distributed variables were compared using Student's t-test, whereas non-normally distributed variables were compared using the Mann-Whitney U test. Categorical variables were compared using Fisher's exact test. Continuous data are summarized as median and interquartile range, and categorical data as absolute frequencies and percentages. Statistical significance was set at $p \leqslant 0.05$.

7.3 Results

7.3.1 Clinical and Demographic Characteristics

The clinical and demographic characteristics of the study population are summarized in Table 7.1. The final dataset included 41 control subjects and 115 patients with BrS. Within the BrS cohort, 35 patients were classified as symptomatic and 80 as asymptomatic, while 37 patients presented spontaneous type-I Brugada pattern and 78 did not.

Compared with controls, patients with BrS were significantly older and included a higher proportion of males. The ΔRR used for restitution analysis was significantly larger in controls than in BrS patients, 430 [336–499] vs 359 [299–455] ms (p=0.024), whereas no significant differences were observed between the BrS subgroups. Within the BrS cohort, symptomatic and asymptomatic patients showed no significant differences in age or sex, although symptomatic patients had a higher prevalence of spontaneous type-I pattern. Patients with spontaneous type-I pattern were older, more frequently male, more often symptomatic, and had a higher proportion of ICD than those without spontaneous type-I pattern. Syncope and major events were also numerically more frequent in BrS-I patients, although these differences did not reach statistical significance.

7.3.2 T-wave Morphology Restitution Markers

Analysis of the original, T-wave-weighted, derivative-weighted implementations of the morphology restitution and variations indices yielded broadly similar results, with the derivative-weighted versions providing the clearest overall pattern of group differences across the different comparisons and analyzed leads. Therefore, all morphology-based results presented hereafter correspond to the derivative-weighted TPEMR, TMR, TPEMV and TMV indices, refereed to simply by their respective acronyms.

As shown in Figure 7.3, compared with CG, patients with BrS showed higher TPEMR values in the PCA-transformed lead (0.009 [0.013] vs 0.005 [0.006], $p = 0.014$), whereas no significant difference was observed in either $V1_{2IC}$ or $V2_{2IC}$. Similarly, ΔTpe was higher in BrS in the PCA-transformed lead (0.019 [0.030] vs 0.012 [0.014], $p = 0.043$), with no significant differences in the two individual leads. No significant differences in TMR were found between CG and BrS in any of the three analyzed leads. The corresponding median values and interquartile ranges are reported in Table 7.2.

Table 7.1: Clinical and demographic characteristics of the study population.

Overall cohort			
Characteristic	CG	BrS	p-value
N	41	115	
Age, years	25.0 [22.8–32.7]	53.1 [41.8–63.6]	$<$ **0.001**
ΔRR	430 [336–499]	359 [299–455]	**0.024**
Male, n (%)	17 (41.5)	74 (64.3)	**0.016**
BrS-I, n (%)	–	37 (32.2)	
BrS-S, n (%)	–	35 (30.4)	
Syncope, n (%)	–	15 (13.0)	
SCD, n (%)	–	5 (4.3)	
ICD, n (%)	–	29 (25.2)	
Major events, n (%)	–	10 (8.7)	
By clinical presentation			
Characteristic	BrS-A	BrS-S	
N	80	35	
Age, years	52.9 [41.7–61.6]	54.1 [41.9–65.7]	0.555
ΔRR	369 [299–459]	339 [299–419]	0.287
Male, n (%)	50 (62.5)	24 (68.6)	0.673
BrS-I, n (%)	20 (25.0)	17 (48.6)	**0.017**
By spontaneous type-I pattern			
Characteristic	BrS-II	BrS-I	
N	78	37	
Age, years	49.8 [38.3–61.1]	58.0 [50.7–65.2]	**0.005**
ΔRR	359 [299–481]	339 [279–419]	0.157
Male, n (%)	44 (56.4)	30 (81.1)	**0.012**
BrS-S, n (%)	18 (23.1)	17 (45.9)	**0.017**
Syncope, n (%)	7 (9.0)	8 (21.6)	0.077
SCD, n (%)	3 (3.8)	2 (5.4)	0.656
ICD, n (%)	12 (15.4)	17 (45.9)	**0.001**
Major events, n (%)	4 (5.1)	6 (16.2)	0.074

Continuous variables are reported as median [Q1–Q3], and categorical variables as absolute frequency and percentage. Bold values indicate significance, $p < 0.05$.

Table 7.2: Median [IQR] values and corresponding p-values for TPEMR, ΔTpe, and TMR in the PCA-transformed lead and the $V1_{2IC}$ and $V2_{2IC}$ leads across the three predefined group comparisons. Bold values indicate statistical significance, $p < 0.05$.

Group	TPEMR			ΔT_{pe}			TMR		
	PCA	$V1_{2IC}$	$V2_{2IC}$	PCA	$V1_{2IC}$	$V2_{2IC}$	PCA	$V1_{2IC}$	$V2_{2IC}$
CG	0.005[0.006]	0.007[0.009]	0.007[0.008]	0.012[0.014]	0.016[0.020]	0.019[0.016]	0.012[0.009]	0.010[0.010]	0.012[0.011]
BrS	0.009[0.013]	0.008[0.009]	0.009[0.015]	0.019[0.030]	0.017[0.025]	0.024[0.028]	0.015[0.012]	0.013[0.012]	0.016[0.012]
p-value	**0.014**	0.622	0.062	**0.043**	0.798	0.051	0.061	0.138	0.055
BrS-A	0.009[0.015]	0.008[0.009]	0.010[0.015]	0.021[0.027]	0.017[0.025]	0.025[0.030]	0.015[0.012]	0.013[0.013]	0.016[0.010]
BrS-S	0.010[0.011]	0.008[0.008]	0.011[0.012]	0.017[0.030]	0.016[0.024]	0.023[0.027]	0.015[0.012]	0.012[0.008]	0.016[0.009]
p-value	0.974	0.981	0.864	0.988	0.745	0.455	0.654	0.895	0.688
BrS-I	0.011[0.013]	0.008[0.010]	0.009[0.008]	0.023[0.030]	0.016[0.026]	0.024[0.025]	0.019[0.013]	0.014[0.015]	0.019[0.011]
BrS-II	0.007[0.014]	0.008[0.009]	0.011[0.014]	0.018[0.027]	0.017[0.024]	0.024[0.029]	0.013[0.011]	0.012[0.011]	0.015[0.008]
p-value	0.071	0.828	0.232	0.236	0.814	0.452	**0.006**	**0.028**	**0.039**

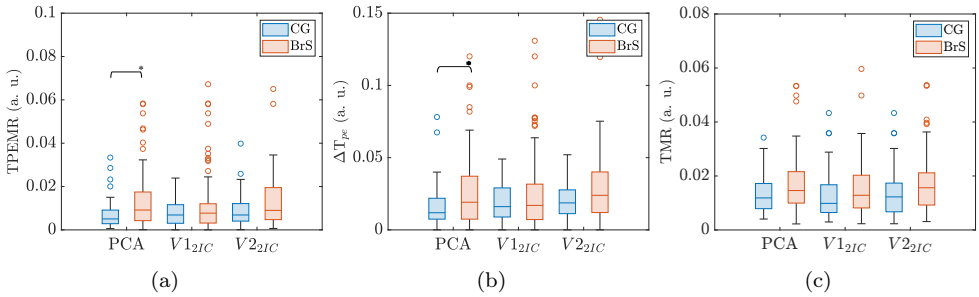


Figure 7.3: Box plot distributions of TPEMR (a), ΔT*pe* (b), and TMR (c) for CG (blue) and BrS patients (red), shown for the PCA-transformed lead, $V1_{2IC}$, and $V2_{2IC}$. * indicates statistical significance, $p < 0.05$.

BrS-I patients showed higher TMR values than BrS-II patients in the PCA-transformed lead (0.019 [0.013] vs 0.013 [0.011], $p = 0.006$), $V1_{2IC}$ lead (0.014 [0.015] vs 0.012 [0.011], $p = 0.028$), and $V2_{2IC}$ lead (0.019 [0.011] vs 0.015 [0.008], $p = 0.039$). No significant differences between BrS-I and BrS-II were observed for TPEMR or ΔT*pe* (Figure 7.4 and Table 7.2).

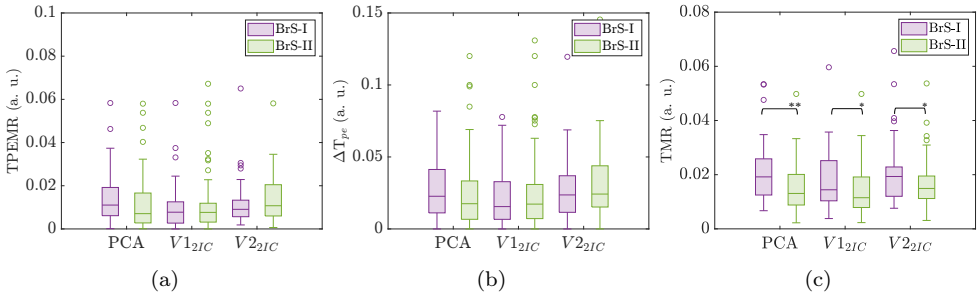


Figure 7.4: Comparison of TPEMR (a), ΔT*pe* (b), and TMR (c) distributions between BrS-I (purple) and BrS-II (green) patients in the PCA-transformed lead and the $V1_{2IC}$ and $V2_{2IC}$ leads. * and ** indicate statistical significance at $p < 0.05$ and $p < 0.01$, respectively.

Figure 7.5 shows the distributions obtained for BrS-A and BrS-S patients. No significant differences between BrS-A and BrS-S patients were observed for TPEMR, ΔT*pe*, or TMR in the PCA-transformed, $V1_{2IC}$, or $V2_{2IC}$ lead, as also summarized in Table 7.2.

7.3.3 T-wave Morphology Variation Markers

As shown in Figure 7.6, TPEMV values in $V1_{4IC}$ were significantly lower in BrS than in CG in 14 of the 15 analyzed RR bins, covering the range from

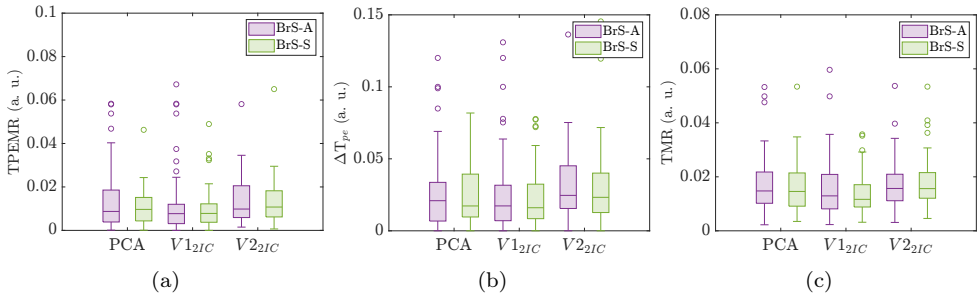


Figure 7.5: Box plot distributions of TPEMR (a), ΔTpe (b), and TMR (c) for BrS-A (purple) and BrS-S (green) patients in the PCA-transformed lead and the $V1_{2IC}$ and $V2_{2IC}$ leads. No statistically significant differences were observed between groups.

650 to 1350 ms. The BrS group showed predominantly more negative values and broader distributions across these intervals. In contrast, the distributions largely overlapped in $V2_{4IC}$, with no significant differences between groups. Differences in TMV were more limited and lead-dependent: BrS showed more negative values only in the 650–700 ms bin in $V1_{4IC}$, whereas values were less negative in five bins covering 600–700 and 750–900 ms in $V2_{4IC}$, as summarized in Table 7.3.

BrS-I patients exhibited more negative TPEMV values than BrS-II patients in both analyzed leads. In $V1_{4IC}$, significant differences were observed in 4 of 15 RR bins, distributed across 600–700, 1100–1150, and 1250–1300 ms, whereas significant differences in $V2_{4IC}$ extended continuously from 1050 to 1350 ms, comprising 6 of 15 bins. For TMV, BrS-I patients also showed more negative values in $V1_{4IC}$ in 6 of 15 bins, corresponding to 850–900 and 1000–1250 ms, while no significant differences were observed in $V2_{4IC}$. These findings are summarized in Table 7.3.

Figure 7.7 shows the TPEMV distributions obtained for BrS-A and BrS-S patients. In $V1_{4IC}$, a significant difference was confined to the 1200–1250 ms RR bin, with BrS-A showing more negative values, whereas no significant differences were observed in $V2_{4IC}$. For TMV, BrS-S showed more negative values in three non-contiguous RR bins in V14IC, corresponding to 700–750, 850–900, and 1050–1100 ms, while no significant differences were found in V24IC. Overall, differences between symptomatic and asymptomatic patients were limited and did not show a consistent pattern across RR intervals, as summarized in Table 7.3.

Table 7.3: Summary of significant group differences for morphology variation markers. For each comparison, the direction of the median difference, the RR intervals showing statistical significance, and the number of significant bins are reported. A dash indicates that no statistically significant RR intervals were identified

Marker/lead	Comparison	Main finding	Significant RR intervals (ms)	Sig. bins
TPEMV $V1_{4IC}$	BrS vs CG	BrS more negative than CG	650–1350	14/15
TPEMV $V1_{4IC}$	BrS-S vs BrS-A	BrS-A more negative	1200–1250	1/15
TPEMV $V1_{4IC}$	BrS-I vs BrS-II	BrS-I more negative	600–700, 1100–1150, 1250–1300	4/15
TPEMV $V2_{4IC}$	BrS vs CG	Overlapping distributions	–	0/15
TPEMV $V2_{4IC}$	BrS-S vs BrS-A	Overlapping distributions	–	0/15
TPEMV $V2_{4IC}$	BrS-I vs BrS-II	BrS-I more negative	1050–1350	6/15
TMV $V1_{4IC}$	BrS vs CG	BrS more negative	650–700	1/15
TMV $V1_{4IC}$	BrS-S vs BrS-A	BrS-S more negative	700–750, 850–900, 1050–1100	3/15
TMV $V1_{4IC}$	BrS-I vs BrS-II	BrS-I more negative	850–900, 1000–1250	6/15
TMV $V2_{4IC}$	BrS vs CG	BrS less negative	600–700, 750–900	5/15
TMV $V2_{4IC}$	BrS-S vs BrS-A	Overlapping distributions	–	0/15
TMV $V2_{4IC}$	BrS-I vs BrS-II	Overlapping distributions	–	0/15

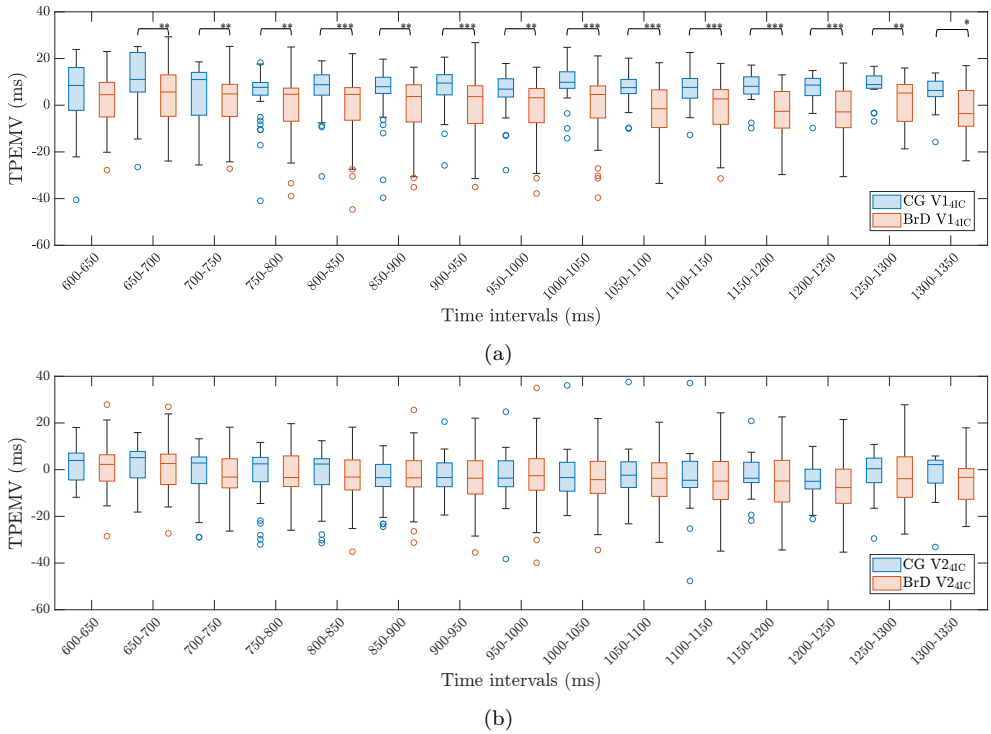


Figure 7.6: Distributions of TPEMV across the analyzed RR intervals for CG (blue) and BrS patients (red) in $V1_{4IC}$ (a) and $V2_{4IC}$ (b). *, **, and ***, indicate $p < 0.05$, $p < 0.01$, and $p < 0.001$, respectively.

7.3.4 Classical Repolarization and Depolarization-related ECG Markers

Compared with CG, patients with BrS showed higher T_{pe} values in $V1_{4IC}$ across 14 of the 15 analyzed RR bins, covering the range from 650 to 1350 ms. In contrast, no significant differences in T_{pe} were observed in $V2_{4IC}$. The results for T_w were lead-dependent: BrS patients showed higher values in 7 of 15 bins in $V1_{4IC}$, whereas lower values were found in 6 bins in $V2_{4IC}$. The most consistent differences were observed for QRS_d, which was higher in BrS across all RR bins in $V1_{4IC}$ and in 12 of 15 bins in $V2_{4IC}$. These results are summarized in Table 7.4.

As shown in Figure 7.8, BrS-I patients exhibited higher T_{pe} values than BrS-II patients in both analyzed leads. Significant differences were observed in 6 of 15 RR bins in $V1_{4IC}$, distributed across 800–900, 1050–1200, and 1250–1300 ms, and in 5 bins in $V2_{4IC}$, covering the continuous range from 1050 to

Table 7.4: Summary of the group comparisons for T_{pe}, T_w, and QRS_d in $V1_{4IC}$ and $V2_{4IC}$. The direction of the median difference, the RR intervals showing statistical significance, and the number of significant bins out of the 15 analyzed bins are reported. A dash indicates that no statistically significant RR intervals were identified.

Marker/lead	Comparison	Main finding	Significant RR intervals (ms)	Sig. bins
T_{pe}, $V1_{4IC}$	BrS vs CG	BrS higher	650–1350	14/15
	BrS-I vs BrS-II	BrS-I higher	800–900, 1050–1200, 1250–1300	6/15
	BrS-S vs BrS-A	Overlapping distributions	–	0/15
T_{pe}, $V2_{4IC}$	BrS vs CG	Overlapping distributions	–	0/15
	BrS-I vs BrS-II	BrS-I higher	1050–1300	5/15
	BrS-S vs BrS-A	BrS-S lower	800–850	1/15
T_w, $V1_{4IC}$	BrS vs CG	BrS higher	750–850, 900–950, 1000–1150, 1200–1250	7/15
	BrS-I vs BrS-II	BrS-I higher	1100–1150	1/15
	BrS-S vs BrS-A	BrS-S higher	650–800	3/15
T_w, $V2_{4IC}$	BrS vs CG	BrS lower	600–650, 750–1000	6/15
	BrS-I vs BrS-II	BrS-I lower	800–1100	6/15
	BrS-S vs BrS-A	Overlapping distributions	–	0/15
QRS_d, $V1_{4IC}$	BrS vs CG	BrS higher	600–1350	15/15
	BrS-I vs BrS-II	BrS-I higher	600–1050	9/15
	BrS-S vs BrS-A	Overlapping distributions	–	0/15
QRS_d, $V2_{4IC}$	BrS vs CG	BrS higher	600–700, 800–1300	12/15
	BrS-I vs BrS-II	BrS-I higher	900–1050, 1100–1300	7/15
	BrS-S vs BrS-A	BrS-S higher	950–1050, 1100–1150	3/15

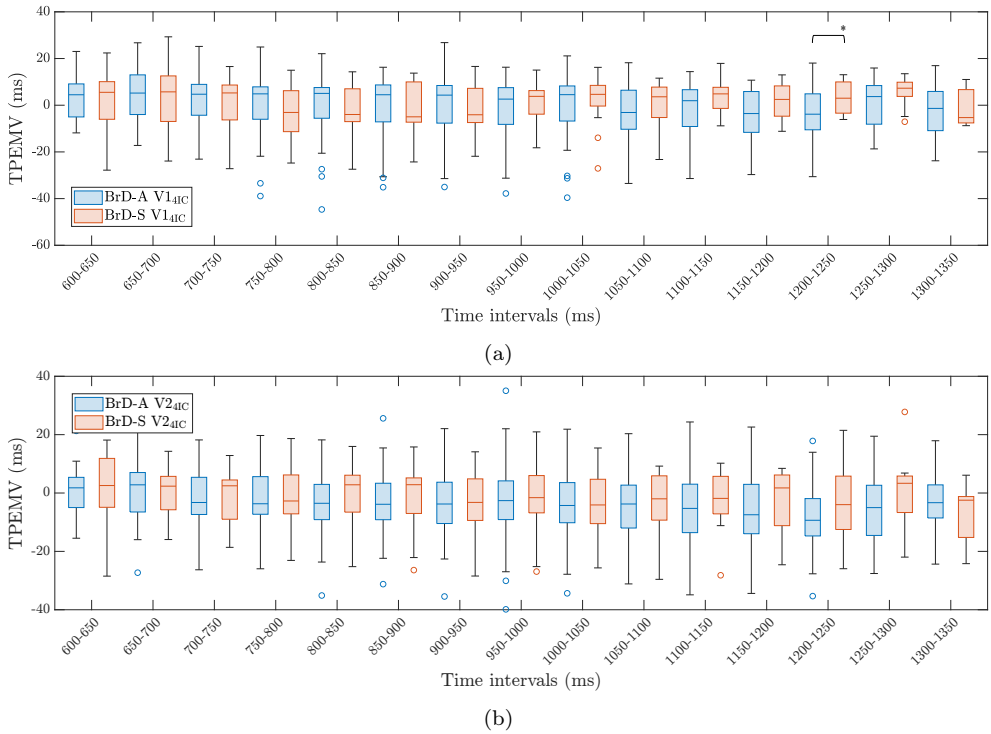


Figure 7.7: Comparison of TPEMV values between BrS-A (blue) and BrS-S (red) patients over the analyzed RR intervals in $V1_{4IC}$ (a) and $V2_{4IC}$ (b). * indicates statistical significance at $p < 0.05$.

1300 ms. For T_w, BrS-I patients showed higher values only in the 1100–1150 ms bin in $V1_{4IC}$, whereas lower values were observed from 800 to 1100 ms in $V2_{4IC}$. BrS-I patients also showed higher QRS_d values in both leads, with significant differences in 9 of 15 bins in $V1_{4IC}$ and 7 of 15 bins in $V2_{4IC}$.

Differences between BrS-A and BrS-S patients were less extensive. No significant differences in T_{pe} were observed in $V1_{4IC}$, while BrS-S patients showed lower values only in the 800–850 ms bin in $V2_{4IC}$. For T_w, BrS-S patients exhibited higher values in three consecutive bins from 650 to 800 ms in $V1_{4IC}$, with no differences in $V2_{4IC}$. No significant differences in QRS_d were found in $V1_{4IC}$, whereas higher values in BrS-S patients were observed in three bins between 950 and 1150 ms in $V2_{4IC}$. The complete results for the three markers are summarized in Table 7.4.

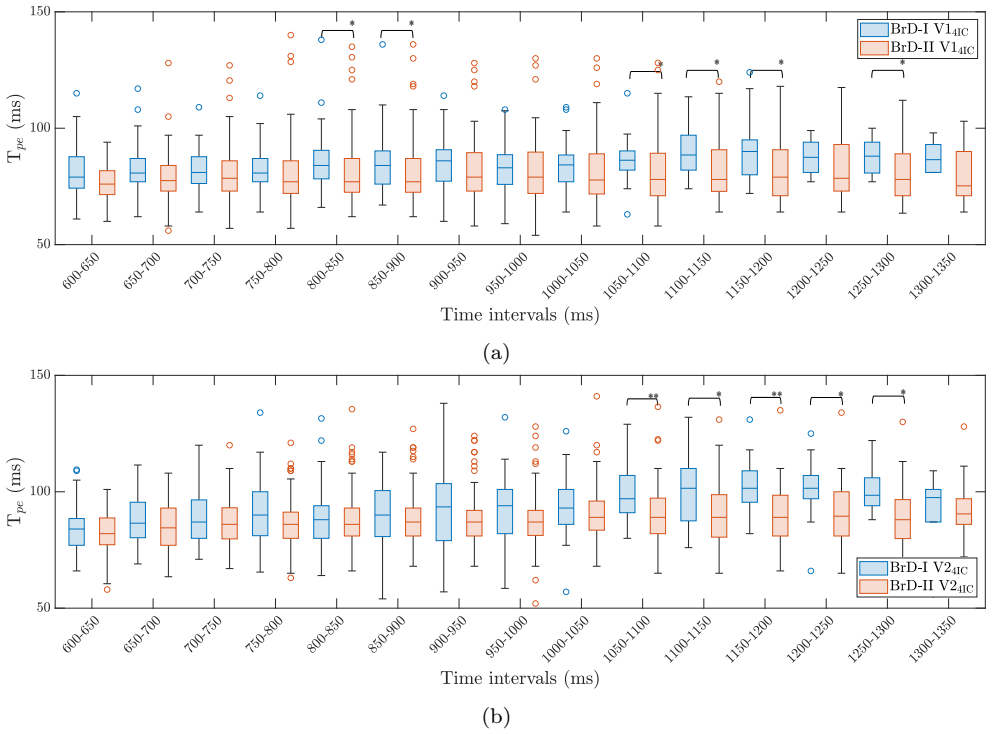


Figure 7.8: Box plot distributions of T*pe* for BrS-I (blue) and BrS-II (red) patients across the analyzed RR intervals in V14IC (a) and V2$_{4IC}$ (b). * indicates statistical significance at $p < 0.05$.

7

7.4 Discussion

In this study, ventricular repolarization and depolarization were characterized in patients with BrS by evaluating morphology restitution and variation indices over both the complete T wave and the T_{pe} interval, together with conventional repolarization and depolarization-related ECG markers. Overall, the morphology-based markers showed limited and lead-dependent discriminatory ability. The main findings were that TPEMR and ΔT_{pe} showed differences between patients in BrS and CG groups only in the PCA-transformed lead, with TPEMR reaching higher significance than ΔT_{pe} reproducing the warping superiority behavior observed in previous chapters and highlighting the ability of the PCA-transformed lead to capture repolarization information distributed across the precordial leads. TMR was associated with the presence of a spontaneous type-I pattern across all three analyzed leads. Among the

population-referenced indices, TPEMV showed the most consistent differences between BrS and CG in $V1_{4IC}$ and between BrS-I and BrS-II in both analyzed leads, while TMV provided less consistent and more lead-dependent results. Importantly, none of the morphology-based indices consistently differentiated BrS-S from BrS-A patients. The classical T_{pe} interval largely reproduced the patterns observed for TPEMV, whereas T_w showed a more heterogeneous lead-dependent behavior. Finally, QRS_d exhibited the most consistent overall differences, with higher values in BrS than in CG and in BrS-I than in BrS-II, while the clearest differences related to clinical presentation were localized in $V2_{4IC}$ at intermediate-to-long RR intervals.

The higher TPEMR and $\Delta T pe$ values observed in patients with BrS suggest a greater rate-dependent variation in terminal ventricular repolarization than in CG (see Figure 7.3 and Table 7.2). However, this comparison should be interpreted with caution because ΔRR was significantly larger in CG than in BrS. Given the nonlinear behavior of restitution, the wider RR range in controls may have contributed to the lower normalized restitution values observed in this group. Importantly, these differences were detected only in the PCA-transformed lead and not in either $V1_{2IC}$ or $V2_{2IC}$. Since the PCA lead integrates information from the six precordial leads while emphasizing their dominant repolarization component, this finding suggests that the alterations captured by TPEMR may be spatially distributed and not consistently projected onto individual right precordial leads. The absence of significant differences in TMR between BrS and CG is consistent with the possibility that restricting the analysis to the T_{pe} interval may improve the detection of BrS-related dynamic changes by reducing the contribution of the earlier ST–T region, whose morphology is markedly influenced by the characteristic Brugada pattern.

A different behavior was observed according to the presence of a spontaneous type-I pattern. BrS-I patients exhibited higher TMR values in all three analyzed leads, whereas neither TPEMR nor ΔT_{pe} differed significantly between BrS-I and BrS-II (see Figure 7.4 and Table 7.2). This suggests that the increased morphological variation with heart rate associated with the spontaneous type-I phenotype may predominantly involve the complete ST–T complex rather than its terminal portion alone. Such an interpretation is compatible with the intrinsically dynamic nature of the Brugada ECG pattern and with invasive studies reporting altered repolarization restitution in patients exhibiting a type-I Brugada ECG and regional repolarization heterogeneity in BrS [156, 266], and also with the prolongation of the late depolarization effects on the initial part of the ST-T complex with the coved ST-segment signature

in type-I. However, none of the restitution markers differentiated BrS-S from BrS-A patients (see Figure 7.5 and Table 7.2). Taken together, these findings suggest that changes in T-wave morphology with heart rate were more clearly associated with the spontaneous type-I pattern than with the presence of symptoms in this cohort.

The comparison with population-matched reference waveforms provided a clearer distinction when the analysis was restricted to the T_{pe} interval. TPEMV showed consistent differences between BrS and CG in $V1_{4IC}$, whereas TMV presented only isolated and lead-dependent differences (see Figure 7.6 and Table 7.3). This suggests that the terminal part of the T-wave contains morphology information associated with the Brugada phenotype that may be partly obscured when the complete T wave is analyzed. The contrasting results between adjacent right precordial leads further indicate that this information is strongly dependent on its spatial projection. Moreover, the separation between BrS and CG across almost the entire RR range in $V1_{4IC}$ suggests that this difference was not restricted to a particular heart-rate range. Since TPEMV is a signed marker, its more negative values in BrS reflect the direction of the time-warping and not a lower morphology variation. Within the BrS cohort, the continuous differences between BrS-I and BrS-II at longer RR intervals in $V2_{4IC}$ suggest that the morphology alterations associated with the spontaneous type-I pattern may become more evident at slower heart rates in this lead, in line with the recognized bradycardic and vagotonic accentuation of the Brugada phenotype [267]. However, neither TPEMV nor TMV consistently differentiated BrS-S from BrS-A, and the isolated significant bins did not support a consistent RR-related pattern.

The classical T_{pe} interval showed a broadly similar behavior to TPEMV, suggesting that the warping-based marker reflects physiologically meaningful alterations in terminal repolarization (see Figure 7.8 and Table 7.4). Importantly, TPEMV extends the classical measurement by characterizing morphology differences and their variation across RR ranges, thereby providing complementary information beyond T_{pe} duration alone. Neither marker consistently differentiated BrS-S from BrS-A, in agreement with the conflicting evidence reported for T_{pe} in BrS: longer values have been associated with recurrent or major arrhythmic events [188, 247, 268], whereas no such association was found in a larger cohort [269]. Differences in clinical endpoints, lead selection, and the use of isolated rather than RR-stratified measurements may partly explain these discrepancies.

The most consistent differences were observed for QRS_d, with higher values in BrS than in CG and in BrS-I than in BrS-II across multiple RR intervals

(see Table 7.4). As expected, these patterns are consistent with the recognized presence of ventricular conduction abnormalities in the Brugada phenotype. In particular, previous studies have similarly associated prolonged QRS duration in V2 with symptoms and arrhythmic vulnerability [270,271], while more recent evidence has shown abnormal rate-dependent QRS prolongation in BrS [272]. In our cohort, the only symptom-related differences were localized in $V2_{4IC}$ at intermediate-to-long RR intervals, suggesting that their expression may depend on both lead location and heart rate. However, these findings should be interpreted considering that QRS_d was measured separately in each lead and may be influenced by QRS-end delineation inaccuracies in the right precordial leads.

Taken together, these findings are consistent with a combined contribution of repolarization and depolarization abnormalities in BrS. Morphology-based markers were more closely related to the Brugada phenotype and spontaneous type-I expression, whereas QRS_d showed the clearest, although localized, differences associated with symptoms. This complementary pattern is consistent with evidence that both conduction delay and repolarization heterogeneity contribute to the arrhythmogenic substrate in BrS [156]. The marked dependence on lead and RR interval further suggests that these abnormalities are spatially localized and dynamically modulated rather than uniformly expressed on the surface ECG.

7.4.1 Limitations

The interpretation of these findings should take into account some aspects of the study design. The relatively limited sample size, particularly within the BrS subgroups, may have reduced the statistical power and stability of some comparisons. The BrS and control groups differed in age and sex distribution, and the subgroup sizes were unequal, which may have influenced the comparisons. No adjustment was performed for potential confounding factors, particularly age, so some of the observed between-group differences may partly reflect these demographic imbalances. For the population-referenced morphology variation indices, the UK Biobank reference waveforms were matched by sex, heart rate, and lead, but not by age. In addition, these reference ECGs were acquired at rest in the supine position, whereas the BrS and control recordings were obtained under ambulatory daily-life conditions. Differences in age, body position, and activity may therefore have contributed to the observed morphology differences relative to the reference waveforms. In addition, the bin-wise analysis across RR intervals was exploratory and involved mul-

tiple comparisons, for which no correction was applied, potentially increasing the probability of false-positive findings, particularly for isolated significant RR bins, while the number of available beats varied among subjects and RR bins. Automated delineation of the QRS end, T-wave peak, and T-wave end may be challenging in the right precordial leads of patients with BrS, potentially increasing measurement variability and contributing to some lead-dependent differences. Therefore, these results should be interpreted cautiously. Finally, classification based primarily on previous symptoms does not provide the same prognostic information as a prospective time-to-event analysis, and validation in an independent prospective cohort is therefore warranted.

7.5 Conclusions

This chapter investigated ventricular repolarization and depolarization in Brugada syndrome using morphology restitution and variation indices together with conventional ECG markers. Overall, the morphology-based markers showed limited and lead-dependent discriminatory ability. TPEMR differentiated BrS from CG only in the PCA-transformed lead, whereas TMR was associated with the spontaneous type-I pattern across all three analyzed leads. Among the morphology variation indices, TPEMV provided the most consistent characterization of both the Brugada phenotype and spontaneous type-I expression, while TMV showed fewer and more lead-dependent differences. None of the morphology-based indices consistently differentiated BrS-S from BrS-A. In contrast, QRS_d showed the broadest overall differences and the clearest, although localized, separation between BrS-S and BrS-A in $V2_{4IC}$. Thus, these findings suggest a complementary role for T-wave morphology analysis in the non-invasive phenotypic characterization of BrS, particularly regarding spontaneous type-I expression, while validation in larger independent cohorts is needed to establish their potential clinical utility.

CHAPTER 8

CONCLUSIONS AND FUTURE WORK

8.1 Discussion of Main Achievements

8.1.1 Methodological Framework for T-wave Morphology Assessment

8.1.2 T-Peak-to-End Morphology in Ischemia-Induced Arrhythmic Risk

8.1.3 T-Wave Morphology Markers in Cardiac Channelopathies

8.1.4 Overall Contribution to Arrhythmic Risk Stratification

8.2 General Conclusions

8.3 Future Work

The main objective of this thesis was to evaluate quantitative ECG-based markers that characterize T-wave morphology for ventricular arrhythmic risk assessment. This objective was motivated by the need to move beyond conventional fiducial-point-based measurements, which may capture only a limited part of the information contained in ventricular repolarization, particularly when repolarization abnormalities are expressed as complex morphological changes rather than as isolated interval prolongation or shortening. To address this limitation, the thesis focused on time-warping-based markers able to quantify morphology differences between T waves and to provide a complementary, morphology-aware description of ventricular repolarization.

The work was developed across complementary scenarios in which malignant ventricular arrhythmias represent a major clinical concern, including myocardial ischemia and infarction, LQTS, and BrS. Within this frameworks, the

thesis aimed to assess whether T-wave morphology markers could improve the non-invasive characterization of arrhythmogenic substrates, provide additional information beyond classical ECG indices, and support ventricular arrhythmic risk assessment in different clinical and experimental settings.

8.1 Discussion of Main Achievements

The main achievements of this thesis can be grouped into three complementary contributions: first, the adaptation of a time-warping methodology to quantify T-peak-to-end morphology changes for arrhythmic risk assessment; second, the evaluation of this marker in human and porcine models of myocardial ischemia and infarction; and third, the assessment of full T-wave morphology markers in cardiac channelopathies, including LQTS and BrS.

8.1.1 Methodological Framework for T-wave Morphology Assessment

A first achievement of the thesis was the design of a ECG processing strategy that integrated a time-warping methodology into a framework for T_{pe} morphology analysis in ventricular arrhythmic risk assessment. This strategy included signal preprocessing, fiducial detection and delineation, spatial transformation through PCA, segmentation into analysis windows and definition of the corresponding reference for morphology comparison, and the computation of morphology markers based on time-warping analysis. This framework made it possible to quantify differences between T waves not only in terms of duration, but also in terms of the time-warping required to align their morphology. In this context, the use of signed and unsigned warping markers, together with T-wave peak-to-end restricted formulations and population-reference approaches, provided a flexible methodological basis for the studies developed in this thesis.

8.1.2 T-Peak-to-End Morphology in Ischemia-Induced Arrhythmic Risk

A central contribution of the thesis was the evaluation of T-wave peak-to-end morphology in ischemic conditions. In the human PCI model, the time-warping-based index restricted to the T-wave peak-to-end interval, $d^{\mathrm{PCA}}_{w,\mathrm{T}_{pe}}$, was shown to track ischemia-induced morphology changes during transient coronary occlusion. This restriction was important because it focused the analysis on a region closely related to ventricular repolarization dispersion while re-

ducing the influence of ST-segment deviations, which are prominent during ischemia and may interfere with markers computed over the entire T wave. The study showed that the changes captured by the marker during PCI clearly exceeded the variability observed in control recordings, supporting its ability to distinguish ischemia-induced repolarization alterations from normal short-term ECG variability. Prevalence analysis further indicated that these alterations were present in a large proportion of patients and appeared early after coronary occlusion, suggesting that T-peak-to-end morphology is rapidly affected when the myocardial blood supply is compromised.

Compared with classical local measurements, the main advantage of the warping-based marker was not simply an earlier response, but a stronger and more sensitive quantification of ischemia-induced changes over the analyzed interval. This was particularly relevant when compared with the conventional T_{pe} interval, since both markers characterize the same region of the T wave, but $d_{w,T_{pe}}^{PCA}$ uses the morphology of the whole T-peak-to-end segment rather than the distance between two fiducial points. Although ST-segment deviation also showed high sensitivity, it reflects injury-current mechanisms rather than repolarization dispersion, reinforcing the complementary nature of the proposed marker. The spatial analysis additionally suggested regional differences according to the occluded artery, with changes tending to appear in leads related to the affected myocardial area, although these findings were exploratory and limited by the available information on the extent and location of ischemic injury. The observed increase in the warping index during ischemia progression suggested that T-wave peak-to-end morphology captures relevant changes in repolarization heterogeneity.

The same marker was subsequently evaluated in a closed-chest porcine myocardial infarction model, where the longer observation period after coronary occlusion allowed the temporal evolution of the marker to be related to VF occurrence. In this setting, dynamic increases in the magnitude of $d_{w,T_{pe}}^{PCA}$ were associated with delayed-VF episodes and showed better predictive performance than the classical T_{pe}^{PCA} interval as ischemia progressed. Beyond confirming that T-peak-to-end morphology changes increased during coronary occlusion, this study showed that the temporal profile of the marker differed between animals that developed delayed-VF and those that did not. While both $d_{w,T_{pe}}^{PCA}$ and T_{pe}^{PCA} increased after occlusion, the warping-based index displayed a smoother and more stable evolution, with greater changes in the delayed-VF group and significant intergroup differences already in the early ischemic intervals. This supported the interpretation that the morphology-based marker captured ischemia-induced repolarization alterations related to arrhythmic vulnerability

more robustly than the classical T_{pe} interval.

The comparison with the warping marker computed over the whole T wave further reinforced the relevance of restricting the analysis to the T-peak-to-end interval in this setting. Although whole T-wave morphology also changed during ischemia, it did not discriminate between delayed-VF and non-VF animals, suggesting that the early part of the T wave and the influence of ST-segment deviations may mask the repolarization changes most closely related to arrhythmic risk. In contrast, $d^{\mathrm{PCA}}_{w,\mathrm{T}_{pe}}$ consistently provided higher discrimination and stronger risk association than $\mathrm{T}^{\mathrm{PCA}}_{pe}$, including comparisons between time intervals aligned with VF occurrence. This result extended the findings from the human PCI study by showing that the morphology changes captured by the warping marker were not only sensitive to ischemia, but also relevant to arrhythmic risk prediction under evolving infarction conditions. Moreover, the focus on delayed-VF episodes gave the analysis potential translational relevance, since these arrhythmias are more closely related to the post-occlusion phase in which clinical intervention may still be possible.

A further step was provided by the analysis using an open-chest porcine infarction model, in which simultaneous body-surface ECG and intramyocardial recordings allowed the warping-based marker to be compared with invasive measurements of DOR. This chapter strengthened the physiological interpretation of the marker by showing that $d^{\mathrm{PCA}}_{w,\mathrm{T}_{pe}}$ may be a potential non-invasive surrogate of the invasive DOR measurement. Unlike the previous porcine study, where the association with delayed-VF supported the prognostic value of the marker, this model provided a direct mechanistic reference by measuring repolarization dispersion from intramyocardial recordings. The parallel temporal changes observed for $d^{\mathrm{PCA}}_{w,\mathrm{T}_{pe}}$ and DOR, together with the increasing separation between Delayed-VF and Non-VF animals, supported the interpretation that the T_{pe} morphology changes captured on the ECG are related to the increase in repolarization dispersion during ischemia.

The agreement between both indices was further supported by individual linear regression analyses across time, which showed that the warping-based marker was not merely associated with the occurrence of VF, but also tracked the invasive DOR index across the ischemic process. Importantly, this relationship was stronger than that observed for the classical T_{pe} interval, indicating that the morphology-based analysis provided additional temporal-morphological information beyond what T_{pe} interval can convey. Moreover, its predictive performance for delayed-VF occurrence was comparable to that of DOR, while performing earlier and more robust than the classical T_{pe} index. This finding is particularly relevant because DOR is an invasive measurement,

whereas $d^{\mathrm{PCA}}_{w,\mathrm{T}_{pe}}$ can be measured from the surface ECG, making it a more feasible candidate for non-invasive risk assessment.

Taken together, the ischemia studies support a coherent progression: the marker detects ischemia-induced repolarization changes in humans, identifies animals at higher risk of VF during myocardial infarction, and shows potential as a non-invasive surrogate of invasive DOR. This sequence provides a stronger physiological and translational basis for T-peak-to-end morphology analysis than any of the individual studies alone, moving from sensitivity to ischemia, to arrhythmic risk association, and finally to mechanistic validation against invasive DOR.

8.1.3 T-Wave Morphology Markers in Cardiac Channelopathies

The thesis also extended the evaluation of time-warping-based T-wave morphology markers to cardiac channelopathies, including LQTS and BrS. In LQT2, the TMV index quantified T-wave morphology abnormalities by comparing each patient's T wave with a sex-, heart-rate-, and lead-matched normal reference. This approach was particularly relevant in LQT2, where arrhythmic risk is not fully explained by repolarization duration and where abnormal T-wave morphologies may carry additional clinical information. By quantifying the time-warping required to align each patient's T wave to a matched reference, TMV provided an integrated descriptor of morphology abnormality from a single-lead, full T-wave, reference-based analysis.

The results showed that TMV in lead I was significantly associated with the risk of cardiac events in LQT2 patients, even after adjustment for QT_c, sex, and MCS. Patients with lower TMV values showed worse event-free survival, supporting the hypothesis that T-wave morphology abnormalities reflect clinically relevant repolarization features. Importantly, the association persisted after accounting for QT_c, indicating that the marker did not simply reproduce the information contained in repolarization duration. The fact that analogous risk analyses using T_{Amp} and MCS were not significantly associated with cardiac events in this cohort further suggested that the time-warping-based marker captured morphology-related risk information not fully represented by existing descriptors of T-wave shape. Overall, these findings support the potential of time-warping-based T-wave morphology analysis as a complementary approach to current risk stratification in LQT2, while also emphasizing the need for larger independent studies to confirm its prognostic value and define its incremental contribution.

In BrS, the time-warping framework was extended to characterize both

the T-wave morphology changes with heart rate and its differences with respect to normal population references. Overall, the morphology-based markers showed limited and lead-dependent discriminatory ability. The evaluation of morphology restitution showed that TPEMR discriminated patients with BrS from control subjects in the PCA-transformed lead, whereas TMR was associated with the presence of a spontaneous type-I pattern across all analyzed leads. These findings suggest that restricting the analysis to the T_{pe} interval may improve the detection of dynamic repolarization differences between BrS and controls, while changes associated with spontaneous type-I expression may involve the complete ST-T complex.

Among the population-reference repolarization morphology markers, TPEMV provided the most consistent characterization of the Brugada phenotype and spontaneous type-I expression. Differences between BrS and controls were observed across most RR intervals in $V1_{4IC}$, while differences between BrS-I and BrS-II patients were found in both analyzed leads and were particularly evident at longer RR intervals in $V2_{4IC}$. In contrast, TMV showed fewer and more lead-dependent differences. None of the morphology-based markers consistently differentiated symptomatic from asymptomatic patients. The broader differences observed for QRS_d, including localized symptom-related differences in $V2_{4IC}$, were consistent with the complementary contribution of repolarization and depolarization abnormalities to the Brugada phenotype. Overall, the marked dependence of the findings on lead location and RR interval suggests that these abnormalities are spatially localized and dynamically modulated rather than uniformly expressed on the surface ECG.

8.1.4 Overall Contribution to Arrhythmic Risk Stratification

Overall, the main achievement of this thesis is the demonstration that time-warping-based analysis of T-wave morphology can provide complementary information for ventricular arrhythmic risk assessment in different contexts. The markers evaluated here should not be interpreted as replacements for established clinical indices, but rather as additional descriptors of repolarization abnormalities. Their value lies in their ability to quantify morphology changes that may remain partially hidden when the analysis is reduced to fiducial intervals such as QT_c or T_{pe}. This morphology-based perspective may help to better characterize the electrical substrate underlying ventricular arrhythmias and to support the development of more individualized risk stratification strategies.

8.2 General Conclusions

The main conclusions of this thesis are:

1. Time-warping-based analysis provides a quantitative framework to characterize T-wave morphology beyond conventional fiducial-point measurements. By estimating the temporal deformation required to align T waves, these markers capture morphology differences that are not fully described by classical duration- or amplitude-based indices.

2. The T-wave peak-to-end restricted warping marker, $d^{\mathrm{PCA}}_{w,\mathrm{T}_{pe}}$, is sensitive to ischemia-induced repolarization changes. Its restriction to the final part of the T wave allows morphology changes related to repolarization to be assessed while reducing the influence of ST-segment deviations during ischemia.

3. In human transient coronary occlusion and porcine myocardial infarction models, $d^{\mathrm{PCA}}_{w,\mathrm{T}_{pe}}$ showed consistent relevance for the characterization of ischemia-induced repolarization abnormalities. In the porcine infarction model, dynamic changes in this marker were associated with delayed-VF occurrence and provided stronger arrhythmic risk information than the classical T_{pe} interval.

4. The comparison with invasive DOR measurements supported the potential role of $d^{\mathrm{PCA}}_{w,\mathrm{T}_{pe}}$ as a non-invasive surrogate descriptor of ventricular repolarization dispersion under ischemic conditions. This finding provides mechanistic support for the use of T-wave peak-to-end morphology analysis in the assessment of ischemia-induced arrhythmic risk.

5. In LQT2, complete T-wave morphology abnormalities quantified by the TMV index were associated with cardiac events even after adjustment for established clinical and electrocardiographic markers. This suggests that TMV may provide complementary risk information beyond QT_c duration in LQT2, although larger independent cohorts are needed to confirm its prognostic value.

6. In BrS, T-wave morphology restitution and variation markers identified repolarization abnormalities associated mainly with the Brugada phenotype and spontaneous Type-I expression. TPEMR differentiated patients with BrS from controls only in the PCA-transformed lead, whereas TMR and TPEMV showed associations with the spontaneous type-I pattern.

However, none of the morphology-based markers consistently differentiated symptomatic from asymptomatic patients, and their performance depended markedly on the specific lead and RR interval bin. Together with the broader differences observed for QRS_d, these findings support the complementary assessment of repolarization and depolarization abnormalities in BrS. They also suggest that morphology-based repolarization markers may be more useful for phenotypic characterization than for clinical risk stratification in this cohort. Nevertheless, their association with clinical outcomes and their potential prognostic value require futher evaluation in larger independent cohorts with prospective clinical follow-up.

7. Taken together, the results of this thesis support the use of time-warping-based T-wave morphology markers as complementary non-invasive tools for the characterization of ventricular repolarization abnormalities and arrhythmic risk across ischemic and cardiac channelopathies. Depending on the electrophysiological mechanisms under investigation, these markers may be derived either from the entire T wave or specifically from the T-peak-to-end interval.

8.3 Future Work

Future research lines derived from the development of this thesis are described in the following:

- In ischemic conditions, future studies should determine whether $d_{w,\mathrm{T}pe}^{\mathrm{PCA}}$ can support clinically useful risk stratification in human populations. The human PCI study demonstrated its ability to monitor transient ischemia-induced repolarization changes, while the porcine infarction models showed its association with delayed-VF and its relationship with invasive DOR. A natural continuation is to evaluate this marker in human cohorts with acute coronary syndromes, myocardial infarction, or other ischemic scenarios where arrhythmic outcomes and clinical follow-up are available.

- The spatial information contained in T-wave morphology changes should be further investigated. The human PCI study suggested regional differences according to the occluded artery, whereas the porcine infarction studies mainly relied on a spatially transformed PCA lead. Future analyses should confirm the value of using the PCA lead for marker compu-

tation and further investigate the spatial distribution of T_{pe} morphology changes across ECG leads in relation to the site of occlusion.

- Future work should address the selection of reference waveforms for morphology comparison. In the controlled experimental studies included in this thesis, reference T waves could be obtained from baseline or control recordings. However, in clinical practice, a stable pre-event reference may not always be available. Alternative approaches for defining the reference waveform should therefore be explored, including patient-specific previous recordings, disease-specific templates, or population-based references, as implemented in the TMV index.

- In LQT2, full T-wave morphology marker should be validated in larger and independent cohorts. The TMV index showed association with cardiac events beyond QT_c duration and other available electrocardiographic descriptors, but the study was retrospective and based on a limited number of patients and events. Larger multicenter cohorts are needed to confirm its prognostic value, evaluate its stability across subgroups defined by sex, genotype, treatment, and QT_c range, and determine whether it improves current risk stratification strategies.

- In BrS, morphology-based repolarization markers should be validated in larger independent cohorts with prospective clinical follow-up. Futures studies should confirm the lead- and RR-dependent patterns, and assess whether their combination with QRS_d improves phenotypic characterization and provides additional value for clinical risk stratification. Futures studies should also included control groups with comparable age and sex distributions to reduce potential demographic confounding.

- The robustness and standardization of the complete processing pipeline should be further assessed. The computation of time-warping-based markers depends on signal quality, preprocessing, delineation, lead selection, PCA transformation, window segmentation, and reference definition. Systematic evaluation of these factors would help determine the most reliable implementation of the methodology and reduce variability across different study settings

- The physiological interpretation of the warping-derived markers should be further explored. The comparison with invasive DOR provided an important step toward mechanistic validation, but additional studies combining surface ECG, intramyocardial recordings, imaging information,

and computational electrophysiological models could clarify how the observed morphology changes relate to spatial and temporal heterogeneity of ventricular repolarization.

- Future studies could further explore the information provided by the time-warping framework beyond the indices used in this thesis. In particular, the local profile of the warping function within the T wave or the T_{pe} interval could be analyzed to determine whether specific regions of the repolarization waveform contribute differently to arrhythmic risk. In addition, future work could investigate the joint contribution of time-warping and residual amplitude differences after alignment, either as complementary markers or as part of combined morphology-based model.

CHAPTER 9

CONCLUSIONES Y TRABAJO FUTURO

9.1 Discusión de las principales aportaciones

9.1.1 Marco metodológico para la evaluación de la morfología de la onda T

9.1.2 Morfología del intervalo entre el pico y el final de la onda T en el riesgo arrítmico inducido por isquemia

9.1.3 Marcadores de la morfología de la onda T en canalopatías cardíacas

9.1.4 Contribución general a la estratificación del riesgo arrítmico

9.2 Conclusiones generales

9.3 Trabajo futuro

El objetivo principal de esta tesis ha sido evaluar marcadores cuantitativos basados en el ECG que caractericen la morfología de la onda T para la evaluación del riesgo de arritmias ventriculares. Este objetivo surgió de la necesidad de ampliar las mediciones convencionales basadas en puntos fiduciales, las cuales pueden captar solo una parte limitada de la información contenida en la repolarización ventricular, especialmente cuando las anomalías de la repolarización se manifiestan como cambios morfológicos complejos en lugar de como una simple prolongación o acortamiento de los intervalos. Para abordar esta limitación, la tesis se centró en marcadores basados en *time-warping* capaces de cuantificar las diferencias morfológicas entre ondas T y de proporcionar una descripción complementaria de la repolarización ventricular que tenga en

cuenta la morfología.

El trabajo se desarrolló en escenarios complementarios donde las arritmias ventriculares malignas representan una preocupación clínica importante, incluyendo la isquemia y el infarto de miocardio, LQT2 y BrS. En este contexto, la tesis tuvo como objetivo evaluar si los marcadores de la morfología de la onda T podían mejorar la caracterización no invasiva de los sustratos arritmogénicos, aportar información adicional a la proporcionada por los índices clásicos del ECG y contribuir a la evaluación del riesgo de arritmias ventriculares en diversos entornos clínicos y experimentales.

9.1 Discusión de las principales aportaciones

Las principales aportaciones de esta tesis pueden agruparse en tres contribuciones complementarias: en primer lugar, la adaptación de una metodología basada en *time-warping* para cuantificar los cambios en la morfología del intervalo del pico al final de la onda T con fines de evaluación del riesgo arrítmico; en segundo lugar, la evaluación de este marcador en modelos humanos y porcinos de isquemia e infarto de miocardio; y en tercer lugar, la evaluación de marcadores de la morfología completa de la onda T en las canalopatías cardíacas LQT2 y BrS.

9.1.1 Marco metodológico para la evaluación de la morfología de la onda T

Un primer logro de la tesis fue el diseño de una estrategia de procesamiento de ECG que integra una metodología de *time-warping* en un marco para el análisis de la morfología del intervalo T_{pe} en la evaluación del riesgo de arritmias ventriculares. Esta estrategia incluye el preprocesamiento de la señal, la detección y delimitación de puntos fiduciales, la transformación espacial mediante PCA, la segmentación en ventanas de análisis y la definición de la referencia correspondiente para la comparación morfológica, así como el cálculo de marcadores morfológicos basados en el análisis de *time-warping*. Este marco permitió cuantificar las diferencias entre ondas T no solo en términos de duración, sino también en función del *time-warping* necesario para alinear sus morfologías. En este contexto, el uso de marcadores basados en *time-warping* con y sin signo, junto con formulaciones restringidas al intervalo entre el pico y el final de la onda T y enfoques basados en referencias poblacionales, proporcionó una base metodológica flexible para los estudios desarrollados en esta

tesis.

9.1.2 Morfología del intervalo entre el pico y el final de la onda T en el riesgo arrítmico inducido por isquemia

Una contribución fundamental de la tesis fue la evaluación de la morfología del intervalo entre el pico y el final de la onda T en condiciones de isquemia. En el modelo humano de PCI, se demostró que el índice basado en *time-warping*, restringido al intervalo entre el pico y el final de la onda T, $d_{w,\mathrm{T}_{pe}}^{\mathrm{PCA}}$, permitía seguir los cambios morfológicos inducidos por la isquemia durante la oclusión coronaria transitoria. Esta restricción resultó importante porque centró el análisis en una región estrechamente relacionada con la dispersión de la repolarización ventricular, al tiempo que reducía la influencia de las desviaciones del segmento ST, las cuales son pronunciadas durante la isquemia y pueden interferir con los marcadores calculados sobre la onda T completa. El estudio mostró que los cambios detectados por el marcador durante la PCI superaban claramente la variabilidad observada en los registros de control, lo que respalda su capacidad para distinguir las alteraciones de la repolarización inducidas por isquemia de la variabilidad normal del ECG a corto plazo. Asimismo, el análisis de prevalencia indicó que dichas alteraciones estaban presentes en una gran proporción de pacientes y aparecían poco después de la oclusión coronaria, lo que sugiere que la morfología del intervalo entre el pico y el final de la onda T se ve afectada rápidamente cuando el riego sanguíneo del miocardio se ve comprometido.

En comparación con las mediciones locales clásicas, la principal ventaja del marcador basado en *warping* no fue simplemente una respuesta más temprana, sino una cuantificación más robusta y sensible de los cambios inducidos por la isquemia a lo largo del intervalo analizado. Esto resultó especialmente relevante al compararlo con el intervalo convencional T_{pe}, dado que ambos marcadores caracterizan la misma región de la onda T, pero el parámetro $d_{w,\mathrm{T}_{pe}}^{\mathrm{PCA}}$ utiliza la morfología de todo el segmento comprendido entre el pico y el final de la onda T, en lugar de la distancia entre dos puntos fiduciales. Aunque la desviación del segmento ST también mostró una elevada sensibilidad, esta refleja mecanismos de corriente de lesión más que la dispersión de la repolarización, lo que refuerza el carácter complementario del marcador propuesto. El análisis espacial sugirió, además, la existencia de diferencias regionales en función de la arteria ocluida, observándose una tendencia a que los cambios aparecieran en las derivaciones correspondientes a la zona miocárdica afectada; no obstante, estos hallazgos tuvieron un carácter exploratorio y estuvieron limitados por la

información disponible sobre la extensión y localización de la lesión isquémica. El incremento observado en el índice de *warping* durante la progresión de la isquemia sugirió que la morfología del segmento entre el pico y el final de la onda T permite captar cambios relevantes en la heterogeneidad de la repolarización.

Posteriormente, se evaluó el mismo marcador en un modelo porcino de infarto de miocardio con tórax cerrado, donde el periodo de observación más prolongado tras la oclusión coronaria permitió relacionar la evolución temporal del marcador con la aparición de VF. En este contexto, los aumentos dinámicos en la magnitud de $d^{\mathrm{PCA}}_{w,\mathrm{T}_{pe}}$ se asociaron con episodios de VF tardía y mostraron una mejor capacidad predictiva que el intervalo clásico $\mathrm{T}^{\mathrm{PCA}}_{pe}$ a medida que progresaba la isquemia. Además de confirmar que los cambios en la morfología del segmento entre el pico y el final de la onda T aumentaban durante la oclusión coronaria, este estudio demostró que el perfil temporal del marcador difería entre los animales que desarrollaron VF tardía y aquellos que no lo hicieron. Si bien tanto $d^{\mathrm{PCA}}_{w,\mathrm{T}_{pe}}$ como $\mathrm{T}^{\mathrm{PCA}}_{pe}$ aumentaron tras la oclusión, el índice basado en *warping* mostró una evolución más suave y estable, con cambios más pronunciados en el grupo con VF tardía y diferencias significativas entre grupos ya desde los intervalos isquémicos iniciales. Esto respaldó la interpretación de que el marcador basado en la morfología captaba de forma más robusta que el intervalo T_{pe} clásico las alteraciones de la repolarización inducidas por la isquemia relacionadas con la vulnerabilidad arrítmica.

La comparación con el marcador de *warping* calculado sobre la onda T completa reforzó aún más la relevancia de limitar el análisis al intervalo entre el pico y el final de la onda T en este contexto. Aunque la morfología de la onda T en su totalidad también varió durante la isquemia, no permitió distinguir entre los animales que presentaron VF tardía y los que no, lo que sugiere que la porción inicial de la onda T y la influencia de las desviaciones del segmento ST podrían enmascarar los cambios en la repolarización más estrechamente vinculados al riesgo arrítmico. Por el contrario, $d^{\mathrm{PCA}}_{w,\mathrm{T}_{pe}}$ mostró de forma consistente una mayor capacidad de discriminación y una asociación más fuerte con el riesgo que $\mathrm{T}^{\mathrm{PCA}}_{pe}$, incluidas las comparaciones entre intervalos temporales alineados con la aparición de la VF. Este resultado amplía las conclusiones del estudio realizado en humanos sometidos a PCI, al demostrar que los cambios morfológicos detectados por el marcador de *warping* no solo eran sensibles a la isquemia, sino también relevantes para predecir el riesgo arrítmico durante la evolución del infarto. Además, centrar el análisis en los episodios de VF tardía le otorgó una potencial relevancia traslacional, dado que estas arritmias están más estrechamente relacionadas con la fase posterior

a la oclusión, momento en el que todavía es posible realizar una intervención clínica.

Un paso adicional fue el análisis realizado en un modelo porcino de infarto a tórax abierto, en el que el registro simultáneo de ECG de superficie y electrogramas intramiocárdicos permitió comparar el marcador basado en *warping* con las mediciones invasivas de DOR. Este capítulo reforzó la interpretación fisiológica del marcador al demostrar que $d_{w,\mathrm{T}_{pe}}^{\mathrm{PCA}}$ podría actuar como un marcador sustituto no invasivo de la medición invasiva de DOR. A diferencia del estudio porcino anterior, donde la asociación con la VF tardía respaldó el valor pronóstico del marcador, este modelo proporcionó una referencia mecanística directa al medir la dispersión de la repolarización a partir de registros intramiocárdicos. Los cambios temporales paralelos observados en $d_{w,\mathrm{T}_{pe}}^{\mathrm{PCA}}$ y la DOR, junto con la creciente separación entre los animales que presentaron VF tardía y los que no, respaldaron la interpretación de que los cambios en la morfología del intervalo T_{pe} captados en el ECG están relacionados con el aumento de la dispersión de la repolarización durante la isquemia.

La concordancia entre ambos índices se vio respaldada adicionalmente por análisis de regresión lineal individuales a lo largo del tiempo, que mostraron que el marcador basado en *warping* no solo estaba asociado a la aparición de VF, sino que también seguía la evolución del índice invasivo DOR durante el proceso isquémico. Es importante destacar que esta relación fue más fuerte que la observada para el intervalo clásico T_{pe}, lo que indica que el análisis basado en la morfología aportó información temporal y morfológica adicional a la que puede aportar dicho intervalo. Asimismo, su capacidad predictiva respecto a la aparición tardía de VF resultó comparable a la del DOR, mostrando a la vez un comportamiento más precoz y robusto que el índice clásico T_{pe}. Este hallazgo es especialmente relevante dado que la DOR es una medida invasiva, mientras que el parámetro $d_{w,\mathrm{T}_{pe}}^{\mathrm{PCA}}$ puede obtenerse a partir del ECG de superficie, lo que lo convierte en un candidato más viable para la evaluación no invasiva del riesgo.

En conjunto, los estudios de isquemia respaldan una progresión coherente: el marcador detecta cambios en la repolarización inducidos por la isquemia en humanos, identifica a animales con mayor riesgo de VF durante el infarto de miocardio y muestra potencial como un indicador subrogado de la DOR medida de forma invasiva. Esta secuencia proporciona una base fisiológica y traslacional más sólida para el análisis de la morfología del intervalo entre el pico y el final de la onda T que cualquiera de los estudios individuales por sí solo, avanzando desde la sensibilidad a la isquemia, pasando por la asociación con el riesgo arrítmico hasta, finalmente, la validación mecanística frente a la

DOR invasiva.

9.1.3 Marcadores de la morfología de la onda T en canalopatías cardíacas

La tesis también amplió la evaluación de los marcadores de morfología basados en *time-warping* a las canalopatías cardíacas LQT2 y BrS. En el caso del LQT2, el índice TMV cuantificó las anomalías morfológicas de la onda T comparando la onda T de cada paciente con una referencia normal ajustada por sexo, frecuencia cardíaca y derivación. Este enfoque resultó especialmente relevante en el LQT2, donde el riesgo arrítmico no se explica totalmente por la duración de la repolarización y donde las morfologías anómalas de la onda T pueden aportar información clínica adicional. Al cuantificar el *time-warping* necesario para alinear la onda T de cada paciente con una referencia emparejada, el TMV proporcionó un descriptor integrado de la anomalía morfológica a partir de un análisis basado en referencias, utilizando la onda T completa y una única derivación.

Los resultados mostraron que el índice TMV en la derivación I se asoció de forma significativa con el riesgo de eventos cardíacos en pacientes con LQT2, incluso después de ajustar por QT_c, sexo y MCS. Los pacientes con valores de TMV más bajos presentaron una peor supervivencia libre de eventos, lo que respalda la hipótesis de que las anomalías en la morfología de la onda T reflejan características de la repolarización clínicamente relevantes. Es importante destacar que la asociación persistió tras tener en cuenta el QT_c, lo que indica que el marcador no se limitaba a reproducir la información contenida en la duración de la repolarización. El hecho de que análisis de riesgo análogos basados en T_{Amp} y MCS no mostraran una asociación significativa con los eventos cardíacos en esta cohorte sugirió, además, que el marcador basado en *warping* capturaba información de riesgo relacionada con la morfología que no estaba totalmente representada por los descriptores existentes de la forma de la onda T. En conjunto, estos hallazgos respaldan el potencial del análisis de la morfología de la onda T basado en *time-warping* como un enfoque complementario a la estratificación de riesgo actual en el LQT2, al tiempo que subrayan la necesidad de realizar estudios independientes de mayor tamaño para confirmar su valor pronóstico y definir su contribución incremental.

En BrS, la metodología de *time-warping* se extendió para caracterizar tanto los cambios en la morfología de la onda T con la frecuencia cardíaca como los cambios con respecto a una referencia de población normal. La evaluación de la restitución morfológica reveló que el TPEMR permitió distinguir a los pa-

cientes con BrS de los sujetos de control utilizando la derivación transformada mediante PCA, mientras que el TMR se asoció con la presencia de un patrón espontáneo de tipo I en todas las derivaciones analizadas. Estos hallazgos sugieren que limitar el análisis al intervalo T_{pe} podría mejorar la detección de diferencias dinámicas en la repolarización entre pacientes con BrS y los controles, al tiempo que los cambios asociados a la expresión espontánea del patrón de tipo I podrían involucrar el complejo ST-T completo.

Entre los marcadores de morfología de la repolarización basados en referencias poblacionales, la TPEMV proporcionó la caracterización más consistente del fenotipo de Brugada y de la expresión espontánea de tipo I. Se observaron diferencias entre los pacientes con BrS y los controles en la mayoría de los intervalos RR de la derivación $V1_{4IC}$, mientras que se hallaron diferencias entre los pacientes con BrS-I y BrS-II en ambas derivaciones analizadas y fueron particularmente evidentes en los intervalos RR más largos en $V2_{4IC}$. Por el contrario, la TMV mostró menos diferencias y una mayor dependencia de la derivación. Ninguno de los marcadores basados en la morfología permitió diferenciar de manera consistente a los pacientes sintomáticos de los asintomáticos. Las diferencias más amplias observadas para QRS_d, incluidas las diferencias localizadas relacionadas con los síntomas en la derivación $V2_{4IC}$, fueron consistentes con la contribución complementaria de las anomalías de la repolarización y la despolarización al fenotipo de Brugada. En conjunto, la marcada dependencia de los hallazgos respecto a la ubicación de la derivación y al intervalo RR sugiere que estas anomalías están localizadas espacialmente y moduladas dinámicamente, en lugar de expresarse de manera uniforme en el ECG de superficie.

9.1.4 Contribución general a la estratificación del riesgo arrítmico

De forma general, la principal aportación de esta tesis fue la demostración de que el análisis de la morfología de la onda T basado en *time-warping* puede aportar información complementaria para evaluar el riesgo de arritmias ventriculares en diversos contextos. Los marcadores evaluados en esta tesis no deben interpretarse como sustitutos de los índices clínicos establecidos, sino más bien como descriptores adicionales de las anomalías en la repolarización. Su valor reside en su capacidad de cuantificar cambios morfológicos que pueden quedar parcialmente ocultos cuando el análisis se limita a intervalos de tiempo como el QT_c o el T_{pe}. Este enfoque basado en la morfología podría contribuir a una mejor caracterización del sustrato eléctrico subyacente a las arritmias ventriculares y a favorecer el desarrollo de estrategias de estratificación del riesgo más personalizadas.

9.2 Conclusiones generales

Las principales conclusiones de esta tesis son:

1. El análisis basado en *time-warping* proporciona un marco cuantitativo para caracterizar la morfología de la onda T de forma más amplia que mediante las mediciones convencionales basadas en puntos fiduciales. Al estimar la deformación temporal necesaria para alinear las ondas T, estos marcadores captan diferencias morfológicas que no quedan completamente descritas por los índices clásicos basados en la duración o la amplitud.

2. El marcador de *warping* restringido al intervalo entre el pico y el final de la onda T, $d^{\mathrm{PCA}}_{w,\mathrm{T}_{pe}}$, es sensible a los cambios de la repolarización inducidos por la isquemia. Su restricción a la parte final de la onda T permite evaluar cambios morfológicos relacionados con la repolarización, reduciendo al mismo tiempo la influencia de las desviaciones del segmento ST durante la isquemia.

3. En la oclusión coronaria transitoria en humanos y en los modelos porcinos de infarto de miocardio, $d^{\mathrm{PCA}}_{w,\mathrm{T}_{pe}}$ mostró una relevancia consistente para la caracterización de las alteraciones de la repolarización inducidas por la isquemia. En el modelo porcino de infarto, los cambios dinámicos de este marcador se asociaron con la aparición de VF tardía y proporcionaron información sobre el riesgo arrítmico más sólida que el intervalo T_{pe} clásico.

4. La comparación con las medidas invasivas de DOR respaldó el papel potencial de $d^{\mathrm{PCA}}_{w,\mathrm{T}_{pe}}$ como descriptor subrogado no invasivo de la dispersión de la repolarización ventricular en condiciones isquémicas. Este hallazgo proporciona respaldo mecanístico al uso del análisis de la morfología del intervalo entre el pico y el final de la onda T en la evaluación del riesgo arrítmico inducido por la isquemia.

5. En LQT2, las alteraciones de la morfología de la onda T completa cuantificadas mediante el índice TMV se asociaron con eventos cardíacos incluso después de ajustar por marcadores clínicos y electrocardiográficos establecidos. Esto sugiere que TMV puede aportar información complementaria sobre el riesgo más allá de la duración del QT_c en LQT2, aunque se necesitan cohortes independientes de mayor tamaño para confirmar su valor pronóstico.

6. En BrS, los marcadores de restitución y variación de la morfología de la onda T identificaron alteraciones de la repolarización asociadas principalmente con el fenotipo de Brugada y la expresión espontánea del patrón tipo I. TPEMR diferenció a los pacientes con BrS de los controles solo en la derivación transformada mediante PCA, mientras que TMR y TPEMV mostraron asociaciones con el patrón tipo I espontáneo. Sin embargo, ninguno de los marcadores basados en la morfología diferenció de manera consistente a los pacientes sintomáticos de los asintomáticos, y su comportamiento dependió notablemente de la derivación y del intervalo RR analizados. Junto con las diferencias más amplias observadas para QRS_d, estos hallazgos respaldan la evaluación complementaria de las alteraciones de la repolarización y la despolarización en BrS. También sugieren que los marcadores de repolarización basados en la morfología pueden ser más útiles para la caracterización fenotípica que para la estratificación clínica del riesgo en esta cohorte. No obstante, su asociación con los resultados clínicos y su posible valor pronóstico requieren una evaluación adicional en cohortes independientes de mayor tamaño con seguimiento clínico prospectivo.

7. En general, los resultados de esta tesis respaldan el uso de marcadores de la morfología de la onda T basados en *time-warping* como herramientas no invasivas complementarias para la caracterización de anomalías de la repolarización ventricular y del riesgo arrítmico, tanto en condiciones isquémicas como en canalopatías cardíacas. Dependiendo de los mecanismos electrofisiológicos estudiados, estos marcadores pueden obtenerse a partir de la onda T completa o específicamente del intervalo entre el pico y el final de la onda T.

9.3 Trabajo futuro

Las futuras líneas de investigación derivadas del desarrollo de esta tesis se describen a continuación:

- En condiciones isquémicas, los estudios futuros deberían determinar si $d_{w,\mathrm{T}_{pe}}^{\mathrm{PCA}}$ puede contribuir a una estratificación del riesgo clínicamente útil en poblaciones humanas. El estudio de pacientes sometidos a PCI demostró su capacidad para monitorizar los cambios de la repolarización inducidos por isquemia transitoria, mientras que los modelos porcinos de infarto mostraron su asociación con la VF tardía y su relación con la

DOR invasiva. Una continuación natural sería evaluar este marcador en cohortes humanas con síndromes coronarios agudos, infarto de miocardio u otros escenarios isquémicos en los que se disponga de información sobre eventos arrítmicos y seguimiento clínico.

- La información espacial contenida en los cambios de la morfología de la onda T debería investigarse con mayor profundidad. El estudio de pacientes sometidos a PCI sugirió diferencias regionales según la arteria ocluida, mientras que los estudios porcinos de infarto se basaron principalmente en una derivación transformada espacialmente mediante PCA. Los análisis futuros deberían confirmar el valor del uso de la derivación de PCA para el cálculo del marcador e investigar con mayor detalle la distribución espacial de los cambios en la morfología del T_{pe} entre las derivaciones del ECG en relación con la localización de la oclusión.

- Los trabajos futuros deberían abordar la selección de las ondas de referencia para la comparación morfológica. En los estudios experimentales controlados incluidos en esta tesis, las ondas T de referencia podían obtenerse a partir de registros basales o de control. Sin embargo, en la práctica clínica, puede no disponerse siempre de una referencia estable previa al evento. Por tanto, deberían explorarse enfoques alternativos para definir la onda de referencia, incluidos registros previos específicos del paciente, plantillas específicas de la enfermedad o referencias poblacionales, como las implementadas en el índice TMV.

- En LQT2, el marcador de la morfología de la onda T completa debería validarse en cohortes independientes y de mayor tamaño. El índice TMV mostró asociación con eventos cardíacos tras considerar la duración del QT_c y otros descriptores electrocardiográficos disponibles, pero el estudio fue retrospectivo y se basó en un número limitado de pacientes y eventos. Se necesitan cohortes multicéntricas de mayor tamaño para confirmar su valor pronóstico, evaluar su estabilidad en subgrupos definidos por sexo, genotipo, tratamiento y rango de QT_c, y determinar si mejora las estrategias actuales de estratificación del riesgo.

- En BrS, los marcadores de repolarización basados en la morfología deberían validarse en cohortes independientes de mayor tamaño y con un seguimiento clínico prospectivo. Los estudios futuros deberían confirmar los patrones dependientes de la derivación y del intervalo RR, y evaluar si su combinación con QRS_d mejora la caracterización fenotípica y

aporta valor adicional para la estratificación clínica del riesgo. Los estudios futuros también deberían incluir grupos control con distribuciones comparables de edad y sexo para reducir posibles factores de confusión demográficos.

- La robustez y la estandarización del proceso completo de procesamiento deberían evaluarse con mayor profundidad. El cálculo de los marcadores basados en *time-warping* depende de la calidad de la señal, el preprocesamiento, la delineación, la selección de derivaciones, la transformación mediante PCA, la segmentación en ventanas y la definición de la referencia. Una evaluación sistemática de estos factores ayudaría a determinar la implementación más fiable de la metodología y a reducir la variabilidad entre diferentes escenarios de estudio.

- La interpretación fisiológica de los marcadores derivados del *warping* debería investigarse con mayor profundidad. La comparación con la DOR invasiva constituyó un paso importante hacia la validación mecanística, pero estudios adicionales que combinen ECG de superficie, registros intramiocárdicos, información de imagen y modelos electrofisiológicos computacionales podrían aclarar cómo se relacionan los cambios morfológicos observados con la heterogeneidad espacial y temporal de la repolarización ventricular.

- Los estudios futuros podrían explorar con mayor profundidad la información proporcionada por la metodología de *time-warping* además de la contenida en los índices utilizados en esta tesis. En particular, podría analizarse el perfil local de la función de *warping* dentro de la onda T o del intervalo T_{pe} para determinar si regiones específicas de la onda de repolarización contribuyen de forma diferente al riesgo arrítmico. Además, los trabajos futuros podrían investigar la contribución conjunta del *time-warping* y de las diferencias residuales de amplitud tras el alineamiento, ya sea como marcadores complementarios o como parte de un modelo combinado basado en la morfología.

BIBLIOGRAPHY

[1] A. Timmis *et al.*, "European Society of Cardiology: the 2023 atlas of cardiovascular disease statistics," *European Heart Journal*, vol. 45, no. 38, pp. 4019–4062, 08 2024. [Online]. Available: https://doi.org/10.1093/eurheartj/ehae466

[2] S. S. Martin *et al.*, "2025 Heart disease and stroke statistics: A report of US and global data from the American Heart Association," *Circulation*, vol. 151, no. 8, pp. e41–e660, 2025. [Online]. Available: https://www.ahajournals.org/doi/abs/10.1161/CIR.0000000000001303

[3] K. E. J. Maddox *et al.*, "Forecasting the burden of cardiovascular disease and stroke in the United States through 2050—prevalence of risk factors and disease: A presidential advisory from the American Heart Association," *Circulation*, vol. 150, no. 4, pp. e65–e88, 2024. [Online]. Available: https://www.ahajournals.org/doi/abs/10.1161/CIR.0000000000001256

[4] Y. Xie *et al.*, "Long-term cardiovascular outcomes of COVID-19," *Nature Medicine*, vol. 28, pp. 583–590, 2022. [Online]. Available: https://doi.org/10.1038/s41591-022-01689-3

[5] G. Tse and B. P. Yan, "Traditional and novel electrocardiographic conduction and repolarization markers of sudden cardiac death," *EP Europace*, vol. 19, no. 5, pp. 712–721, 10 2016. [Online]. Available: https://doi.org/10.1093/europace/euw280

[6] F. L. Burton and S. M. Cobbe, "Dispersion of ventricular repolarization and refractory period," *Cardiovascular Research*, vol. 50, no. 1, pp. 10–23, 04 2001. [Online]. Available: https://doi.org/10.1016/S0008-6363(01)00197-3

[7] T. V. Kenttä *et al.*, "Repolarization heterogeneity measured with T-wave area dispersion in standard 12-lead ECG predicts sudden cardiac death in general

population," *Circulation: Arrhythmia and Electrophysiology*, vol. 11, no. 2, p. e005762, 2018. [Online]. Available: https://www.ahajournals.org/doi/abs/10.1161/CIRCEP.117.005762

[8] M. S. Fuller *et al.*, "Estimates of repolarization dispersion from electrocardiographic measurements," *Circulation*, vol. 102, no. 6, pp. 685–691, 2000. [Online]. Available: https://www.ahajournals.org/doi/abs/10.1161/01.CIR.102.6.685

[9] C. Antzelevitch, "Role of spatial dispersion of repolarization in inherited and acquired sudden cardiac death syndromes," *American Journal of Physiology-Heart and Circulatory Physiology*, vol. 293, no. 4, pp. H2024–H2038, 2007, pMID: 17586620. [Online]. Available: https://doi.org/10.1152/ajpheart.00355.2007

[10] A. J. Moss, "Measurement of the QT interval and the risk associated with QTc interval prolongation: A review," *The American Journal of Cardiology*, vol. 72, no. 6, pp. B23–B25, 1993, qT"c Interval Prolongation: Is it Beneficial or Harmful? [Online]. Available: https://www.sciencedirect.com/science/article/pii/000291499390036C

[11] G.-X. Yan and C. Antzelevitch, "Cellular basis for the normal T wave and the electrocardiographic manifestations of the long-QT syndrome," *Circulation*, vol. 98, no. 18, pp. 1928–1936, 1998. [Online]. Available: https://www.ahajournals.org/doi/abs/10.1161/01.CIR.98.18.1928

[12] A. Mincholé *et al.*, "Quantification of restitution dispersion from the dynamic changes of the T-wave peak to end, measured at the surface ECG," *IEEE Transactions on Biomedical Engineering*, vol. 58, no. 5, pp. 1172–1182, 2011.

[13] M. Baumert *et al.*, "QT interval variability in body surface ECG: measurement, physiological basis, and clinical value: position statement and consensus guidance endorsed by the European Heart Rhythm Association jointly with the ESC Working Group on Cardiac Cellular Electrophysiology," *EP Europace*, vol. 18, no. 6, pp. 925–944, 01 2016. [Online]. Available: https://doi.org/10.1093/europace/euv405

[14] S. M. Narayan, "T-wave alternans and the susceptibility to ventricular arrhythmias," *JACC*, vol. 47, no. 2, pp. 269–281, 2006. [Online]. Available: https://www.jacc.org/doi/abs/10.1016/j.jacc.2005.08.066

[15] E. Pueyo *et al.*, "Characterization of QT interval adaptation to RR interval changes and its use as a risk-stratifier of arrhythmic mortality in amiodarone-treated survivors of acute myocardial infarction," *IEEE Transactions on Biomedical Engineering*, vol. 51, no. 9, pp. 1511–1520, 2004.

[16] J. ichi Okada *et al.*, "Ionic mechanisms of ST segment elevation in electrocardiogram during acute myocardial infarction," *The Journal of Physiological Sciences*, vol. 70, no. 1, p. 36, 2020. [Online]. Available: https://www.sciencedirect.com/science/article/pii/S1880654624003421

[17] X. Wang *et al.*, "Tpeak-Tend/QT interval predicts ST-segment resolution and major adverse cardiac events in acute ST-segment elevation myocardial infarction patients undergoing percutaneous coronary intervention," *Medicine*, vol. 97, 2018. [Online]. Available: https://journals.lww.com/md-journal/fulltext/2018/10260/tpeak_tend_qt_interval_predicts_st_segment.52.aspx

[18] K. Thygesen *et al.*, "Fourth universal definition of myocardial infarction (2018)," *Circulation*, vol. 138, no. 20, pp. e618–e651, 2018. [Online]. Available: https://www.ahajournals.org/doi/abs/10.1161/CIR.0000000000000617

[19] S. S. Al-Zaiti *et al.*, "Clinical utility of ventricular repolarization dispersion for real-time detection of non-ST elevation myocardial infarction in emergency departments," *Journal of the American Heart Association*, vol. 4, no. 7, p. e002057, 2015. [Online]. Available: https://www.ahajournals.org/doi/abs/10.1161/JAHA.115.002057

[20] T. A. N. Ahmed *et al.*, "Electrocardiographic measures of ventricular repolarization dispersion and arrhythmic outcomes among ST elevation myocardial infarction patients with pre-infarction angina undergoing primary percutaneous coronary intervention," *Annals of Noninvasive Electrocardiology*, vol. 24, no. 4, p. e12637, 2019. [Online]. Available: https://onlinelibrary.wiley.com/doi/abs/10.1111/anec.12637

[21] C. Haarmark *et al.*, "The prognostic value of the Tpeak-Tend interval in patients undergoing primary percutaneous coronary intervention for ST-segment elevation myocardial infarction," *Journal of Electrocardiology*, vol. 42, no. 6, pp. 555–560, 2009. [Online]. Available: https://www.sciencedirect.com/science/article/pii/S0022073609002544

[22] T. Opthof *et al.*, "Is there a significant transmural gradient in repolarization time in the intact heart?" *Circulation: Arrhythmia and Electrophysiology*, vol. 2, no. 1, pp. 89–96, 2009. [Online]. Available: https://www.ahajournals.org/doi/abs/10.1161/CIRCEP.108.825356

[23] P. Taggart *et al.*, "Transmural repolarisation in the left ventricle in humans during normoxia and ischaemia," *Cardiovascular Research*, vol. 50, no. 3, pp. 454–462, 06 2001. [Online]. Available: https://doi.org/10.1016/S0008-6363(01)00223-1

[24] M. Srutova *et al.*, "Electrocardiographic discrimination of long QT syndrome genotypes: A comparative analysis and machine learning approach," *Sensors*, vol. 25, no. 7, 2025. [Online]. Available: https://www.mdpi.com/1424-8220/25/7/2253

[25] D. J. Abrams and C. A. MacRae, "Long QT syndrome," *Circulation*, vol. 129, no. 14, pp. 1524–1529, 2014. [Online]. Available: https://www.ahajournals.org/doi/abs/10.1161/CIRCULATIONAHA.113.003985

[26] M. Rieder *et al.*, "Genotype-specific ECG-based risk stratification approaches in patients with long-QT syndrome," *Frontiers in Cardiovascular Medicine*, vol. Volume 9 - 2022, 2022. [Online]. Available: https://www.frontiersin.org/journals/cardiovascular-medicine/articles/10.3389/fcvm.2022.916036

[27] F. Extramiana *et al.*, "Beat-to-beat T-wave amplitude variability in the long QT syndrome," *EP Europace*, vol. 12, no. 9, pp. 1302–1307, 05 2010. [Online]. Available: https://doi.org/10.1093/europace/euq137

[28] J. Brugada *et al.*, "Present status of Brugada syndrome," *JACC*, vol. 72, no. 9, pp. 1046–1059, 2018. [Online]. Available: https://www.jacc.org/doi/abs/10.1016/j.jacc.2018.06.037

[29] S. M. Al-Khatib *et al.*, "2017 AHA/ACC/HRS guideline for management of patients with ventricular arrhythmias and the prevention of sudden cardiac death," *JACC*, vol. 72, no. 14, pp. e91–e220, 2018. [Online]. Available: https://www.jacc.org/doi/abs/10.1016/j.jacc.2017.10.054

[30] J. E. Hall, *Guyton and Hall Textbook of Medical Physiology*, 13th ed. Philadelphia, PA: Elsevier, 2016, international edition.

[31] R. K. Clark, *Anatomy And Physiology: Understanding The Human Body*, 1st ed. Sudbury, MA: Jones and Bartlett, 2005, pp.288-297.

[32] L. Sörnmo and P. Laguna, *Bioelectrical Signal Processing in Cardiac and Neurological Applications*. Academic press, 2005.

[33] S. B. Prenner *et al.*, "Repolarization heterogeneity: Beyond the QT interval," *Journal of the American Heart Association*, vol. 5, no. 5, p. e003607, 2016. [Online]. Available: https://www.ahajournals.org/doi/abs/10.1161/JAHA.116.003607

[34] G.-X. Yan *et al.*, "Characteristics and distribution of M cells in arterially perfused canine left ventricular wedge preparations," *Circulation*, vol. 98, no. 18, pp. 1921–1927, 1998. [Online]. Available: https://www.ahajournals.org/doi/abs/10.1161/01.CIR.98.18.1921

[35] T. Stankovicova *et al.*, "M cells and transmural heterogeneity of action potential configuration in myocytes from the left ventricular wall of the pig heart," *Cardiovascular Research*, vol. 45, no. 4, pp. 952–960, 03 2000. [Online]. Available: https://doi.org/10.1016/S0008-6363(99)00418-6

[36] E. Drouin *et al.*, "Electrophysiologic characteristics of cells spanning the left ventricular wall of human heart: Evidence for presence of M cells," *Journal of the American College of Cardiology*, vol. 26, no. 1, pp. 185–192, 1995. [Online]. Available: https://www.sciencedirect.com/science/article/pii/073510979500167X

[37] F. G. Akar *et al.*, "Cellular basis for dispersion of repolarization underlying reentrant arrhythmias," *Journal of Electrocardiology*, vol. 33,

pp. 23–31, 2000, research and Technology Transfer in Computerized Electrocardiology. [Online]. Available: https://www.sciencedirect.com/science/article/pii/S0022073600800035

[38] S. H. Litovsky and C. Antzelevitch, "Transient outward current prominent in canine ventricular epicardium but not endocardium." *Circulation Research*, vol. 62, no. 1, pp. 116–126, 1988. [Online]. Available: https://www.ahajournals.org/doi/abs/10.1161/01.RES.62.1.116

[39] T. Furukawa *et al.*, "Differences in transient outward currents of feline endocardial and epicardial myocytes," *Circulation Research*, vol. 67, no. 5, pp. 1287–1291, 1990. [Online]. Available: https://www.ahajournals.org/doi/abs/10.1161/01.RES.67.5.1287

[40] T. Opthof *et al.*, "Dispersion of repolarization in canine ventricle and the electrocardiographic T wave: T_{p-e} interval does not reflect transmural dispersion," *Heart Rhythm*, vol. 4, no. 3, pp. 341–348, 2007. [Online]. Available: https://www.sciencedirect.com/science/article/pii/S154752710602217X

[41] Y. Xia *et al.*, "In vivo validation of the coincidence of the peak and end of the T wave with full repolarization of the epicardium and endocardium in swine," *Heart Rhythm*, vol. 2, no. 2, pp. 162–169, 2005. [Online]. Available: https://www.sciencedirect.com/science/article/pii/S154752710400791X

[42] E. P. Anyukhovsky *et al.*, "The controversial M cell," *Journal of cardiovascular electrophysiology*, vol. 10, no. 2, pp. 244–260, 1999.

[43] P. Taggart *et al.*, "Electrotonic cancellation of transmural electrical gradients in the left ventricle in man," *Progress in Biophysics and Molecular Biology*, vol. 82, no. 1, pp. 243–254, 2003, mechano-Electric Feedback and Cardiac Arrhythmias. [Online]. Available: https://www.sciencedirect.com/science/article/pii/S0079610703000257

[44] A. V. Glukhov *et al.*, "Transmural dispersion of repolarization in failing and nonfailing human ventricle," *Circulation Research*, vol. 106, no. 5, pp. 981–991, 2010. [Online]. Available: https://www.ahajournals.org/doi/abs/10.1161/CIRCRESAHA.109.204891

[45] F. G. Akar *et al.*, "Unique topographical distribution of M cells underlies reentrant mechanism of torsade de pointes in the long-QT syndrome," *Circulation*, vol. 105, no. 10, pp. 1247–1253, 2002. [Online]. Available: https://www.ahajournals.org/doi/abs/10.1161/hc1002.105231

[46] D.-W. Liu and C. Antzelevitch, "Characteristics of the delayed rectifier current (I_{Kr} and I_{Ks}) in canine ventricular epicardial, midmyocardial, and endocardial myocytes," *Circulation Research*, vol. 76, no. 3, pp. 351–365, 1995. [Online]. Available: https://www.ahajournals.org/doi/abs/10.1161/01.RES.76.3.351

[47] D. Fedida and W. R. Giles, "Regional variations in action potentials and transient outward current in myocytes isolated from rabbit left ventricle." *The*

Journal of Physiology, vol. 442, no. 1, pp. 191–209, 1991. [Online]. Available: https://physoc.onlinelibrary.wiley.com/doi/abs/10.1113/jphysiol.1991.sp018789

[48] R. B. Clark *et al.*, "Heterogeneity of action potential waveforms and potassium currents in rat ventricle," *Cardiovascular Research*, vol. 27, no. 10, pp. 1795–1799, 10 1993. [Online]. Available: https://doi.org/10.1093/cvr/27.10.1795

[49] M. Näbauer *et al.*, "Regional differences in current density and rate-dependent properties of the transient outward current in subepicardial and subendocardial myocytes of human left ventricle," *Circulation*, vol. 93, no. 1, pp. 168–177, 1996. [Online]. Available: https://www.ahajournals.org/doi/abs/10.1161/01.CIR.93.1.168

[50] E. Wettwer *et al.*, "Transient outward current in human ventricular myocytes of subepicardial and subendocardial origin." *Circulation Research*, vol. 75, no. 3, pp. 473–482, 1994. [Online]. Available: https://www.ahajournals.org/doi/abs/10.1161/01.RES.75.3.473

[51] T. Watanabe *et al.*, "Heterogeneity of the action potential in isolated rat ventricular myocytes and tissue." *Circulation Research*, vol. 52, no. 3, pp. 280–290, 1983. [Online]. Available: https://www.ahajournals.org/doi/abs/10.1161/01.RES.52.3.280

[52] S. M. Bryant *et al.*, "Regional differences in the delayed rectifier current (I_{Kr} and I_{Ks}) contribute to the differences in action potential duration in basal left ventricular myocytes in guinea-pig," *Cardiovascular Research*, vol. 40, no. 2, pp. 322–331, 11 1998. [Online]. Available: https://doi.org/10.1016/S0008-6363(98)00133-3

[53] J. Cheng *et al.*, "Heterogeneous distribution of the two components of delayed rectifier K+ current: a potential mechanism of the proarrhythmic effects of methanesulfonanilideclass III agents," *Cardiovascular Research*, vol. 43, no. 1, pp. 135–147, 07 1999. [Online]. Available: https://doi.org/10.1016/S0008-6363(99)00061-9

[54] G.-R. Li *et al.*, "Transmural heterogeneity of action potentials and I_{to1} in myocytes isolated from the human right ventricle," *American Journal of Physiology-Heart and Circulatory Physiology*, vol. 275, no. 2, pp. H369–H377, 1998, pMID: 9683422. [Online]. Available: https://doi.org/10.1152/ajpheart.1998.275.2.H369

[55] N. Ueda *et al.*, "Functional and transmural modulation of M cell behavior in canine ventricular wall," *American Journal of Physiology-Heart and Circulatory Physiology*, vol. 287, no. 6, pp. H2569–H2575, 2004, pMID: 15331367. [Online]. Available: https://doi.org/10.1152/ajpheart.00526.2004

[56] T. Volk *et al.*, "Regional alterations of repolarizing K+ currents among the left ventricular free wall of rats with ascending aortic stenosis," *The Journal of Physiology*, vol. 530, no. 3, pp. 443–455, 2001. [Online]. Available: https://physoc.onlinelibrary.wiley.com/doi/abs/10.1111/j.1469-7793.2001.0443k.x

[57] M. Hiraoka and S. Kawano, "Mechanism of increased amplitude and duration of the plateau with sudden shortening of diastolic intervals in rabbit ventricular cells." *Circulation Research*, vol. 60, no. 1, pp. 14–26, 1987. [Online]. Available: https://www.ahajournals.org/doi/abs/10.1161/01.RES.60.1.14

[58] Y. Kobayashi *et al.*, "Cellular mechanisms of differential action potential duration restitution in canine ventricular muscle cells during single versus double premature stimuli." *Circulation*, vol. 86, no. 3, pp. 955–967, 1992. [Online]. Available: https://www.ahajournals.org/doi/abs/10.1161/01.CIR.86.3.955

[59] M. Watanabe *et al.*, "Biphasic restitution of action potential duration and complex dynamics in ventricular myocardium," *Circulation Research*, vol. 76, no. 5, pp. 915–921, 1995. [Online]. Available: https://www.ahajournals.org/doi/abs/10.1161/01.RES.76.5.915

[60] M. Orini *et al.*, "Interactions between activation and repolarization restitution properties in the intact human heart: In-vivo whole-heart data and mathematical description," *PLOS ONE*, vol. 11, no. 9, pp. 1–20, 09 2016. [Online]. Available: https://doi.org/10.1371/journal.pone.0161765

[61] M. R. Franz *et al.*, "Cycle length dependence of human action potential duration in vivo. effects of single extrastimuli, sudden sustained rate acceleration and deceleration, and different steady-state frequencies." *The Journal of Clinical Investigation*, vol. 82, no. 3, pp. 972–979, 9 1988. [Online]. Available: https://www.jci.org/articles/view/113706

[62] M. R. FRANZ, "The electrical restitution curve revisited," *Journal of Cardiovascular Electrophysiology*, vol. 14, no. s10, pp. S140–S147, 2003. [Online]. Available: https://onlinelibrary.wiley.com/doi/abs/10.1046/j.1540.8167.90303.x

[63] M. L. Riccio *et al.*, "Electrical restitution and spatiotemporal organization during ventricular fibrillation," *Circulation Research*, vol. 84, no. 8, pp. 955–963, 1999. [Online]. Available: https://www.ahajournals.org/doi/abs/10.1161/01.RES.84.8.955

[64] A. Garfinkel *et al.*, "Preventing ventricular fibrillation by flattening cardiac restitution," *Proceedings of the National Academy of Sciences*, vol. 97, no. 11, pp. 6061–6066, 2000. [Online]. Available: https://www.pnas.org/doi/abs/10.1073/pnas.090492697

[65] J. N. Weiss *et al.*, "From pulsus to pulseless," *Circulation Research*, vol. 98, no. 10, pp. 1244–1253, 2006. [Online]. Available: https://www.ahajournals.org/doi/abs/10.1161/01.RES.0000224540.97431.f0

[66] K. H. W. J. ten Tusscher and A. V. Panfilov, "Alternans and spiral breakup in a human ventricular tissue model," *American Journal of Physiology-Heart and Circulatory Physiology*, vol. 291, no. 3, pp. H1088–H1100, 2006, pMID: 16565318. [Online]. Available: https://doi.org/10.1152/ajpheart.00109.2006

[67] M. P. Nash *et al.*, "Whole heart action potential duration restitution properties in cardiac patients: a combined clinical and modelling study," *Experimental Physiology*, vol. 91, no. 2, pp. 339–354, 2006. [Online]. Available: https://physoc.onlinelibrary.wiley.com/doi/abs/10.1113/expphysiol.2005.031070

[68] H.-N. PAK *et al.*, "Spatial dispersion of action potential duration restitution kinetics is associated with induction of ventricular tachycardia/fibrillation in humans," *Journal of Cardiovascular Electrophysiology*, vol. 15, no. 12, pp. 1357–1363, 2004. [Online]. Available: https://onlinelibrary.wiley.com/doi/abs/10.1046/j.1540-8167.2004.03569.x

[69] A. Mincholé *et al.*, "ECG-based estimation of dispersion of APD restitution as a tool to stratify sotalol-induced arrhythmic risk," *Journal of Electrocardiology*, vol. 48, no. 5, pp. 867–873, 2015. [Online]. Available: https://www.sciencedirect.com/science/article/pii/S0022073615001879

[70] J. J. Goldberger and J. Ng, *Practical signal and image processing in clinical cardiology*. Springer, 2010.

[71] I. Andršová *et al.*, "Influence of heart rate correction formulas on QTc interval stability," *Scientific Reports*, vol. 11, p. 14269, 2021. [Online]. Available: https://doi.org/10.1038/s41598-021-93774-9

[72] E. FRANK, "An accurate, clinically practical system for spatial vectorcardiography," *Circulation*, vol. 13, no. 5, pp. 737–749, 1956. [Online]. Available: https://www.ahajournals.org/doi/abs/10.1161/01.CIR.13.5.737

[73] C. Antzelevitch, "M cells in the human heart," *Circulation Research*, vol. 106, no. 5, pp. 815–817, 2010. [Online]. Available: https://www.ahajournals.org/doi/abs/10.1161/CIRCRESAHA.109.216226

[74] J. Garcıa *et al.*, "Comparative study of local and Karhunen-Loève-based ST-T indexes in recordings from human subjects with induced myocardial ischemia," *Computers and Biomedical Research*, vol. 31, no. 4, pp. 271–292, 1998. [Online]. Available: https://www.sciencedirect.com/science/article/pii/S0010480998914811

[75] S. A. Immanuel *et al.*, "T-wave morphology can distinguish healthy controls from LQTS patients," *Physiological Measurement*, vol. 37, no. 9, p. 1456, aug 2016. [Online]. Available: https://doi.org/10.1088/0967-3334/37/9/1456

[76] A. Porta-Sánchez *et al.*, "T-wave morphology analysis in congenital long QT syndrome discriminates patients from healthy individuals," *JACC: Clinical Electrophysiology*, vol. 3, no. 4, pp. 374–381, 2017. [Online]. Available: https://www.sciencedirect.com/science/article/pii/S2405500X16304066

[77] B. Acar *et al.*, "Spatial, temporal and wavefront direction characteristics of 12-lead T-wave morphology," *Medical & Biological Engineering & Computing*, vol. 37, pp. 574–584, 1999. [Online]. Available: https://doi.org/10.1007/BF02513351

[78] A. Sugrue *et al.*, "Architectural T-wave analysis and identification of on-therapy breakthrough arrhythmic risk in type 1 and type 2 long-QT syndrome," *Circulation: Arrhythmia and Electrophysiology*, vol. 10, no. 11, p. e005648, 2017. [Online]. Available: https://www.ahajournals.org/doi/abs/10.1161/CIRCEP.117.005648

[79] S. Al-Zaiti *et al.*, "Spatial indices of repolarization correlate with non-ST elevation myocardial ischemia in patients with chest pain," *Medical & Biological Engineering & Computing*, vol. 56, pp. 1–12, 2018. [Online]. Available: https://doi.org/10.1007/s11517-017-1659-1

[80] D. T. Tardo *et al.*, "The diagnostic role of T wave morphology biomarkers in congenital and acquired long QT syndrome: A systematic review," *Annals of Noninvasive Electrocardiology*, vol. 28, no. 1, p. e13015, 2023, e13015 ANEC-22-4595. [Online]. Available: https://onlinelibrary.wiley.com/doi/abs/10.1111/anec.13015

[81] R. A. Byrne *et al.*, "2023 ESC Guidelines for the management of acute coronary syndromes: Developed by the task force on the management of acute coronary syndromes of the European Society of Cardiology (ESC)," *European Heart Journal. Acute Cardiovascular Care*, vol. 13, no. 1, pp. 55–161, 09 2023. [Online]. Available: https://doi.org/10.1093/ehjacc/zuad107

[82] S. Q. Khan and P. F. Ludman, "Percutaneous coronary intervention," *Medicine*, vol. 50, no. 7, pp. 437–444, 2022, cardiovascular Medicine Part 2 of 4. [Online]. Available: https://www.sciencedirect.com/science/article/pii/S1357303922001025

[83] A. D. Krahn *et al.*, "Congenital long QT syndrome," *JACC: Clinical Electrophysiology*, vol. 8, no. 5, pp. 687–706, 2022. [Online]. Available: https://www.jacc.org/doi/abs/10.1016/j.jacep.2022.02.017

[84] A. S. Vink *et al.*, "Determination and interpretation of the QT interval," *Circulation*, vol. 138, no. 21, pp. 2345–2358, 2018. [Online]. Available: https://www.ahajournals.org/doi/abs/10.1161/CIRCULATIONAHA.118.033943

[85] P. J. Schwartz *et al.*, "Prevalence of the congenital long-QT syndrome," *Circulation*, vol. 120, no. 18, pp. 1761–1767, 2009. [Online]. Available: https://www.ahajournals.org/doi/abs/10.1161/CIRCULATIONAHA.109.863209

[86] P. J. Schwartz *et al.*, "Long-QT syndrome," *Circulation: Arrhythmia and Electrophysiology*, vol. 5, no. 4, pp. 868–877, 2012. [Online]. Available: https://www.ahajournals.org/doi/abs/10.1161/CIRCEP.111.962019

[87] A. O. Grant, "Cardiac ion channels," *Circulation: Arrhythmia and Electrophysiology*, vol. 2, no. 2, pp. 185–194, 2009. [Online]. Available: https://www.ahajournals.org/doi/abs/10.1161/CIRCEP.108.789081

[88] P. J. Schwartz *et al.*, "Genotype-phenotype correlation in the long-QT syndrome," *Circulation*, vol. 103, no. 1, pp. 89–95, 2001. [Online]. Available: https://www.ahajournals.org/doi/abs/10.1161/01.CIR.103.1.89

[89] A. J. Moss *et al.*, "Comparison of clinical and genetic variables of cardiac events associated with loud noise versus swimming among subjects with the long QT syndrome," *The American Journal of Cardiology*, vol. 84, no. 8, pp. 876–879, 1999. [Online]. Available: https://www.sciencedirect.com/science/article/pii/S0002914999004580

[90] P. B. Bennett *et al.*, "Molecular mechanism for an inherited cardiac arrhythmia," *Nature*, vol. 376, pp. 683–685, 1995. [Online]. Available: https://doi.org/10.1038/376683a0

[91] W. Shimizu and C. Antzelevitch, "Cellular basis for the ECG features of the LQT1 form of the long-QT syndrome," *Circulation*, vol. 98, no. 21, pp. 2314–2322, 1998. [Online]. Available: https://www.ahajournals.org/doi/abs/10.1161/01.CIR.98.21.2314

[92] W. Shimizu and C. Antzelevitch, "Sodium channel block with mexiletine is effective in reducing dispersion of repolarization and preventing torsade de pointes in LQT2 and LQT3 models of the long-QT syndrome," *Circulation*, vol. 96, no. 6, pp. 2038–2047, 1997. [Online]. Available: https://www.ahajournals.org/doi/abs/10.1161/01.CIR.96.6.2038

[93] K. Gima and Y. Rudy, "Ionic current basis of electrocardiographic waveforms," *Circulation Research*, vol. 90, no. 8, pp. 889–896, 2002.

[94] A. J. Moss *et al.*, "ECG T-wave patterns in genetically distinct forms of the hereditary long QT syndrome," *Circulation*, vol. 92, no. 10, pp. 2929–2934, 1995. [Online]. Available: https://www.ahajournals.org/doi/abs/10.1161/01.CIR.92.10.2929

[95] A. Sugrue *et al.*, "Identification of concealed and manifest long QT syndrome using a novel T wave analysis program," *Circulation: Arrhythmia and Electrophysiology*, vol. 9, no. 7, p. e003830, 2016. [Online]. Available: https://www.ahajournals.org/doi/abs/10.1161/CIRCEP.115.003830

[96] K. Zeppenfeld *et al.*, "2022 ESC Guidelines for the management of patients with ventricular arrhythmias and the prevention of sudden cardiac death: Developed by the task force for the management of patients with ventricular arrhythmias and the prevention of sudden cardiac death of the European Society of Cardiology (ESC) Endorsed by the Association for European Paediatric and Congenital Cardiology (AEPC)," *European Heart Journal*, vol. 43, no. 40, pp. 3997–4126, 08 2022. [Online]. Available: https://doi.org/10.1093/eurheartj/ehac262

[97] A. A. Wilde *et al.*, "Auditory stimuli as a trigger for arrhythmic events differentiate HERG-related ($LQTS_2$) patients from KVLQT1-related patients ($LQTS_1$)," *JACC*, vol. 33, no. 2, pp. 327–332, 1999. [Online]. Available: https://www.jacc.org/doi/abs/10.1016/S0735-1097%2898%2900578-6

[98] A. D. Krahn *et al.*, "Congenital long QT syndrome," *JACC: Clinical Electrophysiology*, vol. 8, no. 5, pp. 687–706, 2022. [Online]. Available: https://www.sciencedirect.com/science/article/pii/S2405500X22002985

[99] S. G. Priori *et al.*, "HRS/EHRA/APHRS expert consensus statement on the diagnosis and management of patients with inherited primary arrhythmia syndromes: Document endorsed by HRS, EHRA, and APHRS in May 2013 and by ACCF, AHA, PACES, and AEPC in June 2013." *Heart Rhythm*, vol. 10, no. 12, pp. 1932–1963, 2013, focus Issue: Devices. [Online]. Available: https://www.sciencedirect.com/science/article/pii/S1547527113005523

[100] P. A. Brink *et al.*, "Phenotypic variability and unusual clinical severity of congenital long-QT syndrome in a founder population," *Circulation*, vol. 112, no. 17, pp. 2602–2610, 2005. [Online]. Available: https://www.ahajournals.org/doi/abs/10.1161/CIRCULATIONAHA.105.572453

[101] P. J. Schwartz *et al.*, "The Jervell and Lange-Nielsen Syndrome," *Circulation*, vol. 113, no. 6, pp. 783–790, 2006. [Online]. Available: https://www.ahajournals.org/doi/abs/10.1161/CIRCULATIONAHA.105.592899

[102] E. A. Nannenberg *et al.*, "Mortality of inherited arrhythmia syndromes," *Circulation: Cardiovascular Genetics*, vol. 5, no. 2, pp. 183–189, 2012. [Online]. Available: https://www.ahajournals.org/doi/abs/10.1161/CIRCGENETICS.111.961102

[103] J. B. Hobbs *et al.*, "Risk of aborted cardiac arrest or sudden cardiac death during adolescence in the long-QT syndrome," *JAMA*, vol. 296, no. 10, pp. 1249–1254, 09 2006. [Online]. Available: https://doi.org/10.1001/jama.296.10.1249

[104] J. Costa *et al.*, "Combined assessment of sex- and mutation-specific information for risk stratification in type 1 long QT syndrome," *Heart Rhythm*, vol. 9, no. 6, pp. 892–898, 2012. [Online]. Available: https://www.sciencedirect.com/science/article/pii/S1547527112000793

[105] A. J. Sauer *et al.*, "Long QT syndrome in adults," *JACC*, vol. 49, no. 3, pp. 329–337, 2007. [Online]. Available: https://www.jacc.org/doi/abs/10.1016/j.jacc.2006.08.057

[106] C. Jons *et al.*, "Risk of fatal arrhythmic events in long QT syndrome patients after syncope," *JACC*, vol. 55, no. 8, pp. 783–788, 2010. [Online]. Available: https://www.jacc.org/doi/abs/10.1016/j.jacc.2009.11.042

[107] J. Mullally *et al.*, "Risk of life-threatening cardiac events among patients with long QT syndrome and multiple mutations," *Heart Rhythm*, vol. 10, no. 3, pp. 378–382, 2013. [Online]. Available: https://www.sciencedirect.com/science/article/pii/S1547527112013343

[108] Z. W. Laksman *et al.*, "Early repolarization is associated with symptoms in patients with type 1 and type 2 long QT syndrome," *Heart Rhythm*, vol. 11, no. 9, pp. 1632–1638, 2014, focus Issue: Atrial Fibrillation. [Online]. Available: https://www.sciencedirect.com/science/article/pii/S154752711400558X

[109] A. Sugrue *et al.*, "Echocardiography-guided risk stratification for long QT syndrome," *JACC*, vol. 76, no. 24, pp. 2834–2843, 2020. [Online]. Available: https://www.jacc.org/doi/abs/10.1016/j.jacc.2020.10.024

[110] I. Goldenberg *et al.*, "Long-QT syndrome after age 40," *Circulation*, vol. 117, no. 17, pp. 2192–2201, 2008. [Online]. Available: https://www.ahajournals.org/doi/abs/10.1161/CIRCULATIONAHA.107.729368

[111] J. F. Liu *et al.*, "Risk factors for recurrent syncope and subsequent fatal or near-fatal events in children and adolescents with long QT syndrome," *JACC*, vol. 57, no. 8, pp. 941–950, 2011. [Online]. Available: https://www.jacc.org/doi/abs/10.1016/j.jacc.2010.10.025

[112] D. Migdalovich *et al.*, "Mutation and gender-specific risk in type 2 long QT syndrome: Implications for risk stratification for life-threatening cardiac events in patients with long QT syndrome," *Heart Rhythm*, vol. 8, no. 10, pp. 1537–1543, 2011. [Online]. Available: https://www.sciencedirect.com/science/article/pii/S1547527111003614

[113] A. A. Wilde *et al.*, "Clinical aspects of type 3 long-QT syndrome," *Circulation*, vol. 134, no. 12, pp. 872–882, 2016. [Online]. Available: https://www.ahajournals.org/doi/abs/10.1161/CIRCULATIONAHA.116.021823

[114] I. Goldenberg *et al.*, "Risk for life-threatening cardiac events in patients with genotype-confirmed long-QT syndrome and normal-range corrected QT intervals," *JACC*, vol. 57, no. 1, pp. 51–59, 2011. [Online]. Available: https://www.jacc.org/doi/abs/10.1016/j.jacc.2010.07.038

[115] W. Zareba *et al.*, "Influence of the genotype on the clinical course of the long-QT syndrome," *New England Journal of Medicine*, vol. 339, no. 14, pp. 960–965, 1998. [Online]. Available: https://www.nejm.org/doi/full/10.1056/NEJM199810013391404

[116] W. Shimizu *et al.*, "RETRACTED:Association of genetic and clinical aspects of congenital long QT syndrome with life-threatening arrhythmias in japanese patients," *JAMA Cardiology*, vol. 4, no. 3, pp. 246–254, 03 2019. [Online]. Available: https://doi.org/10.1001/jamacardio.2018.4925

[117] I. Goldenberg *et al.*, "Corrected QT variability in serial electrocardiograms in long QT syndrome," *JACC*, vol. 48, no. 5, pp. 1047–1052, 2006. [Online]. Available: https://www.jacc.org/doi/abs/10.1016/j.jacc.2006.06.033

[118] M. Tomás *et al.*, "Polymorphisms in the *NOS1AP*gene modulate QT interval duration and risk of arrhythmias in the long QT syndrome," *JACC*, vol. 55, no. 24, pp. 2745–2752, 2010. [Online]. Available: https://www.jacc.org/doi/abs/10.1016/j.jacc.2009.12.065

[119] S. G. Priori *et al.*, "Association of long QT syndrome loci and cardiac events among patients treated with β-Blockers," *JAMA*, vol. 292, no. 11, pp. 1341–1344, 09 2004. [Online]. Available: https://doi.org/10.1001/jama.292.11.1341

[120] M. Koponen *et al.*, "Clinical and molecular genetic risk determinants in adult long QT syndrome type 1 and 2 patients," *BMC Medical Genetics*, vol. 19, p. 56, 2018. [Online]. Available: https://doi.org/10.1186/s12881-018-0574-0

[121] A. Mazzanti *et al.*, "Interplay between genetic substrate, QTc duration, and arrhythmia risk in patients with long QT syndrome," *JACC*, vol. 71, no. 15, pp. 1663–1671, 2018. [Online]. Available: https://www.jacc.org/doi/abs/10.1016/j.jacc.2018.01.078

[122] L. Crotti *et al.*, "The common long-QT syndrome mutation KCNQ1/A341V causes unusually severe clinical manifestations in patients with different ethnic backgrounds," *Circulation*, vol. 116, no. 21, pp. 2366–2375, 2007. [Online]. Available: https://www.ahajournals.org/doi/abs/10.1161/CIRCULATIONAHA.107.726950

[123] A. Winbo *et al.*, "Low incidence of sudden cardiac death in a swedish Y111C type 1 long-QT syndrome population," *Circulation: Cardiovascular Genetics*, vol. 2, no. 6, pp. 558–564, 2009. [Online]. Available: https://www.ahajournals.org/doi/abs/10.1161/CIRCGENETICS.108.825547

[124] A. J. Moss *et al.*, "Increased risk of arrhythmic events in long-QT syndrome with mutations in the pore region of the human ether-a-go-go–related gene potassium channel," *Circulation*, vol. 105, no. 7, pp. 794–799, 2002. [Online]. Available: https://www.ahajournals.org/doi/abs/10.1161/hc0702.105124

[125] W. Shimizu *et al.*, "Mutation site-specific differences in arrhythmic risk and sensitivity to sympathetic stimulation in the LQT1 form of congenital long QT syndrome," *JACC*, vol. 44, no. 1, pp. 117–125, 2004. [Online]. Available: https://www.jacc.org/doi/abs/10.1016/j.jacc.2004.03.043

[126] A. J. Moss *et al.*, "Clinical aspects of type-1 long-QT syndrome by location, coding type, and biophysical function of mutations involving the KCNQ1 gene," *Circulation*, vol. 115, no. 19, pp. 2481–2489, 2007. [Online]. Available: https://www.ahajournals.org/doi/abs/10.1161/CIRCULATIONAHA.106.665406

[127] D. Cortez *et al.*, "Quantitative T-wave morphology assessment from surface ECG is linked with cardiac events risk in genotype-positive KCNH2 mutation carriers with normal QTc values," *Journal of Cardiovascular Electrophysiology*, vol. 30, no. 12, pp. 2907–2913, 2019. [Online]. Available: https://onlinelibrary.wiley.com/doi/abs/10.1111/jce.14210

[128] P. Brugada and J. Brugada, "Right bundle branch block, persistent ST segment elevation and sudden cardiac death: A distinct clinical and electrocardiographic syndrome: A multicenter report," *Journal of the American College of Cardiology*, vol. 20, no. 6, pp. 1391–1396, 1992. [Online]. Available: https://www.sciencedirect.com/science/article/pii/073510979290253J

[129] Y. Mizusawa and A. A. Wilde, "Brugada syndrome," *Circulation: Arrhythmia and Electrophysiology*, vol. 5, no. 3, p. 606 – 616, 2012, cited by: 238; All

Open Access, Bronze Open Access. [Online]. Available: https://www.scopus.com/inward/record.uri?eid=2-s2.0-84863649450&doi=10.1161%2fCIRCEP.111.964577&partnerID=40&md5=760e7b28c04e6076ab7d51784e73af6f

[130] J. Brugada *et al.*, "Present status of Brugada syndrome: JACC state-of-the-art review," *Journal of the American College of Cardiology*, vol. 72, no. 9, pp. 1046–1059, 2018. [Online]. Available: https://www.sciencedirect.com/science/article/pii/S0735109718353622

[131] A. D. Krahn *et al.*, "Brugada syndrome," *JACC: Clinical Electrophysiology*, vol. 8, no. 3, pp. 386–405, 2022. [Online]. Available: https://www.sciencedirect.com/science/article/pii/S2405500X2101080X

[132] Q. Chen *et al.*, "Genetic basis and molecular mechanism for idiopathic ventricular fibrillation," *Nature*, vol. 392, pp. 293–296, 1998. [Online]. Available: https://doi.org/10.1038/32675

[133] S. Casini *et al.*, "Characterization of a novel SCN5A mutation associated with Brugada syndrome reveals involvement of DIIIS4–S5 linker in slow inactivation," *Cardiovascular Research*, vol. 76, no. 3, pp. 418–429, 12 2007. [Online]. Available: https://doi.org/10.1016/j.cardiores.2007.08.005

[134] A. E. Pfahnl *et al.*, "A sodium channel pore mutation causing Brugada syndrome," *Heart Rhythm*, vol. 4, no. 1, pp. 46–53, 2007. [Online]. Available: https://www.sciencedirect.com/science/article/pii/S1547527106020546

[135] B. Benito *et al.*, "Brugada syndrome," *Revista Española de Cardiología (English Edition)*, vol. 62, no. 11, pp. 1297–1315, 2009. [Online]. Available: https://www.sciencedirect.com/science/article/pii/S1885585709733572

[136] X.-Q. Quan *et al.*, "A meta-analytic review of prevalence for Brugada ECG patterns and the risk for death," *Medicine (United States)*, vol. 95, no. 50, p. e5643, 2016, cited by: 44; All Open Access, Gold Open Access, Green Open Access. [Online]. Available: https://www.scopus.com/inward/record.uri?eid=2-s2.0-85007480677&doi=10.1097%2fMD.0000000000005643&partnerID=40&md5=f2c2530fa5f2fa78d8fa5d760ce5ba76

[137] Q. Chen *et al.*, "Genetic basis and molecular mechanism for idiopathic ventricular fibrillation," *Nature*, vol. 392, no. 6673, p. 293 – 296, 1998, cited by: 1627. [Online]. Available: https://www.scopus.com/inward/record.uri?eid=2-s2.0-0032546384&doi=10.1038%2f32675&partnerID=40&md5=c4889d138c24b1dfb13ea1fc8b220a69

[138] Z.-S. Zhang *et al.*, "Sodium channel kinetic changes that produce Brugada syndrome or progressive cardiac conduction system disease," *American Journal of Physiology-Heart and Circulatory Physiology*, vol. 292, no. 1, pp. H399–H407, 2007, pMID: 16877553. [Online]. Available: https://doi.org/10.1152/ajpheart.01025.2005

[139] S. Chakrabarti *et al.*, "MOG1 rescues defective trafficking of nav1.5 mutations in Brugada syndrome and sick sinus syndrome," *Circulation: Arrhythmia and Electrophysiology*, vol. 6, no. 2, p. 392 – 401, 2013, cited by: 52; All Open Access, Bronze Open Access, Green Open Access. [Online]. Available: https://www.scopus.com/inward/record.uri?eid=2-s2.0-84878064672&doi=10.1161%2fCIRCEP.111.000206&partnerID=40&md5=0ef33a0642972e3f0a866ef3ffb903ee

[140] M. Pérez-Hernández *et al.*, "Brugada syndrome trafficking–defective Nav1.5 channels can trap cardiac Kir2.1/2.2 channels," *JCI Insight*, vol. 3, no. 18, 9 2018. [Online]. Available: https://insight.jci.org/articles/view/96291

[141] A. A. Wilde and A. S. Amin, "Clinical spectrum of SCN5A mutations: Long QT syndrome, Brugada syndrome, and cardiomyopathy," *JACC: Clinical Electrophysiology*, vol. 4, no. 5, pp. 569–579, 2018. [Online]. Available: https://www.sciencedirect.com/science/article/pii/S2405500X18302081

[142] S. M. Hosseini *et al.*, "Reappraisal of reported genes for sudden arrhythmic death," *Circulation*, vol. 138, no. 12, pp. 1195–1205, 2018. [Online]. Available: https://www.ahajournals.org/doi/abs/10.1161/CIRCULATIONAHA.118.035070

[143] J. D. Kapplinger *et al.*, "An international compendium of mutations in the SCN5A-encoded cardiac sodium channel in patients referred for Brugada syndrome genetic testing," *Heart Rhythm*, vol. 7, no. 1, pp. 33–46, 2010. [Online]. Available: https://www.sciencedirect.com/science/article/pii/S1547527109011424

[144] D. Hu *et al.*, "Mutations in SCN10A are responsible for a large fraction of cases of Brugada syndrome," *Journal of the American College of Cardiology*, vol. 64, no. 1, pp. 66–79, 2014. [Online]. Available: https://www.sciencedirect.com/science/article/pii/S0735109714023584

[145] E. R. Behr *et al.*, "Role of common and rare variants in SCN10A: results from the Brugada syndrome QRS locus gene discovery collaborative study," *Cardiovascular Research*, vol. 106, no. 3, pp. 520–529, 02 2015. [Online]. Available: https://doi.org/10.1093/cvr/cvv042

[146] H. Riuró *et al.*, "A missense mutation in the sodium channel $\beta 2$ subunit reveals SCN2B as a new candidate gene for Brugada syndrome," *Human Mutation*, vol. 34, no. 7, pp. 961–966, 2013. [Online]. Available: https://onlinelibrary.wiley.com/doi/abs/10.1002/humu.22328

[147] M. Cerrone *et al.*, "Missense mutations in plakophilin-2 cause sodium current deficit and associate with a Brugada syndrome phenotype," *Circulation*, vol. 129, no. 10, p. 1092 – 1103, 2014, cited by: 289; All Open Access, Bronze Open Access, Green Open Access. [Online]. Available: https://www.scopus.com/inward/record.uri?eid=2-s2.0-84896749603&doi=10.1161%2fCIRCULATIONAHA.113.003077&partnerID=40&md5=d093598457fe7148ca06fd3eef2a8c2c

[148] N. Belbachir *et al.*, "RRAD mutation causes electrical and cytoskeletal defects in cardiomyocytes derived from a familial case of Brugada syndrome," *European Heart Journal*, vol. 40, no. 37, pp. 3081–3094, 05 2019. [Online]. Available: https://doi.org/10.1093/eurheartj/ehz308

[149] J. R. Giudicessi *et al.*, "Transient outward current (Ito) gain-of-function mutations in the KCND3-encoded Kv4.3 potassium channel and Brugada syndrome," *Heart Rhythm*, vol. 8, no. 7, pp. 1024–1032, 2011. [Online]. Available: https://www.sciencedirect.com/science/article/pii/S1547527111001834

[150] E. Burashnikov *et al.*, "Mutations in the cardiac L-type calcium channel associated with inherited J-wave syndromes and sudden cardiac death," *Heart Rhythm*, vol. 7, no. 12, pp. 1872–1882, 2010. [Online]. Available: https://www.sciencedirect.com/science/article/pii/S1547527110008969

[151] M. Cerrone and M. Delmar, "Desmosomes and the sodium channel complex: Implications for arrhythmogenic cardiomyopathy and Brugada syndrome," *Trends in Cardiovascular Medicine*, vol. 24, no. 5, pp. 184–190, 2014. [Online]. Available: https://www.sciencedirect.com/science/article/pii/S1050173814000140

[152] E. R. Behr *et al.*, "Brugada syndrome and reduced right ventricular outflow tract conduction reserve: a final common pathway?" *European Heart Journal*, vol. 42, no. 11, pp. 1073–1081, 01 2021. [Online]. Available: https://doi.org/10.1093/eurheartj/ehaa1051

[153] A. A. Wilde *et al.*, "The pathophysiological mechanism underlying Brugada syndrome: Depolarization versus repolarization," *Journal of Molecular and Cellular Cardiology*, vol. 49, no. 4, pp. 543–553, 2010. [Online]. Available: https://www.sciencedirect.com/science/article/pii/S0022282810002762

[154] P. G. Meregalli *et al.*, "Pathophysiological mechanisms of Brugada syndrome: Depolarization disorder, repolarization disorder, or more?" *Cardiovascular Research*, vol. 67, no. 3, pp. 367–378, 08 2005. [Online]. Available: https://doi.org/10.1016/j.cardiores.2005.03.005

[155] P. G. Postema *et al.*, "Slow and discontinuous conduction conspire in Brugada syndrome: a right ventricular mapping and stimulation study." *Circulation. Arrhythmia and electrophysiology*, vol. 1, no. 5, p. 379 – 386, 2008, cited by: 126; All Open Access, Bronze Open Access. [Online]. Available: https://www.scopus.com/inward/record.uri?eid=2-s2.0-67651128831&doi=10.1161%2fCIRCEP.108.790543&partnerID=40&md5=61576973391c0fd80ce605f9ee66f882

[156] P. Lambiase *et al.*, "High-density substrate mapping in Brugada syndrome: Combined role of conduction and repolarization heterogeneities in arrhythmogenesis," *Circulation*, vol. 120, no. 2, p. 106 – 117, 2009, cited by: 154; All Open Access, Bronze Open Access. [Online]. Available: https://www.scopus.com/inward/record.uri?eid=2-s2.

0-67651097488&doi=10.1161%2fCIRCULATIONAHA.108.771401&partnerID=40&md5=1336b14e1b084c922ae1d7a0a6c035cf

[157] G.-X. Yan and C. Antzelevitch, "Cellular basis for the Brugada syndrome and other mechanisms of arrhythmogenesis associated with ST-segment elevation," *Circulation*, vol. 100, no. 15, p. 1660 – 1666, 1999, cited by: 994; All Open Access, Bronze Open Access. [Online]. Available: https://www.scopus.com/inward/record.uri?eid=2-s2.0-0032879716&doi=10.1161%2f01.CIR.100.15.1660&partnerID=40&md5=4e4d035e0c80340a7891ba880247cf46

[158] C. Antzelevitch *et al.*, "Brugada syndrome: Report of the second consensus conference," *Circulation*, vol. 111, no. 5, pp. 659–670, 2005. [Online]. Available: https://www.ahajournals.org/doi/abs/10.1161/01.CIR.0000152479.54298.51

[159] G.-X. Yan and C. Antzelevitch, "Cellular basis for the Brugada syndrome and other mechanisms of arrhythmogenesis associated with ST-segment elevation," *Circulation*, vol. 100, no. 15, pp. 1660–1666, 1999. [Online]. Available: https://www.ahajournals.org/doi/abs/10.1161/01.CIR.100.15.1660

[160] C. ANTZELEVITCH, "Brugada syndrome," *Pacing and Clinical Electrophysiology*, vol. 29, no. 10, pp. 1130–1159, 2006. [Online]. Available: https://onlinelibrary.wiley.com/doi/abs/10.1111/j.1540-8159.2006.00507.x

[161] G.-X. Yan *et al.*, "Phase 2 reentry as a trigger to initiate ventricular fibrillation during early acute myocardial ischemia," *Circulation*, vol. 110, no. 9, p. 1036 – 1041, 2004, cited by: 144. [Online]. Available: https://www.scopus.com/inward/record.uri?eid=2-s2.0-4844226196&doi=10.1161%2f01.CIR.0000140258.09964.19&partnerID=40&md5=dcc17b95c48203cc21d953fe35e0a1af

[162] K. HISAMATSU *et al.*, "Relationships between depolarization abnormality and repolarization abnormality in patients with Brugada syndrome:," *Journal of Cardiovascular Electrophysiology*, vol. 15, no. 8, pp. 870–876, 2004. [Online]. Available: https://onlinelibrary.wiley.com/doi/abs/10.1046/j.1540-8167.2004.03675.x

[163] M. YOKOKAWA *et al.*, "Spatial distribution of repolarization and depolarization abnormalities evaluated by body surface potential mapping in patients with Brugada syndrome," *Pacing and Clinical Electrophysiology*, vol. 29, no. 10, pp. 1112–1121, 2006. [Online]. Available: https://onlinelibrary.wiley.com/doi/abs/10.1111/j.1540-8159.2006.00505.x

[164] N. Nishii *et al.*, "Abnormal restitution property of action potential duration and conduction delay in Brugada syndrome: both repolarization and depolarization abnormalities," *EP Europace*, vol. 12, no. 4, pp. 544–552, 01 2010. [Online]. Available: https://doi.org/10.1093/europace/eup432

[165] C. Antzelevitch *et al.*, "J-wave syndromes expert consensus conference report: Emerging concepts and gaps in knowledge," *Heart Rhythm*, vol. 13, no. 10, pp. e295–e324, 2016, focus Issue: Sudden Death. [Online]. Available: https://www.sciencedirect.com/science/article/pii/S1547527116303721

[166] C. Veltmann *et al.*, "Insights into the location of type i ECG in patients with Brugada syndrome: Correlation of ECG and cardiovascular magnetic resonance imaging," *Heart Rhythm*, vol. 9, no. 3, pp. 414–421, 2012. [Online]. Available: https://www.sciencedirect.com/science/article/pii/S1547527111013154

[167] S. Sangwatanaroj *et al.*, "New electrocardiographic leads and the procainamide test for the detection of the Brugada sign in sudden unexplained death syndrome survivors and their relatives," *European Heart Journal*, vol. 22, no. 24, pp. 2290–2296, 12 2001. [Online]. Available: https://doi.org/10.1053/euhj.2001.2691

[168] M. Govindan *et al.*, "Utility of high and standard right precordial leads during ajmaline testing for the diagnosis of Brugada syndrome," *Heart*, vol. 96, no. 23, pp. 1904–1908, 2010. [Online]. Available: https://heart.bmj.com/content/96/23/1904

[169] A. S. Amin *et al.*, "Fever increases the risk for cardiac arrest in the Brugada syndrome," *Annals of Internal Medicine*, vol. 149, no. 3, pp. 216–218, 2008, pMID: 18678856. [Online]. Available: https://doi.org/10.7326/0003-4819-149-3-200808050-00020

[170] C. C. Cheung *et al.*, "Comparison of ajmaline and procainamide provocation tests in the diagnosis of Brugada syndrome," *JACC: Clinical Electrophysiology*, vol. 5, no. 4, pp. 504–512, 2019. [Online]. Available: https://www.sciencedirect.com/science/article/pii/S2405500X19301495

[171] M. H. Gollob *et al.*, "Recommendations for the use of genetic testing in the clinical evaluation of inherited cardiac arrhythmias associated with sudden cardiac death: Canadian cardiovascular Society/Canadian Heart Rhythm Society joint position paper," *Canadian Journal of Cardiology*, vol. 27, no. 2, pp. 232–245, 2011. [Online]. Available: https://www.sciencedirect.com/science/article/pii/S0828282X10000942

[172] M. C. Gonzalez Corcia *et al.*, "Brugada syndrome in the young: An assessment of risk factors predicting future events," *Europace*, vol. 19, no. 11, p. 1864 – 1873, 2017, cited by: 39; All Open Access, Bronze Open Access, Green Open Access. [Online]. Available: https://www.scopus.com/inward/record.uri?eid=2-s2.0-85034833643&doi=10.1093%2feuropace%2feuw206&partnerID=40&md5=1099b65a0c8b59bb758e2a1a735fd307

[173] A. Andorin *et al.*, "Impact of clinical and genetic findings on the management of young patients with Brugada syndrome," *Heart Rhythm*, vol. 13, no. 6, pp. 1274–1282, 2016. [Online]. Available: https://www.sciencedirect.com/science/article/pii/S154752711600182X

[174] S. G. Priori *et al.*, "Natural history of Brugada syndrome: Insights for risk stratification and management," *Circulation*, vol. 105, no. 11, p. 1342 – 1347, 2002, cited by: 926. [Online]. Available: https://www.scopus.com/inward/record.uri?eid=2-s2.0-0037133593&doi=10.1161%2fhc1102.105288&partnerID=40&md5=3767286ec2774e412dc312f3931404ff

[175] S. G. Priori *et al.*, "Risk stratification in Brugada syndrome: Results of the PRELUDE (PRogrammed Electrical stimUlation preDictive valuE) registry," *Journal of the American College of Cardiology*, vol. 59, no. 1, pp. 37–45, 2012. [Online]. Available: https://www.sciencedirect.com/science/article/pii/S07351097110453OX

[176] V. Probst *et al.*, "Long-term prognosis of patients diagnosed with Brugada syndrome: Results from the finger Brugada syndrome registry," *Circulation*, vol. 121, no. 5, p. 635 – 643, 2010, cited by: 729; All Open Access, Bronze Open Access, Green Open Access. [Online]. Available: https://www.scopus.com/inward/record.uri?eid=2-s2.0-76649101444&doi=10.1161%2fCIRCULATIONAHA.109.887026&partnerID=40&md5=4b76e1edfc53fa8a08f03b2168c26b2f

[177] H. Kawazoe *et al.*, "Risk stratification of ventricular fibrillation in Brugada syndrome using noninvasive scoring methods," *Heart Rhythm*, vol. 13, no. 10, pp. 1947–1954, 2016, focus Issue: Sudden Death. [Online]. Available: https://www.sciencedirect.com/science/article/pii/S1547527116305100

[178] A. Ueoka *et al.*, "Prognostic significance of the sodium channel blocker test in patients with Brugada syndrome," *Journal of the American Heart Association*, vol. 7, no. 10, 2018, cited by: 19; All Open Access, Gold Open Access, Green Open Access. [Online]. Available: https://www.scopus.com/inward/record.uri?eid=2-s2.0-85046950671&doi=10.1161%2fJAHA.118.008617&partnerID=40&md5=e3fb5ab679a435aa83871d1d5059bd4f

[179] S. Honarbakhsh *et al.*, "A primary prevention clinical risk score model for patients with Brugada syndrome (BRUGADA-RISK)," *JACC: Clinical Electrophysiology*, vol. 7, no. 2, pp. 210–222, 2021. [Online]. Available: https://www.sciencedirect.com/science/article/pii/S2405500X20308197

[180] P. Berthome *et al.*, "Clinical presentation and follow-up of women affected by Brugada syndrome," *Heart Rhythm*, vol. 16, no. 2, pp. 260–267, 2019. [Online]. Available: https://www.sciencedirect.com/science/article/pii/S1547527118309032

[181] M. Subramanian *et al.*, "A novel prediction model for risk stratification in patients with a type 1 Brugada ECG pattern," *Journal of Electrocardiology*, vol. 55, pp. 65–71, 2019. [Online]. Available: https://www.sciencedirect.com/science/article/pii/S0022073618307891

[182] P. Delise *et al.*, "Risk stratification in individuals with the Brugada type 1 ECG pattern without previous cardiac arrest: usefulness of a combined clinical and electrophysiologic approach," *European Heart Journal*, vol. 32, no. 2, pp. 169–176, 10 2010. [Online]. Available: https://doi.org/10.1093/eurheartj/ehq381

[183] J.-M. J. Juang *et al.*, "Prevalence and prognosis of Brugada electrocardiogram patterns in an elderly Han chinese population: a nation-wide community-based study (HALST cohort)," *EP Europace*, vol. 17, no. suppl_2, pp. ii54–ii62, 02 2016. [Online]. Available: https://doi.org/10.1093/europace/euv141

[184] J. Sieira *et al.*, "A score model to predict risk of events in patients with Brugada syndrome," *European Heart Journal*, vol. 38, no. 22, pp. 1756–1763, 03 2017. [Online]. Available: https://doi.org/10.1093/eurheartj/ehx119

[185] G. Tse *et al.*, "Incorporating latent variables using nonnegative matrix factorization improves risk stratification in Brugada syndrome," *Journal of the American Heart Association*, vol. 9, no. 22, 2020, cited by: 33; All Open Access, Gold Open Access, Green Open Access. [Online]. Available: https://www.scopus.com/inward/record.uri?eid=2-s2.0-85096347878&doi=10.1161%2fJAHA.119.012714&partnerID=40&md5=1bb184a0d9b719bfb75b91b2da0a606e

[186] S. Kamakura *et al.*, "Long-term prognosis of probands with Brugada-pattern ST-elevation in leads V 1-V 3," *Circulation: Arrhythmia and Electrophysiology*, vol. 2, no. 5, p. 495 – 503, 2009, cited by: 243; All Open Access, Bronze Open Access. [Online]. Available: https://www.scopus.com/inward/record.uri?eid=2-s2.0-74449088794&doi=10.1161%2fCIRCEP.108.816892&partnerID=40&md5=5b5f7b3a97b112e1a8fd4d24afa9f8fb

[187] L. Rivard *et al.*, "Predictors of ventricular arrhythmias and sudden death in a Québec cohort with Brugada syndrome," *Canadian Journal of Cardiology*, vol. 32, no. 11, pp. 1355.e1–1355.e7, 2016. [Online]. Available: https://www.sciencedirect.com/science/article/pii/S0828282X16300010

[188] S. Zumhagen *et al.*, "Tpeak–Tend interval and Tpeak–Tend/QT ratio in patients with Brugada syndrome," *EP Europace*, vol. 18, no. 12, pp. 1866–1872, 03 2016. [Online]. Available: https://doi.org/10.1093/europace/euw033

[189] J. P. Martínez *et al.*, "The STAFF III database: ECGs recorded during acutely induced myocardial ischemia," in *2017 Computing in Cardiology (CinC)*, 2017, pp. 1–4.

[190] M. M. Demidova *et al.*, "ST-segment dynamics during reperfusion period and the size of myocardial injury in experimental myocardial infarction," *Journal of Electrocardiology*, vol. 44, no. 1, pp. 74–81, 2011. [Online]. Available: https://www.sciencedirect.com/science/article/pii/S0022073610005558

[191] A. S. Tsvetkova *et al.*, "Contribution of depolarization and repolarization changes to J-wave generation and ventricular fibrillation in ischemia," *Frontiers in Physiology*, vol. Volume 11 - 2020, 2020. [Online]. Available: https://www.frontiersin.org/journals/physiology/articles/10.3389/fphys.2020.568021

[192] N. Gómez *et al.*, "Risk stratification of patients with type 2 long-QT syndrome through analysis of T-wave morphology," *Journal of the American Heart Association*, vol. 15, p. e048388, 2026. [Online]. Available: https://www.ahajournals.org/doi/abs/10.1161/JAHA.125.048388

[193] N. Gómez *et al.*, "T-wave peak-to-end morphology restitution as biomarker in Brugada syndrome," in *2025 Computing in Cardiology (CinC)*, vol. 52, 2025, pp. 1–4.

[194] L. Sörnmo and P. Laguna, *Electrocardiogram (ECG) Signal Processing*. John Wiley & Sons, Ltd, 2006. [Online]. Available: https://onlinelibrary.wiley.com/doi/abs/10.1002/9780471740360.ebs1482

[195] J. Martinez *et al.*, "A wavelet-based ECG delineator: evaluation on standard databases," *IEEE Transactions on Biomedical Engineering*, vol. 51, no. 4, pp. 570–581, 2004.

[196] P. Laguna *et al.*, "Automatic detection of wave boundaries in multilead ECG signals: Validation with the CSE database," *Computers and Biomedical Research*, vol. 27, no. 1, pp. 45–60, 1994. [Online]. Available: https://www.sciencedirect.com/science/article/pii/S0010480984710068

[197] F. Castells *et al.*, "Principal component analysis in ECG signal processing," *EURASIP Journal on Advances in Signal Processing*, vol. 2007, pp. 1–21, 2007.

[198] F. Palmieri *et al.*, "Monitoring blood potassium concentration in hemodialysis patients by quantifying T-wave morphology dynamics," *Scientific Reports*, vol. 11, p. 3883, 2021. [Online]. Available: https://doi.org/10.1038/s41598-021-82935-5

[199] M. W. Rivolta *et al.*, "Quantification of spatial heterogeneity of ventricular repolarization during early-stage cardiac ischemia induced by coronary angioplasty," in *2019 41st Annual International Conference of the IEEE Engineering in Medicine and Biology Society (EMBC)*, 2019, pp. 4250–4253.

[200] C. Graff *et al.*, "Covariate analysis of QTc and T-wave morphology: New possibilities in the evaluation of drugs that affect cardiac repolarization," *Clinical Pharmacology & Therapeutics*, vol. 88, no. 1, pp. 88–94, 2010. [Online]. Available: https://ascpt.onlinelibrary.wiley.com/doi/abs/10.1038/clpt.2010.51

[201] C. Graff *et al.*, "Identifying drug-induced repolarization abnormalities from distinct ECG patterns in congenital long QT syndrome," *Drug Safety*, vol. 32, pp. 599–611, 2009. [Online]. Available: https://doi.org/10.2165/00002018-200932070-00006

[202] J. Ramírez *et al.*, "Variability of ventricular repolarization dispersion quantified by time-warping the morphology of the T-waves," *IEEE Transactions on Biomedical Engineering*, vol. 64, no. 7, pp. 1619–1630, 2017.

[203] J. Ramírez *et al.*, "T-wave morphology restitution predicts sudden cardiac death in patients with chronic heart failure," *Journal of the American Heart Association*, vol. 6, no. 5, p. e005310, 2017. [Online]. Available: https://www.ahajournals.org/doi/abs/10.1161/JAHA.116.005310

[204] J. Ramírez *et al.*, "ECG T-wave morphologic variations predict ventricular arrhythmic risk in low- and moderate-risk populations," *Journal of the American Heart Association*, vol. 11, no. 17, p. e025897, 2022. [Online]. Available: https://www.ahajournals.org/doi/abs/10.1161/JAHA.121.025897

[205] H. A. Bukhari *et al.*, "Monitoring of serum potassium and calcium levels in end-stage renal disease patients by ECG depolarization morphology analysis," *Sensors*, vol. 22, no. 8, 2022. [Online]. Available: https://www.mdpi.com/1424-8220/22/8/2951

[206] J. O. Ramsay and X. Li, "Curve registration," *Journal of the Royal Statistical Society: Series B (Statistical Methodology)*, vol. 60, no. 2, pp. 351–363, 1998. [Online]. Available: https://rss.onlinelibrary.wiley.com/doi/abs/10.1111/1467-9868.00129

[207] A. Srivastava *et al.*, "Registration of Functional Data Using Fisher-Rao Metric," *arXiv e-prints*, p. arXiv:1103.3817, Mar. 2011.

[208] J. D. Tucker *et al.*, "Generative models for functional data using phase and amplitude separation," *Computational Statistics & Data Analysis*, vol. 61, pp. 50–66, 2013. [Online]. Available: https://www.sciencedirect.com/science/article/pii/S0167947312004227

[209] D. P. Bertsekas, *Dynamic programming and optimal control*. Belmont, MA: Athena Scientific, 1995.

[210] H. A. Bukhari *et al.*, "Characterization of T wave amplitude, duration and morphology changes during hemodialysis: Relationship with serum electrolyte levels and heart rate," *IEEE Transactions on Biomedical Engineering*, vol. 68, no. 8, pp. 2467–2478, 2021.

[211] O. Sayadi *et al.*, "A novel method to capture the onset of dynamic electrocardiographic ischemic changes and its implications to arrhythmia susceptibility," *Journal of the American Heart Association*, vol. 3, no. 5, p. e001055, 2014. [Online]. Available: https://www.ahajournals.org/doi/abs/10.1161/JAHA.114.001055

[212] J. M. Di Diego and C. Antzelevitch, "Acute myocardial ischemia: Cellular mechanisms underlying ST segment elevation," *Journal of Electrocardiology*, vol. 47, no. 4, pp. 486–490, 2014. [Online]. Available: https://www.sciencedirect.com/science/article/pii/S0022073614000545

[213] O. Mazumder *et al.*, "In silico cardiac model to evaluate myocardial ischemia effect on hemodynamic parameters," in *2020 28th European Signal Processing Conference (EUSIPCO)*, 2021, pp. 1105–1109.

[214] M. N. Niemeijer *et al.*, "Short-term QT variability markers for the prediction of ventricular arrhythmias and sudden cardiac death: a systematic review," *Heart*, vol. 100, no. 23, pp. 1831–1836, 2014. [Online]. Available: https://heart.bmj.com/content/100/23/1831

[215] J. Martinez *et al.*, "Characterization of repolarization alternans during ischemia: time-course and spatial analysis," *IEEE Transactions on Biomedical Engineering*, vol. 53, no. 4, pp. 701–711, 2006.

[216] S. Palacios *et al.*, "Sudden cardiac death prediction in chronic heart failure patients by periodic repolarization dynamics," in *2020 Computing in Cardiology*, 2020, pp. 1–4.

[217] J. E. Azarov *et al.*, "Progressive increase of the Tpeak-Tend interval is associated with ischaemia-induced ventricular fibrillation in a porcine myocardial infarction model," *EP Europace*, vol. 20, no. 5, pp. 880–886, 05 2017. [Online]. Available: https://doi.org/10.1093/europace/eux104

[218] M. NAKAGAWA *et al.*, "Gender differences in ventricular repolarization:," *Pacing and Clinical Electrophysiology*, vol. 26, no. 1p1, pp. 59–64, 2003. [Online]. Available: https://onlinelibrary.wiley.com/doi/abs/10.1046/j.1460-9592.2003.00151.x

[219] M. NAKAGAWA *et al.*, "Gender differences in the dynamics of terminal T wave intervals," *Pacing and Clinical Electrophysiology*, vol. 27, no. 6p1, pp. 769–774, 2004. [Online]. Available: https://onlinelibrary.wiley.com/doi/abs/10.1111/j.1540-8159.2004.00526.x

[220] S. S. Virani *et al.*, "Heart disease and stroke statistics—2021 update," *Circulation*, vol. 143, no. 8, pp. e254–e743, 2021. [Online]. Available: https://www.ahajournals.org/doi/abs/10.1161/CIR.0000000000000950

[221] A. Timmis *et al.*, "European society of cardiology: Cardiovascular disease statistics 2019," *European Heart Journal*, vol. 41, no. 1, pp. 12–85, 12 2019. [Online]. Available: https://doi.org/10.1093/eurheartj/ehz859

[222] D. S. Sim *et al.*, "Cardioprotective effect of substance P in a porcine model of acute myocardial infarction," *International Journal of Cardiology*, vol. 271, pp. 228–232, 2018. [Online]. Available: https://www.sciencedirect.com/science/article/pii/S0167527318322551

[223] A. F. Lubberding *et al.*, "Comparison of hemodynamics, cardiac electrophysiology, and ventricular arrhythmia in an open- and a closed-chest porcine model of acute myocardial infarction," *American Journal of Physiology-Heart and Circulatory Physiology*, vol. 318, no. 2, pp. H391–H400, 2020, pMID: 31922881. [Online]. Available: https://doi.org/10.1152/ajpheart.00406.2019

[224] K. Li *et al.*, "A robust percutaneous myocardial infarction model in pigs and its effect on left ventricular function," *Journal of Cardiovascular Translational Research*, vol. 14, pp. 1075–1084, 2021. [Online]. Available: https://doi.org/10.1007/s12265-021-10123-x

[225] E. López *et al.*, "Identification of very early inflammatory markers in a porcine myocardial infarction model," *BMC Veterinary Research*, vol. 15, p. 91, 2019. [Online]. Available: https://doi.org/10.1186/s12917-019-1837-5

[226] C. Antzelevitch *et al.*, "Does Tpeak–Tend provide an index of transmural dispersion of repolarization?" *Heart Rhythm*, vol. 4, no. 8, pp. 1114–1116, 2007. [Online]. Available: https://www.sciencedirect.com/science/article/pii/S1547527107006054

[227] C. Antzelevitch *et al.*, "Tpeak-Tend as a predictor of ventricular arrhythmogenesis," *International Journal of Cardiology*, vol. 249, pp. 75–76, 12 2017, doi: 10.1016/j.ijcard.2017.09.005. [Online]. Available: https://doi.org/10.1016/j.ijcard.2017.09.005

[228] E. Kaplinsky *et al.*, "Two periods of early ventricular arrhythmia in the canine acute myocardial infarction model." *Circulation*, vol. 60, no. 2, pp. 397–403, 1979. [Online]. Available: https://www.ahajournals.org/doi/abs/10.1161/01.CIR.60.2.397

[229] U. MENKEN *et al.*, "Prophylaxis of ventricular fibrillation after acute experimental coronary occlusion by chronic beta- adrenoceptor blockade with atenolol1," *Cardiovascular Research*, vol. 13, no. 10, pp. 588–594, 10 1979. [Online]. Available: https://doi.org/10.1093/cvr/13.10.588

[230] N. Gómez *et al.*, "Time-warping analysis of the T-wave peak-to-end interval to quantify ventricular repolarization dispersion during ischemia," *IEEE Journal of Biomedical and Health Informatics*, vol. 27, no. 11, pp. 5314–5325, 2023.

[231] E. Hedström *et al.*, "Infarct evolution in man studied in patients with first-time coronary occlusion in comparison to different species - implications for assessment of myocardial salvage," *Journal of Cardiovascular Magnetic Resonance*, vol. 11, no. 1, p. 38, 2009. [Online]. Available: https://www.sciencedirect.com/science/article/pii/S1097664723005197

[232] C. S. Kuo *et al.*, "Characteristics and possible mechanism of ventricular arrhythmia dependent on the dispersion of action potential durations." *Circulation*, vol. 67, no. 6, pp. 1356–1367, 1983. [Online]. Available: https://www.ahajournals.org/doi/abs/10.1161/01.CIR.67.6.1356

[233] A. S. Tsvetkova *et al.*, "Melatonin prevents early but not delayed ventricular fibrillation in the experimental porcine model of acute ischemia," *International Journal of Molecular Sciences*, vol. 22, no. 1, 2021. [Online]. Available: https://www.mdpi.com/1422-0067/22/1/328

[234] N. V. Arteyeva, "Dispersion of ventricular repolarization: Temporal and spatial," *World Journal of Cardiology*, vol. 12, no. 9, p. 437, 2020.

[235] Y. Xia *et al.*, "Tpeak-Tend interval as an index of global dispersion of ventricular repolarization: Evaluations using monophasic action potential mapping of the epi- and endocardium in swine," *Journal of Interventional Cardiac Electrophysiology*, vol. 14, pp. 79–87, 2005. [Online]. Available: https://doi.org/10.1007/s10840-005-4592-4

[236] M. Meo *et al.*, "Body surface mapping of ventricular repolarization heterogeneity: An ex-vivo multiparameter study," *Frontiers in Physiology*, vol. Volume 11 - 2020, 2020. [Online]. Available: https://www.frontiersin.org/journals/physiology/articles/10.3389/fphys.2020.00933

[237] O. G. Bernikova *et al.*, "Prolonged repolarization in the early phase of ischemia is associated with ventricular fibrillation development in a porcine model," *Frontiers in Physiology*, vol. Volume 14 - 2023, 2023. [Online]. Available: https://www.frontiersin.org/journals/physiology/articles/10.3389/fphys.2023.1035032

[238] N. V. Arteyeva *et al.*, "What does the Tpeak-Tend interval reflect? An experimental and model study," *Journal of Electrocardiology*, vol. 46, no. 4, pp. 296.e1–296.e8, 2013. [Online]. Available: https://www.sciencedirect.com/science/article/pii/S0022073613000137

[239] J. A. Kors *et al.*, "The meaning of the Tp-Te interval and its diagnostic value," *Journal of Electrocardiology*, vol. 41, no. 6, pp. 575–580, 2008. [Online]. Available: https://www.sciencedirect.com/science/article/pii/S0022073608002938

[240] A. S. Poselyaninov *et al.*, "Duration of electrocardiographic TPEAK-TEND interval in ischemia: Dispersion of repolarization vs. myocardium area at risk," *Journal of Electrocardiology*, vol. 93, p. 154129, 2025. [Online]. Available: https://www.sciencedirect.com/science/article/pii/S0022073625002572

[241] N. Gómez *et al.*, "T-wave peak-to-end changes quantified by time-warping predicts ventricular fibrillation in a porcine myocardial infarction model," *IEEE Transactions on Biomedical Engineering*, vol. 71, no. 10, pp. 2968–2977, 2024.

[242] T. C. Pataky, "One-dimensional statistical parametric mapping in Python," *Computer Methods in Biomechanics and Biomedical Engineering*, vol. 15, no. 3, pp. 295–301, 2012, pMID: 21756121. [Online]. Available: https://doi.org/10.1080/10255842.2010.527837

[243] W. Xianpei *et al.*, "Tpeak-Tend dispersion as a predictor for malignant arrhythmia events in patients with vasospastic angina," *International Journal of Cardiology*, vol. 249, pp. 61–65, 2017. [Online]. Available: https://www.sciencedirect.com/science/article/pii/S0167527317319289

[244] G. Mugnai *et al.*, "Tpeak-to-Tend/QT is an independent predictor of early ventricular arrhythmias and arrhythmic death in anterior ST elevation myocardial infarction patients," *European Heart Journal. Acute Cardiovascular Care*, vol. 5, no. 6, pp. 473–480, 10 2016. [Online]. Available: https://doi.org/10.1177/2048872615598616

[245] T. M. Rosenthal *et al.*, "T-peak to T-end interval for prediction of ventricular tachyarrhythmia and mortality in a primary prevention population with systolic cardiomyopathy," *Heart Rhythm*, vol. 12, no. 8, pp. 1789–1797, 2015. [Online]. Available: https://www.sciencedirect.com/science/article/pii/S1547527115005457

[246] S. Aoki *et al.*, "Tpeak to Tend interval is a short term prognostic factor of cardiac death in acute heart failure syndrome patients with reduced ejection fraction," *Journal of the American College of Cardiology*,

vol. 65, no. 10, Supplement, p. A823, 2015. [Online]. Available: https://www.sciencedirect.com/science/article/pii/S0735109715608233

[247] P. Maury *et al.*, "Increased Tpeak-Tend interval is highly and independently related to arrhythmic events in Brugada syndrome," *Heart Rhythm*, vol. 12, no. 12, pp. 2469–2476, 2015, focus Issue: Devices. [Online]. Available: https://www.sciencedirect.com/science/article/pii/S154752711500942X

[248] M. Bombelli *et al.*, "Prognostic relevance of electrocardiographic Tpeak-Tend interval in the general and in the hypertensive population: Data from the pressioni arteriose monitorate e loro associazioni study," *Journal of Hypertension*, vol. 34, no. 9, p. 1823 – 1830, 2016, cited by: 10. [Online]. Available: https://www.scopus.com/inward/record.uri?eid=2-s2.0-84976320579&doi=10.1097%2fHJH.0000000000001005&partnerID=40&md5=d8ea37e4186e7fa2f90587612208502d

[249] G. Tse *et al.*, "The Tpeak-Tend interval as an electrocardiographic risk marker of arrhythmic and mortality outcomes: A systematic review and meta-analysis," *Heart Rhythm*, vol. 14, no. 8, pp. 1131–1137, 2017. [Online]. Available: https://www.sciencedirect.com/science/article/pii/S1547527117306458

[250] W. Zareba and I. Cygankiewicz, "Long QT syndrome and short QT syndrome," *Progress in Cardiovascular Diseases*, vol. 51, no. 3, pp. 264–278, 2008, sudden Cardiac Death. [Online]. Available: https://www.sciencedirect.com/science/article/pii/S0033062008000947

[251] I. Goldenberg and A. J. Moss, "Long QT syndrome," *Journal of the American College of Cardiology*, vol. 51, no. 24, pp. 2291–2300, 2008. [Online]. Available: https://www.sciencedirect.com/science/article/pii/S0735109708011364

[252] R. W. Sy *et al.*, "Derivation and validation of a simple exercise-based algorithm for prediction of genetic testing in relatives of LQTS probands," *Circulation*, vol. 124, no. 20, pp. 2187–2194, 2011. [Online]. Available: https://www.ahajournals.org/doi/abs/10.1161/CIRCULATIONAHA.111.028258

[253] C. Lang *et al.*, "Electro-mechanical dysfunction in long QT syndrome: Role for arrhythmogenic risk prediction and modulation by sex and sex hormones," *Progress in Biophysics and Molecular Biology*, vol. 120, no. 1, pp. 255–269, 2016, recent Developments in Biophysics & Molecular Biology of Heart Rhythm. [Online]. Available: https://www.sciencedirect.com/science/article/pii/S007961071500259X

[254] P. G. Platonov *et al.*, "Risk stratification of type 2 long-QT syndrome mutation carriers with normal QTc interval," *Circulation: Arrhythmia and Electrophysiology*, vol. 11, no. 7, p. e005918, 2018. [Online]. Available: https://www.ahajournals.org/doi/abs/10.1161/CIRCEP.117.005918

[255] J.-P. Couderc *et al.*, "T-wave morphology abnormalities in benign, potent, and arrhythmogenic Ikr inhibition," *Heart Rhythm*, vol. 8, no. 7, pp. 1036–1043,

2011. [Online]. Available: https://www.sciencedirect.com/science/article/pii/S1547527111001421

[256] M. Vaglio *et al.*, "A quantitative assessment of T-wave morphology in LQT1, LQT2, and healthy individuals based on Holter recording technology," *Heart Rhythm*, vol. 5, no. 1, pp. 11–18, 2008. [Online]. Available: https://www.sciencedirect.com/science/article/pii/S1547527107008922

[257] B. J. M. Hermans *et al.*, "Support vector machine-based assessment of the T-wave morphology improves long QT syndrome diagnosis," *EP Europace*, vol. 20, no. suppl_3, pp. iii113–iii119, 11 2018. [Online]. Available: https://doi.org/10.1093/europace/euy243

[258] C. Sudlow *et al.*, "UK Biobank: An open access resource for identifying the causes of a wide range of complex diseases of middle and old age," *PLOS Medicine*, vol. 12, no. 3, pp. 1–10, 03 2015. [Online]. Available: https://doi.org/10.1371/journal.pmed.1001779

[259] P. A. Harris *et al.*, "Research electronic data capture (REDCap)—A metadata-driven methodology and workflow process for providing translational research informatics support," *Journal of Biomedical Informatics*, vol. 42, no. 2, pp. 377–381, 2009. [Online]. Available: https://www.sciencedirect.com/science/article/pii/S1532046408001226

[260] P. A. Harris *et al.*, "The REDCap consortium: Building an international community of software platform partners," *Journal of Biomedical Informatics*, vol. 95, p. 103208, 2019. [Online]. Available: https://www.sciencedirect.com/science/article/pii/S1532046419301261

[261] M. Andersen *et al.*, "A robust method for quantification of IKr-related T-wave morphology abnormalities," in *2007 Computers in Cardiology*, 2007, pp. 341–344.

[262] E. H. Locati *et al.*, "Age- and sex-related differences in clinical manifestations in patients with congenital long-QT syndrome," *Circulation*, vol. 97, no. 22, pp. 2237–2244, 1998. [Online]. Available: https://www.ahajournals.org/doi/abs/10.1161/01.CIR.97.22.2237

[263] I. Goldenberg *et al.*, "Risk prediction in women with congenital long QT syndrome," *Journal of the American Heart Association*, vol. 10, no. 14, p. e021088, 2021. [Online]. Available: https://www.ahajournals.org/doi/abs/10.1161/JAHA.121.021088

[264] H.-N. PAK *et al.*, "Spatial dispersion of action potential duration restitution kinetics is associated with induction of ventricular tachycardia/fibrillation in humans," *Journal of Cardiovascular Electrophysiology*, vol. 15, no. 12, pp. 1357–1363, 2004.

[265] S. Romagnoli *et al.*, "ECG-based spatiotemporal characterization of delayed and heterogeneous ventricular activation in Brugada syndrome," *IEEE Transactions on Biomedical Engineering*, pp. 1–12, 2026. [Online]. Available: https://ieeexplore.ieee.org/abstract/document/11652913

[266] M. Hayashi *et al.*, "Ventricular repolarization restitution properties in patients exhibiting type 1 Brugada electrocardiogram with and without inducible ventricular fibrillation," *JACC*, vol. 51, no. 12, pp. 1162–1168, 2008. [Online]. Available: https://www.jacc.org/doi/abs/10.1016/j.jacc.2007.11.050

[267] T. Miyazaki *et al.*, "Autonomic and antiarrhythmic drug modulation of ST segment elevation in patients with Brugada syndrome," *Journal of the American College of Cardiology*, vol. 27, no. 5, pp. 1061–1070, 1996. [Online]. Available: https://www.sciencedirect.com/science/article/pii/0735109795006133

[268] J. C. Hevia *et al.*, "Tpeak-Tend and Tpeak-Tend dispersion as risk factors for ventricular tachycardia/ventricular fibrillation in patients with the Brugada syndrome," *JACC*, vol. 47, no. 9, pp. 1828–1834, 2006. [Online]. Available: https://www.jacc.org/doi/abs/10.1016/j.jacc.2005.12.049

[269] G. Mugnai *et al.*, "Role of electrocardiographic Tpeak-Tend for the prediction of ventricular arrhythmic events in the Brugada syndrome," *The American Journal of Cardiology*, vol. 120, no. 8, pp. 1332–1337, 2017. [Online]. Available: https://www.sciencedirect.com/science/article/pii/S0002914917311785

[270] K. Ohkubo *et al.*, "Prolonged QRS duration in lead V2 and risk of life-threatening ventricular arrhythmia in patients with Brugada syndrome," *International Heart Journal*, vol. 52, no. 2, pp. 98–102, 2011.

[271] M. J. JUNTTILA *et al.*, "Differences in 12-lead electrocardiogram between symptomatic and asymptomatic Brugada syndrome patients," *Journal of Cardiovascular Electrophysiology*, vol. 19, no. 4, pp. 380–383, 2008. [Online]. Available: https://onlinelibrary.wiley.com/doi/abs/10.1111/j.1540-8167.2007.01050.x

[272] P. Chakraborty *et al.*, "Exercise-induced QRS prolongation in Brugada syndrome: Implications for improving disease phenotyping and diagnosis," *JACC: Clinical Electrophysiology*, vol. 10, no. 8, pp. 1813–1824, 2024. [Online]. Available: https://www.sciencedirect.com/science/article/pii/S2405500X24002949

PUBLICATIONS DERIVED FROM THE THESIS

Journal Publications

- **N. Gómez**, J. Ramírez, J. P. Martínez, and P. Laguna, "Time-warping analysis of the T-wave peak-to-end interval to quantify ventricular repolarization dispersion during ischemia," IEEE Journal of Biomedical and Health Informatics, vol. 27, no. 11, pp. 5314–5325, 2023. doi: 10.1109/JBHI.2023.3310878

- **N. Gómez**, J. Ramírez, A. Martín-Yebra, M. M. Demidova, P. Platonov, J. P. Martínez, and P. Laguna, "T-wave peak-to-end changes quantified by time-warping predicts ventricular fibrillation in a porcine myocardial infarction model," IEEE Transactions on Biomedical Engineering, vol. 71, no. 10, pp. 2968–2977, 2024. doi:10.1109/TBME.2024.3404254

- **N. Gómez**, A. S. Abramochkina, J. Ramírez, A. O. Ovechkin, O. G. Bernikova, P. Platonov, J. E. Azarov, P. Laguna, J. P. Martínez, "T-wave peak-to-end Changes, quantified by time-warping, surrogates ventricular repolarization dispersion for ventricular fibrillation prediction in a porcine myocardial infarction model," IEEE Transactions on Biomedical Engineering, doi: 10.1109/TBME.2026.3683284, *In press.*

- **N. Gómez**, J. Ramírez, A. A. Savelev, P. Dahlberg, A. Svensson, N. Larsson, E. Ljungström, U. Chaudhry, J. P. Martínez, P. Laguna, P. G. Platonov "Risk stratification of type 2 long QT syndrome patients through analysis of T-wave morphology," Journal of the American Heart Association, vol. 15, p. e048388, 2026. doi:10.1161/JAHA.125.048388

Conference Publications

- **N. Gómez**, J. Ramírez, J. P. Martínez, and P. Laguna, "Time-warping based end-of-T-wave shape marker reflects repolarization changes during ischemia," in 2022 Computing in Cardiology (CinC), vol. 498, pp. 1–4, 2022.

- **N. Gómez**, J. Ramírez, A. Martín-Yebra, M. M. Demidova, P. Platonov, J. P. Martínez, and P. Laguna, "Changes in T-peak-to-T-end morphology measured by time-warping are associated with ischemia-induced ventricular fibrillation in a porcine model," in 2023 Computing in Cardiology (CinC), vol. 50, pp. 1–4, 2023.

- **N. Gómez**, J. Ramírez, A. M. Yebra, M. Demidova, P. Platonov, J. Martínez, and P. Laguna, "Los cambios en la morfología del pico al fin de la onda T, cuantificados mediante "time-warping", están asociados con la aparición de fibrilación ventricular en un modelo porcino de isquemia aguda," in CASEIB 2023. Libro de Actas del XLI Congreso Anual de la Sociedad Española de Ingeniería Biomédica (CASEIB 2023), pp. 2–5, Sociedad Española de Ingeniería Biomédica (SEIB), 2023.

- **N. Gómez**, J. Ramírez, A. S. Tsvetkova, P. Platonov, J. E. Azarov, J. P. Martínez, and P. Laguna, "Dynamics of T-peak-to-T-end morphology changes in an open-chest porcine model, and its relation to arrhythmic events," in 2024 Computing in Cardiology (CinC), vol. 51, pp. 1–4, 2024.

- **N. Gómez**, J. Ramírez, J. P. Martínez, and P. Laguna, "Evaluation of T-wave time-warping dynamics in patients with long QT syndrome.," in 2024 13th Conference of the European Study Group on Cardiovascular Oscillations (ESGCO), pp. 1–2, 2024

- **N. Gómez**, J. Ramírez, A. Isabel Roquero, F. Palmieri, E. Arbelo Lainez, J. P. Martínez Cortés, and P. Laguna Lasaosa, "Evaluación de los cambios en la morfología del pico al fin de la onda T, cuantificados mediante "time-warping", en pacientes con síndrome de Brugada," in Actas XLII Congreso Anual de la Sociedad Española de Ingeniería Biomédica (CASEIB 2024), pp. 29–32, Sociedad Española de Ingeniería Biomédica (SEIB), 2024.

- **N. Gómez**, J. Ramírez, A. I. Roquero, F. Palmieri, E. Arbelo, J. P. Martínez, and P. Laguna, "T-wave peak-to-end morphology restitution

as biomarker in Brugada syndrome," in 2025 Computing in Cardiology (CinC), vol. 52, pp. 1–4, 2025.

- **N. Gómez**, J. Ramírez, A. Martín-Yebra, P. Platonov, J. P. Martínez, and P. Laguna, "Los cambios en la morfología del intervalo Tpico-Tfin medidos mediante time-warping se asocian con la fibrilación ventricular inducida por la isquemia en un modelo porcino," in Jornada de Jóvenes Investigadores. I3A, vol. 11, 2023, doi: 10.26754/jjii3a.20239065.

- **N. Gómez**, J. Ramírez, J. P. Martínez, and P. Laguna, "Evaluación de la dinámica de la onda T en pacientes con síndrome de QT largo," in Jornada de Jóvenes Investigadores. I3A, vol. 12, 2024, doi: 10.26754/jjii3a.202410680.

- **N. Gómez**, J. Ramírez, A. Martín-Yebra, M. M. Demidova, P. Platonov, J. P. Martínez, and P. Laguna, "Robust Tp/Tpe measurement in a porcine ischemia model," in 19^{th} STAFF-MALT Studies Symposium, Mölle, Sweden, 2023.

- **N. Gómez**, A. S. Abramochkina, J. Ramírez, A. O. Ovechkin, P. Platonov, J. E. Azarov, P. Laguna, and J. P. Martínez, "Repolarization dynamics of T-peak-to-T-end time warping in an open-chest porcine infarction model and its relation to arrhythmic events," in 20^{th} STAFF-MALT Studies Symposium, Maastricht, The Netherlands, 2024.

- **N. Gómez**, A. S. Abramochkina, J. Ramírez, A. O. Ovechkin, O. G. Bernikova, P. Platonov, J. E. Azarov, P. Laguna, J. P. Martínez, "Time-warping-derived T-wave peak-to-end morphology as a non-invasive surrogate of ventricular repolarization dispersion in a porcine myocardial infarction model," in II Jornada de Personal Científico Joven del CIBER, Madrid, Spain, 2026.

LIST OF FIGURES

1.1 Anatomical overview of the heart showing the four chambers, valve system and main blood flow pathways. Regions in red represent oxygenated blood circulation, whereas blue regions represent deoxygenated blood circulation. Extracted from [31]. 4

1.2 Ventricular action potential waveform divided into phases (0–4), together with the principal inward and outward ionic flows that underlie each phase. Adapted from https://studmed.uio.no/ 7

1.3 Longitudinal heart section showing the conduction system responsible for coordinated electrical activation. Adapted from `https://smart.servier.com/`. 8

1.4 Representative APD-RR restitution curves obtained at different cardiac locations, illustrating regional differences in restitution behavior. The markers α_1 and α_2 denote the maximum and minimum local slopes, respectively, evaluated at RR = 600 ms. Extracted from [69] 10

1.5 Illustration of an ECG recording over two cardiac cycles, highlighting the principal waves and the most relevant time intervals. Extracted from [32]. 12

1.6 Illustration of lead-axis directions for the standard 12-lead ECG: frontal-plane limb leads (left) and transverse-plane precordial leads (right). Extracted from [32]. 16

1.7 Schematic overview of percutaneous coronary intervention (PCI): coronary catheter and guidewire positioning (left) and the main procedural steps (right), including balloon inflation, stent delivery, stent expansion, and the final result. Extracted from [82]. . . 21

1.8 Effects of representative LQTS mechanisms. Panel (a) illustrates the effects of ion channel mutations on simulated ventricular APs and the corresponding ECG manifestations across major genotypes (LQT1-LQT3), highlighting how different repolarization alterations can yield distinct QT and T-wave phenotypes. Panel (b) provides representative example of experimental data [91, 92] that are consistent with the patterns modeled in (a). Adapted from: [93] 22

1.9 Schematic representation of the AP patterns modifications and their corresponding manifestations on the surface ECG as proposed mechanism of ST-segment elevation in Brugada syndrome. Panel A illustrates a normal setting with minimal epicardial-endocardial voltage gradients and an isoelectric ST segment. Panels B and C depict Brugada-type morphologies in which an accentuated notch in certain regions of the epicardium creates a transmural voltage gradient that appears on the surface ECG (lead V2) as J-point/ST-segment elevation, yielding a saddleback (B) or coved (C) morphology. Extracted from [160]. 26

1.10 Representation of the (Top) standard- and (Buttom) high- lead placement alongside their corresponding precordial ECGs in a Brugada patient. Note the correspondence between hV5/hV6 on the high-lead ECG and V1/V2 on the standard-lead ECG. Extracted from [131]. 28

1.11 Overview of the common methodological basis and the clinical and experimental study branches used to evaluate T-wave morphology markers in ischemia, LQT2, and Brugada syndrome. Abbreviations: PCI, percutaneous coronary intervention; ECG, electrocardiogram; DOR, dispersion of repolarization; EGM, electrogram; LQT2, long QT syndrome type 2. 31

2.1 Example of the signal processing workflow from the original multilead ECG to the spatially PCA representation used for subsequent analysis. Panel (a) displays a 5 s segment of the original ECG from the 8 independent leads. Panel (b) shows the same segment after filtering, as described in Section 2.1.1, together with the delineation marks obtained as described in Section 2.1.2: the R peak (red dashed line), T-wave onset and end (blue dashed lines), and T-wave peak (red square). Panel (c) shows the corresponding principal components after applying spatial PCA to the 8 independent leads, as detailed in Section 2.1.3, with the same fiducial marks displayed on the dominant component. 38

2.2 Schematic overview of the time-warping analysis used to separate temporal and amplitude differences between two T-wave morphologies. Panel (a) shows the reference T wave $\boldsymbol{f}^r(\boldsymbol{t}^r)$ (blue line) and studied T wave $\boldsymbol{f}^s(\boldsymbol{t}^s)$ (red line), the latter showing longer duration and larger amplitude. (b) Corresponding square-root slope function representations of both waveforms in (a). (c) Warping function optimally relating $\boldsymbol{t}^r$ and $\boldsymbol{t}^s$. (d) Square-root slope function representations of the reference waveform and the warped studied waveform. (e) Warped studied T wave, $\boldsymbol{f}^s(\gamma^*(\boldsymbol{t}^r))$, where time-domain differences have been compensated and the remaining mismatch with respect to the reference waveform only reflects amplitude variability. 44

2.3 Illustration of the T_{pe}-restricted time-warping analysis. Panel (a) shows the reference T_{pe} waveform $\boldsymbol{f}^r(\boldsymbol{t}^r)$ (blue line) and the studied T_{pe} waveform $\boldsymbol{f}^s(\boldsymbol{t}^s)$ (red line). Panel (b) shows their corresponding square-root slope function representations. Panel (c) shows the optimal warping function $\gamma^*(\boldsymbol{t}^r)$. Panel (d) shows the square-root slope function representations of the reference waveform and the warped studied waveform, while panel (e) shows the warped studied waveform, $\boldsymbol{f}^s(\gamma(\boldsymbol{t}^r))$. 48

2.4 Overview of the weighting strategy applied to the computation of weighted time-warping markers. Panel (a) shows the reference and studied T waves, $\boldsymbol{f}^r(\boldsymbol{t}^r)$ and $\boldsymbol{f}^s(\boldsymbol{t}^s)$, respectively. Panels (b) and (c) display the weighting functions $\mathcal{W}_T(\boldsymbol{t}^r)$ and $\mathcal{W}_D(\boldsymbol{t}^r)$, derived from the reference T wave and its derivative, respectively. Panel (d) shows the unweighted warping function $\gamma^*(\boldsymbol{t}^r)$ ($\mathcal{W}_O(\boldsymbol{t}^r) = 1$) and the corresponding unweighted marker. Panels (e) and (f) show the weighted warping functions $\gamma^*_T(\boldsymbol{t}^r)$ and $\gamma^*_D(\boldsymbol{t}^r)$, together with the corresponding weighted markers. Light and dark green areas indicate the unweighted and weighted time-warping markers, respectively. 50

3.1 MWTPE $\boldsymbol{f}^s(\boldsymbol{t}^s)$ estimation and reference MWTPE $\boldsymbol{f}^r(\boldsymbol{t}^r)$ selection rule at the STAFF-III data-set. The $\boldsymbol{f}^s(\boldsymbol{t}^s)$ MWTPE was estimated from time-windows of 15 seconds duration and 10 seconds of overlap throughout the entire record. The reference $\boldsymbol{f}^r(\boldsymbol{t}^r)$ MWTPE was selected among the MWTPEs within 1 minute period, at the control recording, and within 30 seconds period at the beginning of the PCI recordings. 57

3.2 Analysis performed for time-warping index estimation from a particular patient of the STAFF-III database during the PCI procedure. Panel (a) displays both the reference $\boldsymbol{f}^r(\boldsymbol{t}^r)$ (solid blue) and a particular s-th $\boldsymbol{f}^s(\boldsymbol{t}^s)$ (doted red line) MWTPE. Panel (b) displays the warping function $\gamma^*(t^r)$ (dotted red line) that optimally relates the reference $\boldsymbol{f}^r(\boldsymbol{t}^r)$ and studied $\boldsymbol{f}^s(\boldsymbol{t}^s)$ MWTPEs. The total amount of warping, quantified by $d^{\mathrm{PCA}}_{w,\mathrm{T}pe}$, is represented by the green area between $\gamma^*(t^r)$ and t^r. Panel (c) displays both the reference $\boldsymbol{f}^r(\boldsymbol{t}^r)$ (blue line) MWTPE and the warped $\boldsymbol{f}^s(\gamma(\boldsymbol{t}^r))$ MWTPE. 59

3.3 Box and whisker plots of the $\mathcal{R}^{\mathrm{PCA}}_d$ amplitudes in each patient classified by occluded artery. 63

3.4 Example of time course evolution of $d^{\mathrm{PCA}}_{w,\mathrm{T}pe}(s)$ series and T-wave peak-to-end shape changes during control and PCI stages from a particular patient. Panel (a) displays $d^{\mathrm{PCA}}_{w,\mathrm{T}pe}(s)$ evolution, where the balloon inflation time is highlighted with a red line. The shape of both the reference $\boldsymbol{f}^r(\boldsymbol{t}^r)$ MWTPE (solid blue) and each s-th $\boldsymbol{f}^s(\boldsymbol{t}^s)$ MWTPE (red dashed line) are shown in panel (c), with letters indicating their corresponding time instants tagged in (a). Panels (b) and (d) show the $\boldsymbol{f}^s(\boldsymbol{t}^s)$ MWTPEs (red lines) corresponding to the $d^{\mathrm{PCA}}_{w,\mathrm{T}pe}(s)$ series for the control and PCI stages, respectively. The blue line represents the reference $\boldsymbol{f}^r(\boldsymbol{t}^r)$ MWTPE. Note that the $d^{\mathrm{PCA}}_{w,\mathrm{T}pe}(s)$ value at the end of the occlusion has already started to decrease. This is a consequence of the 15-second window, centered at the analyzing point, which enters in the computation of $\boldsymbol{f}^s(\boldsymbol{t}^s)$ and then already introducing parts where the ischemia is reducing 64

3.5 Time course of $d^{\mathrm{PCA}}_{w,\mathrm{T}pe}(s)$, represented as the average across all patients $\overline{d}^{\mathrm{PCA}}_{w,\mathrm{T}pe}$, in the study population and segregated by occluded artery. Alignment was performed relative to (a) the recording onset in control records and (b) the onset of the balloon inflation in PCI records. The upper panels show the number of averaged recordings, $P(s)$ at a given time s. 65

3.6 Percentage of patients with $\mathcal{R}^l_d > 2$ (blue bars), $\mathcal{R}^l_d > 5$ (red bars) and $\mathcal{R}^l_d > 10$ (orange bars) in each individual lead l measured at the end of occlusion and segregated by occluded coronary artery group: (a) RCA, (b) LAD and (c) LCX. 66

3.7 Average lead distributions of $\bar{d}^l_{w,\mathrm{T}pe}$ in each occluded coronary artery, segregated by group: (a) RCA, (b) LAD and (c) LCX. The square represents the mean and the error bars represent $\pm$ standard deviation. 67

3.8 Average over patients of the $\mathcal{R}^{\mathrm{PCA}}_{\mathcal{I}}$ time-course aligned to the onset of the balloon inflation during PCI recording, and numbers of patients averaged at a given time. Dash black line and the left y-axis correspond to the number of averaged recordings. 68

3.9 Percentage of patients with $\mathcal{R}^{\mathrm{PCA}}_{\mathcal{I}} \geqslant 2, 5, 10$ segregated by different occlusion times group: 1 min, 2 min, 3 min and 4 min after balloon inflation. 69

4.1 Diagram of the method to obtain each MWTPE, the reference MWTPE, and the $d^{\mathrm{PCA}}_{w,\mathrm{T}_{pe}}$ series. The MWTPE $\boldsymbol{f}^s(\boldsymbol{t}^s)$ was extracted from each s-th 15-second windows (represented by red color), with 5 seconds sliding and 10 seconds overlap the entire record, while MWTPE $\boldsymbol{f}^r(\boldsymbol{t}^r)$ was estimated from the waves within the first 60 seconds, at the beginning of the baseline period (blue color). The bottom rightmost graph shown the warping function $\gamma^*(t^r)$ (dotted red line) relating optimally the reference $\boldsymbol{f}^r(\boldsymbol{t}^r)$ and studied $\boldsymbol{f}^s(\boldsymbol{t}^s)$ MWTPEs. The green region between $\gamma^*(t^r)$ and t^r denotes the total warping amount, quantified by $d^{\mathrm{PCA}}_{w,\mathrm{T}_{pe}}$. 79

4.2 Example of an ECG signal and T_{pe} interval waveform changes during coronary occlusion for a particular pig. Panel (a) shows representative QRST complexes recorded in 8 independent ECG leads and their projection on the first PCA transformed lead at 1, 3, 6, 9, 12, 15, 18, 20th and 21th minutes of LAD-occlusion, followed by ventricular fibrillation episode. Note that from the 20:21 min onwards the ECG beat shape is lost and the VF episode starts. Panel (b) shows the MWTPEs at the first PCA lead corresponding to each s-th window where ECG beat from panel (a) is contained, the blue line represents the reference $\boldsymbol{f}^r(\boldsymbol{t}^r)$ MWTPE and the red line each s-th given $\boldsymbol{f}^s(\boldsymbol{t}^s)$ MWTPE. 81

4.3 Example of $d^{\mathrm{PCA}}_{w,\mathrm{T}_{pe}}(s)$ time course evolution along baseline and occlusion period for two particular animals, one who suffered a VF event (top) and one who did not (bottom). The black dashed line represents the onset of balloon inflation and the red dashed line, the occurrence of the VF episode. 82

4.4 Average time course of $d^{\mathrm{PCA}}_{w,\mathrm{T}_{pe}}$ and $\mathrm{T}^{\mathrm{PCA}}_{pe}$ indices (mean (blue line) $\pm$ standard deviation (cyan lines)) relative to the onset of the recording in baseline and to the balloon inflation onset during occlusion stage for pigs who suffered VF (Delayed-VF group) in panel (a) and for Non-VF group in panel (b). Purple line and the right y-axis indicate the number of averaged recordings at each given time. Note that the time span of the Delayed-VF and Non-VF groups are different for the occlusion stage due to the VF episodes occurrence. At baseline, the recording time is variable among pigs. 83

4.5 Box plots distributions of $d^{\mathrm{PCA}}_{w,\mathrm{T}_{pe}}$ (a), $\mathrm{T}^{\mathrm{PCA}}_{pe}$ (b) and $d^{\mathrm{PCA}}_{w,\mathrm{T}}$ (c) for the Delayed-VF group (red) and Non-VF group (blue), measured in the first five minutes, 0-5, after the recording onset, at the last five minutes, 5-0, prior the occlusion onset, during occlusion recording at the 1-5, 5-10, 10-15, 15-20, 20-25 five minutes intervals and at the 15-10, 10-5 and 5-0 five minutes intervals prior to VF episode. The black dashed line represents the beginning of balloon inflation and * indicates statistical significance for comparison between groups. 86

4.6 Identification of the optimal $d^{\mathrm{PCA}}_{w,\mathrm{T}_{pe}}$, $\mathrm{T}^{\mathrm{PCA}}_{pe}$ and $d^{\mathrm{PCA}}_{w,\mathrm{T}}$ cut-off values to predict VF during the occlusion. The ROC curve for three intervals: 0-5 minutes (panel (a)) and 5-10 five minutes intervals (panel (b)) after beginning of the occlusion and 5-0 five minutes interval prior to VF episode (panel (c)), are presented. The value of the area under the curve (AUC) is reported at the inside of the panels and the location on the ROC of the optimal thresholds have been marked using color coded arrows. 88

4.7 Kaplan–Meier survival curves for the pigs with $d^{\mathrm{PCA}}_{w,\mathrm{T}_{pe}} \geqslant 20.0$ ms and $d^{\mathrm{PCA}}_{w,\mathrm{T}_{pe}} < 20.0$ ms (a) and for the pigs with $\mathrm{T}^{\mathrm{PCA}}_{pe} \geqslant 85.4$ and $\mathrm{T}^{\mathrm{PCA}}_{pe} < 85.4$ (b) at the 5-10 minutes interval from the balloon inflation onset. The p value (Long Rank) is indicated. 88

5.1 Time-warping analysis underlining the calculation of $d^{\mathrm{PCA}}_{w,\mathrm{T}_{pe}}$ index for a particular pig at two moments of the protocol: (a) baseline (at 5 min before occlusion onset) and (b) at 5 min after ischemia onset. In each panel, the left subpanel shows the reference MWTPE $\boldsymbol{f}^r$ (blue) and the study MWTPE $\boldsymbol{f}^s$ (red), showing the non-uniform temporal reparemetrization required for alignment. The right subpanels displays the corresponding optimal warping function $\gamma^*(\boldsymbol{t}^r)$ (red) relative to the reference $\boldsymbol{t}^r$ (blue). The green shaded area represents the amount of warping quantified by $d^{\mathrm{PCA}}_{w,\mathrm{T}_{pe}}$ index. 98

5.2 Representative time course of $d^{\mathrm{PCA}}_{w,\mathrm{T}_{pe}}$ index during baseline and coronary occlusion for two pigs, one that developed VF (top panel) and one that remained VF-free (bottom panel). The black dashed line marks the onset of occlusion, and the red dashed line the occurrence of VF event. At the predefined study instants $t \in \mathcal{T}$ (blue dashed lines), both the $d^{\mathrm{PCA}}_{w,\mathrm{T}_{pe}}$ (purple) and the DOR (dark red) values (both in ms) are indicated. 101

5.3 Boxplots distribution of $d^{\mathrm{PCA}}_{w,\mathrm{T}_{pe}}$, DOR and T_{pe} values at predefined time points, shown for the delayed-VF group (red) and the Non-VF group (blue). Specific time points were at baseline (5 min before occlusion onset), during coronary occlusion (at 1, 2.5, 5, 10, 15, 20, 25, 30, 35, and 40 min), and immediately before VF onset (at points from 0–5 and 5–10 min intervals prior to VF). In Non-VF pigs, these two additional reference measurements were taken with respect to 27:10 min from occlusion onset. BO and BVF denote before occlusion onset and before VF onset, respectively. * indicates statistical significance for comparison between groups. 104

5.4 SPM results for the comparison between Delayed-VF and Non-VF groups over the time window (5 min before occlusion, 1, 2.5, 5, 10, and 15 min after occlusion onset) for $d^{\mathrm{PCA}}_{w,\mathrm{T}_{pe}}$, DOR and T_{pe}. The solid black curve represents the SPM(t) statistic, and the dashed red lines indicate the critical threshold for statistical significance. Significant temporal clusters are highlighted in gray, with the corresponding cluster-level p-values reported in each panel. BO denotes before occlusion onset. 105

5.5 ROC analysis for delayed-VF risk prediction of $d^{\mathrm{PCA}}_{w,\mathrm{T}_{pe}}$, DOR and T_{pe} indices at t of 5 (a), 10 (b), and 15 (c) minutes after coronary occlusion. Optimal cut-off values for delayed-VF prediction are marked on the plot. The AUC is also indicated. 106

5.6 Kaplan-Meier survival curves for VF occurrence based on thresholds derived from ROC analysis. Panels (a–c) show survival probabilities stratified by $d^{\mathrm{PCA}}_{w,\mathrm{T}_{pe}}$ at 5, 10, and 15 minutes after coronary occlusion, respectively. Panels (d–f) and (g-i) depict the corresponding results at the same time points for DOR and T_{pe}, respectively. Threshold values are indicated within each plot, and Log-Rank p-values are reported. 108

6.1 Diagram of the method to obtain the time-warping-based index, TMV. The color blue across panels corresponds to the healthy general condition, and the red one to LQT2. A, illustrative median ECG beat derived from the 10-second ECG recording in lead I for a particular patient. B, a median T-wave (red line) extracted from panel A for an individual patient together its corresponding sex-, heart rate–, and lead-specific normal reference wave (blue line) derived from the UKB cohort represented by panel C. The green dashed lines illustrate temporal pointwise differences that would be necessary to optimally match $\boldsymbol{f}^s$ wave with $\boldsymbol{f}^r$ wave. D, warping function $\gamma(\boldsymbol{t}^r)$ (solid red line) that optimally relates the reference $\boldsymbol{f}^r(\boldsymbol{t}^r)$ and studied $\boldsymbol{f}^s(\boldsymbol{t}^s)$ waves. TMV index representing the total amount of warping is depicted by the green dashed line area between $\gamma(\boldsymbol{t}^r)$ and $\boldsymbol{t}^r$ 120

6.2 Probability of cardiac-event-free survival over lifetime censored at age of 60 in LQT2 patients dichotomized by the 25th percentile cut-off of the lead I-derived TMV index: time to first cardiac event (panel A) and time to first ventricular arrhythmia (panel B). 126

7.1 Estimation of the T-wave peak-to-end morphology restitution index, TPEMR. (a) Histogram of RR intervals; the orange bar indicates the median RR interval, while blue and red bars denote the two bins defining the maximum intra-subject RR range, ΔRR. (b) MWTPEs corresponding to the RR values highlighted in panel (a). (c) Estimation of the $d^{\mathrm{PCA}}_{w,\mathrm{T}_{pe}}$ index obtained by time-warping of the two MWTPEs, where the sum of the green and yellow areas represent the original unweighted estimatation, while the yellow area represents the derivative-weighted estimation. The TPEMR index is calculated as $|d^{\mathrm{PCA}}_{w,\mathrm{T}_{pe}}|$ normalized by ΔRR. 137

7.2 Diagram of the method to obtain the time-warping-based index, TPEMV. Beats from the 24-hour Holter ECG recording were assigned to RR interval bins, B_b, according to their corresponding RR value. For each RR bin and analyzed lead, a patient-specific MWTPE was computed from the beats retained within that bin. The median RR interval of the beats in the bin was used, together with sex and lead information, to select the corresponding normal reference waveform from the UK Biobank-derived reference library. The TPEMV index was then obtained by the time-warping of the patient-specific MWTPE and its matched reference waveform. The resulting warping function quantified the morphology variation between both T_{pe} segments, with the shaded area in green representing the amount of warping used to compute TPEMV. 139

7.3 Box plot distributions of TPEMR (a), ΔT*pe* (b), and TMR (c) for CG (blue) and BrS patients (red), shown for the PCA-transformed lead, $V1_{2IC}$, and $V2_{2IC}$. * indicates statistical significance, $p < 0.05$. 144

7.4 Comparison of TPEMR (a), ΔT*pe* (b), and TMR (c) distributions between BrS-I (purple) and BrS-II (green) patients in the PCA-transformed lead and the $V1_{2IC}$ and $V2_{2IC}$ leads. * and ** indicate statistical significance at $p < 0.05$ and $p < 0.01$, respectively. 144

7.5 Box plot distributions of TPEMR (a), ΔT*pe* (b), and TMR (c) for BrS-A (purple) and BrS-S (green) patients in the PCA-transformed lead and the $V1_{2IC}$ and $V2_{2IC}$ leads. No statistically significant differences were observed between groups. 145

7.6 Distributions of TPEMV across the analyzed RR intervals for CG (blue) and BrS patients (red) in $V1_{4IC}$ (a) and $V2_{4IC}$ (b). *, **, and ***, indicate $p < 0.05$, $p < 0.01$, and $p < 0.001$, respectively. 147

7.7 Comparison of TPEMV values between BrS-A (blue) and BrS-S (red) patients over the analyzed RR intervals in $V1_{4IC}$ (a) and $V2_{4IC}$ (b). * indicates statistical significance at $p < 0.05$. 149

7.8 Box plot distributions of T*pe* for BrS-I (blue) and BrS-II (red) patients across the analyzed RR intervals in V14IC (a) and $V2_{4IC}$ (b). * indicates statistical significance at $p < 0.05$. 150

LIST OF TABLES

3.1 $\mathcal{R}_d^{\mathrm{PCA}}$ prevalence classification in the study population according to the stage test 61

3.2 $\mathcal{R}_d^{\mathrm{PCA}}$ prevalence classification in the study population according to the occluded artery, gender, and evidence of previous infarction. 62

3.3 Classification of $\mathcal{R}_{\mathcal{I}}^{\mathrm{PCA}}$ prevalence and time instant in which it was exceeded in the study population according to the different indices. 68

4.1 Pig population and VF distribution. 77

4.2 Median and p-value from selected intervals for $d_{w,\mathrm{T}_{pe}}^{\mathrm{PCA}}$, $\mathrm{T}_{pe}^{\mathrm{PCA}}$ and $d_{w,\mathrm{T}}^{\mathrm{PCA}}$ indices segregated by VF susceptibility. 85

4.3 Threshold values together with sensibility and specificity values for VF prediction, and the AUC for $d_{w,\mathrm{T}_{pe}}^{\mathrm{PCA}}$, $\mathrm{T}_{pe}^{\mathrm{PCA}}$ and $d_{w,\mathrm{T}}^{\mathrm{PCA}}$ indices, calculated at three different time intervals. 87

4.4 Association of $d_{w,\mathrm{T}_{pe}}^{\mathrm{PCA}}$ and $\mathrm{T}_{pe}^{\mathrm{PCA}}$ with the ocurrence of VF episodes. 88

5.1 Distribution of VF incidence by groups 100

5.2 Values of the indexes across the cohort, median [IQR] (ms) in baseline and occlusion period 102

5.3 Medians and p-values at specific time points for $d^{\mathrm{PCA}}_{w,\mathrm{T}_{pe}}$, DOR and T_{pe} indices stratified by delayed-VF susceptibility. For Non-VF animals, the two last measurements were taken considering 27:10 min from occlusion onset as the reference. 103

5.4 ROC-derived threshold values, sensitivity, specificity, and AUC for delayed-VF prediction using $d^{\mathrm{PCA}}_{w,\mathrm{T}_{pe}}$, DOR and T_{pe} indices, calculated at $t \in \{5, 10, 15\}$ minutes after coronary occlusion. p-values from DeLong's test for correlated ROC curves are also reported for the comparisons $d^{\mathrm{PCA}}_{w,\mathrm{T}_{pe}}$ vs DOR and $d^{\mathrm{PCA}}_{w,\mathrm{T}_{pe}}$ vs T_{pe} . . 107

5.5 Cox regression results for delayed-VF stratification by $d^{\mathrm{PCA}}_{w,\mathrm{T}_{pe}}$, DOR and T_{pe} indices at 5, 10, and 15 minutes after occlusion, including ROC-derived thresholds, hazard ratios, 95% CI, and p-values 109

5.6 Slope and R^2 for $d^{\mathrm{PCA}}_{w,\mathrm{T}_{pe}}$ vs. DOR and T_{pe} vs. DOR; median [IQR] across pigs 109

6.1 Clinical characteristics of LQT2 patients 123

6.2 Characteristics of LQT2 patients based on cut-offs of the 25th percentile (Q1) of the TMV index 125

6.3 Risk of cardiac events and ventricular arrhythmias in LQT2 patients: Cox regression analysis dichotomized by the 25th percentile of the TMV index derived from lead I. 127

6.4 Risk of cardiac events in LQT2 patients: Cox regression analysis dichotomized by the 25th percentile of the TMV index derived from leads PC1, II and V1–V6. 127

7.1 Clinical and demographic characteristics of the study population. 142

7.2 Median [IQR] values and corresponding p-values for TPEMR, $\Delta \mathrm{T}pe$, and TMR in the PCA-transformed lead and the $\mathrm{V1}_{\mathrm{2IC}}$ and $\mathrm{V2}_{\mathrm{2IC}}$ leads across the three predefined group comparisons. Bold values indicate statistical significance, $p < 0.05$. 143

7.3 Summary of significant group differences for morphology variation markers. For each comparison, the direction of the median difference, the RR intervals showing statistical significance, and the number of significant bins are reported. A dash indicates that no statistically significant RR intervals were identified 146

7.4 Summary of the group comparisons for T_{pe}, T_w, and QRS_d in $V1_{4IC}$ and $V2_{4IC}$. The direction of the median difference, the RR intervals showing statistical significance, and the number of significant bins out of the 15 analyzed bins are reported. A dash indicates that no statistically significant RR intervals were identified. 148